

MATHEMATICAL MODELLING OF AN INDUSTRIAL STEAM METHANE REFORMER

by

Dean Latham

A thesis submitted to the Department of Chemical Engineering

In conformity with the requirements for
the degree of Master of Science (Engineering)

Queen's University

Kingston, Ontario, Canada

(December 2008)

Copyright © Dean Andrew Latham, 2008

Abstract

A mathematical model of a steam-methane reformer (SMR) was developed for use in process performance simulations and on-line monitoring of tube-wall temperatures. The model calculates temperature profiles for the outer-tube wall, inner-tube wall, furnace gas and process gas. Reformer performance ratios and composition profiles are also computed. The model inputs are the reformer inlet-stream conditions, the geometry and material properties of the furnace and catalyst-bed. The model divides the furnace and process sides of the reformer into zones of uniform temperature and composition. Radiative-heat transfer on the furnace side is modeled using the Hottel Zone method. Energy and material balances are performed on the zones to produce non-linear algebraic equations, which are solved using the Newton-Raphson method with a numerical Jacobian. Model parameters were ranked from most-estimable to least estimable using a sensitivity-based estimability analysis tool, and model outputs were fitted to limited data from an industrial SMR. The process-gas outlet temperatures were matched within 4 °C, the upper and lower peep-hole temperatures within 12 °C and the furnace-gas outlet temperature within 4 °C. The process-gas outlet pressure, composition and flow rate are also accurately matched by the model. The values of the parameter estimates are physically realistic. The model developed in this thesis has the capacity to be developed into more specialized versions. Some suggestions for more specialized models include modeling of separate classes of tubes that are in different radiative environments, and detailed modeling of burner configurations, furnace-gas flow patterns and combustion heat-release patterns.

Acknowledgements

I would like to thank the following people for their support during this project: My supervisors Kim McAuley and Brant Peppley, our industrial contact Troy Raybold, our combustion expert and emeritus professor Henry Becker, Royal Military College professor Chris Thurgood, our RADEX contacts Duncan Lawson, Robert Tucker and Jason Ward, the technical support of Hartmut Schmider, Dustin Bepalko and Jon Pharoah, my officemates Saeed Variziri, Duncan Thompson, Shaohua Wu, Dharmesh Goradia, Hui Yuan and Valeria Koeva, and my Mom and Dad.

Kim and Brant I would like to thank you for the opportunity to work on this project. I appreciate your time, patience and hard work. Troy, your practical advice, industrial experience and attention to detail have been invaluable in developing a useful product. I hope that you are able to put this thesis to good use in the future. Mom and Dad, thank you for your encouragement and moral support. You knew that I could do this even before I did.

Table of Contents

Abstract.....	ii
Acknowledgements.....	iii
Table of Contents.....	iv
List of Figures.....	x
List of Tables.....	xvi
List of Symbols.....	xviii
Chapter 1 Introduction.....	1
1.1 Problem Statement.....	1
1.2 Steam-Methane Reforming Process Overview.....	3
1.3 Furnace Geometry.....	6
1.4 Available Data.....	8
1.5 Important Physical Phenomena.....	9
1.6 References.....	14
Chapter 2 Literature Review.....	15
2.1 Radiative Heat Transfer Methods used in Furnace Models.....	21
Roesler Flux Method.....	21
Hottel Zone Method.....	24
2.2 Combustion and Heat Release Patterns used in Furnace Models.....	27
2.3 Gas Flow Patterns used in Furnace Models.....	29
2.4 Furnace-Gas-to-Tube-Convective-Heat-Transfer Coefficients used in Furnace Models.....	29
2.5 Fixed Bed Reactor Models used in Reforming Models.....	30
2.6 Reaction Kinetics used in Process Models.....	32
2.7 Pressure Drop Correlations used in Process-Side Models.....	33
2.8 Tube-to-Process-Gas Heat-Transfer Coefficients used in Process-Side Models.....	34
2.9 Sub-Models Chosen for Mathematical Modeling Study.....	37

Comparison and Choice of Furnace Radiation Model.....	38
Choices Limited by Runtime Requirements	41
Widely-Accepted Choices	42
Choices with No Clear Literature Consensus	42
2.10 References.....	43
Chapter 3 Mathematical Modeling Studies.....	50
3.1 Cube-Furnace Model	53
Assumptions in the Cube-Furnace Model.....	54
Cube-Furnace Model Equations	56
Validation of Results.....	56
3.2 Segmented-Tube Model.....	57
Assumptions in the Segmented-Tube Model.....	61
Segmented-Tube Model Equations.....	62
Heat-Release Profile Calculation.....	66
Preliminary Results from the Segmented-Tube Model.....	68
Limitations of the Segmented-Tube Model	72
3.3 Average-Tube Model.....	72
Assumptions in the Average-Tube Model	75
Average-Tube Model Equations	76
3.4 References.....	86
Chapter 4 Model Fitting Using Experimental Data	88
4.1 Available Data, Model Outputs, Inputs and Parameters.....	88
Available Data and Model Outputs.....	88
Model Inputs.....	90
Model Parameters	92

4.2 Calculation of Furnace Heat Loss Coefficient U_{refrac}	96
4.3 Choosing the Number of Vertical Sections.....	98
4.4 Effect of Model Parameters on Simulations	105
4.5 Parameter Ranking.....	114
4.6 Parameter Estimation.....	116
4.7 References.....	126
Chapter 5 Conclusions and Recommendations.....	128
5.1 Conclusions.....	128
5.2 Recommendations.....	131
5.3 References.....	140
Appendix A Radiative Heat Transfer Background	142
Definition of a Blackbody.....	142
Gray Surfaces, Surface Absorptivity and Surface Emissivity	143
Surface Reflectivity	143
Definition of Solid Angle.....	144
Radiation Intensity.....	144
Diffuse Surfaces.....	146
Gas Emissivity and Absorptivity	146
Gas Transmissivity.....	148
Gray Gases.....	148
Kirchoff's Law.....	149
Real Gases.....	150
Weighted-Sum-of-Gray-Gases Model	151
References.....	154
Appendix B Hottel Zone Method	155

Zone Method Overview	155
Exchange and Flux Areas	157
Direct-Exchange Areas	157
Total-Exchange Areas.....	159
Directed-Flux Areas.....	160
Calculation of Directed-Flux Areas.....	165
Total-Exchange Areas and Directed-Flux Areas in this Thesis	166
References.....	167
Appendix C Derivation of Model Equations	169
Cube-Furnace Model Derivations.....	169
Furnace-Surface-Zone Energy Balance (f_i , $i=1..6$)	169
Volume-Zone Energy Balance (f_7)	170
Segmented-Tube Model Derivations	172
Furnace Feed Calculations.....	172
Furnace-Surface Zone Energy Balance (f_i $i=1..50$).....	177
Furnace-Obstacle-Zone Energy Balance (f_i , $i=51..62$)	179
Furnace-Volume-Zone Energy Balance (f_i , $i=63..74$).....	180
Inner-Tube-Surface Energy Balance (f_i , $i=75..86$).....	182
Process-Gas Energy Balance (f_i , $i=87..98$)	183
Process-Gas Material Balance (f_i , $i=99..170$)	187
Pressure-Drop Correlation (f_i , $i=171..174$)	189
Average-Tube Model Derivations (10-Vertical-Section Model).....	190
Calculation of Q_{halokane} : Energy Balance on Isothermal Water-Cracking.....	191
Furnace-Surface-Zone Energy Balance (f_i , $i=1..38$)	193
Furnace-Obstacle-Zone Energy Balance (f_i , $i=39..51$)	194

Furnace-Volume-Zone Energy Balance (f_i , $i=52..62$).....	195
Inner-Tube-Surface Energy Balance (f_i , $i=62..71$).....	196
Process-Gas Energy Balance (f_i , $i=72..81$)	196
Process-Gas Material Balance (f_i , $i=82..140$)	197
Pressure Drop Correlation (f_i , $i=141..150$).....	197
Overall Energy Balances.....	198
Appendix D Solution of Model Equations.....	203
Newton-Raphson Method	203
Initial Guesses	205
Common-Vertical-Segment Initial-Guess Method	205
Sequential-Solution Initial-Guess Method.....	207
Direct-Assignment Initial-Guess Method	207
References.....	208
Appendix E Supplemental Correlations Used in Model.....	209
Enthalpy of Reaction.....	209
Constant Pressure Heat Capacity	209
Furnace-Gas-to-Tube Convective-Heat-Transfer Coefficient	210
Tube-to-Process-Gas Convective-Heat-Transfer Coefficient	211
Gas Viscosity Calculations	212
Gas Thermal Conductivity Calculations	214
Steam-Methane Reforming Reaction Kinetics	215
Friction Factor.....	218
References.....	219
Appendix F Geometric Restrictions, Furnace-Geometry Storage and Process-Side Geometry	
Storage	220
Geometric Subset of RADEX Understood by Model.....	220

Numbering of Zones in RADEX	221
Numbering of Surface Zones in RADEX	222
Numbering of Volume and Obstacle Zones in RADEX	223
Storage and Recollection of Furnace-Zone Properties	227
Storage of Relative Furnace Geometry in Reference Coordinates	228
Volume and Obstacle-Zone Reference Coordinates	228
Surface-Zone Reference Coordinates	229
Recollection of Furnace Geometry	229
Process-Side Geometry	232
Recollection of Process Geometry	233
References	234
Appendix G Validation of RADEX	235
References	237
Appendix H Plant Data	239
Plant Input Data	239
Plant Output Data	242
Appendix I Sensitivity of the Average-Tube Model to Radiation Parameters	243
Appendix J Unfitted Preliminary Simulation Results	246
Appendix K Parameters Values, Temperature Profiles and Composition Profiles for Additional Parameter Sets that Fit the Plant Data	251

List of Figures

Figure 1. Steam-Methane Reforming Process Diagram	3
Figure 2. Detailed Front View of Steam-Methane Reforming Furnace.....	7
Figure 3. Detailed Top View of Steam-Methane Reforming Furnace.....	8
Figure 4. Cross-Section of Quadralobe Catalyst Particle	10
Figure 5. Summary of Furnace Heat Transfer Mechanisms	12
Figure 6. Radiant energy balance on a differential section of furnace.....	22
Figure 7. Cross-Section of Reformer Showing Tubes, Coffin Boxes and Spatial Discretization.	52
Figure 8. Vertical Section without Coffin Boxes in Average-Tube Reformer Model.....	52
Figure 9. Vertical Slab with Coffin Boxes in Average-Tube Reformer Model.....	53
Figure 10. Cube Furnace Numbering Scheme	53
Figure 11. Furnace Feed Mixing and Pre-Combustion.....	63
Figure 12. Comparison of the Segmented-Tube Model Temperature Profiles for the Base Case and Twice the Fuel Flow Rate	70
Figure 13. Comparison of the Segmented-Tube Model Composition Profiles for the Base Case and Twice the Fuel Flow Rate	70
Figure 14. Comparison of the Segmented-Tube Model Temperature Profiles for the Base Case and a Steam-to-Carbon Ratio of 6:1	71
Figure 15. Comparison of the Segmented-Tube Model Composition Profiles for the Base Case and a Steam-to-Carbon Ratio of 6:1	72
Figure 16. Simulated Treatment of Higher Alkanes by Overall Water-Cracking	78
Figure 17. Overall-Energy Balance Diagram	83

Figure 18. Heat release profile for the 10-, 20- and 40-vertical section models. No heat of combustion is released after the zone ending at 3.75 m. The vertical grid lines show the division of the top 3.75 m of the reformer into sections for the 40-vertical-section model.....	99
Figure 19. Cumulative-heat-release profile for the 10-, 20- and 40-vertical-section models. The vertical grid lines show the division of the top 3.75 m of the reformer for the 40-vertical section model.	100
Figure 20. Comparison of the Temperature Profiles for the Average-Tube Model with 10 and 20 Vertical Sections.....	101
Figure 21. Comparison of the Temperature Profiles for the Average-Tube Model with 20 and 40 Vertical Sections.....	102
Figure 22. Comparison of the Composition Profiles for the Average-Tube Model with 10 and 20 Vertical Sections.....	103
Figure 23. Comparison of Process-Gas Composition Profiles for the Average-Tube Model with 10 and 20 Vertical Sections.....	103
Figure 24. Comparison of Temperature Profiles for Models with 15 non-uniform and 20 uniform vertical zones.....	105
Figure 25. Base Case Temperature Profiles Produced using the Parameter Values in Table 18 and the Inputs from Plant B. Plant output data are also shown.....	106
Figure 26. Comparison of the Temperature Profiles for a Heat-Release Length of 6.10 m and the 3.66 m Base Case.....	107
Figure 27. Comparison of the Temperature Profiles for a Fraction of Combustion in Top Furnace Zone of 0.05 and 0.18 Base Case.....	108
Figure 28. Comparison of the Temperature Profiles with a Tube-To-Process-Gas Convective-Heat-Transfer-Coefficient Factor of 2 and 1.....	109

Figure 29. Comparison of the Temperature Profiles for an Adjustable Pre-exponential Parameter of 2 and 1.	110
Figure 30. Comparison of the Temperature Profiles for an Adjustable Pre-exponential Parameter of 0.05 and 1.	111
Figure 31. Comparison of the Temperature Profiles for a PSA Off Gas Flow Rate of 100% ($f_{nOffGas} = 1.0$) and 90% ($f_{nOffGas} = 0.9$).	112
Figure 32. Comparison of the Temperature Profiles for a Combustion Air Flow Rate of 100% ($f_{nCombAir}=1.0$) and 90% ($f_{nCombAir}=0.9$).	113
Figure 33. Comparison of the Temperature Profiles with a Furnace-Gas-To-Tube Convective-Heat-Transfer-Coefficient Factor of 0.5 and 1.....	114
Figure 34. Plot of the Objective Function Value vs the Number of Parameters Estimated for a Heat-release Length of 3.66 m.....	117
Figure 35. Plot of the Objective Function Value vs the Number of Parameters Estimated for a Heat-release Length of 4.27 m.....	118
Figure 36. Plot of the Objective Function Value vs the Number of Parameters Estimated for a Heat-release Length of 4.88 m.....	119
Figure 37. Plot of the Objective Function Value vs the Number of Parameters Estimated for a Heat-release Length of 5.49 m.....	119
Figure 38. Plot of the Objective Function Value vs the Number of Parameters Estimated for a Heat-release Length of 6.10 m.....	120
Figure 39. Plant A Temperature Profiles using the Best-fit Parameters from Table 22	122
Figure 40. Plant B Temperature Profiles using the Best-fit Parameters from Table 22	123
Figure 41. Plant C1 Temperature Profiles using the Best-fit Parameters from Table 22.....	123
Figure 42. Plant C2 Temperature Profile using the Best-fit Parameters from Table 22	124

Figure 43. Vertical section of reformer showing two classes of tubes. Wall tubes are shown in gray and internal tubes shown in white.....	136
Figure 44. Top view of reformer showing the location of wall tubes and gap tubes.....	137
Figure 45. Vertical section in the reformer with the furnace-volume zone divided to simulate rows of hot gas beneath the burner rows.....	139
Figure 46. Geometry of a Ray of Radiation.....	145
Figure 47. A Diffuse Emitter	146
Figure 48. Definition of Gas Emissivity	147
Figure 49. Definition of Gas Absorptivity.....	147
Figure 50. Dependence of Absorption Coefficient on Wavelength.....	151
Figure 51. Representation of a Real Gas as Three Gray Gases and one Clear Gas	152
Figure 52. Diagram of the Left-Handed Coordinate System used in RADEX and a Cube defined by Vertices in the XY-plane and Projection into the Z-direction.	220
Figure 53. RADEX Zone Numbering Example.....	224
Figure 54. Segmented-Tube Model Zone Numbering	225
Figure 55. Average-Tube Model Zone Numbering	226
Figure 56. Zone Numbering Pattern in RADEX and the Average-Tube Model.....	227
Figure 57. Reference Coordinates for the Average Tube Model.....	230
Figure 58. The Location of Unknowns on the Process Side of the Average Tube Model.....	232
Figure 59. Diagram of cylinder.....	237
Figure 60. Comparison of Temperature Profiles between the base case (tube emissivity of 0.85) and a case with a tube emissivity of 0.95. The values of the adjustable parameters are shown in Table 18 with the exception of the heat-release profile which is the 3.66 m profile from Table 20. The input data is from Plant B.	243

Figure 61. Comparison of Temperature Profiles between the base case (refractory emissivity of 0.60) and a case with a refractory emissivity of 0.75. The values of the adjustable parameters are shown in Table 18 with the exception of the heat-release profile which is the 3.66 m profile from Table 20. The input data is from Plant B.	244
Figure 62. Comparison of Temperature Profiles between the base case ($K_1 = 0.300 \text{ m}^{-1}$ $K_2 = 3.10 \text{ m}^{-1}$ and $K_3 = 42.9 \text{ m}^{-1}$) and a case with 20% more carbon dioxide in the furnace gas ($K_1 = 0.331 \text{ m}^{-1}$ $K_2 = 3.72 \text{ m}^{-1}$ $K_3 = 51.5 \text{ m}^{-1}$). The values of the adjustable parameters are shown in Table 18 with the exception of the heat-release profile which is the 3.66 m profile from Table 20. The input data is from Plant B.	245
Figure 63. Temperature Profiles Generated using the Inputs from Plant A and the Unfitted Parameter Values from Table 18	246
Figure 64. Composition Profiles Generated using the Inputs from Plant A and the Unfitted Parameter Values from Table 18	247
Figure 65. Temperature Profiles Generated using the Inputs from Plant B and the Unfitted Parameter Values from Table 18	247
Figure 66. Composition Profiles Generated using the Inputs from Plant B and the Unfitted Parameter Values from Table 18	248
Figure 67. Temperature Profiles Generated using the Inputs from Plant C1 and the Unfitted Parameter Values from Table 18	248
Figure 68. Composition Profiles Generated using the Inputs from Plant C1 and the Unfitted Parameter Values from Table 18	249
Figure 69. Temperature Profiles Generated using the Inputs from Plant C2 and the Unfitted Parameter Values from Table 18	249
Figure 70. Composition Profiles Generated using the Inputs from Plant C2 and the Unfitted Parameter Values from Table 18	250

Figure 71. Temperature Profiles Generated using the Inputs from Plant A and the Parameter Values from Table 32.....	251
Figure 72. Composition Profiles Generated using the Inputs from Plant A and the Parameter Values from Table 32.....	252
Figure 73. Temperature Profiles Generated using the Inputs from Plant C2 and the Parameter Values from Table 32.....	252
Figure 74. Composition Profiles Generated using the Inputs from Plant C2 and the Parameter Values from Table 32.....	253
Figure 75. Temperature Profiles Generated using the Inputs from Plant A and the Parameter Values from Table 33.....	254
Figure 76. Composition Profiles Generated using the Inputs from Plant A and the Parameter Values from Table 33.....	254
Figure 77. Temperature Profiles Generated using the Inputs from Plant C2 and the Parameter Values from Table 33.....	255
Figure 78. Composition Profiles Generated using the Inputs from Plant C2 and the Parameter Values from Table 33.....	255

List of Tables

Table 1. Complete Steam-Methane Reforming Models	16
Table 2. Furnace Side Models	18
Table 3. Process Side Models	20
Table 4. Comparison of Hottel zone and Roesler Flux Methods.....	40
Table 5. Incremental Model Development	51
Table 6. Cube-Furnace Model Structure.....	54
Table 7. Vector Equation f and Unknown Vector x for the Cube-Furnace Model.....	54
Table 8. Cube-Furnace Model Constants.....	55
Table 9. Solution to Cube-Furnace Model.....	57
Table 10. Structure of the Segmented-Tube Model.....	58
Table 11. Vector Equation $f=0$ and Unknown Vector x for the Segmented-Tube Model.....	59
Table 12. Parameter Values for Preliminary Segmented Tube Simulations.....	69
Table 13. Structure of the Average-Tube Model with 10 Vertical Sections.....	73
Table 14. Vector Equation $f=0$ and Unknown Vector x for the Average-Tube Model with 10 Vertical Sections	74
Table 15. Model Outputs and Plant Data used in Parameter Estimation	89
Table 16. Model Inputs	90
Table 17. List of Non-adjustable Parameters.....	93
Table 18. Adjustable Parameters	96
Table 19. Computation Time for Models with 10, 20, 40 and 15.....	104
Table 20. Heat-release Profiles used in Estimability Analysis. The Profiles were generated using equations (36) to (42).....	115
Table 21. Ranking of Adjustable Parameters using the Estimability.....	116

Table 22. Best-Fit Values of the Estimable Parameters, including the Heat-Release Length	121
Table 23. Comparison of Model Outputs and Plant Data used in Parameter Estimation but not shown in Figure 39 to Figure 42.	124
Table 24. Furnace-Zone Type and Process-Side Segment Initial	206
Table 25. Structure of the Furnace Zone Properties Database	227
Table 26. Summary of How to Switch Between Zone Indices and Tube Segments.....	233
Table 27. Comparison of total exchange areas from RADEX and figure 7-13 of Hottel and Sarofim (1968) for cubes with different side lengths and absorption coefficients	236
Table 28. Comparison of view factors from RADEX and configuration 4 of Sparrow and Cess (1978) for the geometry in Figure 59.....	237
Table 29. Furnace-Side Input Data	239
Table 30. Process-Side Input Data.....	241
Table 31. Model Outputs and Plant Data used in Parameter Estimation	242
Table 32. Parameter Values for the 4.88 m Heat-Release Length with 4 Fitted Parameters	251
Table 33. Parameter Values for the 5.49 m Heat-Release Length with 7 Fitted Parameters	253

List of Symbols

Symbol	Units	Name
$a_k, a_k(T)$	[none]	Gray-gas weighting coefficient for atmosphere k
a, b, c	$\left[\frac{1}{m^2}\right], \left[\frac{1}{m}\right], [\text{none}]$	Coefficients in the parabolic heat release profile
A, A_i	$[m^2]$	Surface or obstacle zone area
$A_{\text{fur cross}}$	$[m^2]$	Cross-sectional area of the furnace
A, B, C, D A_i, B_i, C_i, D_i	$\left[\frac{J}{\text{gmol} \cdot K}\right], \left[\frac{J}{\text{gmol} \cdot K^2}\right],$ $\left[\frac{J}{\text{gmol} \cdot K^3}\right], \left[\frac{J}{\text{gmol} \cdot K^4}\right]$	Constant pressure heat capacity parameters Constant pressure heat capacity parameters for species i
$b_{1,k}$	[none]	Parameter one for Taylor and Foster weighting coefficient model in gray gas atmosphere k
$b_{2,k}$	$\left[\frac{1}{K}\right]$	Parameter two for Taylor and Foster weighting coefficient model in gray gas atmosphere k
C_p $C_{p,i}$	$\left[\frac{J}{\text{gmol} \cdot K}\right]$	Constant pressure heat capacity of a gas mixture Constant pressure heat capacity of species i
$D_{\text{fur hydr}}$	[m]	Hydraulic diameter of the furnace
D_p	[m]	Equivalent particle diameter
E_{fur} E_{proc} E_{refrm}	$\left[\frac{J}{h}\right]$	Error in the overall furnace-side energy balance Error in the overall process-side energy balance Error in the overall reformer energy balance

E_{ni}	$\left[\frac{\text{gmol}_i}{\text{h}} \right]$	Error in the process-side material balance for species i
$\Delta E_{\text{reaction}}$ $\Delta E_{T\text{-change}}$	$\left[\frac{\text{J}}{\text{gmol}} \right]$	Internal energy change due to a generic reaction Internal energy change due to medium temperature change
f	[none]	Friction factor
f_i	Various Units	Model equation i
G_s	$\left[\frac{\text{kg}}{\text{m}^2\text{h}} \right]$	Superficial mass velocity
h_{gso} h_{tg}	$\left[\frac{\text{J}}{\text{m}^2\text{h} \cdot \text{K}} \right]$	Furnace-gas-to-surface convective heat transfer coefficient Tube-to-process-gas convective heat transfer coefficient
H_i	$\left[\frac{\text{J}}{\text{gmol}} \right]$	Enthalpy of stream i
$\Delta H_{f,i}^T$	$\left[\frac{\text{J}}{\text{gmol}} \right]$	Enthalpy of formation of species i at temperature T
$\Delta H_{\text{reaction}}$ $\Delta H_{\text{comb},i}$ ΔH_i $\Delta H_{\text{wcrack},i}$	$\left[\frac{\text{J}}{\text{gmol}} \right]$	Heat of reaction for a generic reaction Heat of combustion for species i Heat of reaction for reactions i Heat of water cracking for species i
k_{refrac} k_{tube} k_{er}	$\left[\frac{\text{J}}{\text{m} \cdot \text{h} \cdot \text{K}} \right]$	Furnace refractory thermal conductivity Reformer tube thermal conductivity Effective thermal conductivity of the packed bed

K_k	$\left[\frac{1}{m} \right]$	Gray-gas absorption coefficient for atmosphere k
L	[m]	Cube side length for cube furnace model
L_Q	[m]	Heat-release length
\dot{m}_{tot} \dot{m}_{fur}	$\left[\frac{kg}{h} \right]$	Total mass flow rate of the process gas Total mass flow rate of the furnace gas
M_k	$\left[\frac{kg}{gmol} \right]$	molar mass of species k
n_Q	[none]	Number of zones where heat is released by combustion
\dot{n}_{fur} \dot{n}_i \dot{n}_{CH_4}	$\left[\frac{gmol}{h} \right]$	Molar flow rate of furnace gas Molar flow rate of stream i Molar flow rate of methane gas
$\Delta n_{reaction}$ Δn_i Δn_{comb}	[none]	Change in the number of moles per mole of reactant consumed with a stoichiometric coefficient of 1 for a generic reaction, reaction i and combustion
P $P_{i,k}$	[kPa]	Total pressure in a zone or tube segment Partial pressure variable i corresponding to species k
Pr	[none]	Prandtl number
Q_{fur}	$\left[\frac{J}{h} \right]$	Rate of combustion heat and work energy released in the furnace by combustion.

r_{out}	[m]	Outer tube radius
r_{in}		Inner tube radius
R	$\left[\frac{J}{\text{gmol} \cdot K} \right]$ or $\left[\frac{\text{kPa} \cdot \text{m}^3}{\text{gmol} \cdot K} \right]$	Universal gas constant
Re	[none]	Reynolds number
t_{refrac}	[m]	Refractory thickness
Δt	[h]	Period of time
T_i , $T_{fur in}$, $T_{adj gas}$, $T_{proc gas}$, T_{surr} , $T_{in wall}$, $T_{out wall}$, $T_{fur abv}$, T_{ref} , T_{std} , T_{adb}	[K]	Temperature of unknown i Furnace inlet temperature Adjacent furnace gas zone temperature Temperature of the process gas in a tube segment Temperature of the surroundings Inner tube wall temperature Outer tube wall temperature Temperature of the above furnace gas zone Reference temperature Standard temperature 536.4°R or 298K Adiabatic flame temperature

v_s	$\left[\frac{m_{pg}^3}{m_{reactor}^2 \cdot h} \right]$	Process gas superficial velocity
V	$[m^3]$	Volume
x_i	Various Units	Unknown variable i in model equations
X_i $X_{i, fur}$ $X_{i, proc}$	$\left[\frac{gmol_i}{gmol_{tot}} \right]$	Mole fraction of species i, Mole fraction of species i in the furnace gas Mole fraction of species i in the process gas
Δy	$[m]$	Height of a vertical section
Y_i	$\left[\frac{kg_i}{kg_{tot}} \right]$	Mass fraction of species i
$\overrightarrow{Z_i Z_j}$	$[m^2]$	Directed-flux area between sending zone i and receiving zone j
$\overline{Z_i Z_j}_k$	$[m^2]$	Total-exchange area between sending zone i and receiving zone j in gray gas atmosphere k
α_{top}	$[none]$	Fraction of combustion heat released in the top furnace volume zone
$\alpha(k_i)$	$[none]$	Fraction of combustion heat released in furnace zone i
$\gamma_{i,j}$	$[none]$	Number of atoms of type i in species j
ϵ_{refrac} ϵ_i	$[none]$	Furnace refractory emissivity Emissivity of unknown i
η_i	$[none]$	Effectiveness factors for reaction i
λ_{pg} λ_{fg}	$\left[\frac{J}{m \cdot h \cdot K} \right]$	Thermal conductivity of the process gas Thermal conductivity of the furnace gas

μ_{pg}	$\left[\frac{\text{kg}}{\text{m} \cdot \text{h}} \right]$	Dynamic viscosity of the process and furnace gas
μ_{fg}		Dyamic viscosity of the furnace gas
$\xi_{\text{reaction},k}$	$\left[\frac{\text{gmol}_k}{\text{gmol}_{\text{reactant}} \text{ with } \xi=1} \right]$	Stoichiometric coefficient for species k in a generic reaction
$\xi_{1-3,k}$		Stoichiometric coefficient for species k in reforming reaction 1, 2 and 3
ρ_{cat}	$\left[\frac{\text{kg}_{\text{cat}}}{\text{m}^3_{\text{tube}}} \right]$	Catalyst packing density
ρ_i	$\left[\frac{\text{kg}}{\text{m}^3} \right]$	Uknown density variable i
ρ_{pg}	$\left[\frac{\text{kg}}{\text{m}^3} \right]$	Mass density of the process gas
σ	$\left[\frac{\text{J}}{\text{h} \cdot \text{m}^2 \text{K}^4} \right]$	Boltzmann constant
ϕ	[none]	Bed porosity on the process-side

Chapter 1

Introduction

1.1 Problem Statement

In steam-methane reforming, methane gas and steam are converted into hydrogen gas, carbon monoxide and carbon dioxide by a sequence of net endothermic reactions. These reactions occur in catalyst-filled tubes contained within a furnace. The furnace is heated by burning natural gas and process offgas. A detailed overview of the steam-methane reforming process is given in section 1.2.

The reformer is the central unit in a steam-methane-reforming plant. The reformer has separate process and furnace sides that interact through the exchange of energy. The process side consists of reactants, intermediates and products and is contained within metal tubes filled with catalyst. The furnace side consists of the combustion products contained by refractory walls. Material from the process side and furnace side do not mix.

The tubes in a steam-methane reformer are one of the most expensive plant components. The cost of retubing a typical 60 Mmol per day (50MMscfd) hydrogen plant is approximately 10% of the installed plant cost (Fisher, 2004). Reformer tubes are made of metal alloys that experience creep at high temperatures. Over time creep can lead to tube failure, resulting in costly tube replacements, plant shut downs and production losses (Cromarty, 2004). Reformer tubes are designed with an expected life, typically 100 000 hours. The expected life of a tube is calculated from its metallurgic properties, the operating pressure and operating temperature (Cromarty, 2004). The expected tube life is very sensitive to changes in operating temperature. A general

rule of thumb is that an increase in tube-wall temperature of 20 °C will decrease the tube life expectancy by half for a given alloy at its design pressure (Farnell, 2003).

The goal of this project is to develop a fundamental model that calculates the outer-tube-wall temperature profile for a given set of inputs. The inputs include furnace geometry, furnace material properties, catalyst properties and reformer feed properties. The model is designed to give acceptable results using minimal computation time, so that the model can be used to monitor tube-wall temperatures online. The tube-wall temperature profiles will help plant operators mitigate the risk of tube failure. In addition to predicting the tube-wall temperature profile, the model will also predict the furnace-gas temperature profile, tube-wall heat-flux profile, process-gas temperature profile, process-gas composition profile and furnace-gas exit composition.

This thesis is organized into five chapters, an introduction, literature review, mathematical modeling studies, model fitting using experimental data, and conclusions and recommendations. The introduction gives an overview of the SMR process and a detailed description of the furnace geometry, available plant data and important physical phenomena. The literature review chapter classifies and summarizes the simplifying assumptions made in existing SMR models and selects a set of simplifying assumptions appropriate for this study. The chapter on mathematical modeling studies describes the progressive development of the model from i) a simple cube-shaped combustion chamber containing combustion gases to ii) a single reformer tube in a rectangular furnace to iii) a complete SMR model with multiple tubes. The chapter on model fitting contains the statistical analysis and parameter estimation using plant data, followed by some simulation results. The conclusions and recommendations chapter summarizes thesis results and suggests areas for model improvement and future studies.

1.2 Steam-Methane Reforming Process Overview

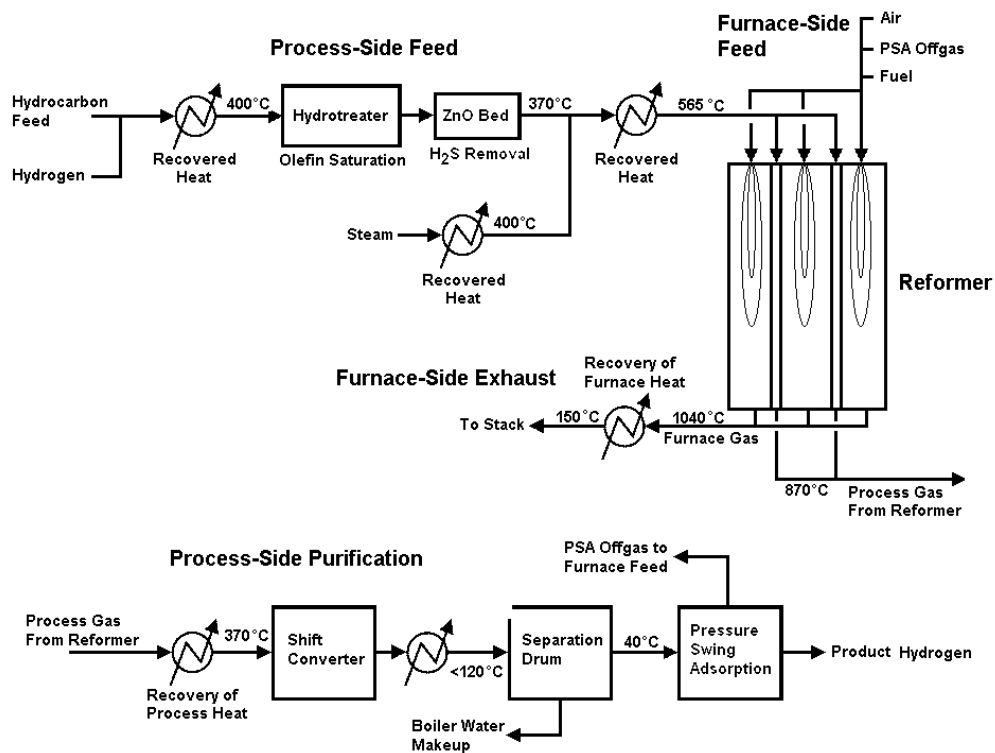


Figure 1. Steam-Methane Reforming Process Diagram
(adapted from Kirk Othmer, 2001 and Rostrup-Nielsen, 1984)

Process-Side Feed

On the process side of a steam-methane-reforming plant the hydrocarbon feed must be pretreated before it is sent to the reformer. The hydrocarbon feed is first mixed with recycled hydrogen and preheated to approximately 400 °C (Rostrup-Nielsen, 1984; p. 14). The heat used to preheat the process-side feed is recovered from gases exiting the reformer. The hydrogen enriched feed is then sent to a hydrotreater where a cobalt-molybdenum or nickel-molybdenum catalyst is used to hydrogenate olefins and to convert organic sulfides into hydrogen sulfide. Olefins are removed from the process-side feed to prevent cracking and carbon formation on the catalyst in the

reformer tubes, and organic sulfides are removed to prevent reformer catalyst poisoning (Kirk Othmer, 2001; p. 778). Next, the process-side feed passes through a zinc-oxide bed to remove the hydrogen sulfide (Kirk Othmer, 2001 pp. 779). The process gas is then mixed with steam, resulting in a molar steam to carbon ratio between 1 and 4. The process-side feed is heated to approximately 565 °C using recovered heat before it is sent to the tube side of the reformer (Rostrup-Nielsen, 1984; p. 14).

Furnace-Side Feed

The furnace-side feed section is much simpler than that of the process-side. Fuel is mixed with offgas (also called purge gas) from the pressure swing absorber. The offgas contains combustible species, such as carbon monoxide, hydrogen and methane, which are separated from the process-side effluent. The furnace feed is mixed with combustion air in the burners at the top of the furnace (Kirk Othmer, 2001; p. 779).

Reformer

The reformer studied in this thesis is top-fired and co-current. The process gas and furnace gas enter at the top of the reformer and exit at the bottom. The process side gas flows through parallel rows of catalyst filled tubes. In the tubes, the hydrocarbons and steam react to form hydrogen, carbon dioxide and carbon monoxide. The reactions are catalyzed by a nickel based catalyst and are predominantly endothermic. The heat needed to drive the endothermic reactions is provided by the combustion of fuel on the furnace side. The process gas temperature typically ranges from 650 °C at the top of the reformer to 870 °C at the bottom (Rostrup-Nielsen, 1984; p. 16). On the furnace side, the rows of tubes are separated by rows of burners. The burners produce long flames that start at the top of the furnace and extend approximately half way down

the tubes. The furnace gas can reach temperatures over 1100 °C (Rostrup-Nielsen, 1984; p. 20). At these temperatures radiative heat transfer is the dominant heat-transfer mechanism. For this reason, the reformer is often referred to as a radiant fire box.

Furnace-Side Exhaust

The furnace gas exits the reformer at approximately 1040 °C (Rostrup-Nielsen, 1984; p. 20). Profitable operation of a SMR plant requires the recovery of heat from the furnace gas. Heat from the furnace gas is used to preheat the process-side feed streams and to generate steam for export to nearby plants (Rostrup-Nielsen, 1984; p. 14).

Process-Side Purification

The process gas exits the reformer as a near equilibrium mixture of hydrogen, carbon monoxide, carbon dioxide, steam and methane. The process effluent is cooled to approximately 370 °C and the waste heat is recovered (Kirk Othmer, 2001; p. 776). In the absence of catalyst, the process gas remains at the reformer exit composition. The process effluent is sent to a shift converter. The shift converter uses the water-gas-shift reaction to convert carbon monoxide and water into carbon dioxide and hydrogen (Kirk Othmer, 2001; p. 779). The shift converter increases the amount of hydrogen product in the process-side effluent. After the shift converter, the process-side effluent is cooled to less than 120 °C and flashed into a separation drum. Nearly all of the steam in the effluent condenses and is collected for use as boiler feed water (Kirk Othmer, 2001; p. 779). The uncondensed process effluent is cooled to 40 °C and sent to the pressure swing absorber. The pressure swing absorber uses a series of adsorption beds to separate hydrogen from the remaining gas species (Kirk Othmer, 2001; p. 779). The remaining gas species (methane, carbon monoxide, carbon dioxide, nitrogen and hydrogen) are collected as offgas. The purified

hydrogen gas is the main product from the plant. Some SMR plants produce purified carbon dioxide as a side product.

1.3 Furnace Geometry

The SMR investigated in this thesis is a top-fired co-current reformer designed by Sela Fluid Processing Corporation. Figure 2 is a detailed front view of the reformer and Figure 3 is a detailed top view of the reformer. The reformer produces 2.83 million standard (101 kPa, 16 °C) cubic meters per day (120 Mmol per day) of high purity hydrogen at 2413 kPa (gauge) and 71 200 kg/h of superheated steam at 390 °C and 4580 kPa (gauge). The furnace contains of seven rows of 48 tubes. The tubes have an external diameter of 14.6 cm and an exposed length of 12.5 m. The rows of tubes are separated by eight rows of twelve burners. Fuel and air enter through the burners, and the fuel combusts over a flame length of 4.5-6 m. The rows of burners next to the furnace walls have a lower fuel rate since they are adjacent to only one row of tubes. At the bottom of the furnace, the rows of tubes are separated by rectangular intrusions known as flue-gas tunnels or coffin boxes. The coffin boxes extend from the front to the back of the furnace, have a height of 2.86 m and have openings 0.6 m from the floor that allow the furnace gas to exit the furnace.

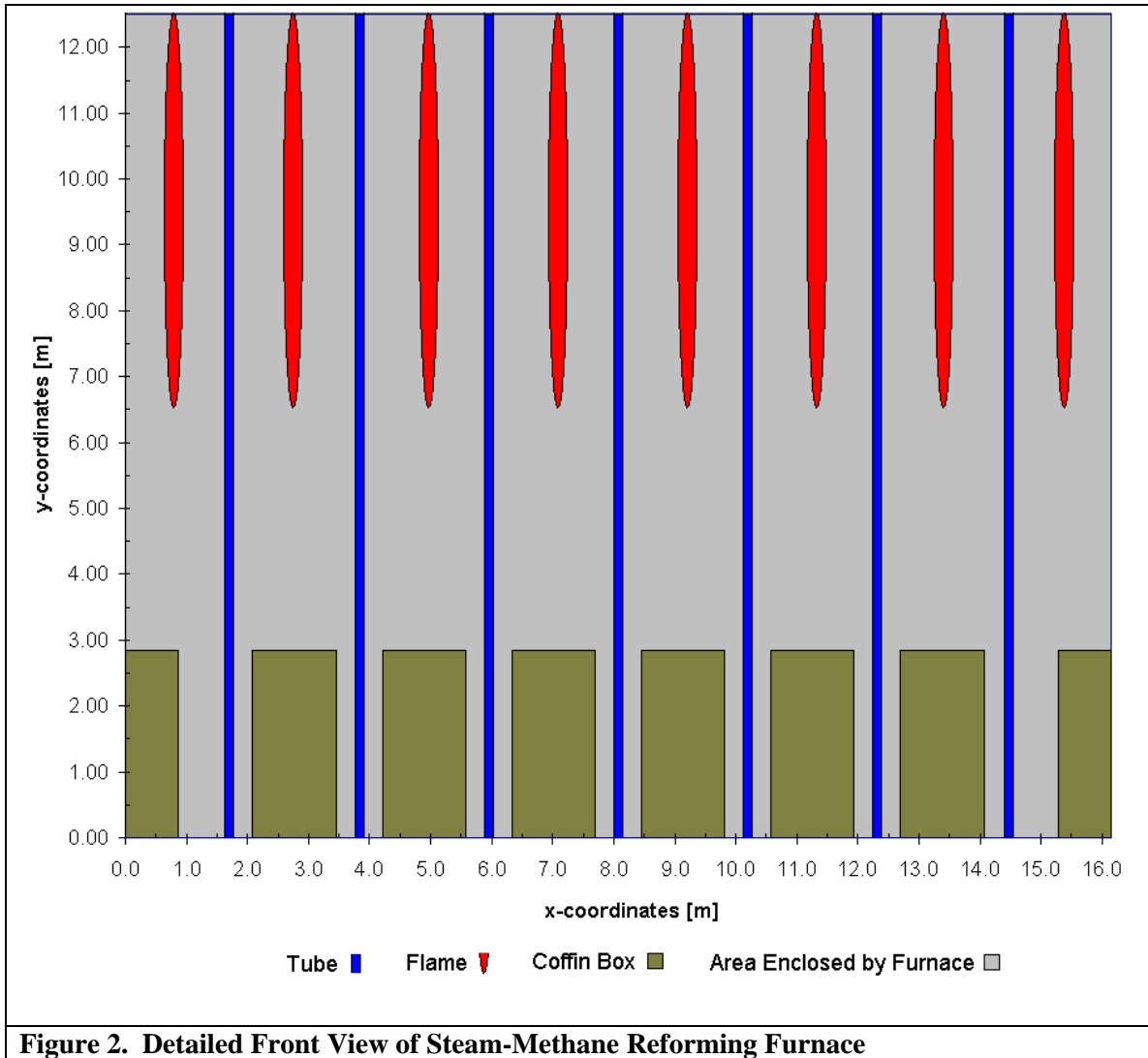
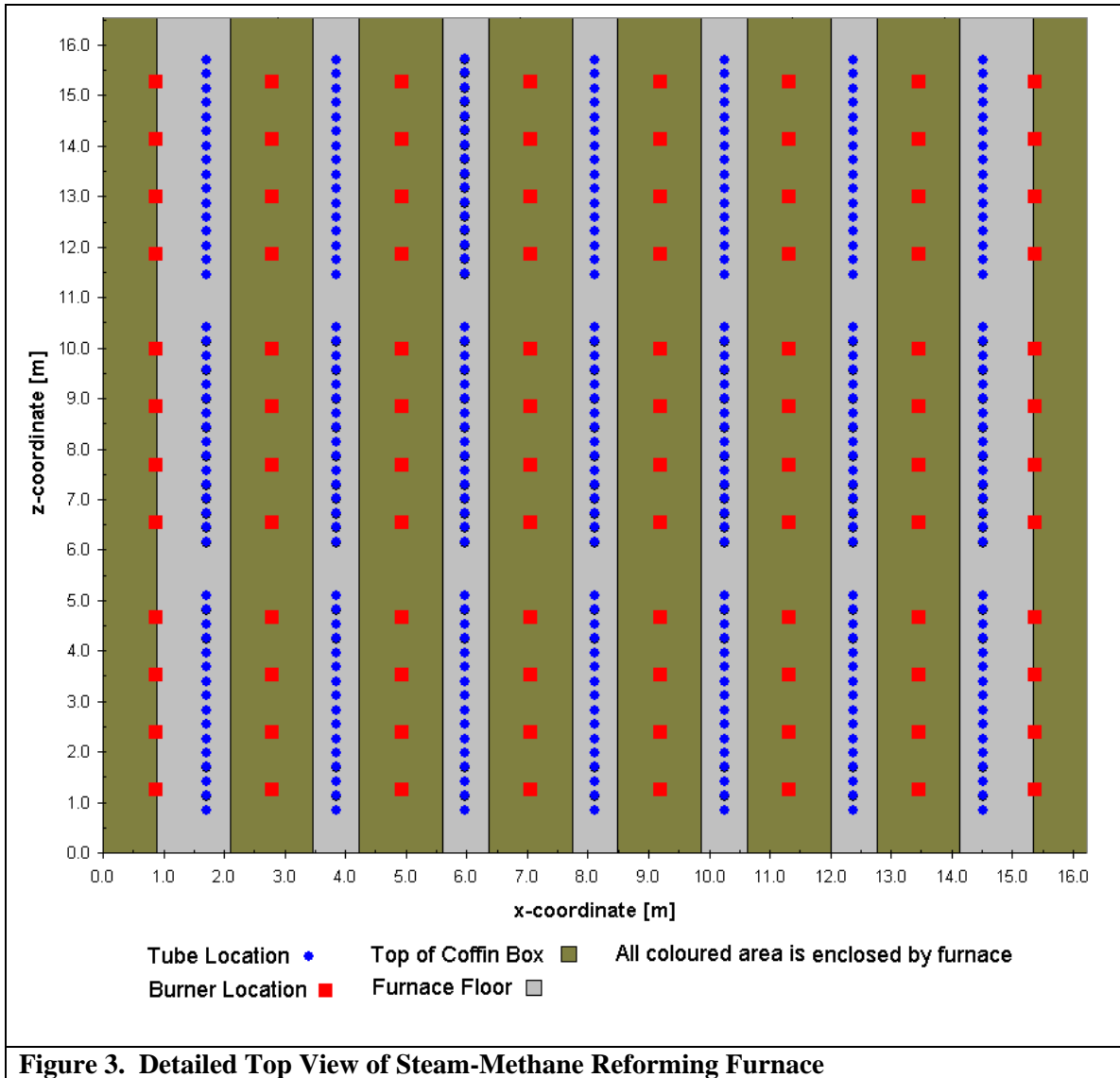


Figure 2. Detailed Front View of Steam-Methane Reforming Furnace



1.4 Available Data

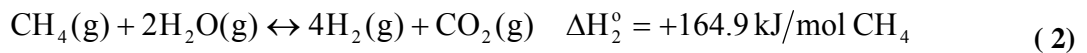
Some of the data for the industrial SMR investigated in this study are collected in real time every second by plant instruments. The data collected in real time can be retrieved from a historical database. The variables available in real time are the temperatures, pressures and flow rates of all streams flowing into and out of the reformer, and the gas chromatography readings for the shift-

converter effluent, pressure-swing adsorber effluent and natural gas (see Figure 1). In addition to the on-line data, plant operators measure the tube wall temperature at the upper and lower peep holes (3.66 and 8.53 m respectively from the top of the reformer tubes) using a hand-held infrared pyrometer on a nightly basis. These measurements are manually logged and can be matched with the historical hourly data. On a quarterly basis, a third-party consultant collects tube-wall temperature measurements and plant data. The plant data are used as inputs to a proprietary reformer model. The reformer model predicts the tube wall temperature profile and reformer outputs. The model outputs are compared to plant data to evaluate plant performance. The hourly historical data, nightly tube temperature readings, third-party temperature readings and proprietary reformer model outputs are all available for this study.

1.5 Important Physical Phenomena

A SMR is designed to create favourable conditions for the production of hydrogen gas by the steam-methane reforming and water-gas shift reactions. The steam-methane reforming reactions are shown in reactions (1) and (2) and the water-gas shift reaction is shown in reaction (3).

Reaction (2) is the sum of reactions (1) and (3).



As the gas mixture flows through the reformer tubes, methane and steam are converted predominantly to hydrogen and carbon dioxide. The rates of conversion of reactants into products and the direction of the reforming reactions and water-gas shift under different conditions (concentration, temperature and pressure) must be accurately accounted for using a reaction kinetics model. In addition to methane, trace amounts of higher alkanes (ethane, propane, ..., hexane) are present in the process-side feed. The carbon-carbon bonds of the higher alkanes are broken incrementally by adsorption of the molecule at the catalyst active site and scission of the adjacent carbon-carbon bond. The single carbon species produced react in a similar manner to adsorbed methane. The process is repeated until all the carbon atoms in the higher alkane are reformed (Rostrup-Nielsen, 1984; p. 54).

Specially-designed nickel-aluminum-oxide catalyst particles (see Figure 4) form a packed bed within the tubes to improve reaction rates. The mass and energy transport of the process gas as it flows through this fixed bed must be considered in the model, along with the pressure losses due to friction in the catalyst bed. The reforming reactions and water-gas shift reaction occur at the catalyst active sites. Reactants and products must diffuse from the bulk process gas to the surface of the catalyst and then into the catalyst pores.

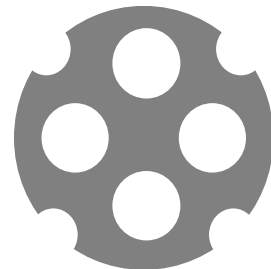


Figure 4. Cross-Section of Quadralobe Catalyst Particle

The reactions in equations (1) and (2) are highly endothermic as indicated by the positive heats of reaction ($\Delta H_1^0 = +206\text{kJ/mol}$, $\Delta H_2^0 = +164.9\text{kJ/mol}$). To produce hydrogen by reactions (1) and (2), heat must be continuously supplied. If too little heat is provided, the temperature of

the process gas drops and the reforming reactions become very slow. The heat to drive the reforming reactions originates on the combustion side of the furnace. The internal energy stored in the chemical bonds of the furnace fuel is released as the fuel combusts, increasing the temperature of the combustion products. In the furnace, fuel and air combust over the flame length and the combustion products flow from the top of the furnace to the exit at the bottom.

The energy released by the combustion of furnace fuel can exit the furnace in three ways: through the tube wall to the process side, through the refractory to the external environment, or out of the furnace with the bulk flow of furnace exit gas. In high-temperature furnaces, the dominant mode of heat transfer to the tubes and the refractory is radiation. In addition to radiative heat transfer, the furnace gas transfers energy by bulk gas motion to other regions of furnace and by convection to the refractory and tubes. The refractory transfers energy by conduction to the external environment and receives energy by radiation and by convection from furnace gas. The tubes transfer energy by conduction to the process side and receive energy by radiation and by convection from the furnace gas. The three heat-transfer modes, radiation, convection and conduction must be appropriately modeled in the reforming furnace. The heat transfer mechanisms are summarized in Figure 5.

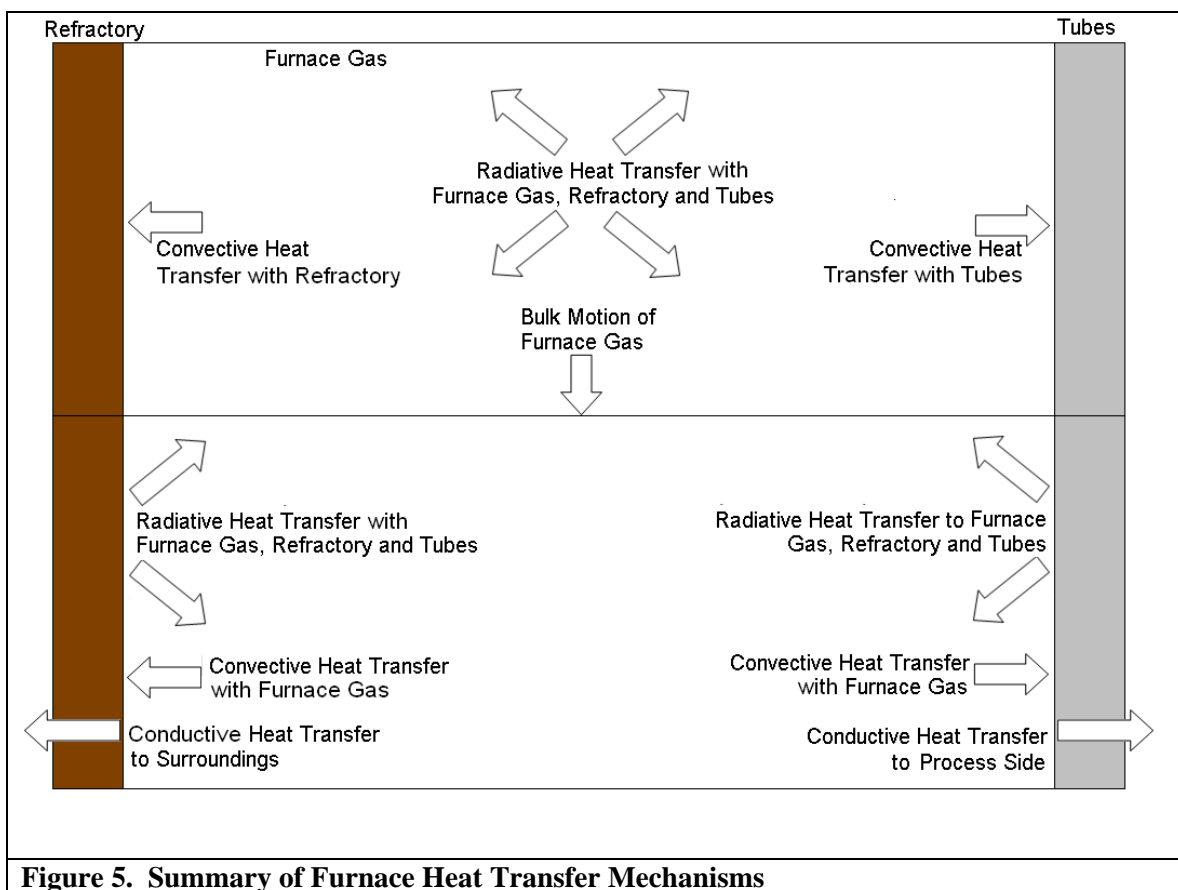


Figure 5. Summary of Furnace Heat Transfer Mechanisms

The energy that is lost through the refractory walls or that exits with furnace gas does not drive the reforming reactions. For heat to reach the active sites of the catalyst, it must pass through the tube walls and into the process gas. On the furnace side, heat arrives at the outer tube surface by radiation or convection. Since the temperature on the inside of the tube is lower than the temperature on the outside, heat travels by conduction through the tube wall. The inside tube surface is in contact with the stationary catalyst and with the moving process gas. The dominant modes of heat transfer inside of the tubes are conduction from the inner tube walls to the catalyst and through the network of catalyst particles, convection from the inner tube wall to the process gas, and convection between the process gas and the catalyst particles. These modes of heat transfer work together to transfer heat from hot regions to cold regions.

The condition of the catalyst is important in SMR operation. Over time, the catalyst can become poisoned by hydrogen sulfide and other impurities, rendered inactive by carbon formation and physically crushed by contraction and expansion of the tubes during temperature changes. SMR operators intentionally load different types of catalyst in different regions of the fixed bed to improve performance and catalyst life. A model that provides a detailed treatment of these catalyst-specific phenomena would be unnecessarily complex.

1.6 References

Cromarty, B. J. (2004) Reformer tubes – failure mechanisms, inspection methods and repair techniques. Johnson-Matthey 12th annual international technical seminar on hydrogen plant operations.

Farnell, P. W. (2003) Modern techniques for Optimization of Primary Reformer Operation. Synetix. Johnson Matthey Group

Fisher, B. R. (2004) Reformer tube metallurgy – design considerations, failure mechanisms, and inspection methods. Johnson-Matthey 12th annual international technical seminar on hydrogen plant operations.

Kirk Othmer Encyclopedia of Chemical Technology. (2001) Hydrogen. John Wiley and Sons Inc. vol. 13 pp. 759-801

Roberts, R. D. and Brightling J. (2005) Process Safety Progress. Maximize Tube Life by Using Internal and External Inspection Devices. vol. 24 pp. 258-265.

Rostrup-Nielsen, J. R. (1984) Catalytic Steam Reforming. Catalysis: science and technology. Springer Verlag. New York, NY. vol 5. pp. 1-117.

Chapter 2 Literature Review

Industrial SMR is a mature technology. As a result, there exist many mathematical models in the academic and commercial literature that simulate steam-methane reformers. These models differ in their intended use and in the simplifying assumptions they use to describe reformer behaviour. In addition to complete steam-methane reforming models, there are many models that simulate either the furnace-side or the process-side of the reformer. Table 1 summarizes the complete SMR models (models that simulate the interactions between process and furnace sides) in the literature, whereas the models listed in Tables 2 and 3 are concerned with furnace-side and process-side models, respectively. Omitted from this table are detailed computational fluid dynamic (CFD) models (e.g., Stefanidis et al., 2006; Han et al., 2006; Baburić et al., 2005; Guo and Maruyama, 2001) because these models have long computational times that make them unsuitable for online use.

The earliest model development began in the 1960s. Models have been used to design, optimize and monitor SMRs and other radiant furnace processes. Furnace-side models can be classified by the approaches used to model radiative heat transfer, combustion patterns, furnace flow patterns and convective heat-transfer coefficients. Process-side models can be classified by whether they consider variation in one or two dimensions (axial or axial plus radial) and by the types of assumptions regarding mass-transfer limitations, reaction kinetics, pressure drop, flow patterns and heat transfer within the packed bed.

Table 1. Complete Steam-Methane Reforming Models

Author	Date	Purpose	Radiation Model	Combustion or Heat Release Pattern	Furnace Flow Pattern	Furnace Gas-Tube Convective Heat Transfer Coefficient	Fixed Bed Reactor Model	Reaction Kinetics	Pressure Drop Correlation	Tube/catalyst-Process Gas convective heat transfer coefficient
McGreavy and Newmann	1969	-monitor refractory and tube temperature	-Roesler 4-flux	N/A	-plug flow	N/A	-1D -neither pseudo-homogeneous or heterogeneous -plug flow	-composition determined equilibrium at T	N/A	N/A
Singh and Saraf	1979	-validated model for future design purposes	-Hottel Zone -weighted sum of gray gases -no geometry effects -one gas zone and one flame zone exchange radiative energy with tubes -walls are no flux zones	-burners are surface zones at the adiabatic flame temperature -all radiation from flame zone reaches the tubes minus the amount absorbed by gas	-well mixed	-none (assumed negligible)	-1D -pseudo-homogeneous -no effectiveness factors used -assumed diffusion limitations accounted for in kinetics -plug flow	-used first-order kinetic rate expressions developed by Haldor Topsoe and shown in Singh and Saraf (1979)	-Ergun (1952) equation with Ergun friction factor	-Beek (1962)
Soliman et. al.	1988	-validated models for side and top fired reformers -tested the impact of modifying inputs	Side Fired -Hottel Zone (Singh and Saraf 1979 assumptions)	-see Singh and Saraf (1979)	-well mixed	-none (assumed negligible)	-1D -heterogeneous -plug flow	Xu and Froment (1989a) diffusion limitations	Fanning equation with the Hicks (1970) friction factor	-Leva and Grummer (1948)
			Top Fired -Roesler 4-flux -modified by Filla 1984 to allow for diffuse reflection off refractory	-Fraction of fuel combusted distribution	-plug flow	N/A	-1D -heterogeneous -plug flow	Xu and Froment (1989a) diffusion limitations		
Murty and Murthy	1988	-validated the model -tested in the impact of modifying inputs	-Roesler 2-flux	-Roesler (1967) heat release pattern	-plug flow	-Dittus-Boelter type correlation	-1D -pseudo-homogeneous -diffusion limitations accounted for in kinetics -plug flow	-used first-order kinetic rate expressions developed by Haldor Topsoe and shown in Singh and Saraf (1979)	-Ergun (1952) equation with Ergun friction factor	-Beek (1962)

Plehiers and Froment	1989	-validated the model with industrial results	-Hottel Zone -unconventional total exchange areas calculated from Monte Carlo simulations -total exchange areas account for intervening real gas	-burners were point sources which emitted a fraction (γ) of combustion heat as radiation - $1-\gamma$ of the heat enters with the flue gas	-cone flow from each burner created zones -velocity at any point was the sum of velocities from each burner	-submerged body correlations (not specified) -velocity varies with position in the furnace	-1D -heterogeneous -plug flow	-Xu and Froment (1989a) diffusion limitations	-Momentum balance with Ergun (1952) friction factor	-Xu and Froment (1989b)
Yu et al.	2006	-validated the model for future optimization	-Hottel Zone -method used to calculate directed-flux areas not stated -sum of gray gases model not stated	Roesler heat release pattern (modified by Selcuk et. al. 1975)	-plug flow	Dittus-Boelter type correlation	-1D -pseudo-homogeneous -plug flow	Yu et al. 2006 -reaction kinetics derived from stoichiometric equations -1D pseudohomogeneous	-Ergun (1952) equation with Ergun friction factor	-Leva and Grummer (1948)
Ebrahimi et al.	2008	-validated the model with industrial data -examined the impact of important (ϵ_{tubes} , ϵ_{refrac} , K_{gas}) parameters	Hottel Zone -simplified-summed-normalized method used to evaluate direct exchange areas -total exchange areas calculated from resulting matrices - weighted-sum-of-gray-gases model not used	-exponential heat-release profile developed by Hyde et al. (1985)	-plug flow	-used correlations of Holman (1990)	-1D -pseudo-homogeneous -plug flow -tube-side model described in Mohamadzaedeth and Zamaniyan (2003)	-Xu and Froment (1989a) diffusion limitations	-Ergun (1952) equation with Ergun friction factor	-Xu and Froment (1989b)

Table 2. Furnace Side Models

Author	Date	Purpose	Radiation Model	Description of Radiation Model	Combustion or Heat Release Model	Furnace Flow Pattern	Furnace Gas-Tube Convective Heat Transfer Coefficient
Hottel and Sarofim	1965	-examine the impact of furnace gas flow pattern on efficiency in a cylindrical furnace	-Hottel Zone	-directed-flux areas calculated from direct exchange areas -direct exchange areas calculated from tables -one clear plus three gray gas model used -used irregular zones based on flow pattern	- plug flow and parabolic: gas zones adjacent to inlet - turbulent jet: percent combustion calculated from the time mean value of fuel concentration (Becker 1961)	-plug flow, parabolic velocity profile, turbulent jet for 3 Craya-Curtet numbers	-N/A -correlations used are not stated -side walls and end walls used different correlations
Roesler	1967	-to show astrophysics techniques can be applied to furnaces	-Roesler Flux	-band and window radiation -integrated radiative transfer equations over two solid angles (forward and reverse hemispheres) -4-flux	-parabolic heat release pattern	-plug flow	-assumed negligible
Steward and Cannon	1971	-to calculate heat flux and temperature profiles in a cylindrical furnace using Monte Carlo methods -to validate Monte Carlo Methods against the results of Hottel and Sarofim (1965) and experimental data	-Monte Carlo	-energy balances on all zones in the furnace were derived -interchange energy was calculated by assigning a value of energy to each ray (radiant energy/number of rays) -rays traced to find absorbing zone	- plug flow and parabolic: gas zones adjacent to inlet - turbulent jet: percent combustion calculated from the time mean value of fuel concentration (Becker 1961)	-plug flow, parabolic velocity profile, turbulent jet for 3 Craya-Curtet numbers	-side walls used Dittus-Boelter type correlation -end wall used Friedman and Mueller (1951)
Selçuk et al.	1975a	-investigated the influence of flame length on maximum tube wall temperature and heat flux profile in a multipass fluid heater	-Roesler Flux	-integrated radiative transfer equation over two solid angles -no band and window radiation -2-flux	-Roesler heat release pattern	-plug flow	-assumed negligible
Selçuk et al.	1975b	-validated the results of Selçuk et al. (1975a) by generating temperature and heat flux profiles for the same furnace using the zone method	-Hottel Zone	-conventional exchange area calculation	-Roesler heat release pattern	-plug flow	-assumed negligible
Rao et al.	1988	-simulated the furnace and process side of a pyrolysis unit -generated furnace wall, furnace gas and tube skin temperature profiles and compared them to industrial results	-Hottel Zone	-Monte Carlo method used to determine exchange areas -gray and clear gas assumptions - ϵ and α are calculated by integrating $E_b \lambda(T_{zone})$ over absorbing bands ($\lambda_i - \lambda_j$) and dividing by the integral over all wavelengths	-burners were point sources which emitted a fraction (γ) of combustion heat as radiation -1- γ of the heat enters with the flue gas	-cone flow from each burner created zones -velocity at any point was the sum of velocities from each burner	N/A

Hobbs and Smith	1990	-presents the equations for a model used to estimate the influence of fuel impurities on furnace performance -compared the two zone model to a single zone model	-Hottel Zone	-conventional Hottel Zone method -only four zones were used -bottom gas zone is a flame zone -flame, gas, soot particle are char cloud emissivities are modeled with different correlations	-all combustion occurs in the lower zone -flame temperature is pseudo-adiabatic	-gas flows from flame zone into upper furnace zone	N/A
Keramida et al.	2000	-compared discrete transfer method and 6-flux Roesler method to each other and to experimental data -compared computational efficiency, ease of application and predictive accuracy for the radiation model	-Roesler Flux -Discrete Transfer Method	-integrated radiative transfer equation over three solid angles -6-flux -run time 530min -finite difference method -hybrid of Monte Carlo, Hottel Zone and Roesler Flux -run time 805min	-eddy dissipation model for the heat release of methane and oxygen	-partial differential equations for the conservation of momentum, heat and mass were solved	N/A
Liu et al.	2001	-built a dynamic model of an oil fired furnace -validated the model using proven model from the literature -calculated the temperature and heat flux distribution in an oil fired furnace	-Hottel Zone method	-Monte Carlo method used to determine total exchange areas -smoothing technique used to check summation and reciprocity of exchange areas -soot is the dominant absorber and emitter -water vapor and carbon dioxide is neglected -a soot model is used	-all combustion occurs in the flame zone -combustion occurs at the adiabatic flame temperature	-well mixed zone around the burner -several plug flow zones after the burner	-Lebedev and Sokolov (1976)

Table 3. Process Side Models

Author	Date	Purpose	Fixed Bed Reactor Model	Catalyst Reaction Kinetics	Pressure Drop Correlation	Tube/catalyst-Process Gas convective heat transfer coefficient
Alhabdan et. al.	1992	-build and validated the model for future design and optimization	-1D heterogeneous -plug flow (not stated) - derived a material balance on a catalyst pellet using characteristic length	-Xu and Froment (1989)	-Froment and Bischoff (1979) momentum balance - Hicks (1970) friction factor	-overall heat transfer coefficient used by Xu and Froment (1989b) -convective heat transfer coefficient of Leva and Grummer (1948)
Elnashaie et al.	1992	-built and validated the model using data from two different industrial reformers	-1D heterogeneous -plug flow	-Xu and Froment (1989)	-N/A	-De Wasch and Froment (1972)
Pedernera et al.	2003	-built a two dimensional model of the tube side of a reformer -tested the impact of varying tube diameter and catalyst activity	-2D heterogenous -partial differential equations from momentum balances	-Xu and Froment (1989)	-Ergun (1952) friction factor	-Dixon and Cresswell (1979)
Wesenberg and Svendsen	2007	-evaluated the impact of interphase transport limitations on the heat transfer and effectiveness factors	-2D heterogeneous	-Xu and Froment (1989)	-Hicks (1970) friction factor	-Peters et al. (1988) -Wako et al. (1979)

2.1 Radiative Heat Transfer Methods used in Furnace Models

SMR and furnace models consider the transfer of heat by radiation between the furnace gas and enclosing surfaces. The two dominant methods for modeling radiative heat transfer in the SMR literature are the Roesler flux method (Roesler, 1967) and Hottel zone method (Hottel and Sarofim, 1960). There are many variations on the original Roesler and Hottel methods. A brief description of both methods is provided below.

Roesler Flux Method

The derivation of the Roesler flux method is complex. The derivation involves the use of vector calculus, integro-differential equations and three-dimensional geometry. The complete derivation and review of the Roesler flux method and subsequent flux methods that build on Roesler's ideas is given in an excellent review paper by Siddall (1974). What follows is a simple explanation of the Roesler flux method, which is written to provide a general understanding of the method without complex derivations.

The Roesler flux method treats radiant energy as a conserved entity (Siddall, 1974), much like chemical engineers treat chemical species in material balances. To understand this analogy, consider the downward flow of a reactant in a vertical plug-flow reactor operating at steady state. The first step in deriving a differential equation to describe the concentration profile within the reactor is to write a material balance on a small section of the reactor with height Δy :

$$0 = \frac{\text{moles of reactant}}{\text{flowing in at } y} - \frac{\text{moles of reactant}}{\text{flowing out at } y + \Delta y} + \frac{\text{moles generated}}{\text{by reaction}} - \frac{\text{moles consumed}}{\text{by reaction}} \quad (4)$$

To obtain a differential equation of the form $dC/dy = f(C)$, equation (4) is divided by Δy before taking the limit as $\Delta y \rightarrow 0$. The Roesler flux method uses an analogous balance on the radiant energy in a section of the furnace of height Δy . The radiant energy in the section of furnace interacts with the process gas, furnace refractory and tubes as shown in Figure 6 and equation (5).

$$0 = \frac{\text{radiant energy}}{\text{flowing in at } y} - \frac{\text{radiant energy}}{\text{flowing out at } y + \Delta y} + \frac{\text{radiant energy}}{\text{emitted by refractory}} - \frac{\text{radiant energy}}{\text{absorbed by refractory}} + \frac{\text{radiant energy}}{\text{emitted by furnace gas}} - \frac{\text{radiant energy}}{\text{absorbed by furnace gas}} + \frac{\text{radiant energy}}{\text{emitted by tubes}} - \frac{\text{radiant energy}}{\text{absorbed by tubes}} \quad (5)$$

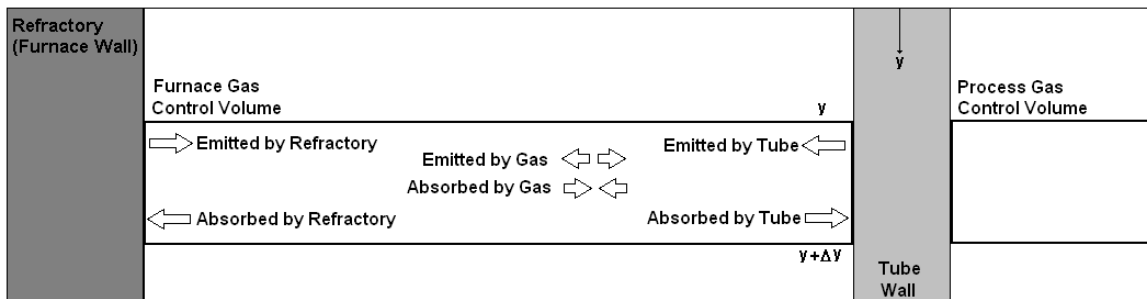


Figure 6. Radiant energy balance on a differential section of furnace

The resulting differential equation describes the change in radiant energy per differential length (dq_{rad}/dy). However, unlike a chemical species, radiant energy can simultaneously travel down the furnace (in the direction of $+y$) or up the furnace (in the direction of $-y$). So the simplest

version of Roesler's method involves two differential equations, one that describes the change in radiant energy per differential length in the positive y-direction and one in the negative y-direction (dq_{rad}^+/dy and dq_{rad}^-/dy). These differential equations are coupled with the furnace gas material balance and the furnace gas energy balance. These coupled differential equations can be solved numerically, using the appropriate boundary conditions. This simplest Roesler method is known as the 2-flux method, since there are two differential equations describing the downward and upward radiation fluxes. In the Roesler 2-flux method, it is assumed that all wavelengths of radiation are absorbed equally by the furnace gas. This is the gray-gas assumption (See Appendix A). To relax this assumption, two types of radiation can be defined, one type that interacts with the furnace gas and one type that does not (Roesler, 1967). The type of radiation that interacts with the furnace gas is called band radiation and the type that does not is called window radiation. Differential equations describing the change in radiant energy per differential length can be derived for band and window types of radiation, increasing the number of differential equations describing radiant energy from two to four (dq_{band}^+/dx , dq_{window}^+/dx , dq_{band}^-/dx and dq_{window}^-/dx). The modeling of band and window radiation is equivalent to assuming that the furnace gas is composed of one gray gas and one clear gas (a clear gas does not absorb any radiation). This extended form of the Roesler method is called the Roesler 4-flux method (Siddall, 1974).

Higher-order Roesler flux methods have been developed by adding additional spatial dimensions or by adding additional gray gases. For example, the 6-flux method (Hoffman and Markatos, 1988; Keramida et al., 2000) assumes that all of the furnace gas is gray, and accounts for radiative fluxes in positive and negative x, y and z directions. A 12-flux method would assume one gray and one clear gas with radiative fluxes in the x, y and z directions. The Roesler method can be further extended to n-dimensions (meaning n differential equations to describe radiative fluxes)

by using multiple types of band radiation (multiple gray gases and one clear gas). The extension of the Roesler flux method in many spatial directions results in the discrete ordinates method (Siddall, 1974).

Hottel Zone Method

The Hottel zone method is a more conventional radiative heat transfer method. In the Hottel zone method the furnace is divided into volume and surface zones. An energy balance that includes two radiative heat transfer terms is performed on each zone (Rhine and Tucker, 1991; p. 216). Example energy balances for volume and surface zones are shown in equations (6) and (7) respectively.

$$\text{Energy Accumulating in Volume Zone} = \text{Radiation In} - \text{Radiation Out} + \text{Enthalpy In} - \text{Enthalpy Out} - \text{Heat out by Convection} \quad (6)$$

$$\text{Energy Accumulating in Surface Zone} = \text{Radiation In} - \text{Radiation Out} + \text{Heat in by Convection} - \text{Heat out by Conduction} \quad (7)$$

For steady-state models, where there is no energy accumulating in the zones, the energy balances produce one algebraic equation for each zone. An iterative algebraic equation solver is used with an initial guess to solve for the temperature of each zone in the furnace.

Due to the medialess nature of radiative heat transfer, any zone in the furnace can receive energy from and transmit radiant energy to every other zone. The rates of radiative heat emission and

absorption by a zone are proportional to the black emissive power (σT^4) of the emitting zone (Rhine and Tucker, 1991; p. 216). The proportionality constant is known as a directed-flux area, and is represented by the symbol $\overrightarrow{Z_i Z_j}$ where zone i is the emitter and zone j is the receiver as shown in equations (8) and (9) (Rhine and Tucker, 1991; p. 216).

$$\text{Radiation In} = \text{Radiation Emitted by other Zones and Absorbed by Zone j} = \sum_{\text{all } i} \overrightarrow{Z_i Z_j} \sigma T_i^4 \quad (8)$$

$$\text{Radiation Out} = \text{Radiation Emitted by Zone j and Absorbed by other Zones} = \sum_{\text{all } i} \overrightarrow{Z_j Z_i} \sigma T_j^4 \quad (9)$$

The most challenging aspect of the Hottel zone method is calculating the directed-flux areas. The directed-flux areas are calculated from total-exchange areas, which are, in turn, calculated from direct-exchange areas (Rhine and Tucker, 1991; p. 217). Direct-exchange areas are calculated by multiple integrations or from view factors (Hottel and Sarofim, 1960; p. 258). They represent the area (or equivalent area for volume zones) of a zone that emits radiation that arrives at and is absorbed by a receiving zone. Direct-exchange areas are calculated by integrating over the geometry of the emitting and receiving zones, while taking into account absorption by the gas separating the zones. Due to the complexity of the integrations, direct-exchange-area charts (Hottel and Cohen, 1958; Hottel and Sarofim, 1960; pp. 260-279; Tucker, 1986) and Monte Carlo simulations (Vercammen and Froment, 1980; Lawson and Ziesler, 1996) have been developed to aid in their evaluation. More details about the Hottel zone method are provided in Appendix B.

The Hottel zone method described above requires explicit definition of furnace geometry and furnace zoning. The method assumes that the intervening gas is composed of multiple gray gases and requires complex directed-flux area calculations. Simpler versions of the Hottel zone method use simplifying assumptions to reduce model complexity. Rhine and Tucker (1991; pp. 244-257) define three classes of Hottel zone methods, the well-stirred model, the long furnace model type 1 and the long furnace model type 2.

The well-stirred model assumes that the furnace gas has uniform composition and temperature and that there are two surface zones in the furnace, a sink and a refractory. The furnace gas consists of a single gray gas and the sink and refractory are gray diffuse emitters. In this model, only three total exchange areas are calculated ($\overline{GS}_{\text{sink}}$, $\overline{GS}_{\text{refract}}$, $\overline{S}_{\text{sink}}\overline{S}_{\text{refract}}$) (Rhine and Tucker, 1991; p. 244). Singh and Saraf (1979) used a version of the well-stirred model to generate tube-wall temperature profiles for an industrial SMR. In the Singh and Saraf version of the Hottel zone method, there are three zone types: burner surface, tube surface and furnace gas. It is assumed that the refractory is a no-flux zone (it reflects all incident radiation). The tube surface is divided into many zones in the axial direction and it is assumed that each axial-tube zone has an equal view of the furnace gas and burner surface. It is assumed that tube zones do not exchange radiant energy with each other. As a result of these assumptions, only two total-exchange areas are needed: the total-exchange area between the gas and an axial-tube zone, and between the burner surface and an axial-tube zone. The model developed by Singh and Saraf (1979) was used by Solimon et al. (1988) to model a side-fired SMR and Farhadi et al. (2005) for a bottom fired MidrexTM reformer.

The long-furnace models divide the furnace gas into volume zones arranged in series. The furnace gas enters the furnace at the first zone and flows sequentially through each zone to the furnace exit. The heat of combustion of furnace fuel can be distributed over the length of the furnace by assuming a fixed percentage of combustion in each zone. The long-furnace model type 1 assumes that the volume zones only exchange radiant energy with the furnace surface zones (there is no gas-to-gas radiative heat transfer) (Rhine and Tucker, 1991; p. 252). While this assumption simplifies directed-flux area calculations, Farhadi et al. (2005) showed that the long-furnace model type 1 did not accurately model a bottom fired Midrex™ reformer. The long-furnace model type 2 is a complete Hottel zone method that accounts for radiative heat transfer between all zones (Rhine and Tucker, 1991; p. 256). The Hottel zone method is not restricted to the simple zoning and flow-pattern assumptions used in the long-furnace models. Very complex furnace geometry, flow patterns and zoning can be readily accommodated if appropriate information about direct-exchange areas and gas flow are available.

2.2 Combustion and Heat Release Patterns used in Furnace Models

An overview of some of the detailed modeling techniques used to simulate combustion in furnaces is given by Rhine and Tucker (1991). These detailed techniques use CFD models, semi-empirical correlations and physical modeling to develop heat-release patterns that can then be applied to simplified furnace models (Rhine and Tucker, 1991; p. 32). Three of the furnace models in Table 1 and Table 2 use these advanced techniques (Hottel and Sarofim, 1965; Stewart and Cannon, 1971; Keramidia et al., 2000). Hottel and Sarofim (1965) and Stewart and Cannon (1971) calculated the percent combustion in each zone from cold flow studies performed by Becker (1961) and Kermamida et al. (2000) used CFD models to solve for the heat-release

pattern. The majority of the furnace models in Table 1 and Table 2 assume complete combustion in a single combustion zone (Hottel and Sarofim, 1965; Steward and Cannon, 1971; Rao et al., 1988; Plehiers and Froment, 1989; Hobbs and Smith, 1990; Lui et al., 2001) or assume a parabolic heat-release profile over the flame length (Roesler, 1967; Selçuk et al., 1975a; Selçuk et al., 1975b; Murty and Murthy, 1988; Soliman et al., 1988; Yu et al., 2006).

Roesler (1967) was the first to use a parabolic heat release profile to distribute the heat of combustion over the flame length. Roesler assumed that the heat released over the flame length is the difference between the enthalpy of the furnace gas at the adiabatic flame temperature of the furnace feed and the enthalpy corresponding to the temperature at the top of the furnace (10).

$$Q_{\text{fur}} = \dot{m}C_p (T_{\text{adb}} - T_{y=0}) \quad (10)$$

Roesler's parabolic heat-release pattern was normalized to release Q_{fur} over the flame length (L_Q) (Roesler, 1967), as shown in equation (10).

$$q(y, L) = 6 \left(\frac{Q_{\text{fur}}}{L} \right) \left(\frac{y}{L} - \frac{y^2}{L} \right) \quad \text{where} \quad Q_{\text{fur}} = \int_{y=0}^{L_Q} q(y) dy \quad (11)$$

The same parabolic heat release pattern can be discretized for use in the Hottel zone method (Selçuk et al., 1975b; Yu et al., 2006).

2.3 Gas Flow Patterns used in Furnace Models

The majority of furnace models in the literature assume plug flow of the gas from the inlet at the burner (where fuel and air enter) to the exit at the end of the furnace (the bottom for the SMR studied in this thesis). Plug flow is a required assumption in Roesler's original two- and four-flux models (Roesler, 1967), and, as a result, authors that used the two- or four-flux Roesler methods assume plug flow (McGreavy and Newmann; 1969, Soliman et al., 1988; Selçuk et al., 1975a). Keramida et al. (2000) showed that the plug flow assumption is not required when using a six-flux or higher-order Roesler method. The Hottel zone method is very flexible in that it allows for the flow of mass between zones in a variety of directions. Despite this flexibility, many modelers who have used Hottel's Zone method assume plug flow (Hotel and Sarofim, 1967; Selçuk et al., 1975b; Yu et al., 2006). A few modelers (Stewart and Cannon, 1970; Rao et al., 1988; Plehiers and Froment, 1989) who used Monte Carlo simulations to compute exchange areas or radiant fluxes have considered more complicated flow patterns.

2.4 Furnace-Gas-to-Tube-Convective-Heat-Transfer Coefficients used in Furnace Models

All of the furnace models that are used to simulate convective heat transfer from the furnace gas (except the model by Liu et al. 2006) use the Dittus-Boelter equation (12) to calculate the convective heat transfer coefficient.

$$h_f = \frac{\lambda_{fg}}{D_{\text{fur hydr}}} (0.023 \text{Re}^{4/5} \text{Pr}^{1/3}) \quad (12)$$

Steward and Cannon (1971) used equation (12) for convective heat transfer to surfaces parallel to the direction of flow and a different correlation for surfaces perpendicular to the direction of flow. Liu et al. (2001) used the correlations developed by Lebedev and Sokolov (1976) shown in equation (13) for surfaces parallel and perpendicular to the direction of gas flow.

$$h_f = \frac{\lambda_{fg}}{D_{\text{fur hydr}}} (A Re^{3/4}) \quad (13)$$

In equation (13) the variable A is an experimentally-determined value that depends on the orientation of the surface with respect to gas flow.

2.5 Fixed Bed Reactor Models used in Reforming Models

The process side of a SMR is modeled as a fixed bed reactor. Fixed bed reactors can be classified by their dimensionality (one-dimension vs two-dimensional) and by their complexity (pseudo-homogeneous vs heterogeneous) (Froment and Bischoff, 1979; p. 401). In a one-dimensional model, gradients are assumed to exist in the axial direction but not in the radial direction. In a two-dimensional model, gradients are assumed in both the axial and radial directions.

To react and form products, the reactive species in the reformer tubes must: diffuse from the bulk gas to the surface of the catalyst particle (external diffusion), diffuse into the pores of particle (internal diffusion), adsorb onto the catalyst surface, react with other reagents at the surface of the catalyst to form products, desorb from the catalyst surface as products, diffuse as products through the pores to the surface and then from the surface to the bulk. For a given reaction, the

slowest step in this process is rate limiting and will dictate the overall rate of reaction. In an industrial SMR, the high bulk-gas velocity renders interfacial particle gradients negligible (Singh and Saraf, 1979). However, the rates of reactions at the catalyst active sites are much faster than the diffusion of reactants and products into and out of the catalyst pores (Alhabdan et al., 1992). As a result, the process is mass-transfer limited and the reactant concentrations in the catalyst pores are lower than the concentrations in the bulk gas. To account for the mass-transfer limitations, the catalyst particles can be modeled in detail, producing a heterogeneous (two-phase model) that describes concentration and temperature gradients within the catalyst particles. Alternatively, simpler pseudo-homogeneous models are used, in which effectiveness factors account for the reduced reaction rates that result from mass-transfer limitations.

In pseudo-homogeneous models, the process gas and catalyst are assumed to be at the same temperature and to be in intimate contact. The pseudo-homogeneous assumption simplifies mass-transfer modeling since external and internal diffusion are not considered explicitly. An effectiveness factor is applied to reaction rates to model the lower concentration of reactants at the catalyst sites. Since the process gas and catalyst are assumed to be at the same temperature, an overall heat-transfer coefficient can be used to describe heat transfer from the inner-tube wall to the catalyst and process gas.

In heterogeneous models, separate material (and energy) balances are performed on the bulk-process gas and on the process gas diffusing through the catalyst particle. Unlike pseudo-homogeneous models, the material balance on the bulk-process gas does not contain a reaction rate expression. Heterogeneous models are complex and require advanced solvers to generate catalyst concentration profiles for catalyst particles at different positions in the reactor. Usually,

the catalyst particles are assumed to be spherical or to be thin slabs. A matrix showing the different combinations of fixed-bed reactor models and a detailed description of each combination is provided by Froment and Bischoff (1979; p. 401).

All of the complete reformer models found in the literature use one-dimensional fixed-bed reactor models, with approximately half of the models being pseudo-homogeneous (Singh and Sarah, 1979; Murty and Murthy, 1988; Yu et al., 2006) and half heterogeneous (Soliman et al., 1988; Plehiers and Froment, 1989). Many two-dimensional heterogeneous models exist in the literature but only a few (Pedernera et al., 2003; Wesenberg and Svendsen, 2007) are reviewed in Table 3. The complex equations and long numerical solution times required for two-dimensional and heterogeneous models make them impractical for online use and are excluded from the remainder of this study.

2.6 Reaction Kinetics used in Process Models

Due to the complexity of the kinetics and mass-transfer phenomena in SMRs, early modelers (McGreavy and Newmann, 1969) determined the concentration of reactants and products at each axial position along the tubes by assuming reaction equilibrium and using the process gas temperature to calculate the equilibrium constant and species concentrations. The equilibrium assumption was surpassed by a kinetic model developed by Topsoe (See Singh and Saraf, 1979 for the Topsoe kinetic expressions) (Singh and Saraf, 1979; Murty and Murthy, 1988). In 1989, Xu and Froment developed the most widely-accepted kinetic model for methane reforming based on Langmuir-Hinshelwood (Houghen-Watson) kinetics (Xu and Froment, 1989a). The Xu and Froment kinetics have been used in almost all SMR models developed since 1989. Xu and

Froment identified three reactions that occur during steam-methane reforming and derived rate expressions for these three reactions. The rate expressions identify the rate limiting step in the absence of mass-transfer limitations. The Xu and Froment (1989a) kinetics are shown in detail in Appendix E.

2.7 Pressure Drop Correlations used in Process-Side Models

The drop in pressure in a fixed-bed reactor can be calculated using the following momentum balance (Froment and Bischoff, 1979; p. 403).

$$\frac{\Delta P}{\Delta y} = f \frac{\rho_{pg} V_s^2}{D_p} \quad (14)$$

In equation (14) f is the friction factor. The most commonly-used friction factor in the academic literature is that of Ergun (1952) (Singh and Saraf, 1979; Murty and Murthy, 1988; Plehiers and Froment, 1989; Alhabdan et al., 1992; Yu et al., 2006), which is show in equation (15).

$$f = \frac{(1-\phi)}{\phi} \left[a + \frac{b(1-\phi)}{Re} \right] \text{ where } a=1.75 \text{ and } b=150 \quad (15)$$

Singh and Saraf (1979) neglected the second term in the square bracket of equation (15) since the Reynolds number for their fixed-bed reactor was large. Hicks (1970) found that the Ergun equation did not adequately predict pressure drop in fixed beds with a flow regime where $Re/(1-$

$\phi) > 500$. Hicks proposed the friction factor in equation (16) for fixed beds with flow regimes from in the range $300 < Re/(1-\phi) < 60\ 000$.

$$f = 6.8 \frac{(1-\phi)^{1.2}}{\phi^3} Re^{-0.2} \quad (16)$$

The Hicks friction factor is used in several process-side models (Soliman et al., 1988; Alhadban et al., 1992; Wesenberg and Svendsen, 2007). Wesenberg and Svendsen (2007) compared the pressure predictions from the Ergun and Hicks friction factors. They found the Hicks friction factor gave a smaller pressure drop and was more suitable for SMR modeling because $Re_p/(1-\phi) > 500$ in most industrial reformers.

2.8 Tube-to-Process-Gas Heat-Transfer Coefficients used in Process-Side Models

Tube-to-process-side heat-transfer coefficients are used to calculate the rate of heat transfer between the inside of the reformer-tube wall and either the process gas or the combined catalyst and process gas. Although it is possible to model radial temperature profiles within the process gas (De Wasch and Froment, 1972; Dixon and Cresswell, 1979; Froment and Bischoff, 1979; pp. 452-455; Wesenberg and Svendsen, 2007), none of the reformer models reviewed in Table 1 considers radial temperature gradients. Wesenberg and Svendsen (2007) in their two-dimensional study of a gas-heated SMR concluded that radial heat transport in the packed bed is rapid and that the radial temperature profile is flat. Beskov et al. (1965) found similar results in a generic study of heat transfer in packed-bed reactors.

Four correlations for the tube-wall-to-process-side heat-transfer coefficient are used in one-dimensional process-side models. Leva and Grummer (1948) experimentally arrived at the empirical correlations shown in equations (17):

$$h_{tg} = f_{htg} 0.813 \frac{\lambda_{pg}}{2r_{in}} \exp\left(-3 \frac{D_p}{r_{in}}\right) \left(\frac{D_p G_s}{\mu_{pg}}\right)^{0.9}, \text{ where } Re = \frac{D_p G_s}{\mu_{pg}} \quad (17)$$

A Reynolds number range for the correlation is not given. The thermal conductivity of the packing influences equation (17) through the adjustable parameter f_{htg} . f_{htg} can be estimated as a function of packing thermal conductivity as done by Leva and Grummer (1948) or can be treated as an adjustable parameter and fit using experimental data. The correlation shown in equation (17) was used by Soliman et al (1988), Yu et al. (2006) and Alhabdan et al. (1992).

The second correlation encountered in the literature was developed by Beek (1961) and is shown in equation (18).

$$h_{tg} = f_{htg} \frac{\lambda_{pg}}{D_p} \left(2.58 Re^{1/3} Pr^{1/3} + 0.094 Re^{4/5} Pr^{0.4}\right), \text{ where } Pr = \frac{\mu_{pg} C_{p,pg}}{\lambda_{pg}} \quad (18)$$

The correlation is only valid for Reynolds numbers greater than 40, and does not account for the thermal conductivity of the packing. Hyman (1968) found that the convective heat-transfer coefficient for an industrial SMR packed with Raschig rings was 40% of the value calculated by

equation (18). Singh and Saraf (1979) and Murty and Murthy (1988) adjusted the correction factor (f_{htg}) to improve the predictions of the correlation.

De Wasch and Froment (1972) developed correlations for the heat transfer in one-dimensional and two dimensional fixed-bed reactor models. The general correlation for the one dimensional model, as provided by Froment and Bishcoff (1979; p. 404), is given in equation (19).

$$h_{tg} = h_{tg}^0 + 0.033 \text{Pr Re} \frac{\lambda_{pg}}{D_p} \quad (19)$$

The parameter h_{tg}^0 is a function of the tube diameter, catalyst properties and catalyst geometry.

Tabulated values for some catalysts are given by De Wasch and Froment (1972).

The two-dimensional fixed-bed reactor model uses a wall heat-transfer coefficient (α_w) and an effective thermal conductivity for the fixed bed (k_{er}) to model radial temperature gradients. The two-dimensional model parameters can be combined to give the heat-transfer coefficient for a one-dimensional model. This method was used by Xu and Froment (1989b) and Plehiers and Froment (1989) to calculate the tube-to-process-side heat-transfer coefficient in one-dimensional-heterogeneous models.

$$h_{tg} = \frac{1}{\frac{r_{in}}{4k_{er}} + \frac{1}{\alpha_w}} \quad (20)$$

The variables α_w and k_{er} are the wall-to-gas heat-transfer coefficient and effective packed-bed thermal conductivity, respectively. α_w and k_{er} can be expressed as functions of one parameter k_{er}^o as shown in equations (21)-(23).

$$\alpha_w = \alpha_w^o + 0.444 \text{ Pr Re} \frac{\lambda_{pg}}{D_p} \quad (21)$$

$$\alpha_w^o = \frac{8.694}{(2r_{in})^{4/3}} k_{er}^o \quad (22)$$

$$k_{er} = k_{er}^o + 0.14 \lambda_{pg} \text{ Re Pr} \quad (23)$$

The parameter k_{er}^o is the static effective thermal conductivity of the packed bed (the thermal conductivity of the bed when there is no fluid flow. It can be calculated from fundamental equations derived by Kuni and Smith (1960).

2.9 Sub-Models Chosen for Mathematical Modeling Study

Tables 1-3 show the sub-models used in furnace and reformer modeling over the past fifty years. Sub-models must be chosen for radiative-heat transfer, furnace-heat-release patterns, furnace-flow patterns, furnace-convective-heat-transfer coefficients, process-side fixed-bed reactor behavior, reforming reaction kinetics, fixed-bed pressure drop and tube-to-process-side convective heat transfer coefficients. The choice of sub-models for each category is informed by

the sub-models' acceptance in the academic literature and by the runtime requirements, important physical phenomena and level of accuracy required by the problem description. The most important sub-model is the radiative heat-transfer method, because it will influence the structure of the overall model, along with its accuracy, capabilities and flexibility. The choices of sub-model for the furnace heat-release pattern, furnace-flow pattern and fixed-bed reactor behavior are limited by the runtime requirements. Particular sub-models for furnace-convective-heat-transfer coefficients and reaction kinetics have been widely accepted in the academic literature while no clear consensus exists for the friction factor used in the momentum balance or the tube-to-process-gas convective heat transfer coefficient.

Comparison and Choice of Furnace Radiation Model

The Hottel zone method and Roseler flux method are the two dominant approaches to radiant furnace modeling. Since the radiative-heat-transfer method will dictate the structure of the process-side model and will influence the model accuracy, capabilities and flexibility, choosing the appropriate method is an important decision in this study.

Studies have been performed to compare the accuracy and computation times of the Hottel zone and Roesler flux methods. A comparison of these methods was performed by Murty et. al. (1989), Selcuk et. al. (1975a,b) and Farhadi et al. (2005).

Selcuk et. al. (1975a,b) used the Hottel zone and Roesler flux methods to predict the tube-skin temperature profile in a bottom-fired multi-pass heat exchanger for different flame lengths. The tube-wall temperature profile was used to predict the location of the maximum tube-wall temperature. The heat exchanger was cylindrical with a diameter of 3.75 m and a height of 11 m.

The tubes were arranged vertically around the perimeter of the furnace and four burners were located in the center. The zone method assumed one gray gas, used direct-exchange areas calculated from tables (Erkku, 1959), and divided the furnace into one radial gas zone and six axial gas zones. The zone method was compared to the Roseler 2-flux method in cylindrical coordinates. The zone method produced a temperature profile closer to the actual heater temperature profile, while the flux method tended to over-predict the tube-wall temperature profile. The online runtime of the zone method was shorter than that of the flux method (zone runtime = 25 s, flux runtime = 40 s).

Murty et al. (1989) compared the zone and flux methods for a cylindrical oil-fired luminous furnace with a diameter of 1 m and length of 4 m. The models were evaluated for accuracy by comparing the wall heat-flux profiles to experimental data. The zone method assumed one gray gas and used total-exchange areas calculated from tabulated direct-exchange areas (Erkku, 1959). The enclosure zoning was investigated and an appropriate number of zones chosen for the comparison. The zone method was compared to the Roesler 2-flux and two-dimensional 4-flux methods. The zone method gave the most accurate predictions, but was computationally intensive (run time = 150 s on a computer equivalent to an IBM 360). The Roesler 2-flux method gave a less accurate prediction than the zone method, but was less computationally intensive (run time = 45 s). The Roesler two-dimensional 4-flux method gave results of similar accuracy to the Roesler 2-flux method, but with a much larger computation time (900 s). The accuracy of the 2-flux method was deemed to be acceptable for furnace design purposes.

Farhadi et. al. (2005) used simplified versions of the Hottel zone method and the Roesler 2-flux and 4-flux methods to predict the outlet gas conditions, tube temperature profile and heat flux

profile in a bottom-fired Midrex™ reformer. The model outputs were compared to plant data. Farhadi et al. considered a well-stirred Hottel zone mode and long-furnace model of type 1 (Rhine and Tucker, 1991; pp. 244-256). The furnace radiation models were coupled to a one-dimensional process-side model. The well-stirred Hottel zone method, 2-flux and 4-flux Roesler methods were deemed to give adequate results. The Hottel long-furnace model of type 1 gave unacceptable results because it neglected gas-to-gas radiative exchange. The well-stirred zone method gave more accurate predictions than the 2-flux or 4-flux methods.

All three comparison studies (Selçuk et al., 1975; Murty et al., 1989; Farhadi et al., 2005) found Hottel zone methods to give more accurate predictions than Roesler flux methods. Although the zone method is generally described as being more computationally intensive, since directed-flux areas must be calculated and furnace flow patterns explicitly defined, the runtimes for the Hottel zone method described by Selçuk et al. (1975a,b) and Murty et al. (1989) were adequate for on-line use (under four minutes) using the computers that were available. In fact Selçuk et al. (1975a,b) found the online runtime for the Hottel zone method to be shorter than the Roesler flux method. The features of the two methods are summarized in Table 4.

Table 4. Comparison of Hottel zone and Roesler Flux Methods

Hottel Zone	Roesler (one dimensional 4-Flux)
Divide furnace into zones	Divide radiation, furnace gas and process gas into streams
Algebraic mass balances in volume zones and energy balances for all zones	Differential balances on streams
Non-linear algebraic equations	Coupled differential equations
Discretized temperature and composition profiles	Continuous profiles
Accommodates detailed geometry	Limited geometric capabilities
Can accommodate complex flow patterns	Must assume plug flow
Easy to add additional gray gases	Difficult to add gray gases

Computation time sufficiently fast for online use	Computation time sufficiently fast for online use
Accurate results if radiation assumptions are not too restrictive	Adequate results

Although the flux method could be adequate for this project, the zone method was chosen to model the reformer firebox. This decision was based on the zone method's simplicity, flexibility and accuracy. The zone method is easier to conceptualize than the flux method. The algebraic mass and energy balances used in the zone method are more intuitive for chemical engineers than the differential radiant-energy balances that arise in the flux method. In addition, the zone method is more flexible than the flux method because it can be readily modified to simulate any furnace geometry, flow pattern and furnace gas composition. For many years, difficulties associated with calculating direct, total and directed-flux areas for complex geometries caused many modelers to avoid the Hottel zone method and to resort to using advanced versions of the Roesler flux method. However, modern computing techniques, including Monte Carlo ray tracing simulations allow for the calculation of exchange areas for complex geometries (Lawson and Ziesler, 1991). Exchange areas can be calculated offline, stored and used for online furnace simulations. This streamlines the most difficult step in the Hottel zone method and allows detailed high-accuracy simulations for complex furnaces in a reasonable time. This choice of radiation model can be classified as the long furnace mode type 2 described in Rhine and Tucker (1991; pp. 241-242).

Choices Limited by Runtime Requirements

Since accurate physical modeling or CFD studies of the furnace gas-flow and heat-release patterns are not available for the SMR considered in this study, the following simple assumptions

are made throughout the remainder of the thesis: plug flow is assumed for the furnace gas and a parabolic heat-release profile is assumed over the flame length. On the process side, the fixed-bed reactor model is a one-dimensional pseudo-homogenous model with plug flow of the gas. Since the Hottel Zone method is used, the furnace side and the process side are divided into discrete zones with uniform temperature and composition. The process side of the reformer is represented as a series of continuous stirred-tank reactors (CSTRs). As the number of CSTRs in series increases, their predicted behavior approaches that of a plug-flow packed-bed reactor (Levenspiel, 1999; p. 126)

Widely-Accepted Choices

There is widespread agreement in the literature on appropriate choices for the furnace convective-heat-transfer coefficient correlation and reaction kinetics. The furnace convective heat-transfer coefficient used in this study is calculated using the Dittus-Boelter equation (12) and the reaction kinetics used are those of Xu and Froment (1989a) (See Appendix E).

Choices with No Clear Literature Consensus

In the academic literature, the choice of a friction factor correlation for the process-side momentum balance is split between the Ergun and Hicks friction factors. Wesenberg and Svendsen (2007) recommend the Hicks friction factor for flow regimes where $Re/(1-\phi) > 500$. Although the flow regime of the industrial SMRs studied in this thesis meets this criterion for the Hicks friction factor, the pressure drop calculated by the Hicks friction factor was too low compared with the pressure drop from the industrial data. As a result, the Ergun friction factor,

which produces a larger predicted pressure drop, is used instead in the current model instead of the Hicks friction factor.

In the academic literature, the two dominant tube-to-process-gas convective-heat-transfer-coefficient correlations are the Leva and Grummer (1948) correlation and the DeWasch and Froment (1972) correlation. Since the experimental work done to develop both correlations was done at small scale, does not account for detailed catalyst geometry and approximates complex radial heat-transfer processes with a single value, it is reasonable for the coefficient calculated by either correlation to be modified by an adjustable parameter to obtain a good fit to the plant data. Since the Leva and Grummer (1948) correlation is simpler than the De Wasch and Froment (1972), this correlation is used in the model.

2.10 References

Alhabdan, F. M., Abashar, M. A. and Elnashaie, S. S. E. (1992) A flexible computer software package for industrial steam reformers and methanators based on rigorous heterogeneous mathematical models. *Mathematical Computer Modeling*. vol. 16 pp. 77-86.

Baburić, M., Duić, N., Raulot, A and Coelho, P. J. (2005) Application of the conservative discrete transfer radiation method to a furnace with complex geometry. *Numerical Heat Transfer, Part A*. vol. 48 pp. 297-313.

Beek, J. (1962) Design of packed catalytic reactors. *Advances in Chemical Engineering*. Academic Press, New York, NY. vol. 3 pp. 232-235.

Beskov, V. S., Kuzin, V. P. and Slin'ko, M. G. (1965) Modeling chemical processes in a fixed bed of catalyst. Radial mass and heat transfer. *International Chemical Engineering*. vol. 5 no. 2.

De Wasch, A. P. and Froment, G. F. (1972) Heat transfer in packed beds. *Chemical Engineering Science*. vol. 27 pp. 567-576.

Dixon, A. G. and Cresswell, D. L. (1979) Theoretical prediction of effective heat transfer parameters in packed beds. *AIChE Journal*. vol. 25 pp. 663-668.

Ebrahimi, H., Mohammadzadeh, J. S. S., Zamaniyan, A. and Shayegh, F. (2008) Effect of design parameters on performance of a top fired natural gas reformer. *Applied Thermal Engineering*. vol. 28 pp. 2203-2211.

Ergun, S. (1952) Fluid flow through packed columns. *Chemical Engineering Progress*. vol. 48 pp. 89-94.

Erkku H. (1959) Radiant heat exchange in gas filled slabs and cylinders. Sc. D. Thesis in Chemical Engineering. Massachusetts Institute of Technology.

Farhadi, F., Bahrami Babaheidari, M., Hashemi, M. (2005) *Applied Thermal Engineering*. Radiative models for the furnace side of a bottom-fired reformer. Vol. 25 pp. 2398-2411.

Froment, G. F. and Bischoff, K. B. (1979) Chemical Reactor Analysis and Design. John Wiley, New York, NY.

Guo, Z. and Maruyama, S. (2001) Prediction of radiative heat transfer in industrial equipment using the radiation element method. Transactions of the ASME. vol. 123 pp. 530-536.

Han, Y., Xiao, R. and Zhang. (2006) Combustion and pyrolysis reactions in a naphtha cracking furnace. Chemical Engineering and Technology. vol. 29 pp. 112-120.

Hicks, R. E. (1970) Pressure Drop in Packed Beds of Spheres. Industrial and Engineering Chemistry Fundamentals. vol. 9 pp. 500-502.

Hoffman, N. and Markatos, N. C. (1988) Thermal radiation effects on fires in enclosures. Applied Mathematical Modeling. vol. 12 pp. 129-139.

Hottel, H. C. and Sarofim, A. F. (1967) Radiative Heat Transfer. McGraw-Hill Inc, New York, NY.

Hottel, H. C. and Sarofim, A. F. (1965) The effect of gas flow pattern on radiative transfer in cylindrical furnaces. International Journal of Heat and Mass Transfer. vol. 8 pp. 1153-1169.

Hyman, M. H. (1968) Simulate methane reformer reactions. Hydrocarbon Processing. vol. 47 pp. 131-137.

Keramida, E. P., Liakos, H. H., Founti, M. A., Boudouvis, A. G. and Markatos, N. C. (2000) Radiative heat transfer in natural gas-fired furnaces. *International Journal of Heat and Mass Transfer*. vol. 43 pp. 1801-1809.

Kuni, D. and Smith, J. M. (1960) Heat transfer characteristics of porous rocks. (1960) *AIChE Journal*. vol. 6 pp. 71-78.

Lawson, D. A. and Ziesler, C. D. (1996) An accurate program for radiation modeling in the design of high-temperature furnaces. *IMA Journal of Mathematics Applied in Business and Industry*. vol. 7 pp. 109-116.

Leva, M. and Grummer M. (1948) Heat transfer to gases through packed tubes: Effect of particle characteristics. *Industrial and Engineering Chemistry*. vol. 40 pp. 415-419.

Lebedev, V. I. and Sokolov, V. A. (1976) Study of the convective component of complex heat exchange in a model of a direct-heating furnace. *Glass and Ceramics*. vol. 33 pp. 352-354

McGreavy, C. and Newmann, M. W. (1969) Development of a mathematical model of a steam methane reformer. *Institution of Electrical Engineering, Conference on the Industrial Applications of Dynamic Modelling*. Durham Sept. 1969.

Mohammadzadeh, J. S. S. and Zamaniyan, A. (2003) Simulation of terrace wall methane-steam reforming reactors. *Iranian Journal of Science and Technology, Transaction B*. vol. 26 pp. 249-260.

Murty, C. V. S. and Murthy, M. V. (1988) Modeling and simulation of a top-fired reformer. Industrial Engineering and Chemistry Research. vol. 27 pp 1832-1840.

Murty, C. V. S., Richter, W. and Krishna Murthy, M. V. (1989) Modeling of thermal radiation in fired heaters. vol. 67 pp. 134-143.

Levenspiel, Octave. (1999) Chemical reaction engineering. John Wiley and Sons, New York, NY.

Ramana Rao, M. V., Plehiers, P. M. and Froment, G. F. (1988) The couples simulation of heat transfer and reaction in a pyrolysis furnace. Chemical Engineering Science. vol. 43 pp. 1223-1229.

Rhine, J. M. and Tucker, R. J. (1991) Modelling of gas-fired furnaces and boilers. McGraw-Hill Book Company, New York, NY.

Roesler, F. C. (1967) Theory of radiative heat transfer in co-current tube furnaces. Chemical Engineering Science. vol. 2 pp. 1325-1336.

Selçuk, N., Siddall, R. G., Beér, J. M. (1975a) A comparison of mathematical models of the radiative behavior of an industrial heater. Chemical Engineering Science. vol. 30 pp. 871-876.

Selçuk, N., Siddall, R. G., Beér, J. M. (1975b) Prediction of the effect of flame length on temperature and radiative heat flux distribution in a process heater. *Journal of the Institute of Fuel*. vol. 48 pp. 89-96.

Singh, C. P. P. and Saraf, D. N. (1979) Simulation of side fired steam-hydrocarbon reformers. *Industrial and Engineering Chemistry Process Design and Development*. vol. 18 pp. 1-7.

Soliman, M. A., El-Nashaie, S. S. E. H., Al-Ubaid, A. S. and Adris, A. (1988) Simulation of steam reformers for methane. *Chemical Engineering Science*. vol. 43 pp. 1801-1806.

Stefanidis, G. D., Merci, B., Heynderickx, G. J. and Marin, G. B. (2006) CFD simulation of steam cracking furnaces using detailed combustion mechanisms. *Computers and Chemical Engineering*. vol. 30 pp. 635-649.

Steward F. R. and Cannon, P. (1971) The calculation of radiative heat flux in a cylindrical furnace using the Monte Carlo Method. *International Journal of Heat and Mass Transfer*. vol. 14 pp. 245-262.

Wakao, N., Kaguei, S. and Funazkri, T. (1979) Effect of fluid dispersion coefficients on particle-to-fluid heat transfer coefficient in packed beds. *Chemical Engineering Science*. vol. 34 pp. 325-336.

Wesenberg, M. H. and Svendsen, H. F. (2007) Mass and heat transfer limitations in a heterogeneous model of a gas-heated steam reformer. *Industrial and Engineering Chemistry Research*. vol. 46 pp. 667-676.

Xu, J. and Froment, G. F. (1989a) Methane steam reforming, methanation and water-gas shift: I intrinsic kinetics. *AIChE Journal*. Vol. 35 pp. 88-96.

Xu, J. and Froment, G. F. (1989b) Methane steam reforming: II limitations and reactor simulation. *AIChE Journal*. Vol. 35 pp. 97-103.

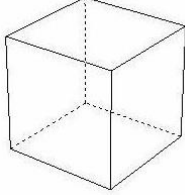
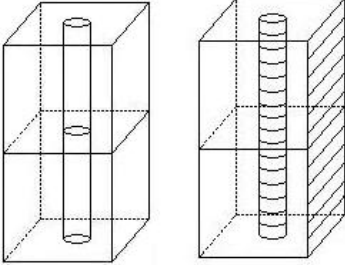
Yu, Z., Cao, E., Wang, Y., Zhou, Z., Dai, Z. (2006) Simulation of Natural Gas Steam Reforming Furnace. *Fuel Processing Technology*. vol. 87 pp. 695-704.

Chapter 3

Mathematical Modeling Studies

In this thesis, model development progresses from modeling i) a simple cube-shaped combustion chamber containing combustion gases to ii) a single reformer tube in a rectangular furnace to iii) a complete SMR model with multiple tubes. These three model versions are referred to as the cube-furnace model, the segmented-tube model and the average-tube model, respectively. An overview of each model stage is shown in Table 5. This incremental approach to model development allows verification of model equations and computer code with simple geometries before more complex situations are considered. This chapter gives a detailed description of each model stage, highlights improvements over the previous stage, states all simplifying assumptions and gives the model equations, many of which are derived in Appendix C. In addition, many supplemental equations are provided in Appendix E.

Table 5. Incremental Model Development

Stage	Title	Diagram	Description
1	Cube-Furnace Model		<ul style="list-style-type: none"> - Furnace wall and gas temperatures are calculated -Combustion occurs in a single gas zone -Radiative and convective heat transfer are modeled -Heat loss to environment is considered
2	Segmented-Tube Model		<ul style="list-style-type: none"> -Furnace wall and gas temperatures are calculated -Inner and outer tube wall temperatures, tube-side gas composition and pressure are calculated -Reaction kinetics, pressure drop, conductive heat transfer are included -Tube and furnace gas are divided into vertical sections to give profiles -Heat of combustion is distributed among furnace zones
3	Average-Tube in Reformer	(See Figure 7, Figure 8 and Figure 9)	<ul style="list-style-type: none"> -Temperature profile is calculated for an average tube -Radiative heat transfer from multiple tubes and gas zones is included -Coffin boxes and unique reformer geometry are accounted for

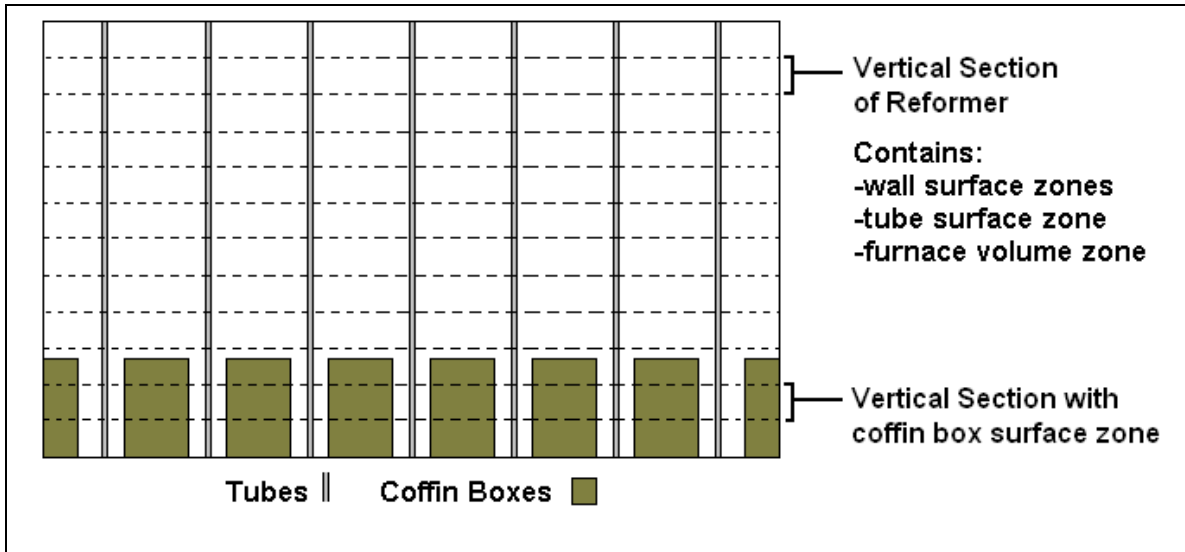


Figure 7. Cross-Section of Reformer Showing Tubes, Coffin Boxes and Spatial Discretization

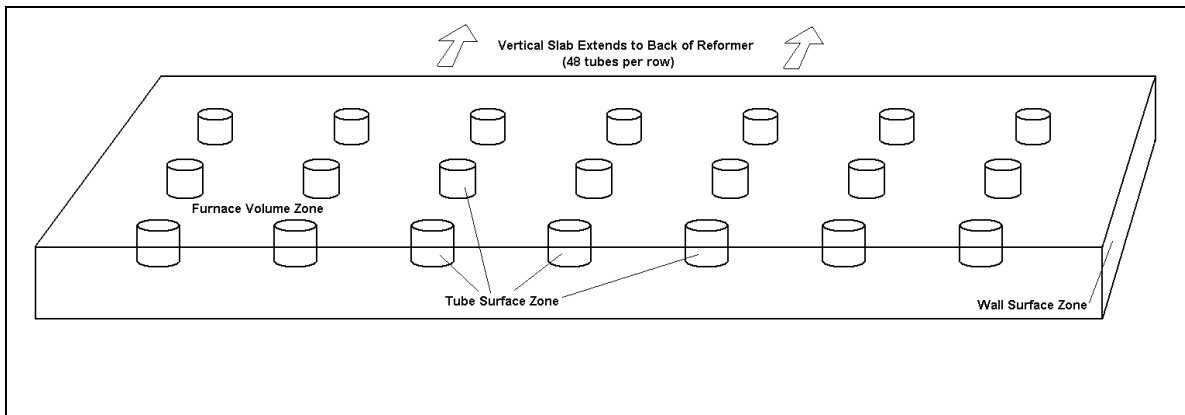


Figure 8. Vertical Section without Coffin Boxes in Average-Tube Reformer Model. Note that all of the tube surface areas constitute a single surface zone and the gas between the tubes constitutes a single volume zone. The total volume of process gas enclosed by all of the tubes is treated as a single vertical segment in the model.

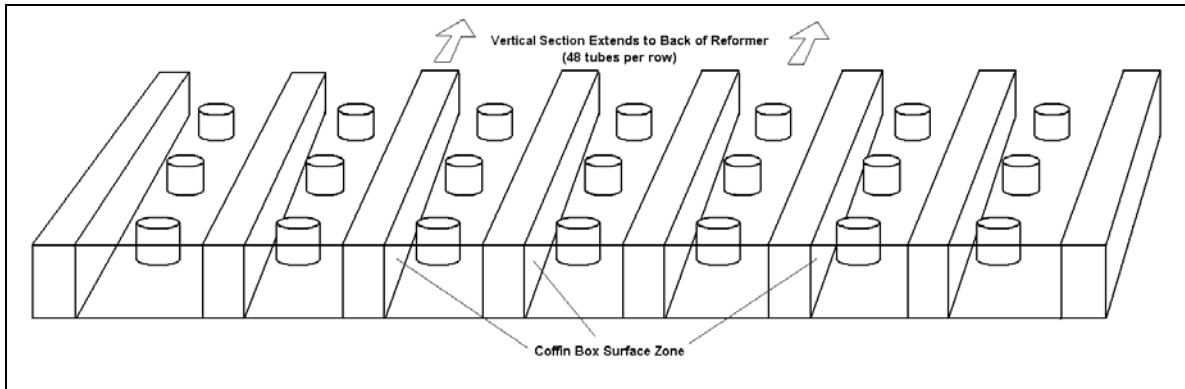


Figure 9. Vertical Slab with Coffin Boxes in Average-Tube Reformer Model.
Note that the areas on the sides of the coffin boxes are grouped together into a single surface zone.

3.1 Cube-Furnace Model

The cube-furnace model simulates the combustion of furnace gases in a combustion chamber. The model calculates the temperature of the furnace walls and the temperature of the furnace gas for a given fuel rate. There are seven unknown temperatures in the model, one temperature for each of the six surface zones and one temperature for the volume zone (See Figure 10).

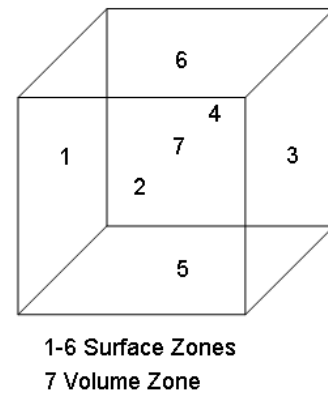


Figure 10. Cube Furnace Numbering Scheme

An energy balance is performed on each zone, producing seven equations and seven unknowns as shown in Table 6. The seven unknown variables ($x_i, i=1..7$) are temperatures of the zones shown in Figure 10. The corresponding energy balance equations, which are of the form $f_i()=0$ are described in Table 7. These energy balances, which are described in detail in equations (24) and (25) are solved iteratively using the Newton-Raphson Method (See Appendix E). Radiative heat transfer, convective heat transfer and fuel combustion

are simulated in the cube furnace model. Radiative heat transfer is accounted for using the Hottel zone method. The purpose of the cube-furnace model is to create a simple test problem to aid in the development of more advanced models. The model is not intended to represent an industrial SMR furnace.

Table 6. Cube-Furnace Model Structure

$$\mathbf{f}(\mathbf{x}) = \begin{bmatrix} f_1(x_1, x_2, \dots, x_7) \\ \vdots \\ f_7(x_1, x_2, \dots, x_7) \end{bmatrix} = \mathbf{0}$$

Number of Equations = 7
Number of Unknowns = 7
Number of Equation Types = 2

Table 7. Vector Equation f and Unknown Vector x for the Cube-Furnace Model

Index in f and x	Equation Type	Unknown Variable
1	Surface-Zone Energy Balance	T ₁ [K]
2	Surface-Zone Energy Balance	T ₂ [K]
3	Surface-Zone Energy Balance	T ₃ [K]
4	Surface-Zone Energy Balance	T ₄ [K]
5	Surface-Zone Energy Balance	T ₅ [K]
6	Surface-Zone Energy Balance	T ₆ [K]
7	Volume-Zone Energy Balance	T ₇ [K]

Assumptions in the Cube-Furnace Model

In the cube-furnace model, many properties that are functions of temperature, composition and pressure are assumed to be constant. The values for these properties are listed in Table 8 and a detailed list of the model assumptions is given below.

1. The furnace feed consists of stoichiometric amounts of methane and oxygen.
2. The fuel to the furnace has a heat of combustion that is independent of temperature.

3. Complete instantaneous combustion occurs as the furnace fuel and oxygen enter the furnace.
4. The furnace gas is uniform in temperature and composition.
5. The heat capacity of the furnace gas is independent of temperature and composition.
6. The convective heat transfer coefficient between the furnace gas and furnace walls is constant.
7. The thermal conductivity between the furnace walls and external environment is constant.
8. The emissivity and absorptivity of the furnace walls are equal and are independent of temperature.
9. The furnace gas is modeled as one gray gas.

Table 8. Cube-Furnace Model Constants

Description	Symbol	Value
Cube side length	L	0.61 m
Temperature of the surroundings	T_{surr}	293 K
Furnace gas heat capacity	C_p	$1006.1 \frac{\text{J}}{\text{kg} \cdot \text{K}}$
Convective heat transfer coefficient	h_{gso}	$1635.3 \frac{\text{kJ}}{\text{m}^2 \cdot \text{h} \cdot \text{K}}$
Heat of combustion	ΔH_{comb}	$-801.2 \frac{\text{kJ}}{\text{gmol}}$
Refractory emissivity	ϵ_{refrac}	0.9
Thermal conductivity	k_{refrac}	$623.1 \frac{\text{kJ}}{\text{m} \cdot \text{h} \cdot \text{K}}$
Refractory thickness	t_{refrac}	0.305 m

Gray gas absorption coefficient	K	1.64 $\frac{1}{m}$
Total mass flow rate of air and furnace fuel	\dot{m}_{fur}	45.34 $\frac{kg}{h}$

Cube-Furnace Model Equations

Energy balance equations for the six surface zones and single volume zone are provided below in equations (24) and (25), respectively.

Furnace-Surface-Zone Energy Balance (f_i , $i=1..6$)

$$f_i = \sigma \sum_{\substack{\text{all furnace} \\ \text{zones } j}} \overline{Z_j Z_i} T_j^4 - \sigma \varepsilon A T_i^4 + h_{gso} A (T_{adj\ gas} - T_i) - \frac{k_{refrac}}{t_{refrac}} A (T_i - T_{surr}) \quad (24)$$

Furnace-Volume-Zone Energy Balance (f_7)

$$f_7 = 0 = \sigma \sum_{\substack{\text{all furnace} \\ \text{zones } j}} \overline{Z_j Z_i} T_j^4 - 4KV\sigma T_7^4 - \sum_{\substack{\text{all surface} \\ \text{zones } j}} h_{gso} A_j (T_7 - T_j) - \dot{m}_{fur} \int_{T_{fur\ in}}^{T_7} C_p dT - \dot{n}_{CH_4} (\Delta H_{comb} - RT_7 \Delta n_{comb}) \quad (25)$$

Validation of Results

The solution for the unknown variables in the cube-furnace model, with the inputs in Table 8, is given in Table 9.

Table 9. Solution to Cube-Furnace Model

Index	Vector of Unknowns x [°C]
1	919.46
2	919.63
3	919.56
4	919.71
5	919.62
6	919.46
7	1000.00

To confirm the results in Table 9, an overall-energy balance was performed on the cube furnace. When the temperatures in Table 9 were entered into equation (26), the left and right sides of the equation were equal.

Heat released by combustion in the volume zone =

Enthalpy of gas in - Enthalpy of gas out

+ Energy lost by conduction through the furnace walls (26)

$$-\dot{n}_{\text{CH}_4} (\Delta H_{\text{comb}} - RT_7 \Delta n_{\text{comb}}) = -\dot{m}_{\text{fur}} \int_{T_{\text{fur in}}}^{T_7} C_p dT + \sum_{\text{surface zones } i} \frac{k_{\text{refrac}}}{t_{\text{refrac}}} A_i (T_i - T_{\text{surr}})$$

3.2 Segmented-Tube Model

The segmented-tube model simulates a simple SMR consisting of a single tube contained in a rectangular furnace. The model calculates the temperature of all the furnace zones, the temperature of the inner- and outer-tube-wall zones and the temperature, composition and

pressure of the process gas in each tube segment. The simplest version of the segmented-tube model shown in this thesis is composed of only two tube segments and the most advanced version contains twelve segments. A diagram of the segmented-tube model is shown in Table 5.

In the segmented-tube model, the furnace-side model is improved by adding multiple furnace zones, by accounting for more complex furnace geometry, and by pre-combusting the furnace fuel and distributing of the heat released by combustion over several volume zones. This approach to heat distribution is used by other SMR modelers (Roesler, 1967; Selçuk et al., 1975a) and b); Solimon et al., 1988; Murty and Murthy, 1988; Yu et al., 2006). As shown in Table 10 and Table 11, the process-side model is coupled to the furnace-side model by conductive heat transfer through the tube wall. On the process side, a fixed-bed reactor model, reaction kinetics expressions, tube thermal conductivity, convective heat-transfer coefficients and a pressure-drop correlation are added to simulate process-side physical and chemical phenomena. Numbering of the furnace zones and tube segments is described in detail in Appendix F.

Table 10. Structure of the Segmented-Tube Model

$$\mathbf{f}(\mathbf{x}) = \begin{bmatrix} f_1(x_1, x_2, \dots, x_{182}) \\ \vdots \\ f_{182}(x_1, x_2, \dots, x_{182}) \end{bmatrix} = \mathbf{0}$$

Number of Equations = 182

Number of Unknowns = 182

Number of Equation Types = 7

Number of Vertical Sections = 12

Table 11. Vector Equation $f=0$ and Unknown Vector x for the Segmented-Tube Model

Index in f and x	Equation Type	Furnace Zone or Tube Segment	Unknown Variable
1	Surface-Zone Energy Balances	Zone 1	T_1 [K]
2		Zone 2	T_2 [K]
...	
50		Zone 50	T_{50} [K]
51	Obstacle-Zone Energy Balances (on outer tube surfaces)	Zone 51	T_{51} [K]
52		Zone 52	T_{52} [K]
...	
62		Zone 62	T_{62} [K]
63	Volume-Zone Energy Balances (on furnace gas)	Zone 63	T_{63} [K]
64		Zone 64	T_{64} [K]
...	
74		Zone 74	T_{74} [K]
75	Inner-Tube-Surface Energy Balances	Segment 1	T_{75} [K]
76		Segment 2	T_{76} [K]
...	
86		Segment 12	T_{86} [K]
87	Process-Gas Energy Balances	Segment 1	T_{87} [K]
88		Segment 2	T_{88} [K]
...	
98		Segment 12	T_{98} [K]

99	Process-Gas Material Balances (on the six chemical species)	Segment 1	P_{99H_2} [kPa]
100		Segment 1	P_{100CO} [kPa]
101		Segment 1	P_{101CH_4} [kPa]
102		Segment 1	P_{102N_2} [kPa]
103		Segment 1	P_{103CO_2} [kPa]
104		Segment 1	P_{104H_2O} [kPa]
...	
165		Segment 12	P_{165H_2} [kPa]
166		Segment 12	P_{166CO} [kPa]
167		Segment 12	P_{167CH_4} [kPa]
168		Segment 12	P_{168N_2} [kPa]
169		Segment 12	P_{169CO_2} [kPa]
170		Segment 12	P_{170H_2O} [kPa]
171	Momentum Balance (Ergun equation)	Segment 1	ρ_{171} [kg/m ³]
172		Segment 2	ρ_{172} [kg/m ³]
...	
174		Segment 12	ρ_{174} [kg/m ³]

Assumptions in the Segmented-Tube Model

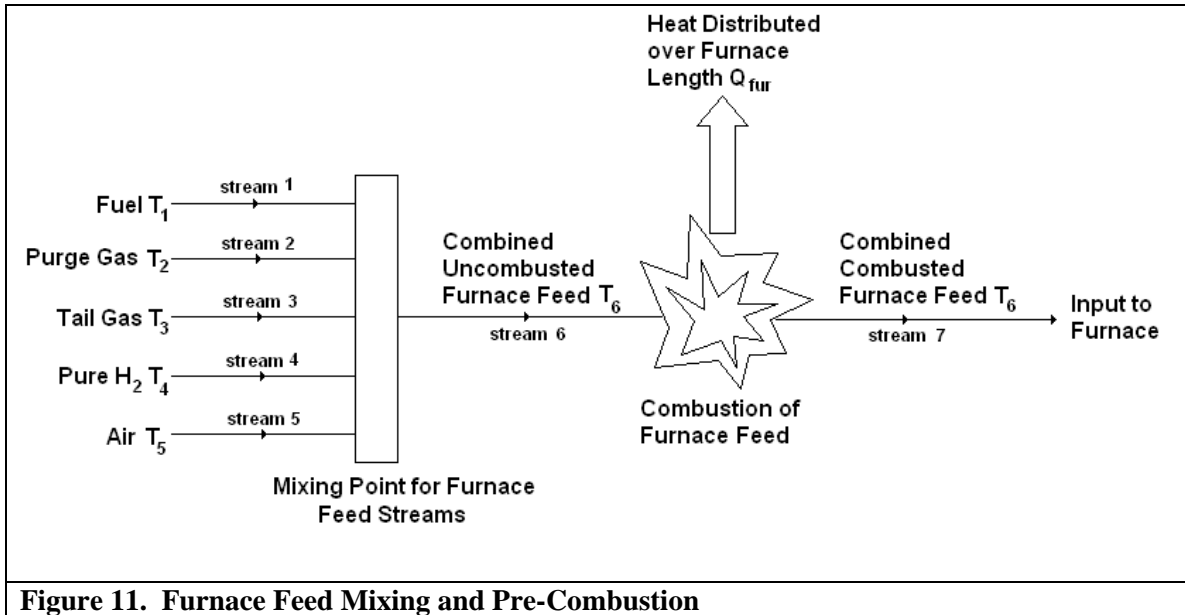
1. The fuel is a mixture of chemical species with a typical composition that is used to feed the industrial SMR furnace.
2. The furnace fuel is isothermally combusted at its inlet temperature before entering the furnace. Combustion is assumed to occur in the presence of excess oxygen and to go to completion. The heat released by this combustion is distributed over a number of zones. This assumption results in a uniform gas composition everywhere in the furnace.
3. For radiative heat-transfer purposes the carbon-dioxide-to-water-vapor ratio is assumed to be near to 1:1 in the furnace gas, so that the Taylor and Foster (1976) gray-gas model can be used.
4. The furnace gas is assumed to consist of one clear gas and three gray gases.
5. The furnace gas moves in perfect plug flow from the top of the furnace, where it enters, to the bottom of the furnace where it exits.
6. The emissivity and absorptivity of all surfaces in the furnace are equal and are independent of temperature.
7. The thermal conductivity of the furnace walls is independent of temperature.
8. The flame is non-luminous and the furnace gas does not scatter radiation.
9. All gases behave as ideal gases.
10. The reference state for furnace-side energy balances are the reactants and products fully formed at the temperature of the inlet temperature of the fuel.
11. Process gas flows from the top tube segment to the bottom. There is no back mixing.
12. Only hydrogen, carbon monoxide, methane, nitrogen, carbon dioxide and water exist on the process side.

13. The reference state for internal energy and enthalpy calculations on the process side is the reactants and products fully formed in the gas state at the temperature of the gas in the previous segment (i.e., the segment above the current segment) and 101.325 kPa.
14. The catalyst particles and process gas are at the same temperature as each other within each tube segment.

Segmented-Tube Model Equations

Furnace Feed Calculations

As shown in Figure 11, the model accepts up to five user-defined furnace-feed streams and calculates the combined uncombusted furnace-feed temperature (T_6) and the heat released by isothermal combustion of the furnace fuel (Q_{fur}) at constant pressure. The furnace inlet streams are labeled fuel, purge gas, tail gas, pure hydrogen and air. These labels are the names of streams commonly fed to the furnace in the industrial SMR of interest. Stream 7 is the combined combusted furnace feed. Since the combustion of the furnace feed is assumed to occur isothermally, stream 7 is at the same temperature as stream 6.



Calculation of T_6 : Energy Balance at the Mixing Point in Figure 11

Since the temperatures of the inlet streams (T_1 to T_5) are known, the temperature of the combined uncombusted furnace feed can be calculated using equation (27). A reference temperature T_{ref} that is close to T_6 is chosen by an iterative method (See Appendix C, which provides a derivation of equation (27)).

$$T_6 = \frac{\sum_{i=1}^5 \dot{n}_i \left(\sum_{\substack{\text{combustion} \\ \text{species } j}} X_j \int_{T_{ref}}^{T_i} C_{p,j} dT \right)}{\dot{n}_6 \sum_{\substack{\text{combustion} \\ \text{species } j}} X_j C_{p,j,T_{ref}}} + T_{ref} \quad (27)$$

Calculation of the Heat Released by Combustion Q_{fur}

An energy balance for the isothermal pre-combustion step is simplified by choosing a reference temperature of T_6 . This assumption sets the enthalpy-in and enthalpy-out terms in the energy balance to zero. Any energy released by the pre-combustion of furnace gases will leave the isothermal combustion zone as Q_{fur} . A more detailed derivation of (28) is shown in Appendix C.

$$Q_{\text{fur}} = -\dot{n}_6 \sum_{\substack{\text{combustion} \\ \text{species } j}} X_{j,6} (\Delta H_{j,\text{comb}} - RT_6 \Delta n_{j,\text{comb}}) \quad (28)$$

Equations (29) to (31) are the furnace-side model equations and equations (32) to (35) are process-side model equations. A detailed derivation of these equations is given in Appendix C.

Furnace-Surface-Zone Energy Balance (f_i , $i=1..50$)

$$f_i = 0 = \sigma \left(\sum_{\substack{\text{furnace} \\ \text{zones } j}} \sum_{\substack{\text{gray gas} \\ \text{atmospheres } k}} \left[(b_{1,k} + b_{2,k} T_j) \overline{Z_j Z}_k \right] T_j^4 - \varepsilon_i A_i T_i^4 \right) + h_{\text{gso}} A_i (T_{\text{adj gas}} - T_i) - \frac{k_{\text{refrac}}}{t_{\text{refrac}}} A_i (T_i - T_{\text{surr}}) \quad (29)$$

Furnace-Obstacle-Zone Energy Balance (f_i, i=51..62)

$$f_i = 0 = \sigma \left(\sum_{\substack{\text{furnace} \\ \text{zones } j}} \sum_{\substack{\text{gray gas} \\ \text{atmospheres } k}} \left[(b_{1,k} + b_{2,k} T_j) \overline{Z_j Z_j} \Big|_k T_j^4 \right] - \varepsilon_i A_i T_i^4 \right) + h_{\text{gso}} A_i (T_{\text{adj gas}} - T_i) - \frac{2\pi k_{\text{tube}} \Delta y (T_i - T_{\text{in wall}})}{\ln \left(\frac{r_{\text{out}}}{r_{\text{in}}} \right)} \quad (30)$$

Furnace-Volume-Zone Energy Balance (f_i, i=63..74)

$$f_i = 0 = \sigma \left(\sum_{\substack{\text{furnace} \\ \text{zones } j}} \sum_{\substack{\text{gray gas} \\ \text{atmospheres } k}} \left[(b_{1,k} + b_{2,k} T_j) \overline{Z_j Z_j} \Big|_k T_j^4 \right] - 4V_i T_i^4 \sum_{\substack{\text{gray gas} \\ \text{atmospheres } k}} [(b_{1,k} + b_{2,k} T_i) K_k] \right) - \sum_{\substack{\text{adjacent surface} \\ \text{and obstacle} \\ \text{furnace zones } j}} [h_{\text{gso}} A_j (T_i - T_j)] + \dot{n}_{\text{fur}} \sum_{\substack{\text{furnace} \\ \text{species } j}} X_j \int_{T_i}^{T_{\text{fur abv}}} C_{p,j} dT + \alpha(k_i) Q_{\text{fur}} \quad (31)$$

Inner-Tube-Surface Energy Balance (f_i, i=75..86)

$$f_i = 0 = \frac{2\pi k_{\text{tube}} \Delta y (T_{\text{out wall}} - T_i)}{\ln \left(\frac{r_{\text{out}}}{r_{\text{in}}} \right)} - h_{\text{tg}} 2\pi r_{\text{in}} \Delta y (T_i - T_{\text{proc gas}}) \quad (32)$$

Process-Gas Energy Balance (f_i , $i=87..98$)

$$f_i = 0 = \dot{m}_{\text{tot}} \sum_{\substack{\text{process} \\ \text{species } j}} \left(\frac{P_{j,\text{seg abv}}}{RT_{\text{seg abv}} \rho_{g,\text{seg abv}}} \int_{T_{\text{ref}}}^{T_{\text{seg abv}}} C_{p,j} dT \right) - \dot{m}_{\text{tot}} \sum_{\substack{\text{process} \\ \text{species } j}} \left(\frac{P_{j,\text{seg}}}{RT_i \rho_{g,\text{seg}}} \int_{T_{\text{ref}}}^{T_i} C_{p,j} dT \right) + h_{\text{tg}} 2\pi r_{\text{in}} \Delta y (T_{\text{in wall}} - T_i) - \Delta y \pi r_{\text{in}}^2 \rho_{\text{cat}} \sum_{\text{reactions } j} \eta_j r_j (\Delta H_j - RT_i \Delta n_j) \quad (33)$$

Process-Gas Material Balance (f_i , $i=99..170$)

$$f_i = 0 = \dot{m}_{\text{tot}} \frac{P_{j,\text{seg abv}} M_k}{RT_{\text{seg abv}} \rho_{g,\text{seg abv}}} - \dot{m}_{\text{tot}} \frac{P_{ij} M_k}{RT_{\text{seg}} \rho_{g,\text{seg}}} + M_k \Delta y \pi r_{\text{in}}^2 \rho_{\text{cat}} \sum_{\substack{\text{reforming} \\ \text{reactions } j}} \eta_j \xi_{j,A} r_j \quad (34)$$

Pressure Drop Correlation (f_i , $i=171-182$)

$$f_i = 0 = P_{\text{seg abv}} - P_{\text{seg}} - f \frac{\rho_i V_s^2}{D_p} \Delta y \quad (35)$$

Heat-Release Profile Calculation

A parabolic heat-release profile is used to distribute the heat released by the pre-combustion of furnace fuel (Q_{fur} in Figure 11) over a heat-release length (L_Q). This strategy was first used by Roesler in 1967 and has been repeated by many other modelers (Selçuk et al. 1975a) and b); Murty and Murthy, 1988; Yu et al., 2006). In this study, a discrete parabola (equation (36)) is used to define the heat release profile.

$$\alpha(k) = a(k\Delta y)^2 + b(k\Delta y) + c \quad (36)$$

When equation (36) is evaluated, $\alpha(1)$ is the fraction of pre-combustion heat (Q_{fur}) released in the top zone and $\alpha(k)$ is the fraction of pre-combustion heat released in the k^{th} zone from the top.

Values for the constants a , b and c are found using conditions (37), (38) and (39) below. Note that n_Q is the number of zones where heat is released by combustion.

$$\alpha(n_Q + 1) = 0 \quad (37)$$

$$\alpha(1) = \alpha_{\text{top}} \quad (38)$$

$$\sum_{k=1}^{n_Q} \alpha(k) = 1 \quad (39)$$

Equation (37) indicates that the first zone after the heat-release length receives no heat from combustion. Equation (38) indicates that the fraction of combustion in the top zone is α_{top} and equation (39) indicates that the sum of all of the fractions released is one. It is assumed that all furnace volume zones have the same height (Δy) and that the heat-release length does not exceed 6.1 m. The analytical solution for the constants a , b and c (in terms of n_Q , Δy and α_{top}) are shown in equations (40), (41) and (42).

$$a = \frac{3((n_Q + 1)\alpha_{top} - 2)}{\Delta y^2 n_Q (n_Q^2 - 1)} \quad (40)$$

$$b = \frac{\alpha_{top} (4n_Q^2 + 9n_Q + 5) - 6n_Q - 12}{\Delta y n_Q (n_Q^2 - 1)} \quad (41)$$

$$c = \frac{\alpha_{top} (n_Q^2 + 3n_Q + 2) - 6}{n_Q (n_Q - 1)} \quad (42)$$

Both $\alpha_{top} > 0$ and $a < 0$ must be true so the parabola will open downward.

Preliminary Results from the Segmented-Tube Model

The segmented-tube model generates temperature and composition profiles for a single reformer tube in a rectangular furnace. While the results from the segmented-tube model do not accurately predict industrial SMR performance, they can be used to get a qualitative sense of reformer behaviour. Two simple examples are used in this section. In the first example, the fuel rate to the furnace is doubled and in the second example the steam-to-carbon ratio of the process feed is doubled. The model inputs used in the simulations (compositions and flow rates) are data from an industrial SMR scaled down for one tube. Input conditions correspond to the Plant A data in Table 29 and Table 30 of Appendix H. Table 12 shows some of the parameter values used in the preliminary simulations. The refractory thermal conductivity was scaled down to 35% of its literature value (Bindar, 1996) to prevent large amounts of heat loss through the refractory walls and to meet the design specification that 5% of the heat released by combustion is lost to the surrounding environment.

Table 12. Parameter Values for Preliminary Segmented Tube Simulations

Symbol	Value	Units	Description
L_Q	3.65	[m]	heat release length
n_Q	6	[none]	number of heat release zones
α_{top}	0.4	[none]	fraction of combustion heat released in the instantaneous combustion zone
k_{refrac}	392.53	$\left[\frac{J}{m \cdot h \cdot K} \right]$	furnace refractory thermal conductivity (Bindar, 1996)
t_{refrac}	0.305	[m]	furnace refractory thickness
ϕ	0.7	[none]	void fraction or porosity of the packed bed

Figure 12 and Figure 13 show the temperature profiles and composition profiles for the base case and for a case with twice the fuel rate. In Figure 12 the temperature profiles for the high-fuel-rate case are at higher temperatures than the temperature profiles for the base case, as expected. The higher process gas temperature of the high-fuel-rate case pushes reforming reactions (1) and (2) to the right. This results in more hydrogen and less methane exiting the tube in the high-fuel-rate case than in the base case (See Figure 13).

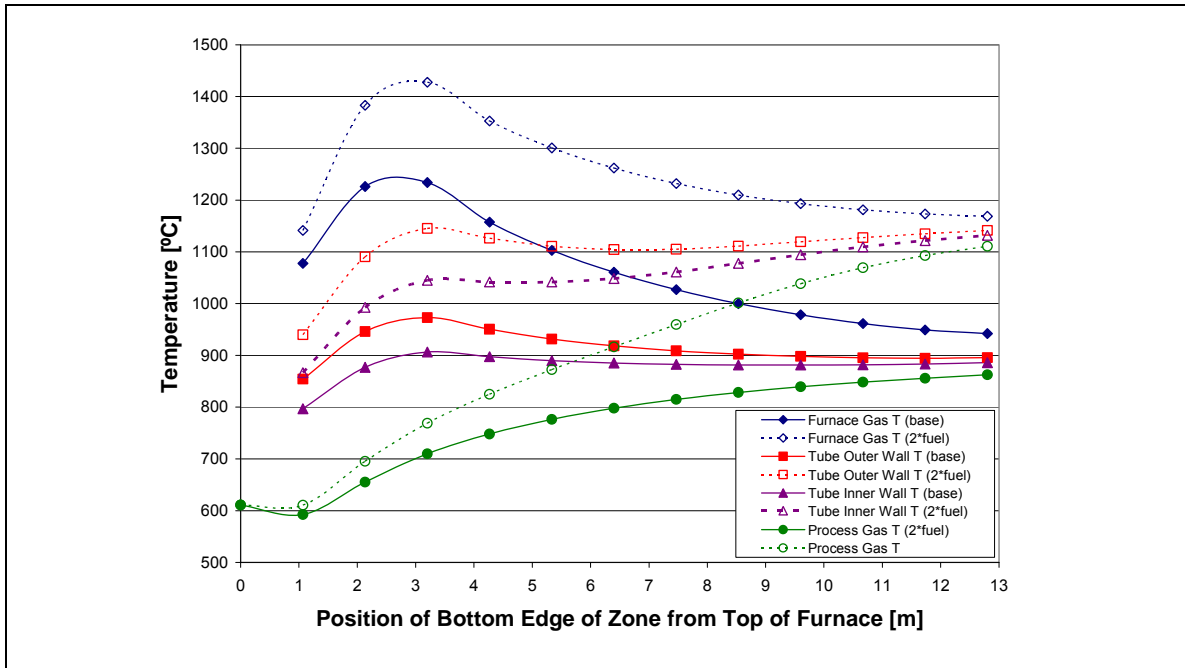


Figure 12. Comparison of the Segmented-Tube Model Temperature Profiles for the Base Case and Twice the Fuel Flow Rate

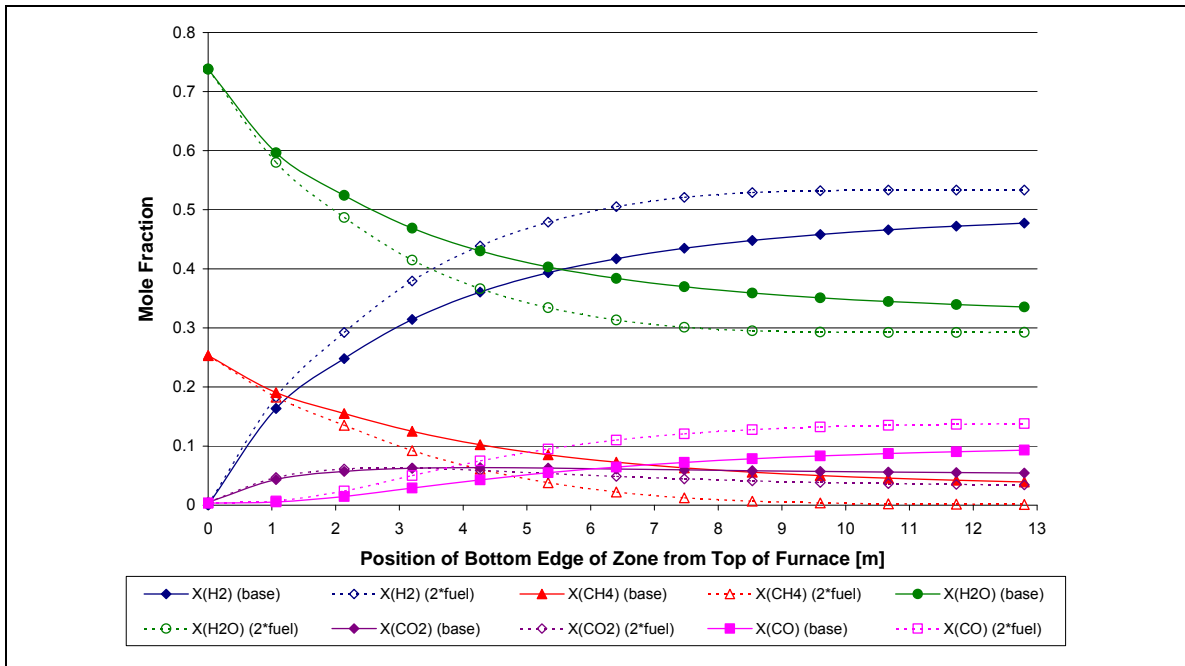
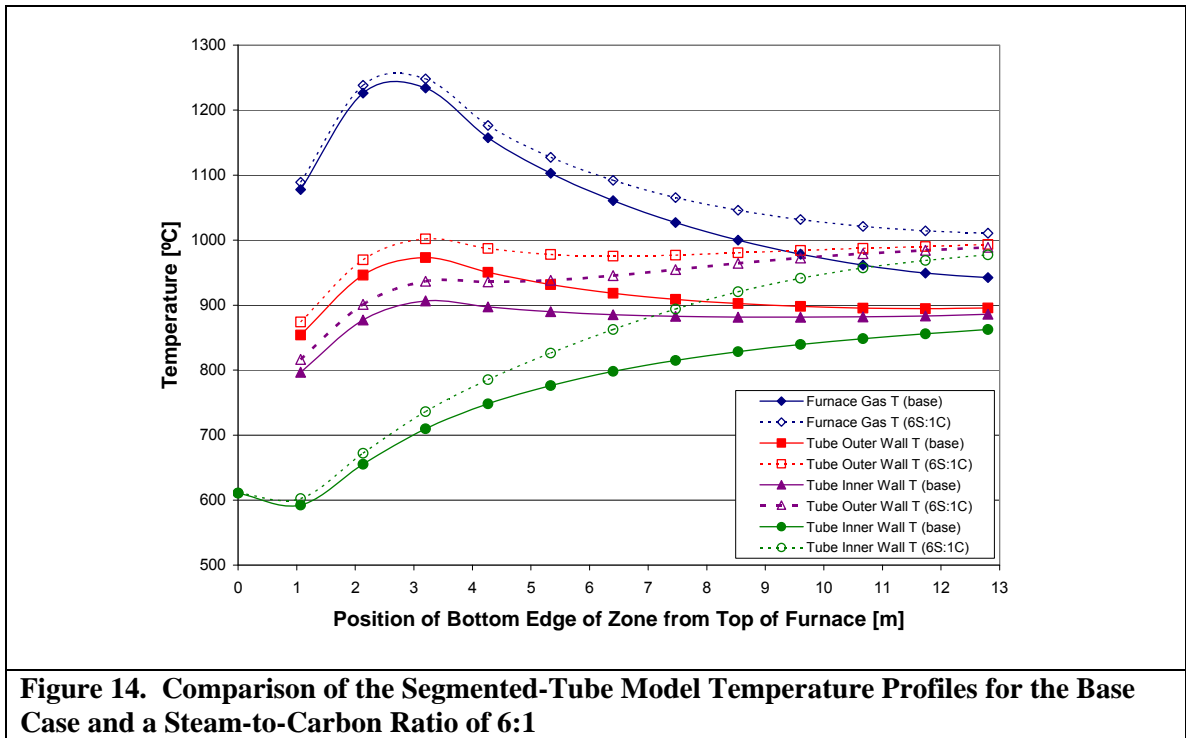
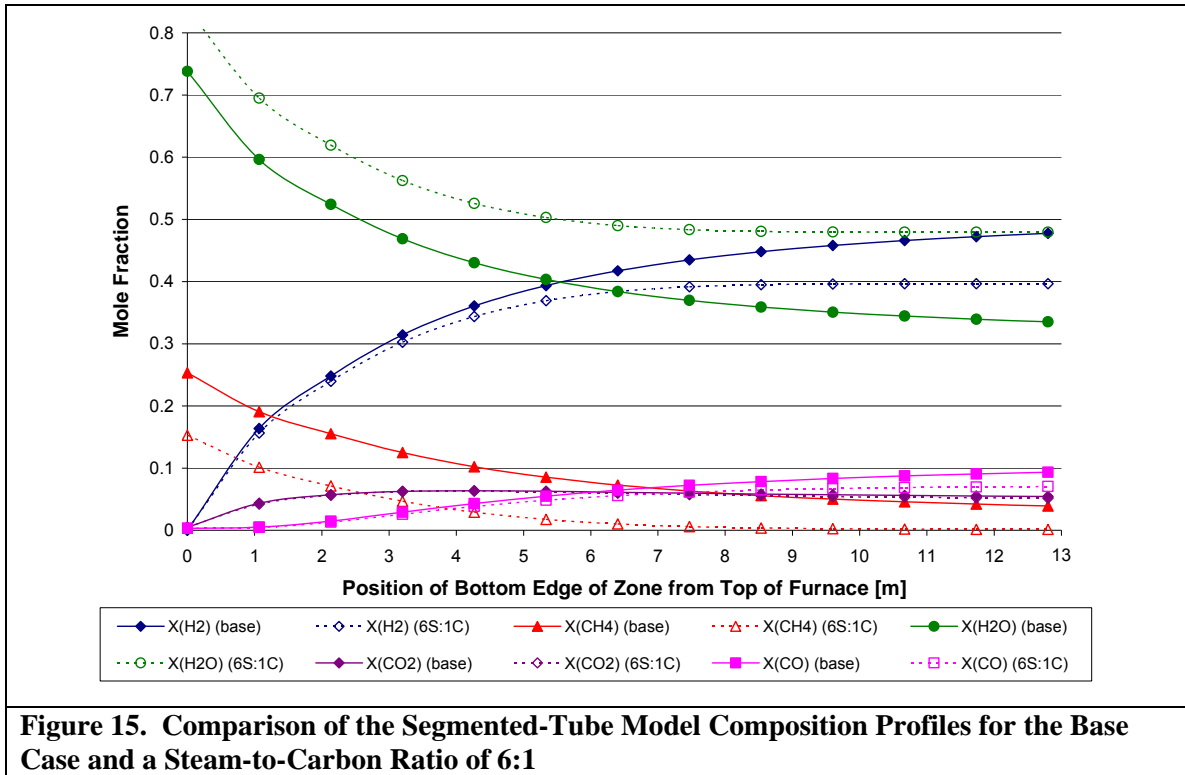


Figure 13. Comparison of the Segmented-Tube Model Composition Profiles for the Base Case and Twice the Fuel Flow Rate

Figure 14 and Figure 15 show the temperature and composition profiles for the base case and for a case with twice the process feed steam-to-carbon ratio. The molar flow rate of the process-side stream remains the same in Figure 14 although the steam-to-carbon ratio has been increased from 3:1 to 6:1. In Figure 14, the temperature profiles for the high steam-to-carbon ratio case are above the profiles for the base case. This trend is expected since a lower methane composition will reduce the extent of the endothermic reforming reaction and reduce the furnace heat consumed by the reforming reactions. In Figure 15, the composition of methane for the high steam-to-carbon ratio case approaches zero around 4.6 m from the top of the reformer. At this point the production of hydrogen by the endothermic reforming reactions slows down and eventually stops. Since no heat is being consumed by the reforming reactions the temperature of the furnace gas should increase. This trend is seen in Figure 14 where the difference between the temperature profiles for the two cases widens starting around 4.6 m from the top of the reformer.





Limitations of the Segmented-Tube Model

The segmented-tube model is a simplified SMR model. It does not account for multiple tubes or coffin boxes and for their effects on radiative heat transfer within the furnace. These details are included in the average-tube model described in the next section.

3.3 Average-Tube Model

The average-tube model simulates a complete SMR. The model calculates temperature profiles for the inner-tube wall, outer-tube wall, furnace gas, process gas and furnace refractory, as well as composition profiles for the process gas. The average-tube model is an advanced version of the segmented-tube model. The furnace-side model is improved by accounting for exact furnace

geometry, including tube-spacing and coffin boxes. The process-side model is improved by accounting for higher alkanes in the feed. An overall-reformer energy balance, overall-furnace-side energy balance and overall-process-side material and energy balances are included in the model to confirm the accuracy of the model results and to provide an indication of numerical error.

The most important improvement in the average-tube model is the addition of exact furnace geometry. The geometry shown in Figure 2 and Figure 3 was entered into RADEX (Lawson and Ziesler, 1996) to generate total-exchange areas. The average-tube model in this thesis was developed using different numbers of vertical sections to investigate the influence of discretization on model accuracy. The version described below in Table 13 has ten equally-spaced vertical sections. Note that this model has fewer equations than the segmented-tube model described in Table 10, because it has fewer vertical sections. Versions of the average-tube model with 15, 20 and 40 vertical sections require the solution of 226, 299 and 594 equations, respectively, and require longer computation times. The model with 10 vertical sections requires approximately 134 seconds to solve on a hp workstation xw4100 (2.8 GHz Intel Pentium 4 processor with 2 GB of RAM) starting from the standard-initial guess as described in Appendix D.

Table 13. Structure of the Average-Tube Model with 10 Vertical Sections

$$\mathbf{f}(\mathbf{X}) = \begin{bmatrix} f_1(x_1, x_2, \dots, x_{151}) \\ \vdots \\ f_{151}(x_1, x_2, \dots, x_{151}) \end{bmatrix} = \mathbf{0}$$

Number of Equations = 151
Number of Unknowns = 151
Number of Equation Types = 9
Number of Vertical Sections = 10

Table 14. Vector Equation $f=0$ and Unknown Vector x for the Average-Tube Model with 10 Vertical Sections

Index in f and x	Equation Type in f	Furnace Zone or Tube Segment	Unknown Variable
1	Surface-Zone Energy	Zone 1	T_1 [K]
...	Balances on
38	Refractory Surfaces	Zone 38	T_{38} [K]
39	Obstacle-Zone Energy	Zone 39	T_{39} [K]
...	Balances
51	on Tube and Coffin Box Surfaces	Zone 51	T_{51} [K]
52	Volume-Zone Energy	Zone 52	T_{52} [K]
...	Balances
61		Zone 61	T_{61} [K]
62	Inner-Tube Surface Energy	Segment 1	T_{62} [K]
...	Balances
71		Segment 10	T_{71} [K]
72	Process-Gas Energy	Segment 1	T_{72} [K]
...	Balances
81		Segment 10	T_{81} [K]
82	Process-Gas Material	Segment 1	P_{82H_2} [kPa]
83	Balances for Six Species	Segment 1	P_{83CO} [kPa]
84		Segment 1	P_{84CH_4} [kPa]

85		Segment 1	P_{85N_2} [kPa]
86		Segment 1	P_{86CO_2} [kPa]
87		Segment 1	P_{87H_2O} [kPa]
...	
136		Segment 10	P_{136H_2} [kPa]
137		Segment 10	P_{137CO} [kPa]
138		Segment 10	P_{138CH_4} [kPa]
139		Segment 10	P_{139N_2} [kPa]
140		Segment 10	P_{140CO_2} [kPa]
141		Segment 10	P_{141H_2O} [kPa]
142	Momentum Balance	Segment 1	ρ_{142} [kg/m ³]
...	(Ergun equation)
151		Segment 10	ρ_{151} [kg/m ³]

Assumptions in the Average-Tube Model

All assumptions (assumptions 1 to 14 in Section 3.2) for the segmented-tube model apply to the average-tube model. Additional assumptions related to the treatment of higher alkanes in the process-side feed and to the physical properties of the coffin boxes are listed below.

- Water cracking of any higher alkanes (see reaction (45)) in the process feed occurs instantaneously and isothermally at the temperature of the process feed. Heat released by this overall cracking reaction is added to the top section of the process side. The

reference state for higher alkane cracking is the fully-formed species in their gaseous state at T_1 (in Figure 16) and 1atm

16. The coffin box walls have the same radiative properties as the furnace walls

17. Conduction through the walls of the coffin boxes is negligible

Average-Tube Model Equations

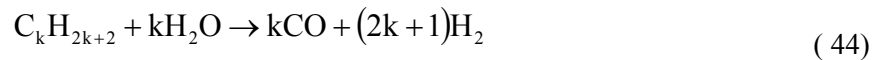
Treatment of Higher Alkanes in the Process Feed

The process-side feed contains trace amounts of higher alkanes (ethane through n-hexane). The molar percentage of higher alkanes in the process-side feed is typically a few percent. In an industrial SMR, the higher alkanes react at the catalyst active sites by a different mechanism than methane (Rostrup-Nielsen, 1984; p. 54). To limit the number of process-side material balances and to simplify the reaction kinetics model, only six species (H_2 , CO , CO_2 , CH_4 , N_2 , H_2O) are accounted for in the process-side model. Higher alkanes in the process-side feed are assumed to instantaneously crack to methane as they enter the process-side and the energy from the cracking reactions is added to the top zone of the reformer. This approach was used by Murty and Murthy (1988), Singh and Saraf (1979) and Hyman (1968). Hyman (1968) used reaction (43) to model higher-alkane cracking.

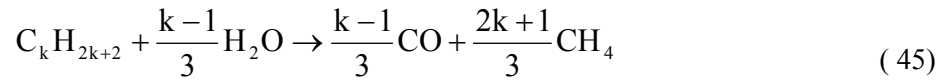


However, if there is not enough hydrogen in the process-side feed to completely crack the higher alkanes then either the process-side model receives a negative amount of hydrogen or some

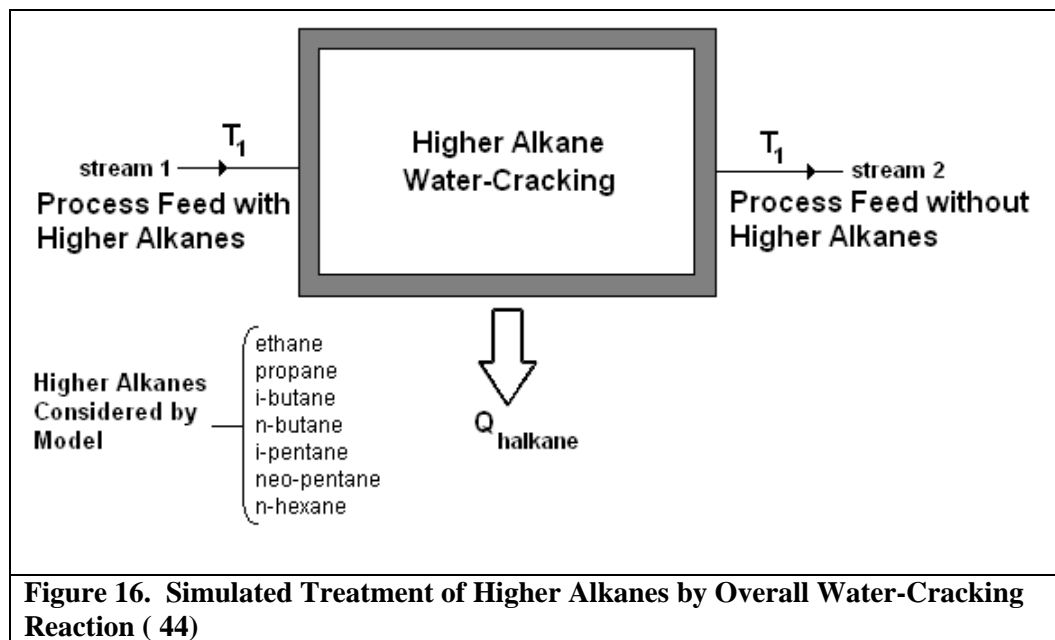
higher alkanes remain unreacted in the process-side feed. A negative amount of hydrogen will cause the kinetic model to fail, and accounting for uncracked higher alkanes will require many additional species and equations be added to the model. To avoid these undesirable consequences, it is assumed that enough hydrogen to crack all of the higher alkanes in the feed is produced from other process-side species. Hydrogen for higher-alkane cracking can be produced from three possible sources i) water and carbon monoxide by the water-gas-shift reaction (3), ii) by steam-methane reforming (1) or iii) by steam-higher-alkane reforming (44).



Since there is typically no carbon monoxide in the process-side feed, producing hydrogen from the water-gas-shift reaction is not possible. If the hydrogen needed to crack higher alkanes is produced by steam-methane reforming then some reaction is forced to occur outside of the reformer tubes without the steam-methane-reforming reaction kinetics. If all the hydrogen needed to crack the higher alkanes is produced by steam-higher-alkane reforming, then the composition of hydrogen in the process-side feed is unchanged. In reaction (44) a large amount of hydrogen, $2k+1$ molecules, is produced for every molecule of higher-alkane reformed. In reaction (43) only a small amount of hydrogen, $k-1$ molecules, is needed to crack a molecule of higher alkane. As a result, only a small amount of steam-higher-alkane reforming is needed to produce the hydrogen required to crack the remaining higher-alkanes. As an added benefit, the endothermic steam-higher-alkane reforming reactions will partially cancel the heat effects of the exothermic cracking reactions. Reactions (43) and (44) can be added to produce reaction (45). Reaction (45) will be referred to as the water cracking of higher alkanes in this thesis.



The higher alkanes in the process-side feed are assumed to be cracked using reaction (45) and the heat released (or absorbed) is added to the top zone of the process side. The pre-treatment of higher alkanes as shown in Figure 16 is similar to the pre-combustion of fuel on the furnace side of the model.



Calculation of Q_{halokane} , the Heat Released by Isothermal Water-Cracking of Higher Alkanes

The energy balance for isothermal water-cracking is simplified by choosing a reference temperature of T_1 . This assumption sets the enthalpy in and enthalpy out terms in the water-cracking energy balance to zero. A complete derivation of equation (46) is given in Appendix C.

$$Q_{\text{halokane}} = -\dot{n}_1 \sum_{\substack{\text{higher-alkane} \\ \text{species } j}} X_{j,\text{proc in}} (\Delta H_{j,\text{comb}} - RT_{\text{proc in}} \Delta n_{j,\text{comb}}) \quad (46)$$

Furnace-Surface-Zone Energy Balances ($f_i, i=1..38$)

The furnace surface zone energy balances are similar for the average-tube model and segmented-tube model. The radiation out term in equation (47) $\left[(b_{1,k} + b_{2,k} T_i) \overline{Z_i Z_{j|k}} T_i^4 \right]$ is different from the radiation out term in equation (29) of the segmented tube model $\left[\epsilon_i A_i T_i^4 \right]$. The segmented-tube model uses the total-exchange area summation rules described in Appendix B to simplify the radiation out term. The summation rules are not used in the average-tube model because the error in the summation rules is larger in the average-tube model than in the segmented-model. The error in the total-exchange area summation rules for the average-tube model prevents the overall furnace energy balance from closing.

$$f_i = 0 = \sigma \left(\sum_{\substack{\text{furnace} \\ \text{zones } j}} \sum_{\substack{\text{gray gas} \\ \text{atmospheres } k}} \left[(b_{1,k} + b_{2,k} T_j) \overline{Z_j Z_i} \Big|_k T_j^4 - (b_{1,k} + b_{2,k} T_i) \overline{Z_i Z_j} \Big|_k T_i^4 \right] \right) \quad (47)$$

$$+ h_{\text{gso}} A_i (T_{\text{adj gas}} - T_i) - \frac{k_{\text{refrac}}}{t_{\text{refrac}}} A_i (T_i - T_{\text{surr}})$$

Furnace-Obstacle-Zone Energy Balance (f_i , $i=39..51$)

In the average tube model, there are two types of obstacle zones, tube obstacle zones and coffin-box obstacle zones. The energy balance for a tube obstacle zone in the average tube model differs from an energy balance for a tube obstacle zone in the segmented tube because there are many tubes ($N_{\text{tubes}}=336$) contained in one vertical section.

$$f_i = 0 = \sigma \left(\sum_{\substack{\text{furnace} \\ \text{zones } j}} \sum_{\substack{\text{gray gas} \\ \text{atmospheres } k}} \left[(b_{1,k} + b_{2,k} T_j) \overline{Z_j Z_i} \Big|_k T_j^4 - (b_{1,k} + b_{2,k} T_i) \overline{Z_i Z_j} \Big|_k T_i^4 \right] \right) \quad (48)$$

$$+ h_{\text{gso}} A_i (T_{\text{adj gas}} - T_i) - \left[\frac{2\pi k_{\text{tube}} \Delta y N_{\text{tubes}} (T_i - T_{\text{in wall}})}{\ln \left(\frac{r_{\text{out}}}{r_{\text{in}}} \right)} \right]_{\text{tube zones only}}$$

The tube and coffin-box obstacle-zone energy balances differ only in the final conduction term. As stated in assumption 17, conduction through the coffin box walls is assumed to be negligible. As a result, the conduction term (the last term) in equation (48) is not present in the energy balance for coffin-box surface zones.

Furnace-Volume-Zone Energy Balance (f_i , $i=52..61$)

$$f_i = 0 = \sigma \left(\sum_{\substack{\text{furnace} \\ \text{zones } j}} \sum_{\substack{\text{gray gas} \\ \text{atmospheres } k}} \left[(b_{1,k} + b_{2,k} T_j) \overline{Z_j Z_i} \Big|_k T_j^4 - (b_{1,k} + b_{2,k} T_i) \overline{Z_j Z_i} \Big|_k T_i^4 \right] \right) \quad (49)$$

$$- \sum_{\substack{\text{adjacent surface} \\ \text{and obstacle} \\ \text{furnace zones } j}} [h_{\text{gso}} A_j (T_i - T_j)] + \dot{n}_{\text{fur}} \sum_{\substack{\text{furnace} \\ \text{species } j}} X_j \int_{T_i}^{T_{\text{fur abv}}} C_{p,j} dT + \alpha(k_i) Q_{\text{comb}}$$

Inner-Tube-Surface Energy Balance (f_i , $i=62..71$)

$$f_i = 0 = \frac{2\pi k_{\text{tube}} \Delta y N_{\text{tubes}} (T_{\text{out wall}} - T_i)}{\ln\left(\frac{r_{\text{out}}}{r_{\text{in}}}\right)} - h_{\text{tg}} f_{\text{htg}} 2\pi r_{\text{in}} \Delta y N_{\text{tubes}} (T_i - T_{\text{proc gas}}) \quad (50)$$

Process-Gas Energy Balance (f_i , $i=72-81$)

$$f_i = 0 = \dot{m}_{\text{tot}} \sum_{\substack{\text{process} \\ \text{species } j}} \left(\frac{P_{j,\text{seg abv}}}{RT_{\text{seg abv}} \rho_{g,\text{seg abv}}} \int_{T_{\text{ref}}}^{T_{\text{seg abv}}} C_{p,j} dT \right) - \dot{m}_{\text{tot}} \sum_{\substack{\text{process} \\ \text{species } j}} \left(\frac{P_{j,\text{seg}}}{RT_i \rho_{g,\text{seg}}} \int_{T_{\text{ref}}}^{T_i} C_{p,j} dT \right) \quad (51)$$

$$+ h_{\text{tg}} f_{\text{htg}} 2\pi r_{\text{in}} \Delta y N_{\text{tubes}} (T_{\text{in wall}} - T_i) - \Delta y N_{\text{tubes}} \pi r_{\text{in}}^2 \rho_{\text{cat}} \sum_{\substack{\text{reforming} \\ \text{reactions } j}} \eta_j r_j (\Delta H_j - RT_i \Delta n_j)$$

$$+ [Q_{\text{halkane}}]_{\text{top furnace zone only}}$$

Note that the final term in equation(51) appears only in the balance for the top process gas segment, where the heat released by water-cracking of higher alkanes is added.

Process-Gas Material Balance ($f_i, i=82..141$)

$$f_i = 0 = \dot{m}_{\text{tot}} \frac{P_{k,\text{seg abv}} M_k}{RT_{\text{seg abv}} \rho_{g,\text{seg abv}}} - \dot{m}_{\text{tot}} \frac{P_{iA} M_k}{RT_{\text{seg}} \rho_{g,\text{seg}}} + M_k \Delta y N_{\text{tubes}} \pi r_{\text{in}}^2 \rho_{\text{cat}} \sum_{\substack{\text{reforming} \\ \text{reactions } j}} \eta_j \xi_{j,k} r_j \quad (52)$$

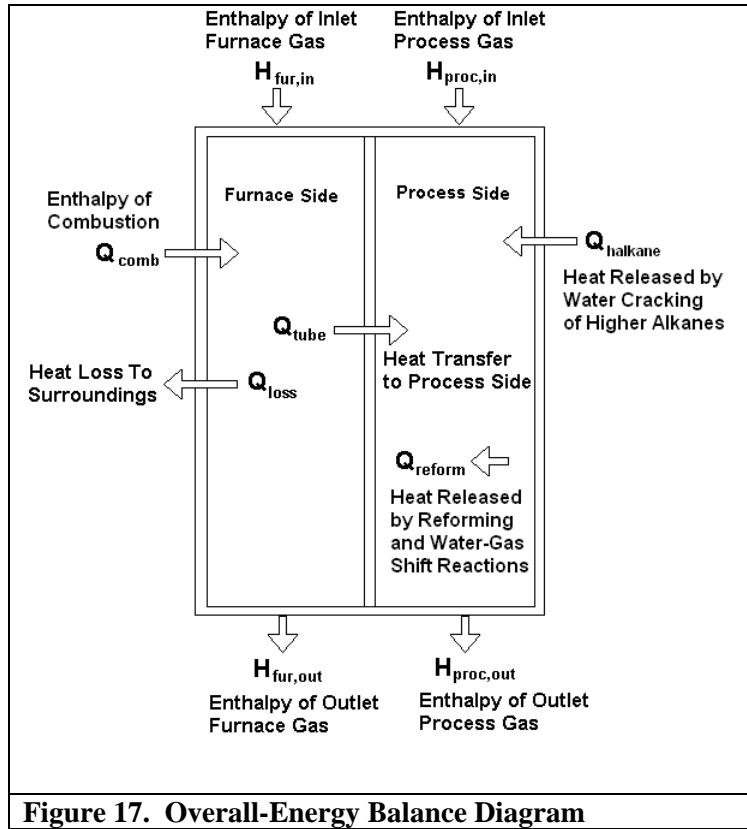
The subscript k in equation (52) refers to the kth species in the process gas.

Pressure Drop Correlation ($f_i, i=142..151$)

$$f_i = 0 = P_{\text{seg abv}} - P_{\text{seg}} - f \frac{\rho_i V_s^2}{D_p} \Delta y \quad (53)$$

Overall-Energy Balances

An energy balance on the complete reformer (furnace and process sides) and separate energy balances on the furnace side and process side are also performed. If the model equations (47) through (53) and their solution are consistent, then the numerical solution should satisfy the overall-energy balances with only a small amount of error. In addition to checking for model consistency, the overall-energy balances allow the calculation of performance ratios of interest to the industrial sponsor. Figure 17 is a simplified diagram of a reformer that shows the flow of energy in and out of the furnace and process sides.



Overall-Energy Balance on Furnace Side

Equation (54) is an overall-energy balance on the furnace side of the SMR. If the unknown vector \mathbf{x} satisfies the vector of equations \mathbf{f} , the error in (E_{fur}) will be small.

$$E_{\text{fur}} = H_{\text{fur,in}} - H_{\text{fur,out}} + Q_{\text{comb}} - Q_{\text{loss}} - Q_{\text{tube}} \quad (54)$$

The terms in equation (54) are evaluated after the model equations are solved. Many of the terms in equation (54) require information from multiple furnace zones or tube segments to be evaluated..

$$\begin{aligned}
E_{\text{fur}} = & \dot{n}_{\text{fur}} \sum_{\text{species } i} X_i \int_{T_{\text{fur,out}}}^{T_{\text{fur,in}}} C_{p_i} dT + Q_{\text{comb}} - \sum_{\substack{\text{refractory} \\ \text{zones } i}} \frac{k_{\text{refrac}}}{t_{\text{refrac}}} A_i (T_i - T_{\text{surr}}) \\
& - \sum_{\substack{\text{outer tube} \\ \text{wall zones } i}} \frac{2\pi k_{\text{tube}} \Delta y N_{\text{tubes}} (T_i - T_{\text{in wall}})}{\ln\left(\frac{r_{\text{out}}}{r_{\text{in}}}\right)}
\end{aligned} \tag{55}$$

Overall-Energy Balance on Process Side

Equations (56) and (57) are energy balances on the entire process side.

$$E_{\text{proc}} = H_{\text{proc,in}} - H_{\text{proc,out}} + Q_{\text{halkane}} - Q_{\text{reform}} + Q_{\text{tube}} \tag{56}$$

Substituting for the various terms in equation (56) gives:

$$\begin{aligned}
E_{\text{proc}} = & \dot{n}_{\text{proc,in}} \sum_{\substack{\text{process} \\ \text{species } i}} X_i \int_{T_{\text{ref}}}^{T_{\text{proc,in}}} C_{p_i} dT - \dot{m}_{\text{tot}} \sum_{\substack{\text{process} \\ \text{species } i}} \left(\frac{P_i}{RT\rho_g} \int_{T_{\text{ref}}}^T C_{p_i} dT \right) \Bigg|_{\text{bot,seg}} + Q_{\text{halkane}} \\
& - \sum_{\substack{\text{all tube} \\ \text{segments } i}} \left[\Delta y \pi r_{\text{in}}^2 \rho_{\text{cat}} \sum_{\substack{\text{reform ing} \\ \text{reactions } j}} \eta_j r_j (\Delta H_j - RT_i \Delta n_j) \right] \\
& + \sum_{\substack{\text{outer tube} \\ \text{wall zones } i}} \frac{2\pi k_{\text{tube}} \Delta y N_{\text{tubes}} (T_i - T_{\text{in wall}})}{\ln\left(\frac{r_{\text{out}}}{r_{\text{in}}}\right)}
\end{aligned} \tag{57}$$

Overall-Energy Balance on Reformer

Equation (58) is an overall-energy balance on the reformer (furnace-side and process-side). Note that equation (58) is the sum of equations (54) and (56).

$$E_{\text{refrm}} = H_{\text{fur,in}} - H_{\text{fur,out}} + H_{\text{proc,in}} - H_{\text{proc,out}} + Q_{\text{halkane}} - Q_{\text{reform}} + Q_{\text{comb}} - Q_{\text{loss}} \quad (58)$$

Atom-Balance on the Process Side

To confirm that the process side material balances are obeyed, atom balances were performed on the four atomic species in the model (H, C, N and O). The atom balance for hydrogen on the process side is shown in equation (60).

$$E_{\text{nH}} = \dot{n}_{\text{H,in,proc}} - \dot{n}_{\text{H,out,proc}} \quad (59)$$

$$E_{\text{nH}} = \dot{n}_{\text{in,proc}} \sum_{\substack{\text{process} \\ \text{species } i}} X_i \gamma_{\text{H},i} - \dot{m}_{\text{tot}} \sum_{\substack{\text{process} \\ \text{species } i}} \left(\frac{P_i}{RT\rho_g} X_i \gamma_{\text{H},i} \right) \Bigg|_{\text{bot,seg}} \quad (60)$$

The variable $\gamma_{\text{H},i}$ in equation (60) is the number of hydrogen atoms in species i .

Solving the Model Equations

The model equations have been solved for the four sets of industrial inlet conditions in Appendix H using the Newton-Raphson method described in Appendix D. Some preliminary simulations, parameter sensitivity analysis and the estimation of unknown model parameters using plant data is described in Chapter 4.

3.4 References

Hyman, M. H. (1968) Simulate methane reformer reactions. *Hydrocarbon Processing*. vol. 47 pp. 131-137.

Lawson, D. A. and Ziesler, C. D. (1996) An accurate program for radiation modeling in the design of high-temperature furnaces. *IMA Journal of Mathematics Applied in Business and Industry*. vol. 7 pp. 109-116.

Murty, C. V. S. and Murthy, M. V. (1988) Modeling and simulation of a top-fired reformer. *Industrial Engineering and Chemistry Research*. vol. 27 pp 1832-1840.

Roesler, F. C. (1967) Theory of radiative heat transfer in co-current tube furnaces. *Chemical Engineering Science*. vol. 2 pp. 1325-1336.

Selçuk, N., Siddall, R. G., Beér, J. M. (1975a) A comparison of mathematical models of the radiative behavior of an industrial heater. *Chemical Engineering Science*. vol. 30 pp. 871-876.

Selçuk, N., Siddall, R. G., Beér, J. M. (1975b) Prediction of the effect of flame length on temperature and radiative heat flux distribution in a process heater. *Journal of the Institute of Fuel*. vol. 48 pp. 89-96.

Singh, C. P. P. and Saraf, D. N. (1979) Simulation of side fired steam-hydrocarbon reformers. *Industrial and Engineering Chemistry Process Design and Development*. vol. 18 pp. 1-7.

Soliman, M. A., El-Nashaie, S. S. E. H., Al-Ubaid, A. S. and Adris, A. (1988) Simulation of steam reformers for methane. *Chemical Engineering Science*. vol. 43 pp. 1801-1806.

Taylor, P. B. and Foster P. J. (1974) The total emissivities of luminous and non-luminous flames. *International Journal of Heat and Mass Transfer*. vol. 17 pp. 1591-1605.

Bindar, Y. (1996) Experimental and numerical investigations of a multi-burner furnace operated with various heat transfer boundary conditions. Ph. D. Thesis in Chemical Engineering. Queen's University.

Yu, Z., Cao, E., Wang, Y., Zhou, Z., Dai, Z. (2006) Simulation of Natural Gas Steam Reforming Furnace. *Fuel Processing Technology*. vol. 87 pp. 695-704.

Chapter 4

Model Fitting Using Experimental Data

4.1 Available Data, Model Outputs, Inputs and Parameters

Available Data and Model Outputs

As described in section 1.4 there are three types of plant data available for parameter estimation:

i) real time plant data for the temperatures, pressures and flow rates of all streams flowing into and out of the reformer ii) nightly tube wall temperature measurements iii) quarterly third party plant analysis and reformer models used to monitor catalyst activity. In this chapter, the model parameters are estimated by matching the model outputs to the plant data. To properly estimate model parameters, the plant data should meet the following criteria:

1. The data should be measurable. Outputs from the third-party model should not be used to fit the current model. The assumptions made in the third-party model are not known, and the model equations and parameters may not be reliable.
2. Raw plant data should not be used, because some measurements are unreliable. Plant data used from parameter estimation should be first reconciled using plant material and energy balances, which are trusted by the company.
3. The same data should be available for multiple runs, at different SMR plant locations, with different operating conditions.

Since the third-party reformer model is reconciled with a plant material and energy balance, a subset of data used in the third-party model that meets criteria 1 and 3 has been selected for parameter fitting. The names, units, uncertainties and descriptions of the output variables used for parameter estimation are shown in Table 15 and the corresponding input variables are provided in Table 16. The model outputs are adjusted to match the plant data by changing the values of the adjustable parameters, which are listed in Table 18. The uncertainties in the output data are estimated from the company's knowledge of measurement accuracy and reliability. For example, plant engineers believe the furnace gas exit temperature measurement is accurate to within 8 °C.

Table 15. Model Outputs and Plant Data used in Parameter Estimation

Symbol	Uncertainty in Value	Units	Description
Process Side Outputs			
$T_{\text{proc,out}}$	±2	[°C]	process side outlet temperature
$P_{\text{proc,out}}$	±36	[kPa]	process side outlet pressure
$n_{\text{proc,out}}$	±227	[kgmol/h]	process side outlet molar flow rate
$X_{\text{H}_2,\text{proc,out}}$	±0.01	[none]	H ₂ fraction in process outlet
$X_{\text{CO},\text{proc,out}}$	±0.005	[none]	CO fraction in process outlet
$X_{\text{CH}_4,\text{proc,out}}$	±0.003	[none]	CH ₄ fraction in process outlet
$X_{\text{N}_2,\text{proc,out}}$	±.01	[none]	N ₂ fraction in process outlet
$X_{\text{CO}_2,\text{proc,out}}$	±.01	[none]	CO ₂ fraction in process outlet
$X_{\text{H}_2\text{O},\text{proc,out}}$	±.01	[none]	H ₂ O fraction in process outlet
Manually Measured Outputs			

T_{upper}	± 3	[°C]	upper peep hole tube temperature measurement
T_{lower}	± 3	[°C]	lower peep hole tube temperature measurement
Furnace Side Outputs			
$T_{\text{fur,out}}$	± 8	[°C]	furnace-gas outlet temperature

Model Inputs

On the furnace side the temperature, pressure, molar flow rate and composition of the input streams are known. The SMR model performs material and energy balances on the furnace-inlet streams to determine the composition, temperature and pressure of the combined furnace-inlet stream (See Figure 11). On the process side, only the compositions and molar flow rates of the individual inlet streams are specified. The temperature and pressure of the combined process inlet streams are entered by the model user. The symbols, units and a description of the model inputs are shown in Table 16 and the four sets of plant data used for parameter estimation can be found in Appendix H.

Table 16. Model Inputs

Symbol	Units	Description
Furnace Side Model Inputs		
T_{fl}	[°C]	temperature of furnace inlet stream 1
P_{fl}	[kPa]	pressure of furnace inlet stream 1
n_{fl}	[kgmol/h]	molar flow rate of furnace inlet stream 1
$X_{\text{H}_2,\text{fl}}$	[none]	H ₂ mole fraction in furnace inlet stream 1
$X_{\text{CO},\text{fl}}$	[none]	CO mole fraction in furnace inlet stream 1

$X_{CH_4,fl}$	[none]	CH ₄ mole fraction in furnace inlet stream 1
$X_{C_2,fl}$	[none]	C2 (ethane) mole fraction in furnace inlet stream 1
$X_{C_3,fl}$	[none]	C3 (propane) mole fraction in furnace inlet stream 1
$X_{i-C_4,fl}$	[none]	i-C4 (iso-butane) mole fraction in furnace inlet stream 1
$X_{n-C_4,fl}$	[none]	n-C4 (n-butane) mole fraction in furnace inlet stream 1
$X_{i-C_5,fl}$	[none]	i-C5 (i-pentane, 2-methylbutane) mole fraction in furnace inlet stream 1
$X_{n-C_5,fl}$	[none]	n-C5 (n-pentane) mole fraction in furnace inlet stream 1
$X_{neo-C_5,fl}$	[none]	neo-C5 (2,2-dimethylpropane) mole fraction in furnace inlet stream 1
$X_{n-C_6,fl}$	[none]	n-C6 (hexane) mole fraction in furnace inlet stream 1
$X_{N_2,fl}$	[none]	N ₂ mole fraction in furnace inlet stream 1
$X_{CO_2,fl}$	[none]	CO ₂ mole fraction in furnace inlet stream 1
$X_{H_2O,fl}$	[none]	H ₂ O mole fraction in furnace inlet stream 1
$X_{O_2,fl}$	[none]	O ₂ mole fraction in furnace inlet stream 1
Up to five furnace inlet streams can be defined.		
P_{fur}	[kPa]	Controlled Furnace Pressure
Process Side Model Inputs		
n_{p1}	[kgmol/h]	molar flow rate of process inlet stream 1
$X_{H_2,p1}$	[none]	H ₂ mole fraction in process inlet stream 1
$X_{CO,p1}$	[none]	CO mole fraction in process inlet stream 1
$X_{CH_4,p1}$	[none]	CH ₄ mole fraction in process inlet stream 1
$X_{C_2,p1}$	[none]	C2 (ethane) mole fraction in process inlet stream 1
$X_{C_3,p1}$	[none]	C3 (propane) mole fraction in process inlet stream 1
$X_{i-C_4,p1}$	[none]	i-C4 (i-butane, 2-methylpropane) mole fraction in process inlet stream 1

$X_{n-C4,p1}$	[none]	n-C4 (n-butane) mole fraction in process inlet stream 1
$X_{i-C5,p1}$	[none]	i-C5 (i-pentane, 2-methylbutane) mole fraction in process inlet stream 1
$X_{n-C5,p1}$	[none]	n-C5 (n-pentane) mole fraction in process inlet stream 1
$X_{neo-C5,p1}$	[none]	neo-C5 (2,2-dimethylpropane) mole fraction in process inlet stream 1
$X_{n-C6,p1}$	[none]	n-C6 (hexane) mole fraction in process inlet stream 1
$X_{N2,p1}$	[none]	N ₂ mole fraction in process inlet stream 1
$X_{CO2,p1}$	[none]	CO ₂ mole fraction in process inlet stream 1
$X_{H2O,p1}$	[none]	H ₂ O mole fraction in process inlet stream 1
$X_{O2,p1}$	[none]	O ₂ mole fraction in process inlet stream 1
Up to three process-inlet streams can be defined.		
$T_{proc,in}$	[°C]	controlled process gas inlet temperature
$P_{proc,in}$	[kPa]	controlled process gas inlet pressure

Model Parameters

Due to the limited amount of plant data, only a small number of parameters can be estimated.

The model parameters are divided into adjustable and non-adjustable parameters as shown in

Table 17 and Table 18. Parameters are classified as non-adjustable if good estimates are

available in the academic literature or if it was known in advance that there is insufficient plant

data to properly estimate the parameter. An example of a parameter with insufficient data to

estimate it is the overall heat loss coefficient for the furnace refractory (U_{refrac}). To accurately

estimate a value for this parameter, the inner and outer furnace-wall temperatures at many

locations in the furnace would be required. As a result an estimate for the overall furnace heat

loss coefficient is calculated in the next section from furnace design specifications. Examples of

parameters that are available in the academic literature are the activation energies for the reforming reactions. The values calculated by Xu and Froment (1989a) have been widely accepted and used in prior models (Soliman et al., 1988; Pliehiers and Froment, 1988; Alabdan et al, 1992; Elnashaie et al., 1992; Pedernera et al., 2003 and Wesenberg and Svendsen, 2007).

Table 17. List of Non-adjustable Parameters

Symbol	Value	Units	Description	Source
U_{refrac}	18 000	$\left[\frac{\text{J}}{\text{m}^2 \cdot \text{h} \cdot \text{K}} \right]$	Assumed overall furnace heat loss coefficient	Calculated from design specifications
D_p	5.40	[mm]	Equivalent particle diameter	Calculated according to Twigg (1989; p. 101)
k_{tube}	106 500	$\left[\frac{\text{J}}{\text{m} \cdot \text{h} \cdot \text{K}} \right]$	Reformer tube thermal conductivity	Davis (2000; p. 473)
Radiation Model Parameters				
$b_{1,0}$	0.41	[none]	Weighting coefficient 1 for clear gas atmosphere	Taylor and Foster (1974)
$b_{2,0}$	$7.43 \cdot 10^{-5}$	$\left[\frac{1}{\text{K}} \right]$	Weighting coefficient 2 for clear gas atmosphere	Taylor and Foster (1974)
$b_{1,1}$	0.284	[none]	Weighting coefficient 1 for gray gas atmosphere 1	Taylor and Foster (1974)
$b_{2,1}$	$2.58 \cdot 10^{-5}$	$\left[\frac{1}{\text{K}} \right]$	Weighting coefficient 2 for gray gas atmosphere 1	Taylor and Foster (1974)
$b_{1,2}$	0.211	[none]	Weighting coefficient 1 for gray gas atmosphere 2	Taylor and Foster (1974)
$b_{2,2}$	$-6.54 \cdot 10^{-5}$	$\left[\frac{1}{\text{K}} \right]$	Weighting coefficient 2 for gray gas atmosphere 2	Taylor and Foster (1974)
$b_{1,3}$	0.0958	[none]	Weighting coefficient 1 for gray gas atmosphere 3	Taylor and Foster (1974)
$b_{2,3}$	$-3.57 \cdot 10^{-5}$	$\left[\frac{1}{\text{K}} \right]$	Weighting coefficient 2 for gray gas atmosphere 3	Taylor and Foster (1974)
K_0	0	$\left[\frac{1}{\text{m}} \right]$	Gas absorption coefficient for clear gas atmosphere	Calculated from Taylor and Foster (1974) and furnace input data

K_1	0.300	$\left[\frac{1}{\text{m}} \right]$	Gas absorption coefficient for atmosphere 1	Calculated from Taylor and Foster (1974) and furnace input data
K_2	3.10	$\left[\frac{1}{\text{m}} \right]$	Gas absorption coefficient for atmosphere 2	Calculated from Taylor and Foster (1974) and furnace input data
K_3	42.9	$\left[\frac{1}{\text{m}} \right]$	Gas absorption coefficient for atmosphere 3	Calculated from Taylor and Foster (1974) and furnace input data
ϵ_{tube}	0.85	[none]	Tube emissivity	Company experience
ϵ_{refrac}	0.60	[none]	Refractory emissivity	Company experience
Reaction Kinetic and Catalyst Parameters				
$\rho_{\text{cat,pk}}$	1100	$\left[\frac{\text{kg}_{\text{cat}}}{\text{m}^3_{\text{tube}}} \right]$	Catalyst packing density	Katalco (2005) 23-4Q Product Bulletin
$\eta_{\text{refrm},1}$	0.05	[none]	Effectiveness factors for the reforming reactions in tube segment 1	Wesenberg and Svendsen (2007)
$\eta_{\text{refrm},2-5}$	0.1	[none]	Effectiveness factors for the reforming reactions in tube segments 3 to 5	Wesenberg and Svendsen (2007)
$\eta_{\text{refrm},6-15}$	0.1	[none]	Effectiveness factors for the reforming reactions in tube segments 6 to 15	Wesenberg and Svendsen (2007)
η_{wgs}	0.1	[none]	Effectiveness factors for the water-gas shift reaction in all tube segments	Assigned the same value as the effectiveness factors for the reforming reactions
A_{r1}	$4.22 * 10^{15}$	$\left[\frac{\text{kgmol} \cdot \text{bar}^{\frac{1}{2}}}{\text{kg}_{\text{cat}} \cdot \text{h}} \right]$	Pre-exponential factor for reforming reaction 1	Xu and Froment (1989a)
A_{r2}	$1.02 * 10^{15}$	$\left[\frac{\text{kgmol} \cdot \text{bar}^{\frac{1}{2}}}{\text{kg}_{\text{cat}} \cdot \text{h}} \right]$	Pre-exponential factor for reforming reaction 2	Xu and Froment (1989a)
A_{r3}	$1.96 * 10^6$	$\left[\frac{\text{kgmol}}{\text{kg}_{\text{cat}} \cdot \text{h} \cdot \text{bar}} \right]$	Pre-exponential factor for the water-gas shift reaction	Xu and Froment (1989a)

E_{r1}	240.1	$\left[\frac{\text{kJ}}{\text{gmol}} \right]$	Activation energy of reforming reaction 1	Xu and Froment (1989a)
E_{r2}	243.9	$\left[\frac{\text{kJ}}{\text{gmol}} \right]$	Activation energy of reforming reaction 2	Xu and Froment (1989a)
E_{r3}	67.13	$\left[\frac{\text{kJ}}{\text{gmol}} \right]$	Activation energy of the water-gas shift reaction	Xu and Froment (1989a)
$\Delta H_{ad,H_2}$	-82.9	$\left[\frac{\text{kJ}}{\text{gmol}} \right]$	Enthalpy of adsorption for H_2	Xu and Froment (1989a)
$\Delta H_{ad,CO}$	-70.65	$\left[\frac{\text{kJ}}{\text{gmol}} \right]$	Enthalpy of adsorption for CO	Xu and Froment (1989a)
$\Delta H_{ad,CH_4}$	-38.2	$\left[\frac{\text{kJ}}{\text{gmol}} \right]$	Enthalpy of adsorption for CH_4	Xu and Froment (1989a)
$\Delta H_{ad,H_2O}$	88.68	$\left[\frac{\text{kJ}}{\text{gmol}} \right]$	Enthalpy of adsorption for H_2O	Xu and Froment (1989a)
A_{ad,H_2}	$6.12 * 10^{-9}$	$\left[\frac{\text{kJ}}{\text{gmol}} \right]$	Pre-exponential factor of adsorption for H_2	Xu and Froment (1989a)
$A_{ad,CO}$	$8.23 * 10^{-5}$	$\left[\frac{\text{kJ}}{\text{gmol}} \right]$	Pre-exponential factor of adsorption for CO	Xu and Froment (1989a)
A_{ad,CH_4}	$6.65 * 10^{-4}$	$\left[\frac{\text{kJ}}{\text{gmol}} \right]$	Pre-exponential factor of adsorption for CH_4	Xu and Froment (1989a)
A_{ad,H_2O}	$1.77 * 10^5$	$\left[\frac{\text{kJ}}{\text{gmol}} \right]$	Pre-exponential factor of adsorption for H_2O	Xu and Froment (1989a)
Thermodynamic Parameters				
$\Delta H_{f,A}^\circ$	many values	$\left[\frac{\text{kJ}}{\text{gmol}} \right]$	Enthalpy of formation of species A at 298K at 1 atm	Reid et al. (1977)
$\Delta S_{f,A}^\circ$	many values	$\left[\frac{\text{kJ}}{\text{gmol} \cdot \text{K}} \right]$	Entropy of formation of species A at 298K at 1 atm	Reid et al. (1977)
A_i, B_i, C_i, D_i	many values		Heat capacity polynomial coefficients	Reid et al. (1977)

The parameters listed in Table 18 are identified as adjustable because good estimates are not available in the academic literature or from company experience. The values shown in Table 18

are the base case values. These values are used in the preliminary simulations, as initial guesses for parameter ranking and as initial guesses for parameter estimation.

Table 18. Adjustable Parameters

Symbol	Value± Uncertainty	Units	Bounds Enforced during Parameter Estimation	Description
L_q	3.66±1.83	[m]	$3.05 \leq L_q \leq 6.10$	heat release length (in increments of 0.61m)
α_{top}	0.18±0.18	[none]	Parabola must open down and heat-release length ≥ 0 in each zone	fraction of combustion enthalpy released in the top furnace-volume zone
f_{htg}	1±1	[none]	$f_{htg} \geq 0$	adjustable factor for tube- to-process-gas convective- heat-transfer coefficient
ϕ	0.7±0.1	[none]	$0.5 \leq \phi \leq 1.0$	void fraction or porosity of the catalyst bed
f_{prx}	1±1	[none]	$f_{prx} \geq 0$	adjustable factor for the pre-exponential factor of reforming reactions
$f_{nOffGas}$	0.9±0.1	[none]	$0.90 \leq f_{nOffGas} \leq 1.10$	adjustable factor for the PSA off-gas flow rate
$f_{nCombAir}$	0.9±0.1	[none]	$0.90 \leq f_{nCombAir} \leq 1.10$	adjustable factor for the combustion air flow rate
f_{ctube}	1.0±0.1	[none]	$f_{ctube} \geq 0$	adjustable factor for the furnace-gas-to-tube convective heat transfer coefficient

4.2 Calculation of Furnace Heat Loss Coefficient U_{refrac}

Furnace design specifications indicate that approximately 2% of the combustion heat is lost to the surroundings. In the average-tube model, heat loss through the furnace walls is assumed to occur by conduction and is calculated using equation (61).

$$Q_{\text{loss}} = \sum_{\substack{\text{surface} \\ \text{zones } i}} \frac{k_{\text{refrac}}}{t_{\text{refrac}}} A_i (T_i - T_{\text{surr}}) \quad (61)$$

The parameters k_{refrac} , t_{refrac} and T_{surr} in equation (61) are well known. The thermal conductivity of the ceramic insulation ($k_{\text{refrac}} = 1\,153 \frac{\text{J}}{\text{m} \cdot \text{h} \cdot \text{K}}$) was taken from the literature (Bindar, 1996), the refractory thickness ($t_{\text{refrac}} = 0.305 \text{ m}$) from furnace design sheets and the temperature of the surrounding environment was assumed to be ambient room temperature ($T_{\text{surr}} = 22 \text{ }^\circ\text{C}$). When these parameters are used in the model, the amount of heat loss to the environment is less than 1 % of the heat released by combustion. The low heat loss predictions from equation (61) are likely due to oversimplification of heat loss mechanisms. In equation (61) it is assumed that all heat loss to the surroundings occurs by conduction through refractory walls of equal thickness. In reality there are peep doors where the furnace insulation is thin and holes in the furnace refractory for monitoring equipment that allow furnace heat to escape. To get a more realistic estimate of the heat loss from the furnace, k_{refrac} and t_{refrac} are combined into an overall heat loss coefficient U_{refrac} . Since data do not exist to estimate U_{refrac} as a parameter, it is calculated from the average furnace-wall temperatures in a third-party study, the heat of combustion of the furnace fuel and the 2% design specification as shown in equation (62) .

$$U_{\text{refrac}} = \frac{0.02Q_{\text{fur}}}{A_{\text{refrac}} \left(T_{\text{refrac average}} - T_{\text{surr}} \right)} \quad (62)$$

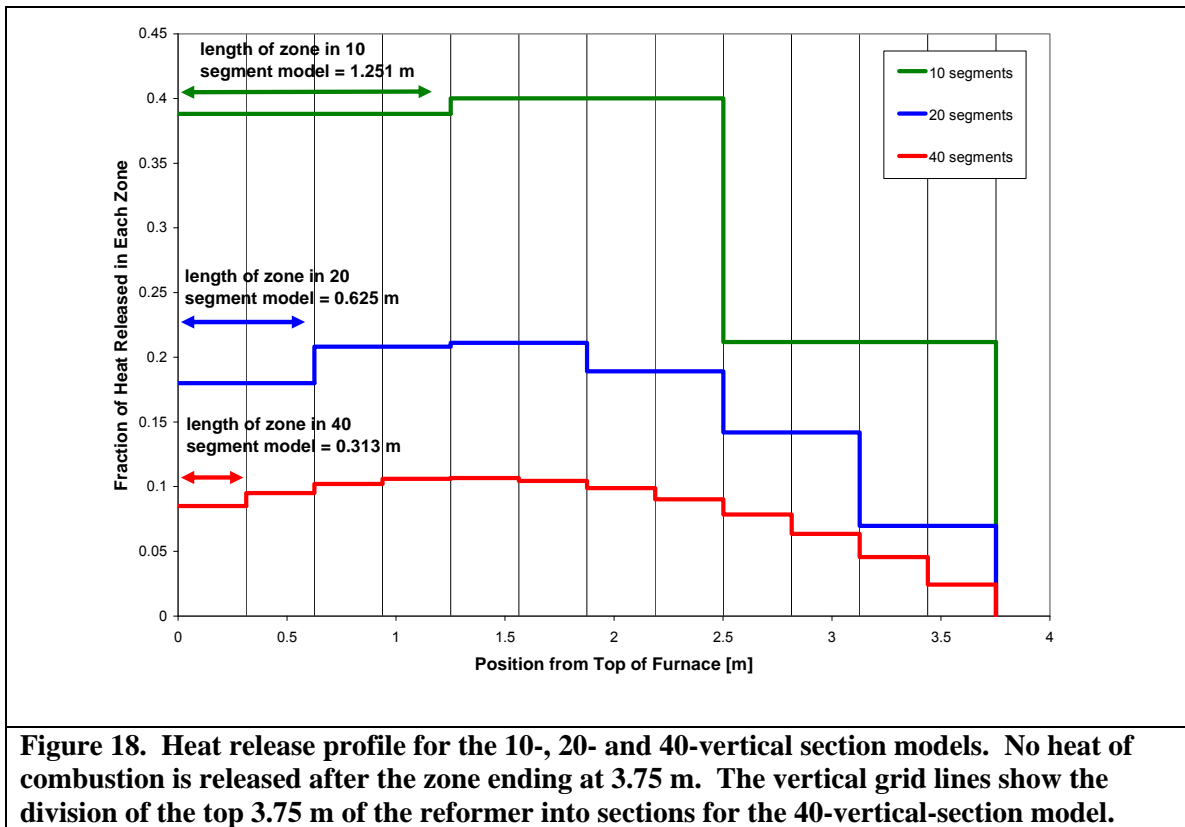
Using this method, U_{refrac} was determined to be $5\,483 \frac{\text{J}}{\text{m} \cdot \text{h} \cdot \text{K}}$ or 4.75 times greater than the thermal conductivity of ceramic insulation.

4.3 Choosing the Number of Vertical Sections

The number of vertical sections in the model can be adjusted by the user. The number of vertical sections is different from the adjustable parameters previously discussed since it is not used to fit model outputs to plant data. Instead the number of vertical sections is chosen to achieve an adequate numerical solution for the temperature profile within an acceptable runtime. As the number of vertical sections increases, the numerical accuracy and the runtime increase. The optimum number of vertical sections is reached when an increase in the number of vertical sections does not produce a noticeable change in the profile. To determine an appropriate number of vertical sections, a comparison of the profiles and runtimes using 10-, 20- and 40- vertical-section models was performed. The adjustable parameters used in the simulations are from Table 18 and the plant data for the simulations are from the data set Plant C1 in Appendix H. The effectiveness factor for the reforming reactions and the water-gas shift was set to 0.1 in all process-side segments.

To make a valid comparison of the temperature and composition profiles for the 10-, 20- and 40-section models, the fraction of combustion heat released at a distance from the top of the reformer remained the same although the number of vertical sections changed. To accomplish this, the combustion-heat-release profile for the 40-section model was summed to generate the heat-release profiles for the 10- and 20-section models. Figure 18 shows the heat-release profiles for

the 10-, 20- and 40-section models and Figure 19 shows the cumulative-heat-release profiles for the 10-, 20- and 40-section models. The sum of the first four fractions in the 40-section model (top profile in Figure 18) is equal to the first fraction in the 10-section model (bottom profile in Figure 18). The result is that the same fraction of combustion heat is released over the top 1.25 m of the 40-section model as over the top 1.25 m of the 10-section model, even though the 40 section model has four zones in the top 1.25 m of the furnace while the 10 section model has only one. This result is confirmed in Figure 19 where the cumulative heat-release profiles for the 10-, 20- and 40-section models are the same.



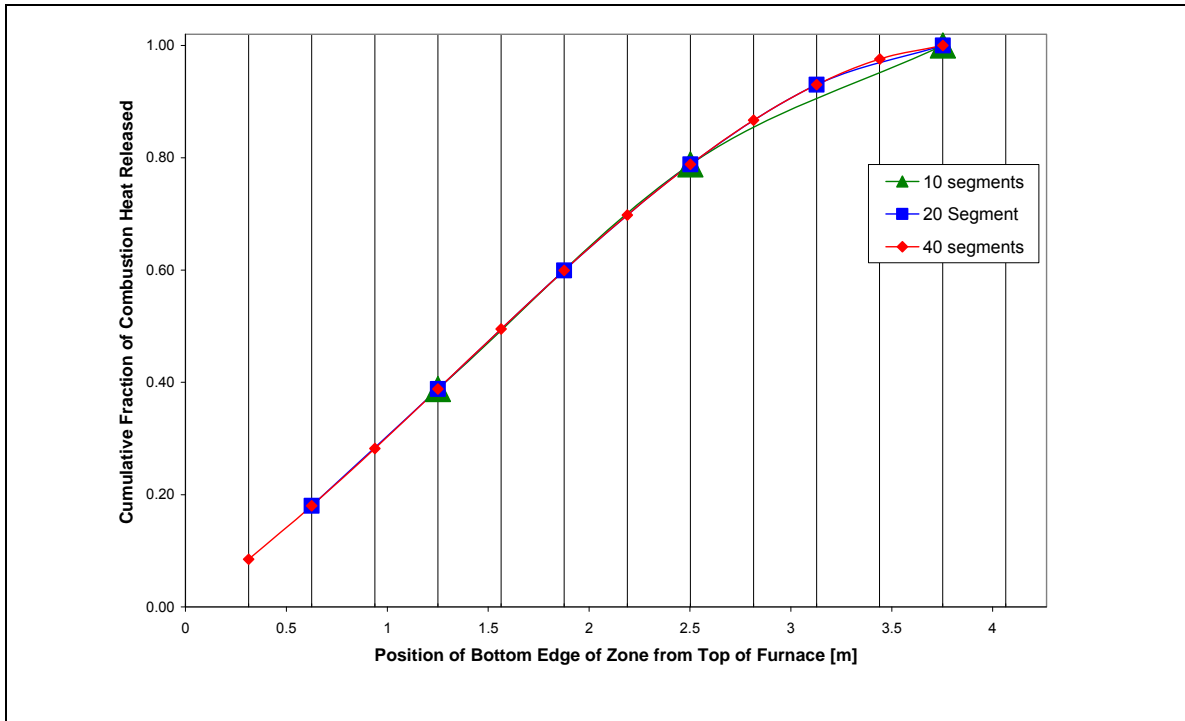


Figure 19. Cumulative-heat-release profile for the 10-, 20- and 40-vertical-section models. The vertical grid lines show the division of the top 3.75 m of the reformer for the 40-vertical section model.

Figure 20 compares the predicted temperature profiles of the 10- and 20-vertical-section models and Figure 21 compares the temperature profiles for the 20- and 40-vertical-segment models. In Figure 20, the furnace-gas-temperature profiles and outer-tube-wall-temperature profiles are very different near the top of the reformer but are similar near the bottom of the reformer. The larger tube segments in the 10-vertical section model predict a lower temperature than the smaller segments of the 20-vertical section model at the top of the reformer. The inner-tube-wall-temperature profile and process-gas-temperature profiles are very similar for the 10- and 20-section models. The process-gas-temperature profile for the 10-section model does not capture the drop in process-gas-temperature at 0.609 m but instead shows a smaller drop at 1.22 m.

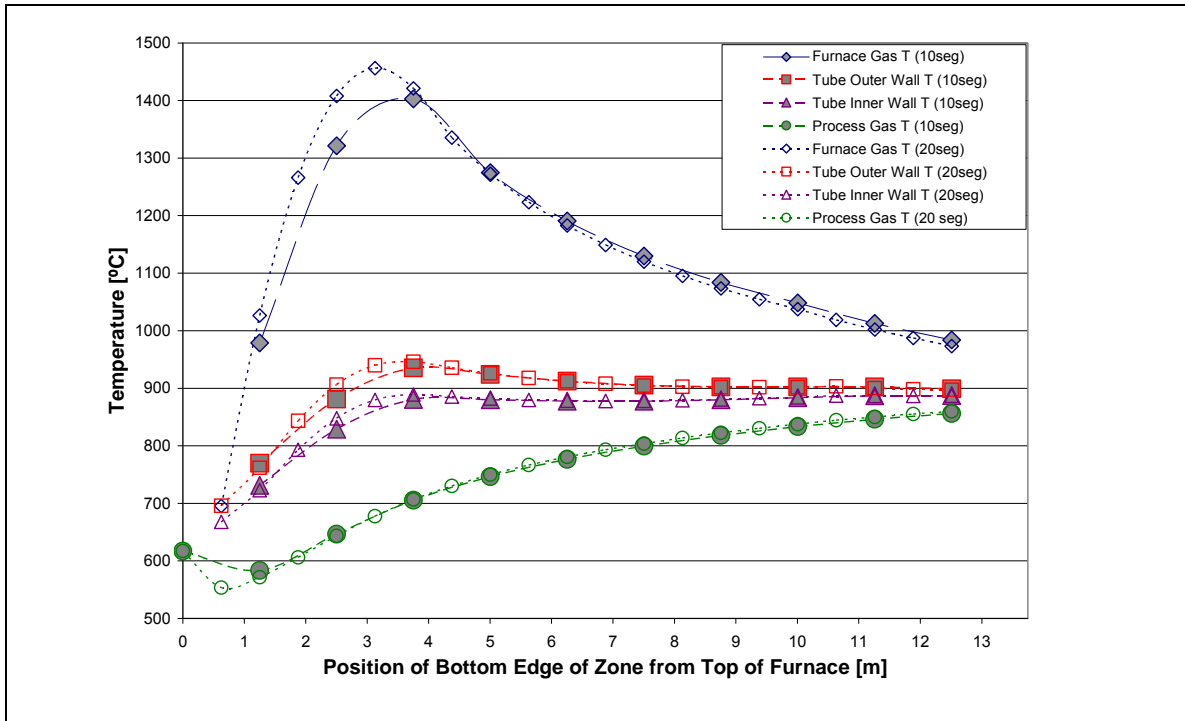


Figure 20. Comparison of the Temperature Profiles for the Average-Tube Model with 10 and 20 Vertical Sections

Figure 21 shows the temperature profiles for the 20- and 40-vertical-section models. There is a small difference in the predicted furnace-gas-temperature profiles and process-gas-temperature profiles for the 20- and 40-section models at the top of the reformer. The inner-tube-wall temperature profiles and process-gas-temperature profiles are nearly identical for the 20- and 40-section models. The 20 section model adequately captures the drop in process-gas temperature at the top of the reformer.

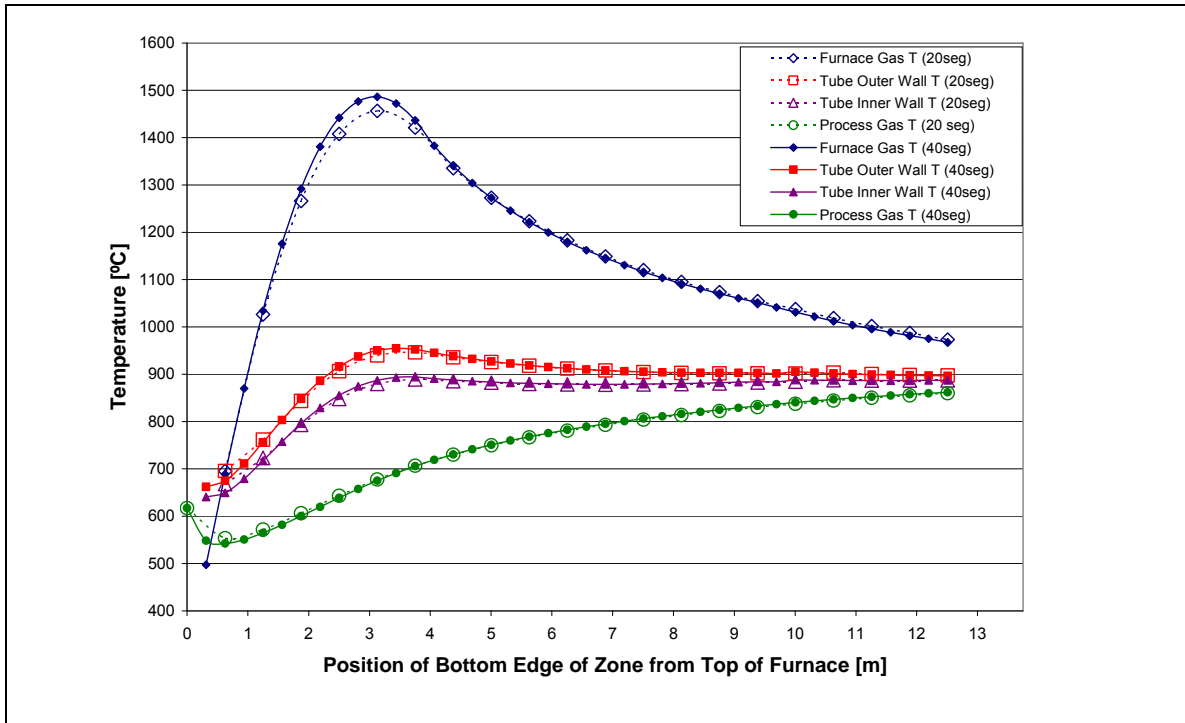


Figure 21. Comparison of the Temperature Profiles for the Average-Tube Model with 20 and 40 Vertical Sections

Figure 22 shows the process-gas composition for the 10- and 20-section models. Figure 23 shows the process-gas composition for the 20- and 40-section models. The process-gas-composition profiles are strongly dependent on the process-gas temperature profile. The 10-section model does not show the minor details of the hydrogen or water profiles seen at 0.61 and 1.52 m in the 20 section models. These minor details are more evident in the 40-section model shown in Figure 23. There is almost no difference in the composition profiles of the 20- and 40-section models.

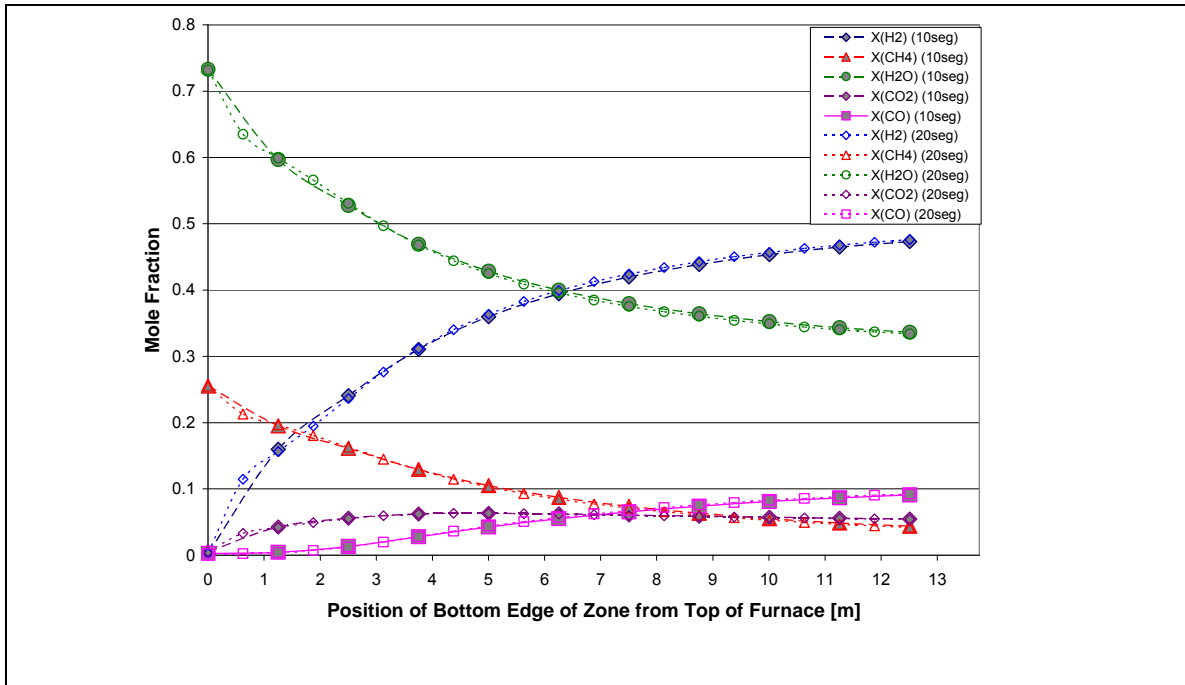


Figure 22. Comparison of the Composition Profiles for the Average-Tube Model with 10 and 20 Vertical Sections

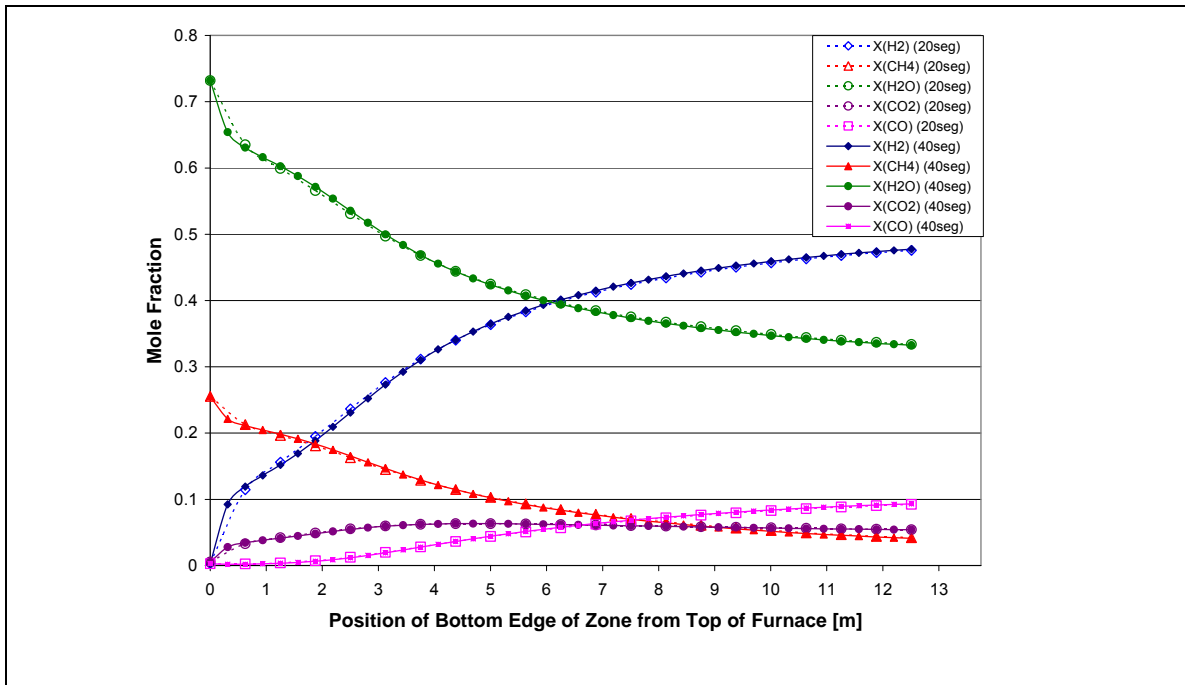


Figure 23. Comparison of Process-Gas Composition Profiles for the Average-Tube Model with 10 and 20 Vertical Sections

The temperature and composition profiles of the 40-section model did not show more detail than the 20-section model. For this reason the additional computation time of the 40-section model does not provide additional benefit (See Table 19). The 10-section model did not show enough detail at the top of the reformer but was adequate for the bottom of the reformer where the rates of the reforming reactions are slower. To further reduce computation time but still capture profile detail, the small vertical sections of the 20-section model are used at the top of the reformer and the larger vertical sections of the 10-section model are used at the bottom of the reformer throughout the remainder of this thesis. Figure 24 shows that very little profile detail is lost by using the larger vertical sections at the bottom of the reformer.

Table 19. Computation Time for Models with 10, 20, 40 and 15 Vertical Sections on a 2.8 GHz Intel Pentium 4 processor with 2GB of RAM Starting from the Common-Segment-Initial-Guess Method Described in Appendix D

Number of Vertical Sections	Computation Time [s]
10	95
20	438
40	1835
15	245

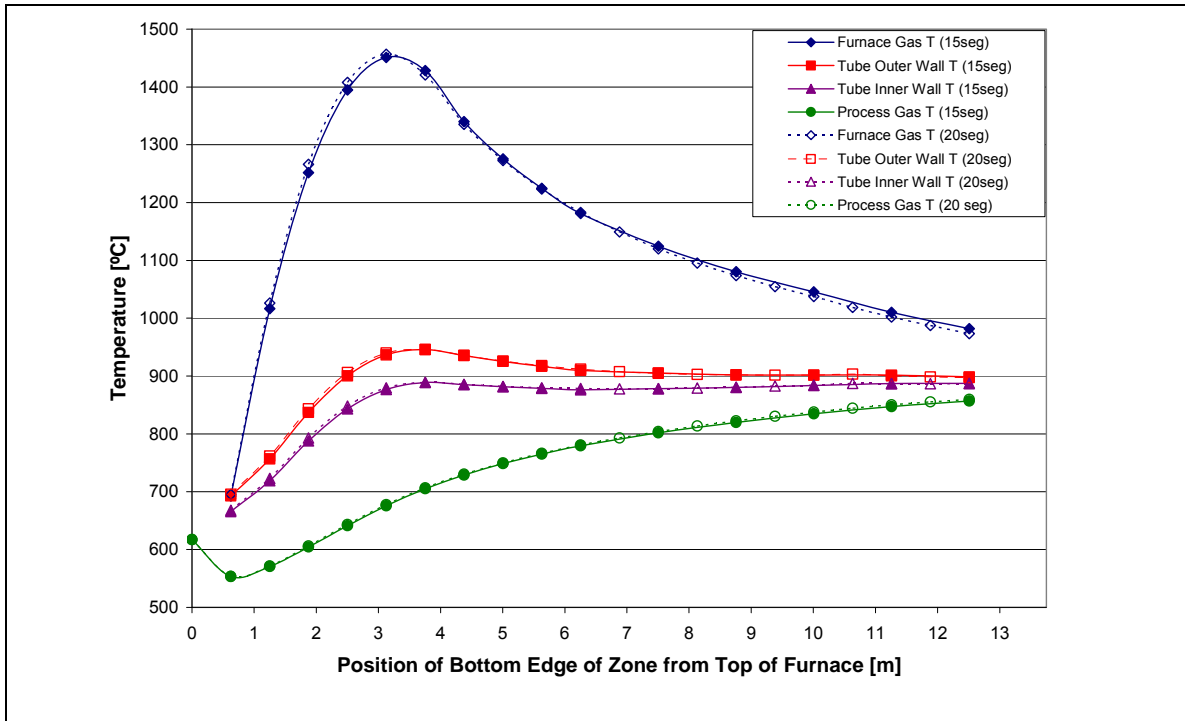


Figure 24. Comparison of Temperature Profiles for Models with 15 non-uniform and 20 uniform vertical zones

4.4 Effect of Model Parameters on Simulations

To qualitatively test the impact of the parameters on the simulation results, reformer temperature profiles were compared when the parameters were adjusted from their initial guesses provided in Table 18. The temperature profiles produced when the parameters are assigned the values in Table 18 are referred to as the base case. The parameters were adjusted one at a time, and the new temperature profiles compared to the base case profiles. The plant inputs used in the simulations are from the data set Plant B in Appendix H. The temperature profiles from the base case are shown in Figure 25. Simulation results for a change in the bed porosity are not shown since an adjustment of the bed porosity (by 0.1) did not produce a visible change in the temperature or concentration profiles.

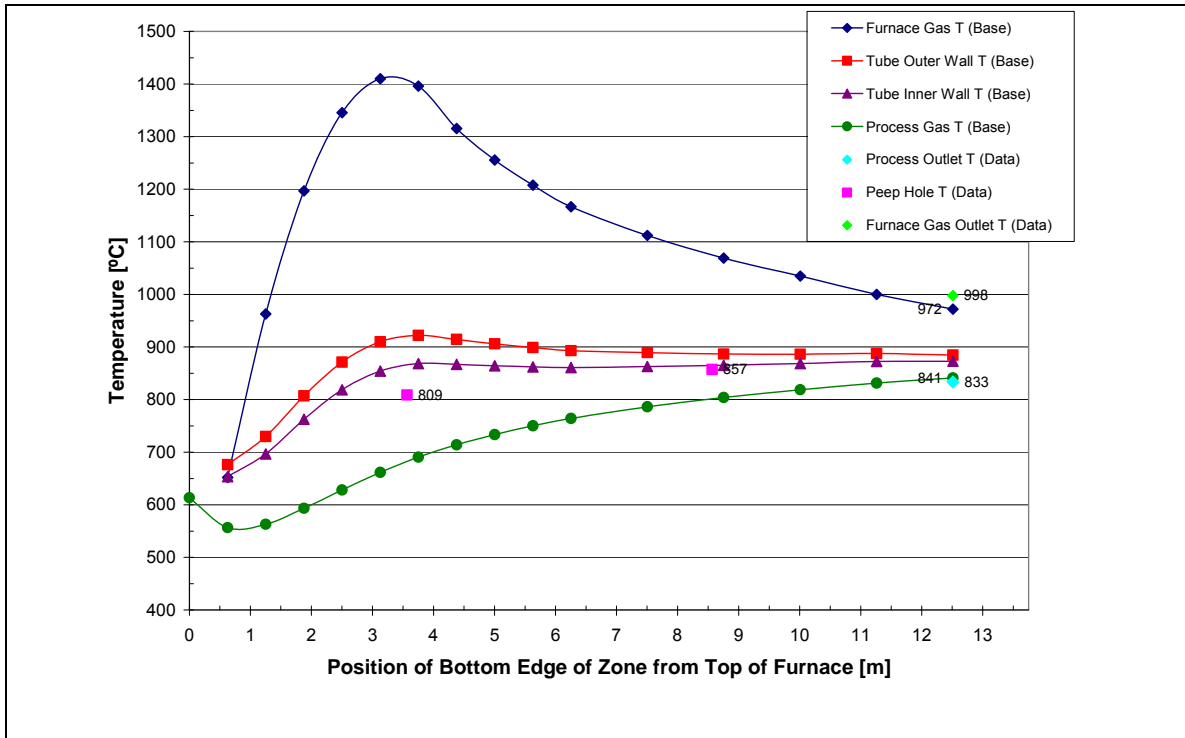


Figure 25. Base Case Temperature Profiles Produced using the Parameter Values in Table 18 and the Inputs from Plant B. Plant output data are also shown.

Figure 26 compares the temperature profiles for a heat-release length (L_q) of 6.10 m to the base case ($L_q=3.66$ m). In Figure 26 the shapes of all the temperature profiles change as a result of the change in the heat-release length. The furnace-gas outlet temperature decreases and the process-gas outlet temperature increases as the heat-release length is increased from 3.66 m to 6.10 m.

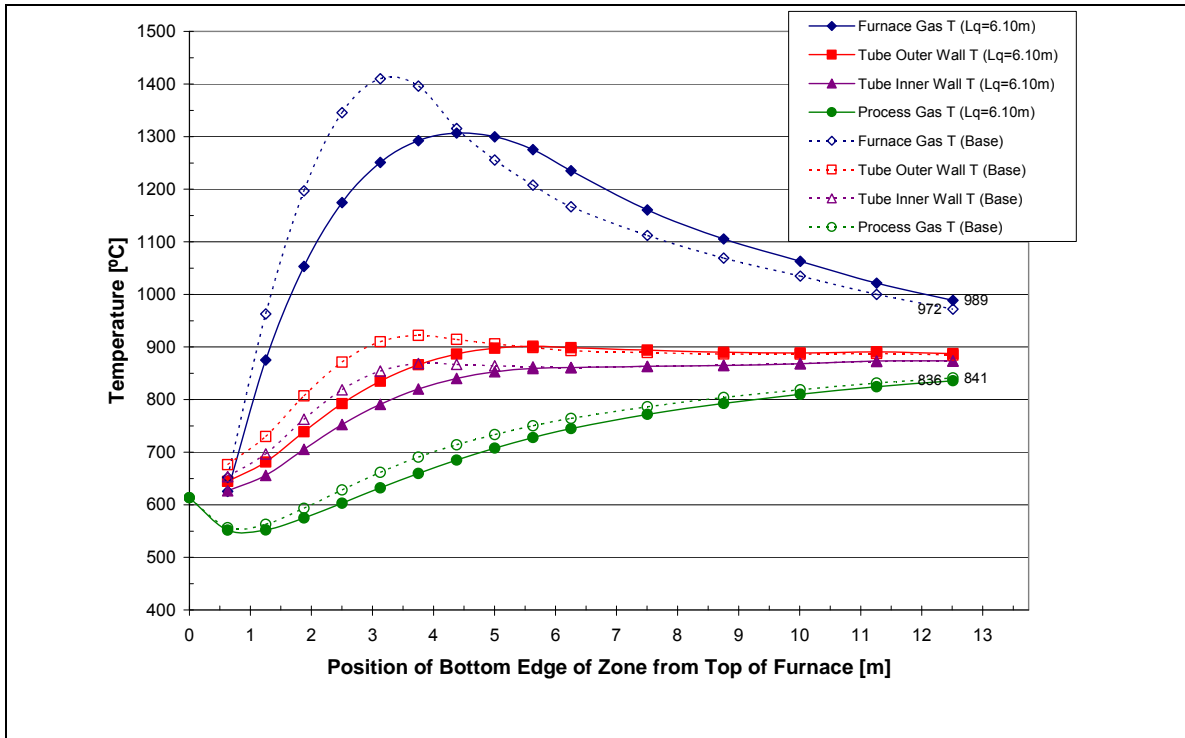


Figure 26. Comparison of the Temperature Profiles for a Heat-Release Length of 6.10 m and the 3.66 m Base Case.

Figure 27 compares the temperature profiles for a fraction of combustion in the top furnace zone (α_{top}) of 0.05 and 0.18. A decrease in the fraction of combustion in the top furnace zone changes the shape of the profiles near the top of the reformer but has only a minor impact on the profiles at the bottom of the reformer. Note that a low value of α_{top} causes the furnace gas at the top of the furnace to be colder than the process gas.

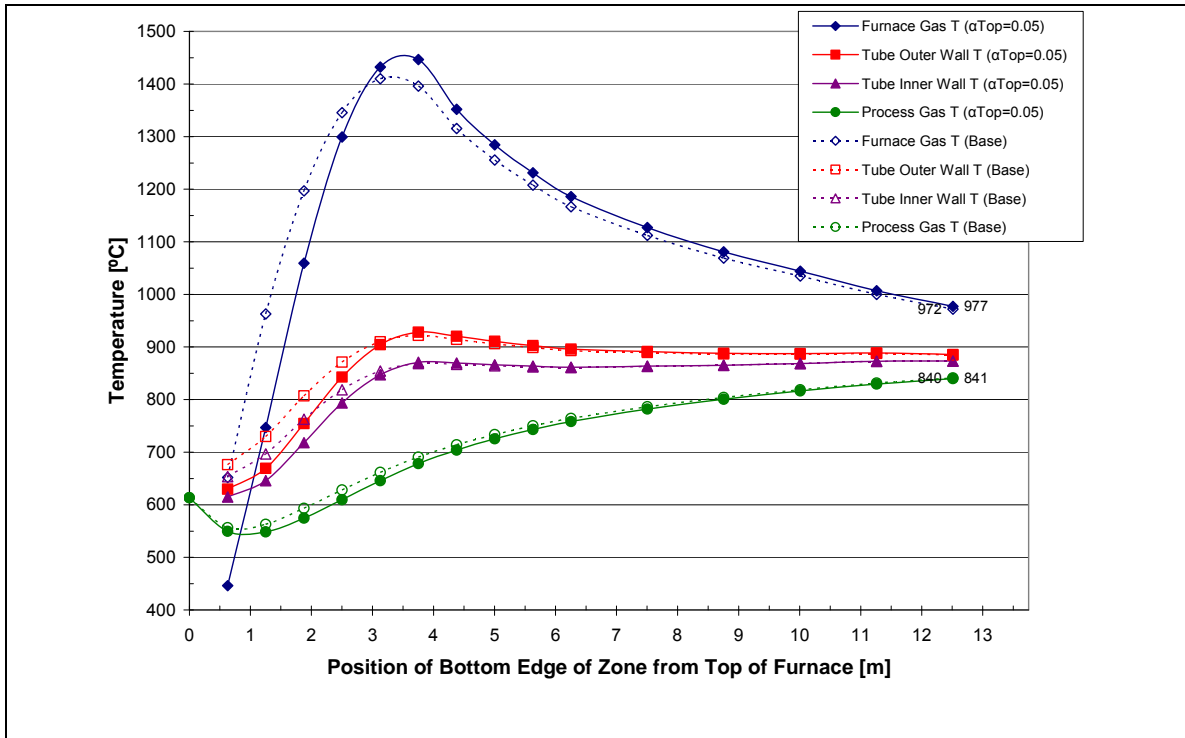


Figure 27. Comparison of the Temperature Profiles for a Fraction of Combustion in Top Furnace Zone of 0.05 and 0.18 Base Case.

Figure 28 shows the temperature profiles for a tube-to-process-gas convective-heat-transfer-coefficient factor (f_{htg}) of 2 and 1. The convective-heat-transfer-coefficient factor has a strong influence on the outer and inner tube-wall temperature profiles but minimal influence on the process and furnace-gas temperature profiles. As the parameter f_{htg} is increased, the outer and inner tube-wall temperature profiles shift. The largest vertical shift occurs 1.52 to 7.62 m from the top of the reformer where the temperature difference between the furnace-gas and process-gas is the greatest.

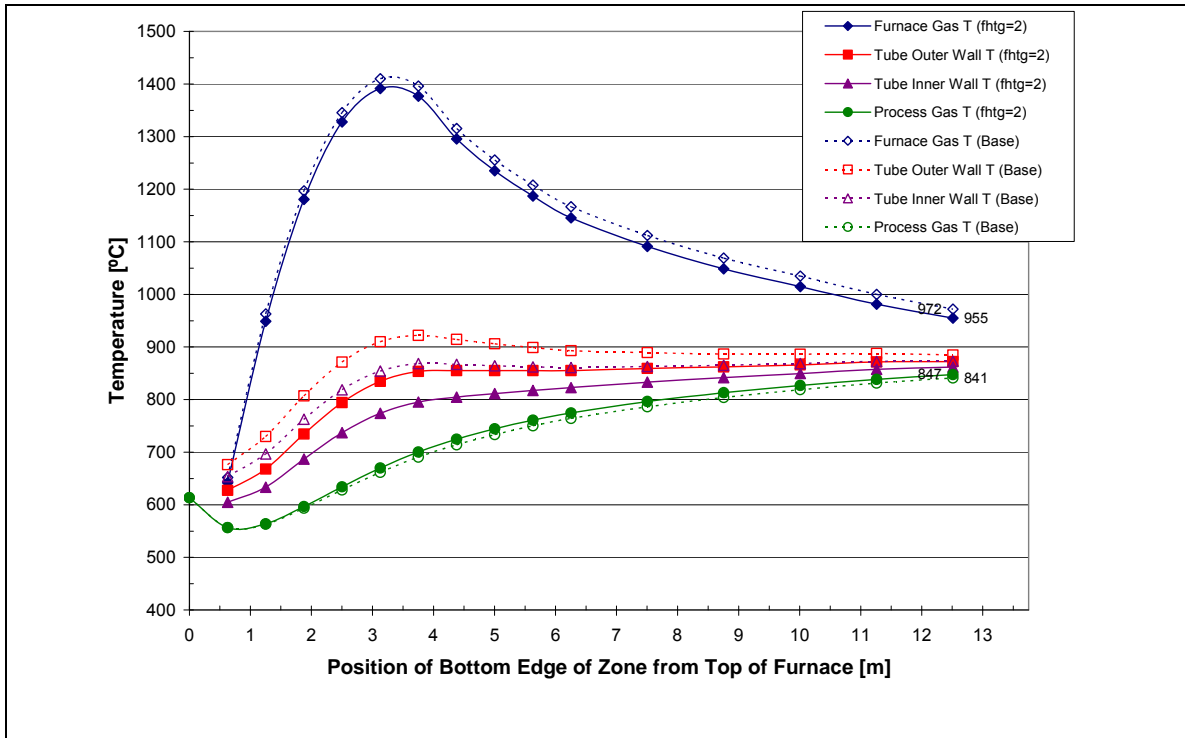


Figure 28. Comparison of the Temperature Profiles with a Tube-To-Process-Gas Convective-Heat-Transfer-Coefficient Factor of 2 and 1.

Figure 29 compares the temperature profiles with adjustable pre-exponential factors (f_{prx}) of 2 and 1. Besides a minor difference in the process-gas temperature profile 0.61 m from the top of the reformer, increasing the adjustable pre-exponential factor to 2 has very little influence on the temperature profiles.

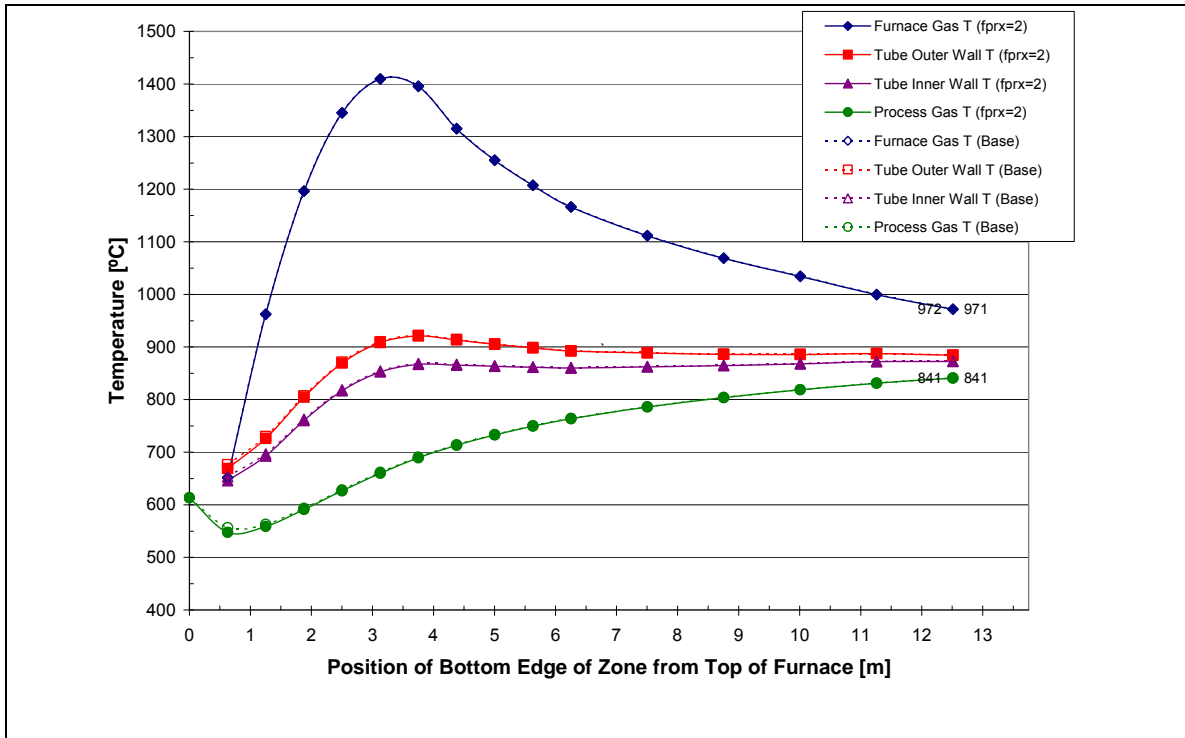


Figure 29. Comparison of the Temperature Profiles for an Adjustable Pre-exponential Parameter of 2 and 1.

Figure 30 compares the temperature profiles for an adjustable pre-exponential parameter of 0.05 and 1. The decrease in the adjustable pre-exponential parameter increased the process-gas temperature profile and the inner and outer-tube-wall temperature profiles but has minimal impact on the furnace-gas temperature profile. Figure 29 shows that the increasing the adjustable pre-exponential parameter has minimal impact on the reformer temperature profiles while Figure 30 shows that decreasing the parameter will alter the profiles.

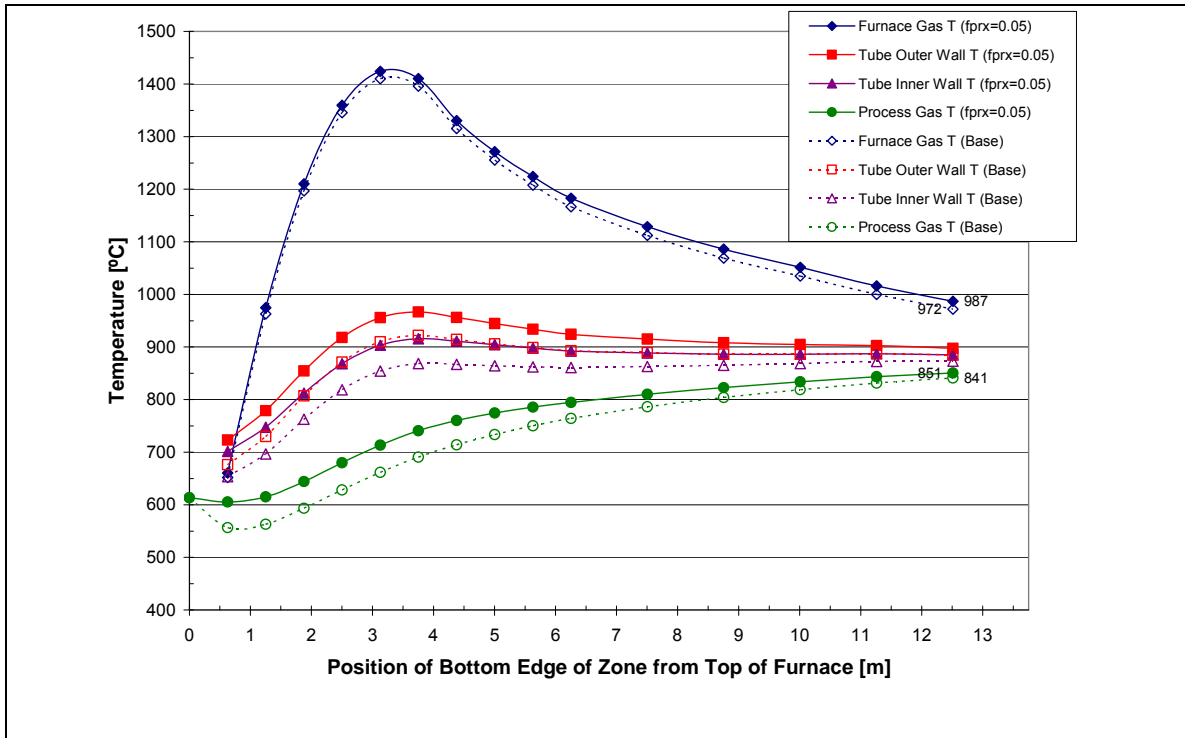


Figure 30. Comparison of the Temperature Profiles for an Adjustable Pre-exponential Parameter of 0.05 and 1.

Figure 31 compares the temperature profiles for a PSA off-gas flow rate of 100% and 90%. Since the PSA off-gas carries a large portion of the combustion heat, changing the parameter $f_{nOffGas}$ is equivalent to changing amount of combustion heat released in the furnace. In Figure 31 the temperatures of all the profiles are increased when the PSA off-gas flow rate is increased.

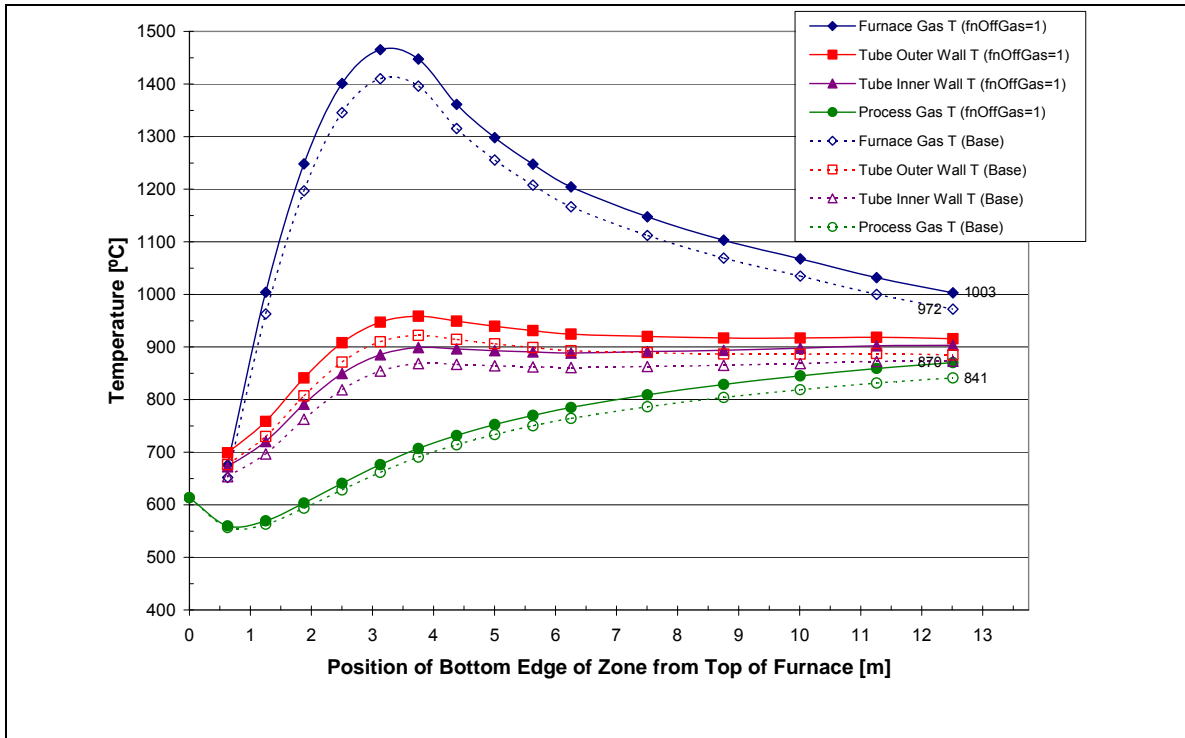


Figure 31. Comparison of the Temperature Profiles for a PSA Off Gas Flow Rate of 100% ($f_{nOffGas} = 1.0$) and 90% ($f_{nOffGas} = 0.9$).

Figure 32 compares the temperature profiles for a combustion air flow rate of 100% and 90%. In Figure 32, the profiles for $f_{nCombAir} = 1.0$ occur at lower temperature than the base case. The extra combustion air reduces the furnace-gas temperature and shifts all the temperature profiles to lower temperatures due to the additional nitrogen and unreacted oxygen in the furnace.

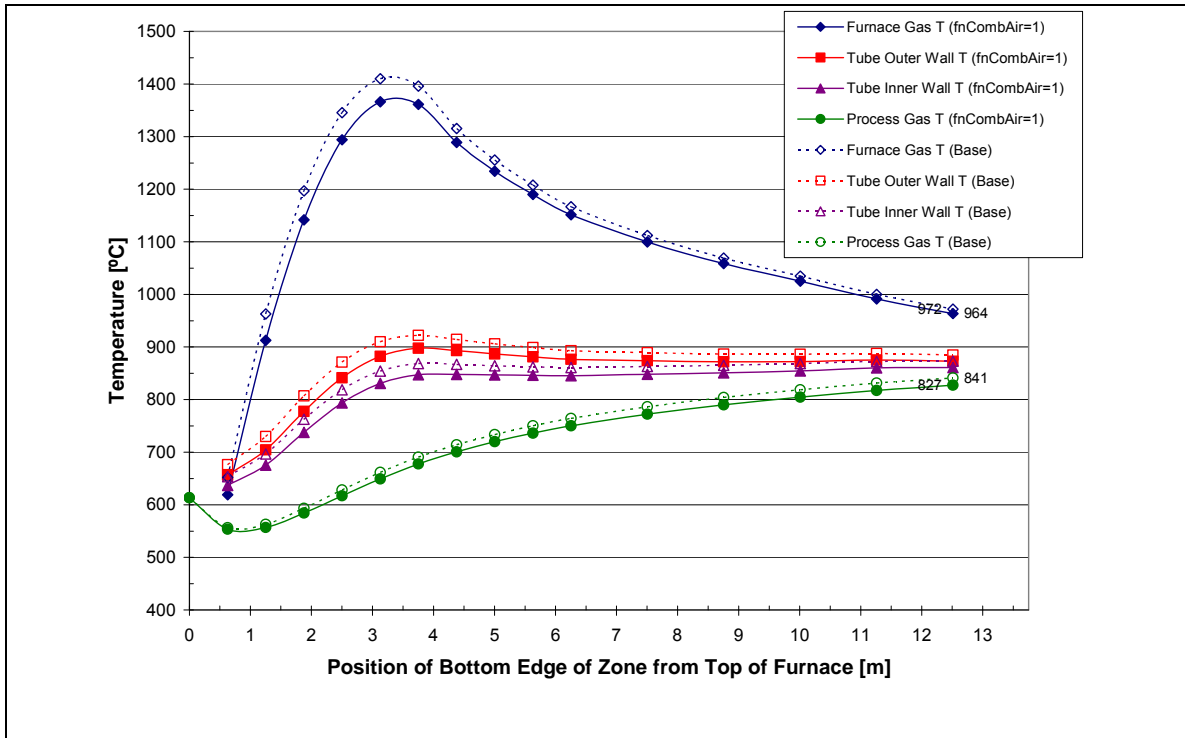


Figure 32. Comparison of the Temperature Profiles for a Combustion Air Flow Rate of 100% ($f_{nCombAir}=1.0$) and 90% ($f_{nCombAir}=0.9$).

Figure 33 compares the temperature profiles for furnace-gas-to-tube convective heat transfer parameters of 0.5 and 1. In Figure 33 the furnace-gas, outer-tube wall and inner-tube wall temperature profiles are shifted to higher temperatures while the process-gas temperature profile is shifted to lower temperatures. This is expected since a lower furnace-gas-to-tube convective heat transfer coefficient should prevent some of the furnace heat from entering the process-side.

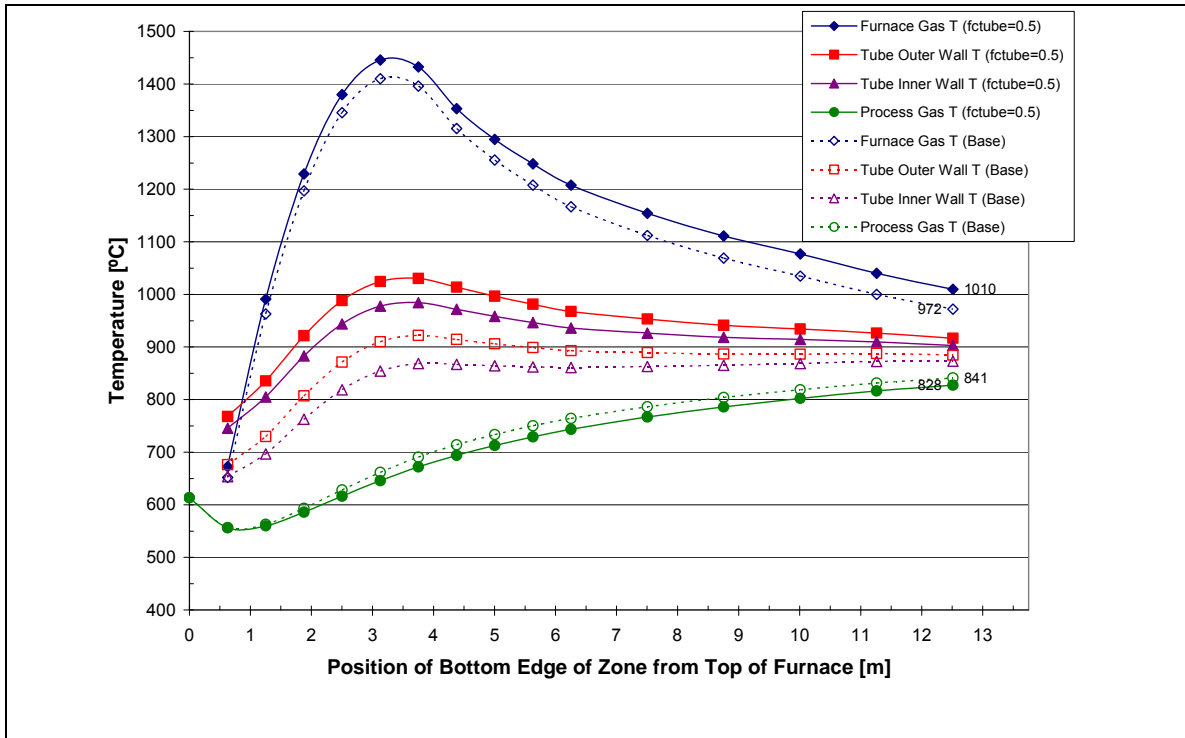


Figure 33. Comparison of the Temperature Profiles with a Furnace-Gas-To-Tube Convective-Heat-Transfer-Coefficient Factor of 0.5 and 1.

4.5 Parameter Ranking

The adjustable parameters were ranked using the estimability analysis technique developed by Yao et al. (2003) and Kou et al. (2005). This estimability analysis technique ranks the adjustable parameters in terms of their impact on the model outputs and their correlated influence with other adjustable parameters. Note that the ranking obtained from estimability analysis depends on the initial guesses for the parameters, because parameter values are required to calculate derivatives of the predicted model outputs with respect to the parameters. The heat-release length was not ranked because it is a discrete parameter that would be difficult to estimate using gradient-based techniques. Figure 26 shows that the model outputs are highly sensitive to changes in the heat-

release length. The effect of the heat-release length on the model outputs will be quantified in the parameter estimation section of this chapter by estimating other key parameters using different fixed values of L_q . The values and uncertainties of the adjustable parameters from Table 18 were used as initial guesses for the estimability analysis with the exception of the fraction of combustion in the top furnace volume zone (α_{top}). The initial guess for α_{top} was recalculated for each heat-release length so that the heat-release profiles are parabolas that open downward and are symmetric about the centre of the heat-release length (Roesler,1967), ensuring that the overall shape of the heat-release profile was the same for the parameter ranking regardless of the heat-release length. The initial heat-release profiles at different values of L_q were generated using equations (36) to (42) and are shown in Table 20. The parameter rankings at heat-release lengths of 3.66, 4.27, 4.88, 5.49 and 6.10 m are shown in Table 21.

Table 20. Heat-release Profiles used in Estimability Analysis. The Profiles were generated using equations (36) to (42).

Furnace-Volume Zone Number from Top	Distance of Bottom-Edge of Furnace-Volume Zone from Top of Reformer [m]	Fraction of Combustion Heat-Released in Each Furnace-Volume Zone for Different Heat-Release Lengths				
		3.66 m	4.27 m	4.88 m	5.49 m	6.10 m
1	0.61	0.1071	0.0833	0.0667	0.0545	0.0455
2	1.22	0.1786	0.1429	0.1167	0.0970	0.0818
3	1.83	0.2143	0.1786	0.1500	0.1273	0.1091
4	2.44	0.2143	0.1905	0.1667	0.1455	0.1273
5	3.05	0.1786	0.1786	0.1667	0.1515	0.1364
6	3.66	0.1071	0.1429	0.1500	0.1455	0.1364
7	4.27	--	0.0833	0.1167	0.1273	0.1273
8	4.88	--	--	0.0667	0.0970	0.1091
9	5.49	--	--	--	0.0545	0.0818
10	6.10	--	--	--	--	0.0455

Table 21. Ranking of Adjustable Parameters using the Estimability Analysis Technique of Kou et al. (2005) and the Parameter Values and Uncertainties from Table 18. Parameters near the Top of the List are Most Estimable.

Parameter Ranking	Heat-Release Length [m]				
	3.66	4.27	4.88	5.49	6.10
1	f_{htg}	f_{htg}	f_{htg}	f_{htg}	f_{htg}
2	$f_{nOffGas}$	$f_{nOffGas}$	$f_{nOffGas}$	$f_{nOffGas}$	α_{top}
3	ϕ	α_{top}	α_{top}	α_{top}	$f_{nOffGas}$
4	$f_{nCombAir}$	ϕ	ϕ	ϕ	ϕ
5	α_{top}	f_{prx}	$f_{nCombAir}$	$f_{nCombAir}$	$f_{nCombAir}$
6	f_{prx}	f_{ctube}	f_{prx}	f_{prx}	f_{prx}
7	f_{ctube}	$f_{nCombAir}$	f_{ctube}	f_{ctube}	f_{ctube}

The parameter rankings in Table 21 show that with the exception of the ranking performed at 4.27 m, the five most estimable parameters are f_{htg} , $f_{nOffGas}$, α_{top} , ϕ and $f_{nCombAir}$ and the two least estimable parameters are f_{prx} and f_{ctube} . The adjustable factor for the tube-to-process-gas convective heat transfer coefficient (f_{htg}) is the most estimable parameter and the importance of α_{top} increases as the heat release-length increases. The assumption of a symmetric heat-release parabola was relaxed when estimating the parameters by letting α_{top} take any value that results in a downward-opening parabola.

4.6 Parameter Estimation

The parameters were estimated using Levenberg-Marquardt method. The single variable Levenberg-Marquardt parameter estimation technique from Numerical Recipes (Press et al. 2002a,b) was adapted to accept multivariate inputs and outputs. To choose the best heat-release length, parameter estimation was performed at heat-release lengths of 3.66, 4.27, 4.88, 5.49 and 6.10 m. The heat-release length with the smallest objective function value was deemed to be the

heat-release length that best matches the plant data. A plot of the objective function value vs the number of parameters estimated for the heat-release length of 3.66 m is shown in Figure 34.

Parameter 1 in Figure 34 is f_{htg} , and additional parameters from the ranked list in Table 21 were included to determine the value of the objective function for different numbers of parameters.

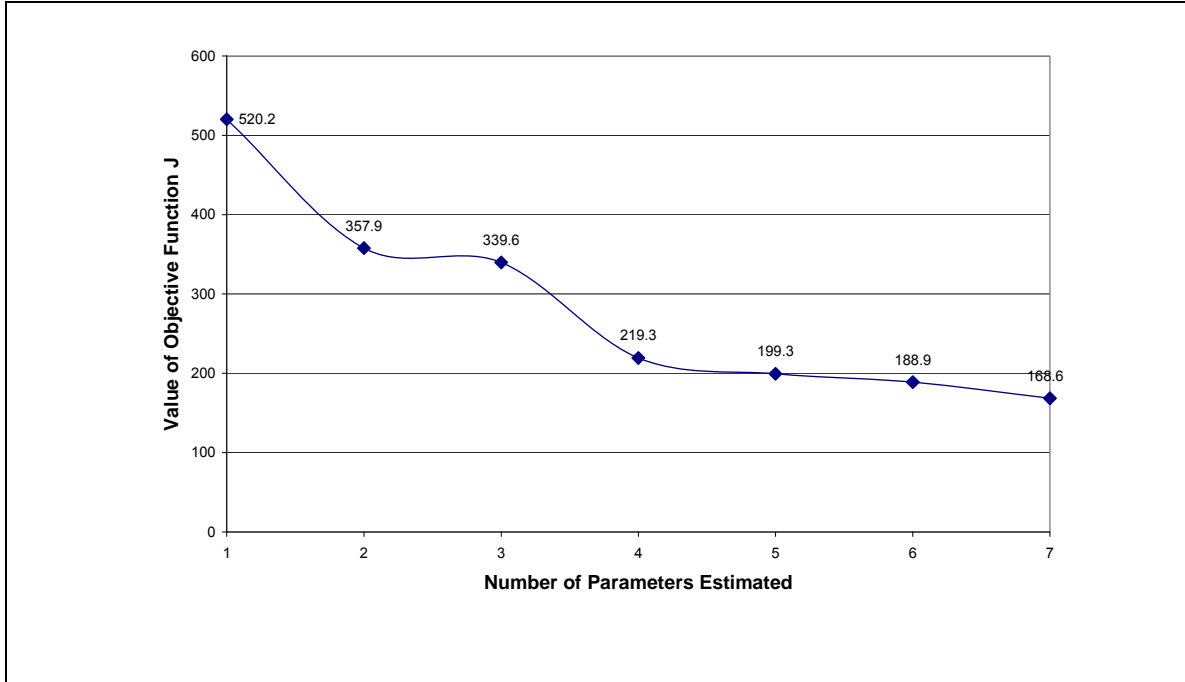


Figure 34. Plot of the Objective Function Value vs the Number of Parameters Estimated for a Heat-release Length of 3.66 m.

The parameter ranking for a heat-release length of 4.27 m differs slightly from the parameter rankings for all other heat-release lengths because $f_{nCombAir}$ is not among the top five most-estimable parameters. Estimation of f_{prx} as the fifth-most estimable parameter had no appreciable influence on the objective function value for a heat-release length of 4.27 m (not shown). To be consistent with the parameter rankings at the other heat-release lengths parameter estimation was also performed using $f_{nCombAir}$ as the fifth most estimable parameter. The results are shown in Figure 35.

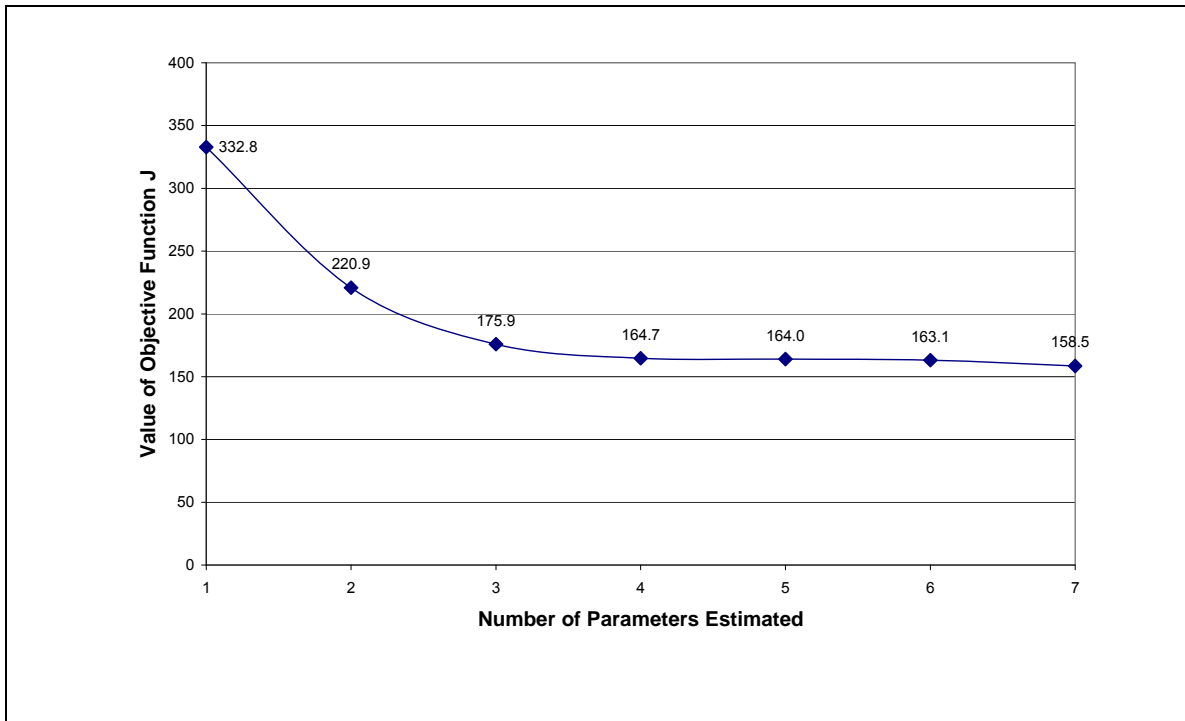


Figure 35. Plot of the Objective Function Value vs the Number of Parameters Estimated for a Heat-release Length of 4.27 m.

Plots of the objective function value vs the number of estimated parameters for heat-release lengths of 4.88, 5.49 and 6.10 m are shown in Figure 36, Figure 37 and Figure 38.

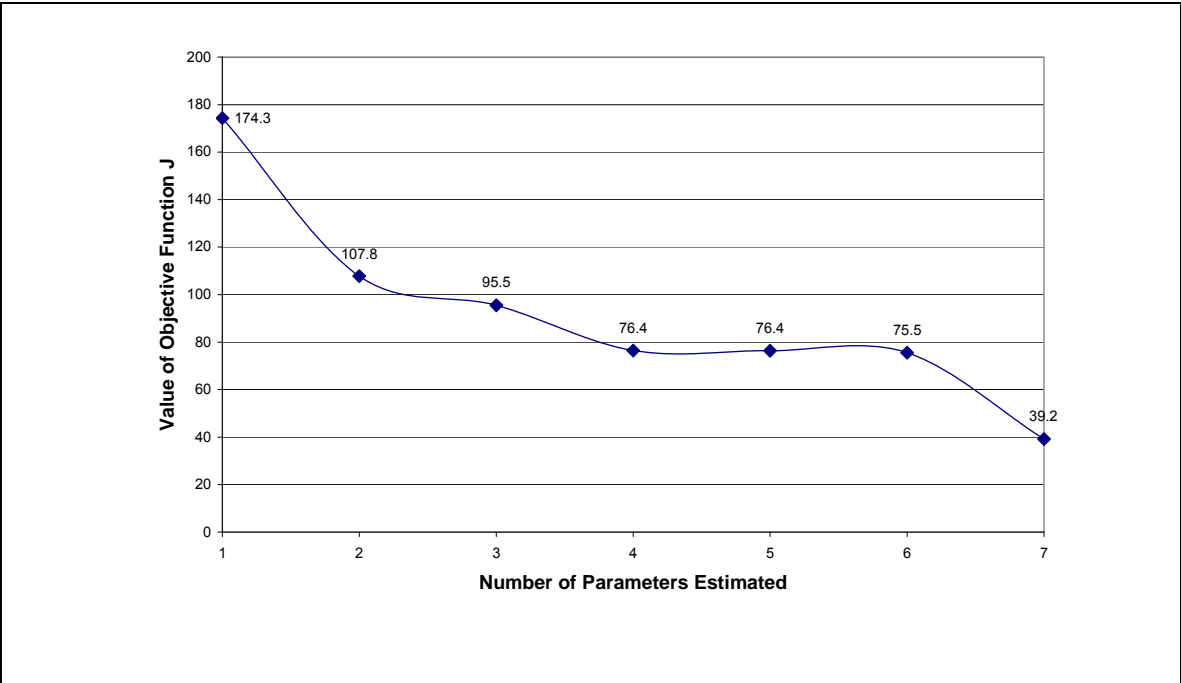


Figure 36. Plot of the Objective Function Value vs the Number of Parameters Estimated for a Heat-release Length of 4.88 m.

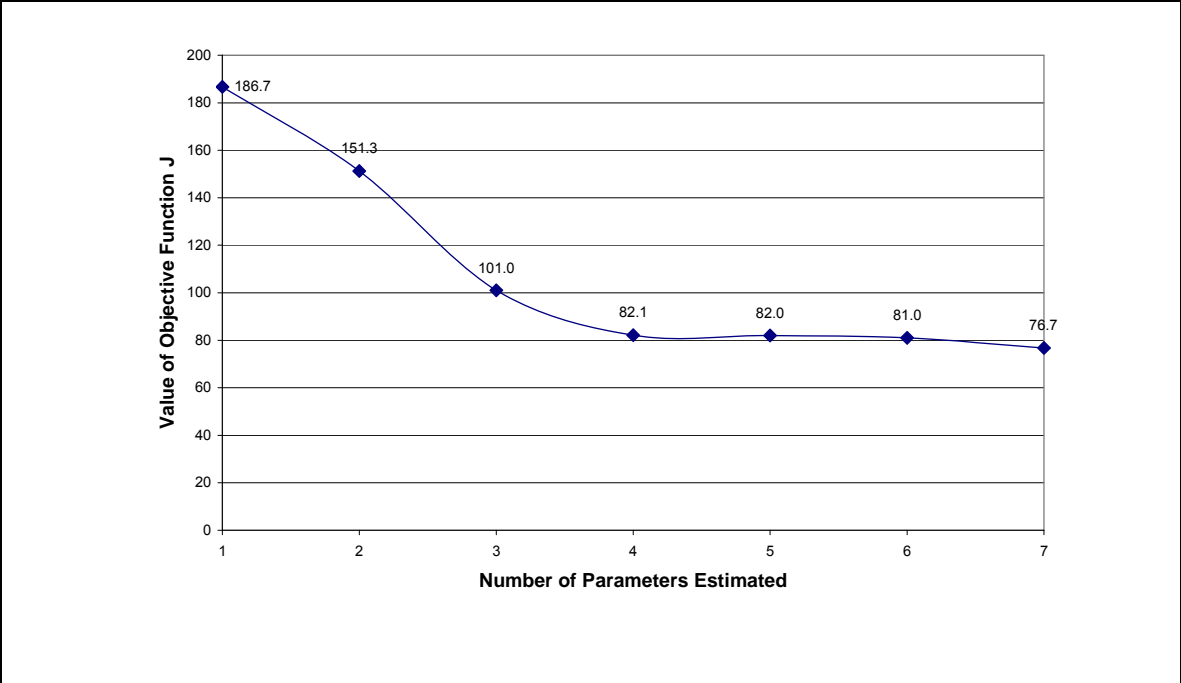


Figure 37. Plot of the Objective Function Value vs the Number of Parameters Estimated for a Heat-release Length of 5.49 m.

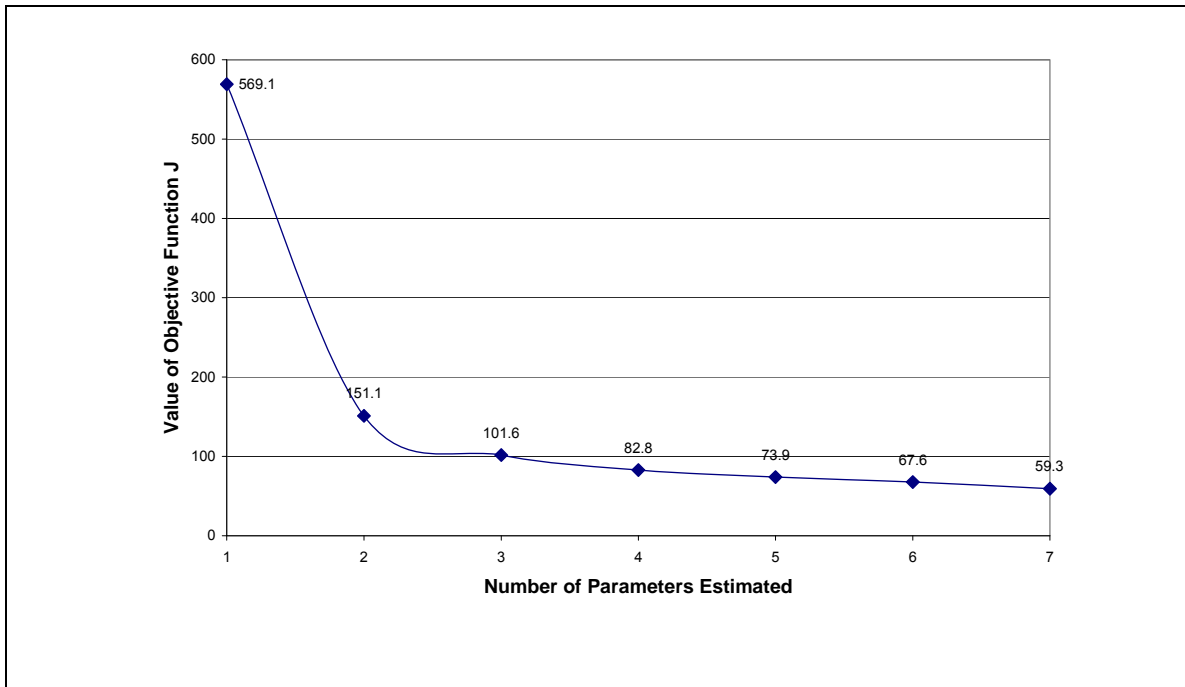


Figure 38. Plot of the Objective Function Value vs the Number of Parameters Estimated for a Heat-release Length of 6.10 m.

The smallest value of the objective function ($J = 39.2$) occurs when the heat-release length is 4.88 m and seven parameters are estimated. However, the value of the parameter f_{ctube} is 0.0004 in the 4.88 m best-fit case. f_{ctube} is the adjustable factor for the furnace-gas-to-tube convective heat transfer coefficient and a value of 0.0004 results in very little convective heat transfer between the furnace-gas and outer-tube wall. Since it is unlikely that convective heat transfer to the tubes is negligible, the parameter estimates that resulted in an objective function value of 39.2 are rejected and the next smallest value of the objective function, which occurs at a heat-release length of 6.10 m with seven estimated parameters, is accepted as the best-fit case. The values of the parameters for the 6.10 m best-fit case are shown in Table 22.

Table 22. Best-Fit Values of the Estimable Parameters, including the Heat-Release Length

Parameter (Symbol) [units]	Best Fit Value
Heat-release Length (L_g) [m]	6.10
Adjustable Factor for Tube-to-process-gas Convective-heat-transfer Coefficient (f_{htg}) [none]	1.680
Fraction of Combustion Enthalpy Released in the Top Furnace-volume Zone (α_{top}) [none]	0.182
Adjustable Factor for the PSA Off-gas Flow Rate ($f_{nOffGas}$) [none]	0.963
Porosity of the Packed Bed (ϕ) [none]	0.607
Adjustable Factor for the Combustion Air Flow Rate ($f_{nCombAir}$) [none]	1.050
Adjustable Parameter for the Pre-exponential Factor of the Reforming Reactions (f_{prx})	0.200
Adjustable Factor for the Furnace-Gas-to-Tube Convective Heat Transfer Coefficient (f_{ctube})	0.381

Although the parameters in Table 22 produced the best-fit between the model outputs and the plant data, any parameter set that produced an objective function value less than 80 was deemed to give an adequate fit. The parameter sets with an objective function value less than 80 were the 4.88 m parameter set when four or more parameters were estimated, the 5.28 m parameter set when seven parameters were estimated and the 6.10 m parameter set when five or more parameters were estimated. An objective function value less than 80 corresponds to a match between the model predictions and the plant data within 7 °C for the process-gas outlet temperature, 27 °C for the furnace-gas outlet temperature, 12 °C for the upper and lower peep hole temperatures and 0.0044 for the wet mole fraction of methane in the process-gas exit stream. The best-fit parameters in Table 22 more accurately matched the process-gas outlet temperature and furnace-gas outlet temperature (within 4 °C for the process-gas outlet temperatures and 4 °C for the furnace-gas outlet temperature).

The temperature profiles predicted by the model using the best-fit parameters in Table 22 and the plant temperature data for Plants A, B, C1 and C2 are shown in Figure 39 to Figure 42. Plant data used to estimate the parameters but not shown in Figure 39 to Figure 42 are shown Table 23. The parameter values and plots for some of the adequate parameter sets are shown in Appendix K.

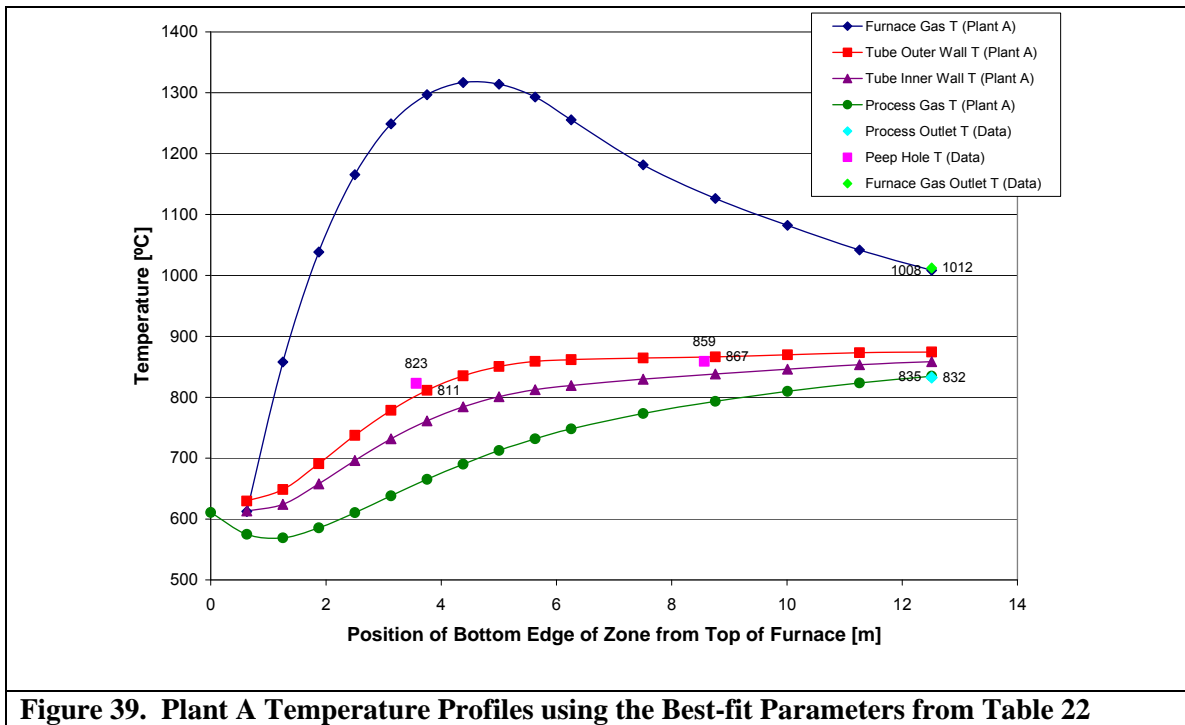


Figure 39. Plant A Temperature Profiles using the Best-fit Parameters from Table 22

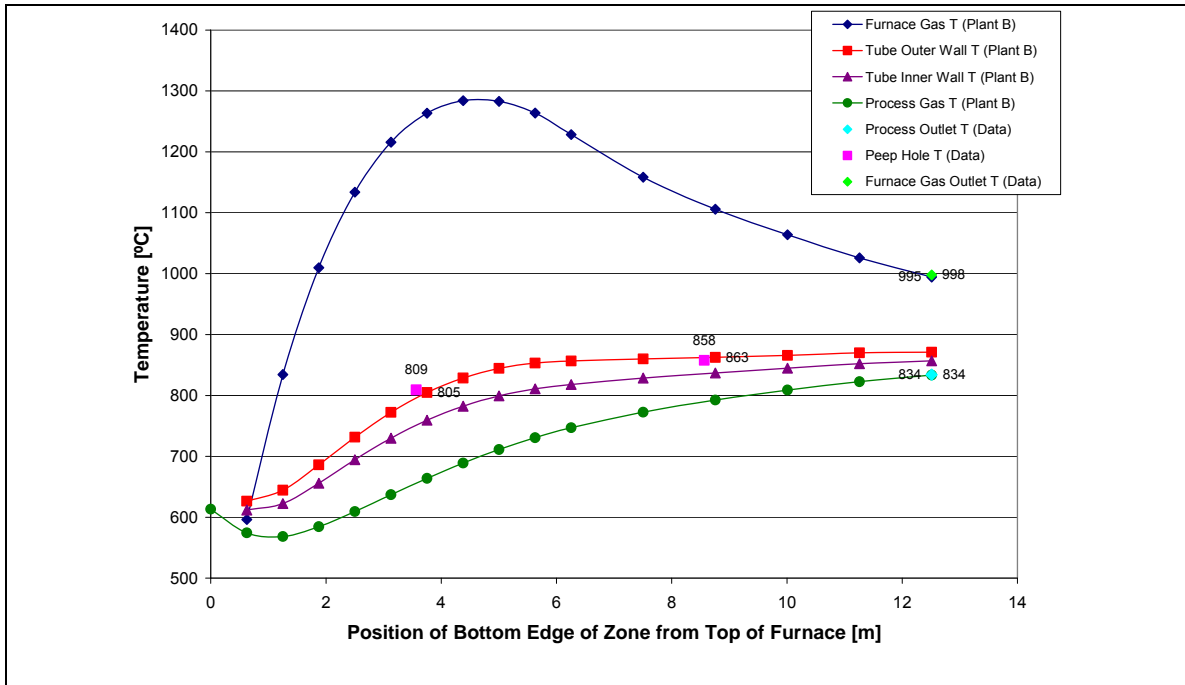


Figure 40. Plant B Temperature Profiles using the Best-fit Parameters from Table 22

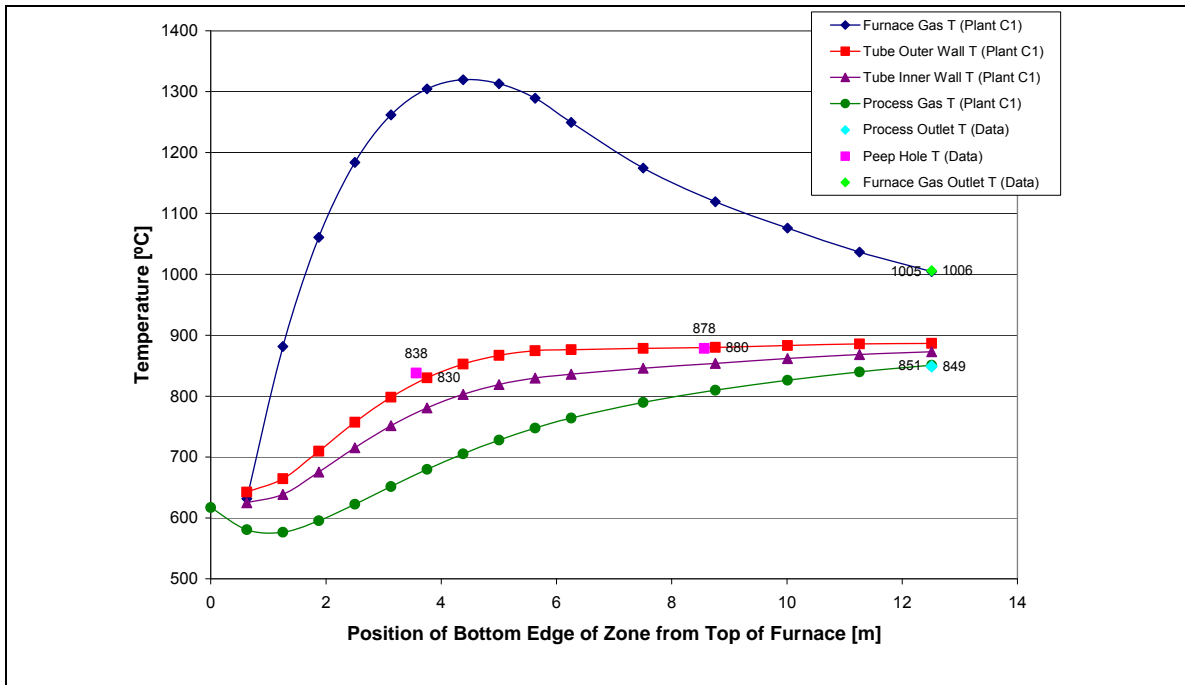


Figure 41. Plant C1 Temperature Profiles using the Best-fit Parameters from Table 22

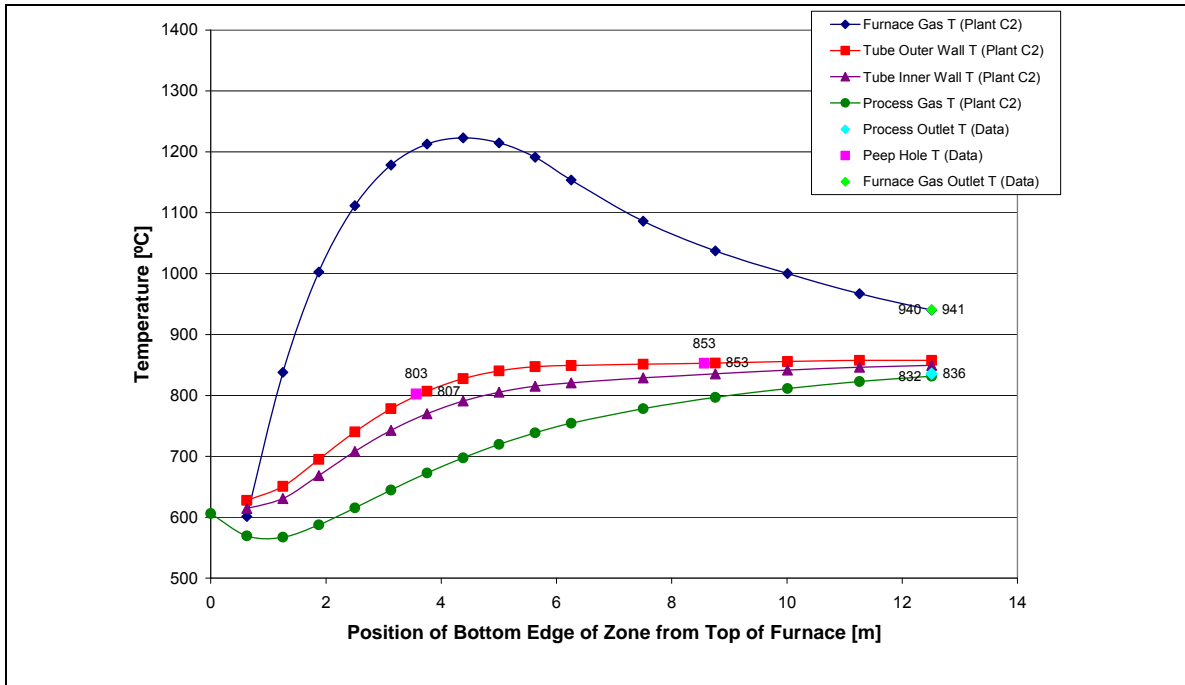


Figure 42. Plant C2 Temperature Profile using the Best-fit Parameters from Table 22

Table 23. Comparison of Model Outputs and Plant Data used in Parameter Estimation but not shown in Figure 39 to Figure 42.

	Plant A		Plant B		Plant C1		Plant C2	
	Plant Data	Model Output	Plant Data	Model Output	Plant Data	Model Output	Plant Data	Model Output
$P_{\text{proc,out}}$ [kPa]	2846.1	2819.4	2879.8	2791.2	2804.0	2869.8	2723.4	2715.8
$\dot{n}_{\text{proc,out}} \left[10^7 \frac{\text{gmol}}{\text{h}} \right]$	1.085	1.080	1.001	0.972	0.978	0.997	0.742	0.737
$X_{\text{H}_2 \text{ proc,out}}$ [none]	0.4582	0.4520	0.4713	0.4560	0.4631	0.4670	0.4655	0.4570
$X_{\text{CO proc,out}}$ [none]	0.0820	0.0810	0.0889	0.0830	0.0845	0.0880	0.0850	0.0820
$X_{\text{CH}_4 \text{ proc,out}}$ [none]	0.0505	0.0530	0.0454	0.0560	0.0526	0.0470	0.0482	0.0530
$X_{\text{N}_2 \text{ proc,out}}$ [none]	0.0005	0.0005	0.0008	0.0010	0.0005	0.0010	0.0010	0.0010

$X_{\text{CO}_2 \text{ proc, out}}$ [none]	0.0582	0.0580	0.0559	0.0570	0.0575	0.0550	0.0574	0.0580
$X_{\text{H}_2\text{O proc, out}}$ [none]	0.3506	0.3560	0.3377	0.3470	0.3417	0.3410	0.3430	0.3500

The temperature profiles in Figure 39 to Figure 42 and the data in Table 23 show that the model adequately matches the upper and lower peep-hole temperatures and the process-gas outlet temperature, pressure, composition and flow rate. Since these criteria were identified by the company as important data to match, the model successfully simulates the SMR considered in this study.

The best-fit between the model outputs and plant data occurred at a heat-release length of 6.10 m when seven parameters were estimated. An adequate fit was achieved at heat-release lengths of 4.88 m when four or more parameters were estimated, 5.49 m when seven parameters were estimated and 6.10 m when five or more parameters were estimated. Heat-release lengths of 3.66 and 4.27 m resulted in the poorest fit between the model outputs and the plant data. To better estimate the parameter values more information such as outer-tube-wall temperature measurements at different elevations, furnace-gas temperature measurements, information about the heat-release length or furnace-wall temperature measurements are needed. To ensure that the parameter estimates are accurate over a range of operating conditions data collected at different plant rates should be used to fit the model. The data for Plants A, B and C1 were collected at plant rates of 99, 92 and 96 percent of the plant capacity, respectively, while the plant rate was 71 per cent when the data for Plant C2 were collected.

4.7 References

Davis, J. R. (2000) Alloy Digest Sourcebook: Stainless Steel. ASM International.

Reid, C. R., Prausnitz, J. M. and Sherwood, T. K. (1977) The properties of Gases and Liquids. McGraw-Hill Book Company, New York, NY.

Katalco (2005) 23-4Q Steam Reforming Catalyst Product Bulletin. Johnson Matthey Catalysts. Oakbrook Terrace, Illinois.

Kou, B., McAuley, K. B., Hsu, C. C., Bacon, D. W. and Yao, K. Z. (2005) Mathematical model and parameter estimation for gas-phase ethylene homopolymerization with supported Metallocene Catalyst. Industrial and Engineering Chemistry Research. vol. 44 pp. 2428-2442.

Press, W. H., Teukolsky, S. A., Vetterling, W. T., Flannery, B. P. and Metcalf, M. (2002a) Numerical recipes in Fortran 90: The Art of Scientific Computing. Cambridge University Press, New York, NY.

Press, W. H., Teukolsky, S. A., Vetterling, W. T. and Flannery, B. P. (2002b) Numerical recipes code cdrom v 2.10. Cambridge University Press, New York, NY.

Taylor, P. B. and Foster P. J. (1974) The total emissivities of luminous and non-luminous flames. International Journal of Heat and Mass Transfer. vol. 17 pp. 1591-1605.

Twigg, M. V. (1989) Catalyst Handbook 2nd edition. Wolf Publishing Limited, London, England.

Yao, K. Z., Shaw, B. M., Kou, B., McAuley, K. B. and Bacon, D. W. (2003) Modeling of ethylene/butane copolymerization with multi-site catalyst: parameter estimability and experimental design. Polymer Reaction Engineering. vol. 11 pp. 563-588.

Wesenberg, M. H. and Svendsen, H. F. (2007) Mass and heat transfer limitations in a heterogeneous model of a gas-heated steam reformer. Industrial and Engineering Chemistry Research. vol. 46 pp. 667-676.

Xu, J. and Froment, G. F. (1989a) Methane steam reforming, methanation and water-gas shift: I Intrinsic Kinetics. AIChE Journal. vol. 35 pp. 88-96.

Chapter 5

Conclusions and Recommendations

5.1 Conclusions

A mathematical model of a steam-methane reformer was developed for on-line simulation and monitoring of tube-temperature profiles in an industrial setting. The model simulates important chemical and physical phenomena in the SMR by dividing the furnace and process sides of the reformer into discrete zones, which are assumed to have uniform composition and temperature. Energy and material balances are performed on the zones producing 226 non-linear algebraic equations with 226 unknowns. Radiative-heat transfer on the furnace side is modeled using the Hottel Zone Method (Hottel and Sarofim, 1967). The program RADEX (Lawson and Ziesler, 1996) is used to calculate total-exchange areas. The 226 equations are solved numerically. The model is designed to run online and has a solution time of less than 4 minutes starting from a reasonable initial guess that can be determined automatically from plant data.

The model calculates temperature profiles for the outer-tube wall, inner-tube wall, furnace gas and process gas. Reformer performance ratios of industrial interest and composition profiles are also computed. The model inputs are the reformer inlet-stream conditions, the geometry and material properties of the furnace and the catalyst-bed.

The model outputs were fit to plant data by adjusting the values of seven poorly known parameters. The impact of the parameters on the model outputs were ranked using the estimability analysis technique of Kou et al. (2005) and the parameters were estimated using a

multivariate Levenberg-Marquardt Method (Press et al., 2002a). Four data sets from three industrial plants with identical geometry were used to estimate the parameters.

The model can be used online to monitor reformer performance and is suitable for inclusion in a real-time optimization scheme. The model can be used offline to assess reformer performance under different scenarios or to calculate uncertain reformer inputs, such as the combustion air flow rate, from reliable outputs, such as the reformer process-gas outlet temperature.

Development of the model proceeded in stages to aid in equation development and code debugging. Reasonable solutions were obtained for a simple cube furnace model and a single tube in a rectangular furnace before proceeding to the complete furnace geometry.

Two validation studies were performed on the program RADEX using simple geometries: i) a cube enclosure containing gray gas and ii) a tube in rectangular furnace enclosure containing a clear gas. Direct-exchange areas computed by RADEX agreed within 8% of the numerical values computed by Hottel and Sarofim (1967) for the cube furnace furnace. View factors computed by RADEX agreed within 1% of values computed by analytical integration (Sparrow and Cess, 1978) for the furnace containing a tube. Increasing the number of rays simulated by RADEX (beyond 20 000 rays per m^2) did not improve the agreement.

When simulating the SMR, 200 000 rays per m^2 were used in RADEX to compute the total-exchange areas. Using additional rays did not result in an appreciable change in the values of the total-exchange areas.

A numerical study was performed to examine the influence of vertical zoning on simulated temperature and composition profiles in the SMR model. Profiles with 10, 20 and 40 equally sized vertical zones were computed. No significant benefit was observed when 40 rather than 20 vertical zones were used. In the 10-vertical-zone profile, the larger spacing was adequate for the bottom half of the reformer but not the top half where concentration and temperature gradients are large. To achieve an appropriate balance between runtime and profile detail and accuracy, a model with ten zones in the top half and five in the bottom half was adopted. This model resulted in 15 vertical sections requiring 226 equations and 226 unknowns.

The five most estimable parameters in the SMR model are f_{htg} (the adjustable factor for the tube-to-process-gas convective heat transfer coefficient), α_{top} (the fraction of combustion heat released in the top furnace volume zone), $f_{nOffGas}$ (the adjustable factor for the PSA off-gas flow rate), ϕ (the catalyst bed porosity) and $f_{nCombAir}$ (the adjustable factor for the combustion air flow rate). The relative importance of these parameters changes with the assumed heat-release length. α_{top} becomes a more sensitive parameter as the heat-release length increases. The two least estimable parameters are f_{prx} (the adjustable parameter for the pre-exponential factor of the reforming reactions) and f_{ctube} (the adjustable factor for the furnace-gas-to-tube convective heat transfer coefficient).

The best-fit between the model outputs and plant data occurred at a heat-release length of 6.10 m when seven parameters were estimated. The process-gas outlet temperatures were matched within 4 °C, the upper and lower peep-hole temperatures within 12 °C and the furnace-gas outlet temperature within 4 °C. The process-gas outlet pressure, composition and flow rate are also

accurately matched by the model. An acceptable fit between the model outputs and plant data can also be obtained at heat-release lengths of 4.88, 5.49 and 6.10 m.

5.2 Recommendations

This section outlines the work that is recommended to make the model usable by plant operators and to develop confidence in the model predictions. In addition, future work is described to enable development of more specialized versions of the model with enhanced capabilities.

1. To make the current model usable by plant operators, an interface between the plant inputs and the model needs to be created and the model runtime may need to be improved.

To run the reformer model online, a program that interfaces between the Visual Basic model and the online plant data needs to be developed. This task is complicated by the fact that some of the plant data that are inputs to the average-tube model are known with poor confidence, for example the flow rates of the off-gas and combustion air, which are inputs to the current model. The average-tube model is structured to accept reformer inputs and calculate profiles and outputs from those inputs. To use the average-tube model to back-calculate uncertain inputs, the model would need to be solved iteratively. The current runtime of the model is approximately 4 minutes on a 2.8 GHz Intel Pentium 4 processor with 2GB of RAM starting from a poor initial guess. For online use, the model run time could be reduced.

There is considerable opportunity to make the model code more efficient. The average-tube model was developed with the intention of being extended for modeling classes of tubes (See Figure 43). As a result, the geometry storage and searching functions used in the current average-

tube model are more detailed than needed. The model code could be made more efficient by simplifying geometry storage and searching functions so that all zones on the furnace side are referenced by only their vertical section instead of a Cartesian reference coordinate (See Appendix F for details of geometry storage and reference coordinates). Also, the code for the average-tube model was written by a chemical engineer with limited software-writing experience. Strict syntax, program structure and naming rules used to develop commercial software programs were not applied to the average-tube mode. It is recommended that a software professional be consulted to improve the efficiency and structure of the code before it is applied for commercial purposes.

The slowest step in solving the model equations is numerical calculation of the Jacobian matrix. The Jacobian is a 226 by 226 matrix that contains partial derivatives of the model equations with respect to the model unknowns (see Appendix D). In the current code, a forward-difference method is used to calculate the elements of the Jacobian, resulting in many function calls that increase the computation time. There are three feasible ways to reduce the Jacobian calculation time. The first way to reduce model runtime is to reduce the number of equations in the average-tube model. This can be done by combining the furnace refractory wall zones at a given elevation into a single zone. Model runtime would be reduced because the number of equations and unknowns is reduced. The second way to reduce model runtime is to implement a more advanced numerical method to evaluate the elements of the Jacobian or to use an analytical Jacobian instead of a numerical Jacobian. Analytical Jacobians requires fewer function calls than numerical Jacobians. To calculate an analytical Jacobian, the model equations must be differentiated analytically by the model unknowns and the resulting equations coded into Visual Basic. Differentiating 226 equations by 226 unknowns manually is not practical, however the

model equations can be readily coded into a commercial software package such as Maple (Maplesoft, 2008) that will differentiate the model equations and convert the derivatives into Visual Basic code. This technique was implemented successfully in the earlier stages of this project (cube-furnace model) but was not used during the development and debugging of the segmented-tube or average-tube models. It is expected that using analytical derivatives will substantially reduce the computation time. The third way to improve runtime is to parallelize the calculation of the Jacobian elements. The calculation of one element of the Jacobian is independent of the calculation of other elements. To improve model runtime, the calculation of different elements can be distributed over multiple central processing units (CPUs). For example one CPU could calculate half of the Jacobian elements while another simultaneously calculates the remaining half.

2. To validate and improve the model predictions, more plant data should be acquired and used to fit the model parameters, and careful studies should be performed to further verify the exchange areas computed by RADEX.

To improve the reliability of the model parameters and the predictive ability of the model, additional plant data should be used to fit the model parameters and to test the model predictions. In this project four data sets, three of which are at a plant rate near 100%, were used to fit the model parameters. Supplementing the existing plant data with additional data sets at different plant rates and operating conditions will give better estimates of the parameter values and will provide a better test of the validity of the model.

One use of the reformer model developed in this thesis is to monitor the outer-tube-wall temperature. However, in the plant data only two outer-tube-wall temperature measurements are available, one located at 3.57 m from the top of the reformer (measured from the upper peep door) and one at 8.56 m from the top (measured from the lower peep door). These tube wall temperatures are averages for several different tubes. Better parameter estimates could be determined if temperature measurements were available at more elevations.

If measuring the outer-tube wall temperature at more elevations is not possible, the model parameters could be fitted using other furnace measurements that are more easily acquired. For example the furnace-refractory temperature profile or the furnace-gas temperature profile might be easier to measure than the outer-tube-wall temperature profile and could be used to fit the model parameters and to gain a better understanding of poorly known furnace phenomena such as the heat-release length.

To verify the model predictions, a more detailed validation of the program RADEX should be completed. The comparison of the direct-exchange areas calculated by RADEX and by figure 7-13 of Hottel and Sarofim (1968) indicated percentage errors as large as 8% (See Appendix G). It is not known whether these errors are mostly the result of inaccuracies in RADEX or assumptions made by Hottel and Sarofim (1968) when developing figure 7-13 using limited numerical integration tools. The view-factor comparison performed in Appendix G and the findings of Lawson and Zielser (1996) indicate that RADEX does accurately calculate view factors, which are then used to calculate direct and total-exchange areas. To further validate the exchange areas calculated by RADEX, the program outputs could be compared to results from other techniques for calculating total-exchange areas such as those used by Ebrahimi et al. (2008).

3. The model can be adapted to simulate industrial steam-methane reformers with different geometries.

The current model describes a SMR with seven rows of tubes and eight rows of burners. It would be relatively straightforward to adapt the model so that it can simulate different industrial top-fired rectangular SMRs with any number of tubes and burners. The new SMR geometries would need to be entered into RADEX so that the required exchange areas can be computed for use in the model.

4. Simplifying assumptions can be removed and more specialized versions of the model can be developed.

The average-tube model developed in this thesis has the capacity to be developed into more specialized versions. Some suggestions for more specialized models include modeling of separate classes of tubes that are in different radiative environments, and detailed modeling of burner configurations, furnace-gas flow patterns and combustion heat-release patterns. The program RADEX was used in this project to calculate total-exchange areas. Because RADEX is a Monte Carlo ray-tracing program, it is capable of evaluating total-exchange areas for almost any geometric configuration and for many partitions of the geometric configuration. In the current model, RADEX calculates total-exchange areas for zones created by a fine grid and then groups those total-exchange areas into the vertical zones shown in Figure 8 and Figure 9. The grouping of fine-grid-exchange areas into larger exchange areas averages the radiative environments of the fine grid zones. For example, the tube segments in Figure 8 and Figure 9 are assumed to be one zone that experiences the same radiative environment. The fine grid exchange areas could be grouped in different arrangements to model classes of tubes that experience similar

radiative environments. For example, if it is believed that tubes near the furnace wall experience higher outer-tube wall temperatures than internal tubes, the wall tubes could be grouped into one radiative environment and modeled separately from the internal tubes. In Figure 43 the shaded tube segments are wall tubes that could be grouped into one tube zone and the unshaded tube segments are internal tubes that could be treated as a separate tube zone.

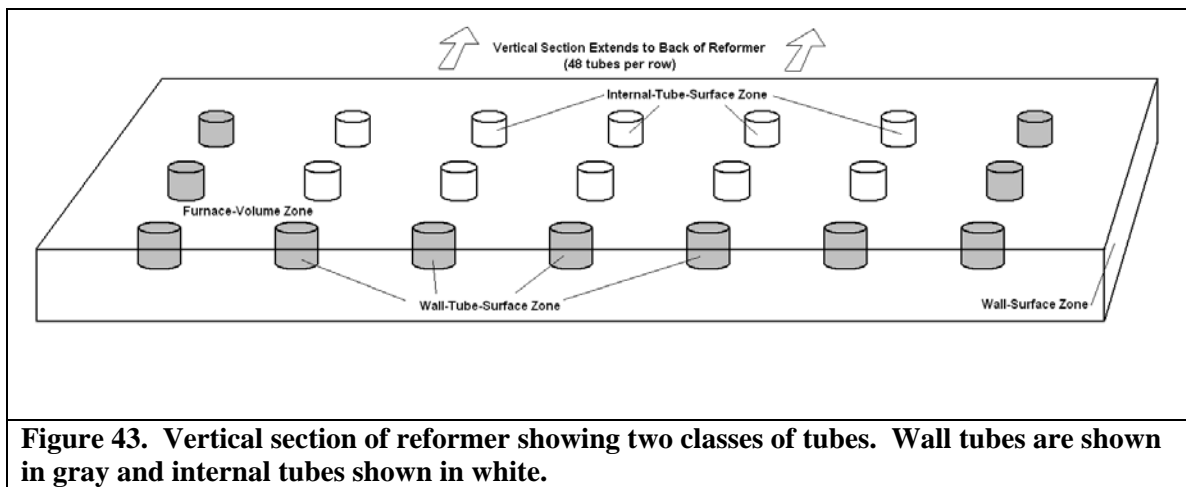
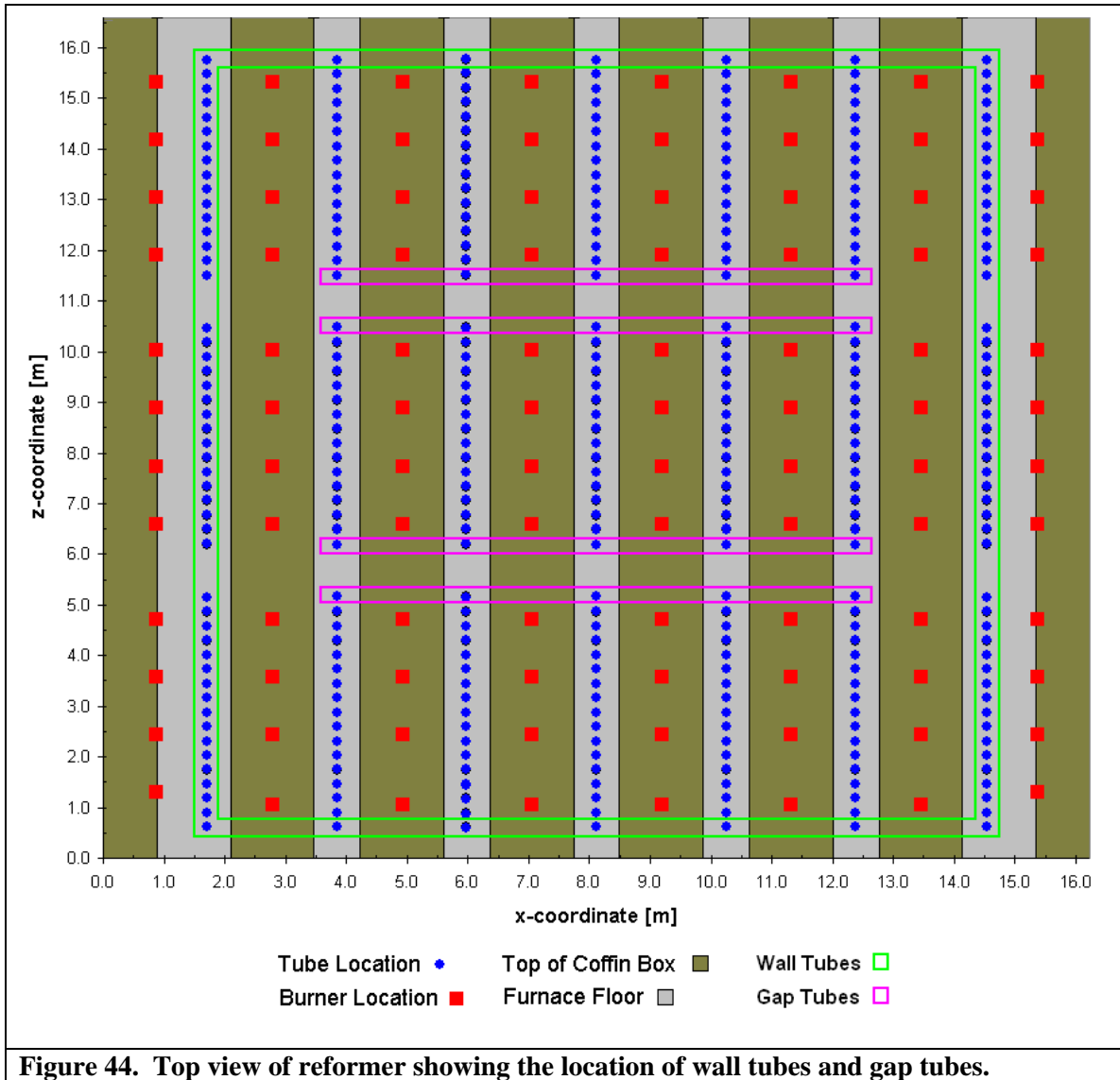


Figure 43. Vertical section of reformer showing two classes of tubes. Wall tubes are shown in gray and internal tubes shown in white.

Another possible interesting class of tube is gap tubes. In the reformers studied in this thesis, there are four gap tubes in each row of tubes. Figure 44 shows a detailed overview of the reformer and highlights the wall tubes and gap tubes. Additional classes of tubes could be identified and modeled as needed.



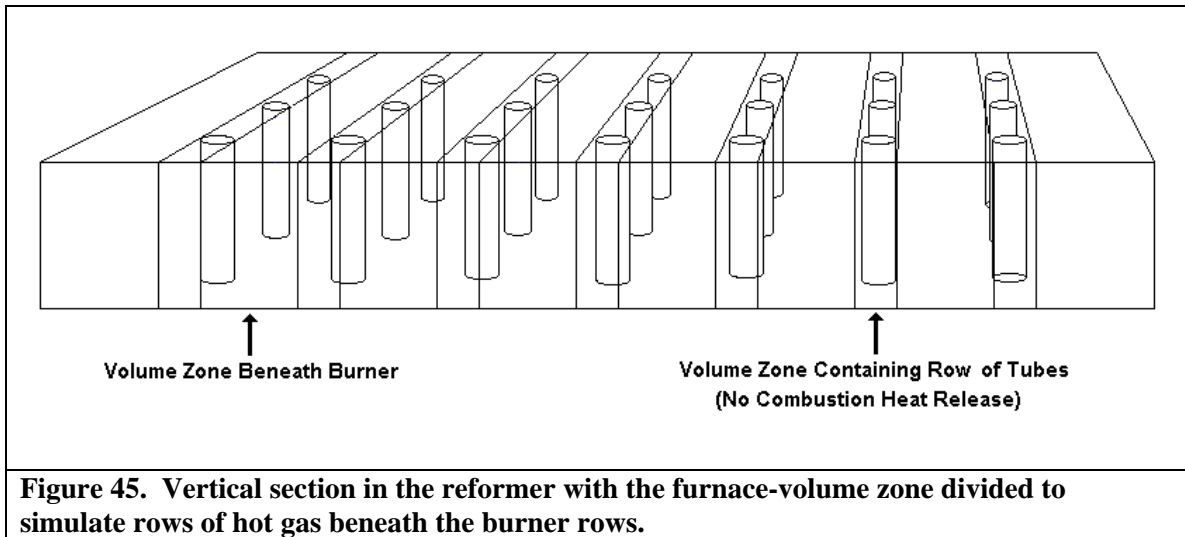
The addition of classes of tubes to the model will increase the number of model equations and unknowns. Adding one class of tubes doubles the number of process-side equations and increases marginally the number of furnace-side equations. It may not be advisable to run the classes of tubes model online unless the runtime of the average-tube mode can be decreased, as described in recommendation 2.

Another improvement that could be added to the model is a more detailed treatment of the furnace gas, which could allow for a more advanced combustion heat-release profile and furnace-gas-flow pattern. The amount of detail that could be added to modeling of the heat-release profile and furnace-gas flow pattern is considerable. The challenge lies in finding reliable data to support the heat-release profile and furnace-gas flow pattern assumptions used in the model and in keeping the solution time below an acceptable limit.

The following suggestions could be implemented immediately in the average-tube model since they do not require adding additional volume zones. In the average-tube model it is assumed that furnace gas enters the top of the reformer and flows to the bottom in perfect plug flow. A simple improvement would be to assume a small amount of backmixing. This backmixing could be added to the model by changing the furnace-volume-zone energy balances. Another simple improvement would be to change the heat-release profile from the parabolic profile used in the average-tube model to a different empirical profile like that used by Ebrahimi et al. (2008). The sensitivity analysis in Chapter 4 indicates that the average-tube model is sensitive to changes in the heat-release profile. Simulations with different heat-release profiles may provide a better match between the model and plant data.

The following suggestions are more advanced methods for making the heat-release pattern and furnace-gas flow pattern assumptions more realistic. They require some model restructuring to account for new types of furnace volume zones. In the average-tube model, the furnace gas is assumed to have uniform temperature within a vertical zone. In reality, the hottest furnace gas would be located directly beneath the rows of burners. RADEX is capable of partitioning the furnace gas into additional zones to better account for the non-uniform temperature distribution in

the furnace gas. Figure 45 shows a vertical section of the reformer with volume zones added below the rows of burners. The tubes are contained within separate volume zones. The furnace-gas volume zones containing tubes would not directly receive heat from the combustion of furnace fuel but instead would receive heat by radiation and the bulk motion of furnace gas.



The more detailed partitioning of the furnace gas would allow for both vertical and horizontal flow patterns to be added to the model. The vertical and horizontal flow patterns must be explicitly defined. To do this, predicted flow patterns computed from computational fluid dynamics studies could be used in the model or simple assumptions could be used to impose simple flow patterns. The furnace gas could be further divided to account for the exact location of individual burners.

5. A sensitivity study should be conducted to investigate the influence of reformer geometry on model predictions.

In this thesis, the segmented-tube model was an intermediate phase in the development of the average-tube model. The main difference between the segmented-tube model and the average-tube model is the addition of detailed reformer geometry. The benefit of the detailed geometry added to the average-tube model has not been quantified. For example, how accurate are the predictions from a segmented-tube model that contains one tube with an effective area equal to the area of 336 reformer tubes? Another way to test the model sensitivity to geometry is to alter the furnace geometry and look for changes in the profiles produced by the average-tube model. For example if several tubes are removed and the reformer inputs are scaled accordingly is there any noticeable change in the predicted profiles or reformer outputs? The latter geometric-sensitivity analysis is easy to perform using the average-tube model but may not produce noticeable results, since the average-tube model combines the radiative environments of all the tubes at a given elevation in the furnace (See Figure 8). More complex versions of the model should be used (See recommendation 4) if detailed and reliable information about the influence of reformer geometry is required.

5.3 References

Ebrahimi, H., Mohammadzadeh, J. S. S., Zamaniyan, A. and Shayegh, F. (2008) Effect of design parameters on performance of a top fired natural gas reformer. *Applied Thermal Engineering*. vol. 28 pp. 2203-2211.

Hottel, H. C. and Sarofim, A. F. (1967) *Radiative Heat Transfer*. McGraw-Hill Book Company.

Kou, B., McAuley, K. B., Hsu, C. C., Bacon, D. W. and Yao, K. Z. (2005) Mathematical model and parameter estimation for gas-phase ethylene homopolymerization with supported Metallocene Catalyst. *Industrial and Engineering Chemistry Research*. vol. 44 pp. 2428-2442.

Lawson, D. A. and Ziesler, C. D. (1996) An accurate program for radiation modeling in the design of high-temperature furnaces. *IMA Journal of Mathematics Applied in Business and Industry*. vol. 7 pp. 109-116.

Maplesoft. (2008) *Maple 12.0: The essential tools for mathematics and modeling*. Waterloo Maple Inc.

Press, W. H., Teukolsky, S. A., Vetterling, W. T., Flannery, B. P. and Metcalf, M. (2002a) *Numerical recipes in Fortran 90: The Art of Scientific Computing*. Cambridge University Press, New York, NY.

Appendix A

Radiative Heat Transfer Background

The definitions and equations presented in this Appendix are designed to provide enough background information to understand the Hottel Zone method as it applies to this thesis. Many important radiative heat-transfer details are omitted from this section. A more thorough explanation of the radiative heat transfer theory is available in the references provided at the end of Appendix A.

Definition of a Blackbody

A blackbody is a surface that acts as a perfect emitter and absorber of radiation. Planck's law states that there is a maximum amount of radiant energy that can be emitted from a surface at a given temperature and wavelength (Sparrow and Cess, 1978; p. 5). The maximum radiant energy emitted from a surface per wavelength, per unit time and per area is defined as the monochromatic blackbody emissive power:

$$E_{b,\lambda} = f(T,\lambda) \left[\frac{\text{energy}}{\text{time} \cdot \text{wavelength} \cdot \text{area}} \right] \quad (63)$$

where the $f(T,\lambda)$ is provided by Sparrow and Cess (1978) and in many other textbooks. The total blackbody emissive power (E_b) is the maximum amount of energy that can be emitted from a surface at a given temperature over all wavelengths (Sparrow and Cess, 1978; p. 8). It is calculated by integrating the spectral emissive power over all wavelengths as shown in equation (64).

$$E_b(T) = \int_{\lambda=0}^{\lambda=\infty} E_{b,\lambda} d\lambda \left[\frac{\text{energy}}{\text{time} \cdot \text{area}} \right] \quad (64)$$

The integral in equation (64) results in the Stefan-Boltzman equation (65).

$$E_b(T) = \sigma T^4 \quad (65)$$

The Stefan-Boltzman equation gives the total black emissive power of a surface as a function of its temperature.

Gray Surfaces, Surface Absorptivity and Surface Emissivity

A gray surface is an imperfect emitter and absorber. Gray surfaces absorb and emit all wavelengths of electromagnetic radiation but absorb and emit only a fraction of the radiant energy of a blackbody (Howell and Siegel, 1972; p. 64). The ratio of the radiant energy absorbed by a gray surface to the energy absorbed by a blackbody is the surface absorptivity (α_s).

Likewise, the ratio of radiant energy emitted by a gray surface to the energy emitted by a blackbody is the surface emissivity (ϵ_s). The surface emissivity and absorptivity can have values ranging from 0 to 1.

Surface Reflectivity

The surface reflectivity (ρ_s) is related to surface absorptivity. If a surface is a perfect absorber, then all incident radiant energy is absorbed. If the surface is not a perfect absorber (meaning it is

a gray surface), then only a fraction of the incident radiation is absorbed. The unabsorbed incident radiation is reflected back into the adjacent media. The fraction of incident radiation that is reflected is the reflectivity. The absorptivity and reflectivity of a gray surface must sum to one (Hottel and Sarofim, 1960 p. 125)

$$\rho_s + \alpha_s = 1 \quad (66)$$

Definition of Solid Angle

A solid angle is a three-dimensional angle that is measured in steradians, where steradians are analogous to radians, which are used to measure two-dimensional angles. A radian is the ratio of arc length to radius of the arc, so that 2π radians are a complete circle. A solid angle is the ratio of the spherical surface area enclosed by a three dimensional arc to the radius of the arc squared. A solid angle is defined so that 4π steradians is a complete sphere. In radiative heat transfer, solid angles are used to quantify field of view. If two obstacles have the same solid angle for a given viewing point, they occupy the same fraction of the field of view, regardless of their distance from the viewing point.

Radiation Intensity

The monochromatic intensity (I_λ) is the radiant energy traveling in the direction of radiation propagation, per unit area of emitter, per unit solid angle, per unit time, per wavelength (Sparrow and Cess, 1972; p. 8). Radiation intensity is a vector property. The direction of propagation of

the radiation ray in Figure 46 is in the direction defined by azimuthal angle ϕ and zenith angle θ .

The intensity is the magnitude of the vector.

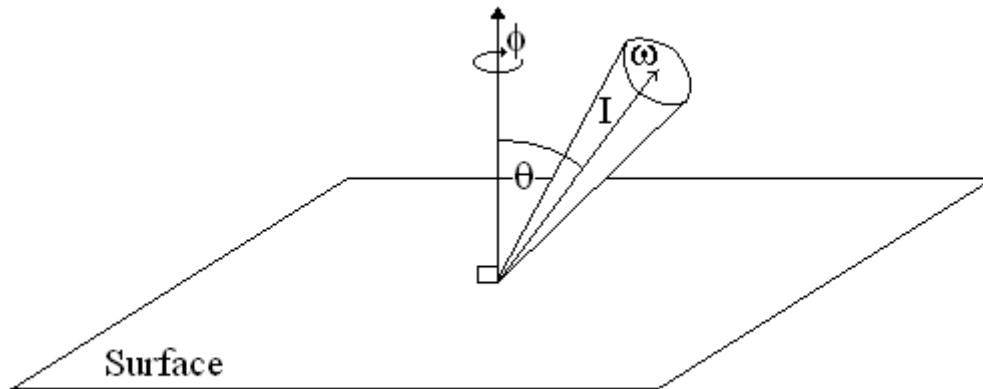


Figure 46. Geometry of a Ray of Radiation

The total intensity (I) is found by integrating over all wavelengths as shown in equation (67).

$$I = \int_{\lambda=0}^{\lambda=\infty} I_{\lambda} d\lambda \quad \left[\frac{\text{energy}}{\text{area} \cdot \text{time} \cdot \text{solid angle}} \right] \quad (67)$$

Radiant energy flux (q) in the direction of radiation propagation is found by integrating the intensity over the solid angle ω shown in Figure 46 (Sparrow and Cess, 1972; p. 8).

$$q = \int I d\omega \quad \left[\frac{\text{energy}}{\text{area} \cdot \text{time}} \right] \quad (68)$$

Diffuse Surfaces

A diffuse surface is a surface that emits, absorbs and reflects radiation with equal intensities in all directions. In Figure 47 the magnitude of the total intensity (I) emitted from a point on the surface is equal in all directions (ϕ, θ) (Howell and Siegel, 1972; p. 64).

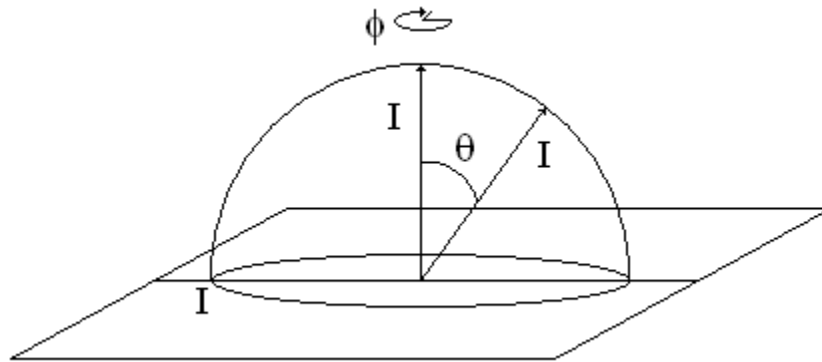


Figure 47. A Diffuse Emitter

Gas Emissivity and Absorptivity

Surface emissivity (ϵ_s) is the ratio of energy emitted from a gray surface to the energy emitted from a black surface. The same definition holds true for gas emissivity (ϵ_g), except that the emission of radiant energy from a gas occurs over a volume instead of an area. Consider the radiant energy emitted by an isothermal volume of gas over a fixed length lying in a specified field of view to and an area of its bounding surface as shown in Figure 48. The gas emissivity is the ratio of radiant energy incident on the bounding surface from the volume of gas to the energy incident on the surface from a black emitter with the same temperature and same field of view as the gas (see Figure 48) (Hottel and Sarofim, 1967; p. 203).

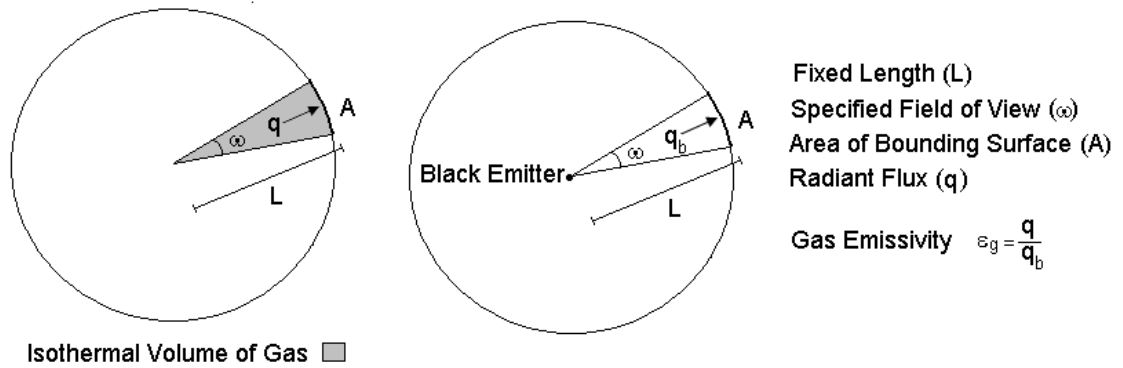


Figure 48. Definition of Gas Emissivity

Gas absorptivity is the fraction of radiant energy absorbed by an isothermal volume of gas over a fixed path length and specified field of view when the radiation is emitted by a black source (see Figure 49) (Hottel and Sarofim, 1967 p. 203).

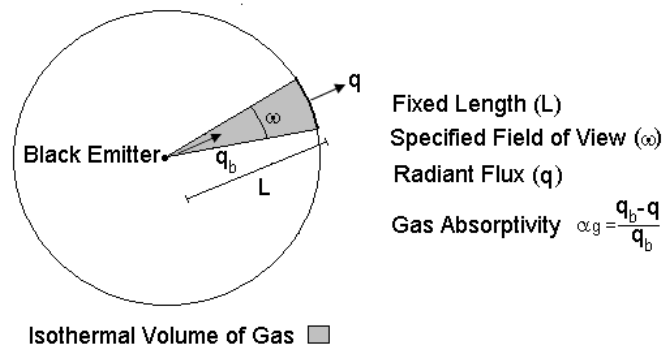


Figure 49. Definition of Gas Absorptivity

If the volume of gas was a perfect absorber (a black media), none of the incident radiation would exit the volume of gas and the absorptivity of the gas would be one.

Gas Transmissivity

Transmissivity (τ) is the fraction of radiation that passes through an isothermal volume of gas (Rhine and Tucker, 1991; p. 201). Transmissivity for gases is analogous to reflectivity for surfaces, because radiation that passes through a volume of gas is either absorbed or transmitted, provided that the gas is a non-scattering medium. The absorptivity and transmissivity of a gas must sum to one.

$$\tau + \alpha = 1 \quad (69)$$

In Figure 49, the transmissivity can be expressed as the ratio of radiant energy exiting the volume of gas to radiant energy incident on the volume of gas or the ratio of exiting intensity to incident intensity (70).

$$\tau = \frac{q}{q_b} = \frac{I}{I_b} \quad (70)$$

Gray Gases

Bouguer's law (71) states that radiation intensity is attenuated in proportion to its intensity (Hottel and Sarofim, 1960; p. 201). The proportionality constant (K) is known as the absorption coefficient.

$$\frac{dI}{dx} = -KI \quad (71)$$

A gray gas is defined as having an absorption coefficient (K) that is independent of radiation wavelength (Howell and Siegel, 1972; p. 444). If the gray-gas assumption is applied to Bouguer's attenuation law the intensity at any penetration depth (x) can be calculated by separating variables and integrating equation (71) from $I = I_0$ to I and $x = 0$ to x:

$$I = I_0 \exp(- Kx) \tag{ 72}$$

The resulting equation is used to relate the absorption coefficient of a gray gas to its absorptivity and transmissivity (Rhine and Tucker, 1991; p. 201):

$$\tau = 1 - \alpha = \frac{I}{I_0} = \exp(- Kx) \tag{ 73}$$

Kirchoff's Law

Kirchoff's law states that the emissivity and absorptivity of a system in thermodynamic equilibrium with its surroundings are equal (Howell and Siegel, 1972; p. 59). Consider two bodies, A and B separated by a vacuum and contained in a vessel with a surface of reflectivity of

1. An energy balances on body A results in equation (74)

$$\begin{aligned} \text{Energy Accumulating} &= \text{Energy Emitted} - \text{Energy Absorbed by} \\ \text{in A} &= \text{by A} - \text{A from B} \end{aligned} \tag{ 74}$$

$$0 = \epsilon_A \sigma T_A^4 - \alpha_A \sigma T_B^4$$

In thermodynamic equilibrium $T_A = T_B$. For equation (74) to evaluate to zero, ϵ_A must be equal to α_A . It is found experimentally that surface emissivity and absorptivity are only weak functions of surface temperature and radiation wavelength (Rhine and Tucker, 1991; p. 197). As a result, surface emissivity and absorptivity are treated as physical properties that are equal to each other and that are constant over large ranges of temperature. This result for surfaces can be extended to gray gases. Equation (73) can be solved for the absorptivity of a gray gas, which is independent of wavelength and temperature. For the emissivity and absorptivity of a gray gas to be equal in thermodynamic equilibrium, the emissivity and absorptivity must always be equal to each other. This result allows the emissivity, absorptivity, transmissivity and absorption coefficient for a gray gas to be related:

$$\epsilon = \alpha = 1 - \tau = 1 - \exp(- Kx) \quad (75)$$

Real Gases

Real gases have absorption coefficients that are significantly dependent on the wavelength (Rhine and Tucker, 1991; p. 9). At certain wavelengths the absorption coefficient of the gas is high, meaning that much of the radiant energy of a particular wavelength is absorbed by the gas, while at other wavelengths the radiant energy passes through the gas unabsorbed. This behavior is caused by the discrete rotational and vibrational modes of the gas molecules. This discrete behaviour produces distinct bands on plots of absorption coefficient (K) vs radiation wavelength (λ) as shown in Figure 50 (Rhine and Tucker, 1991; p. 9). Note that Gas A in Figure 50 is a fictional gas mixture. If a gas is composed of multiple species, there will be different sets of

bands for each species and some of these bands may overlap (Rhine and Tucker, 1991; p. 9). The gray gas absorption coefficient is plotted on Figure 50 for comparison.

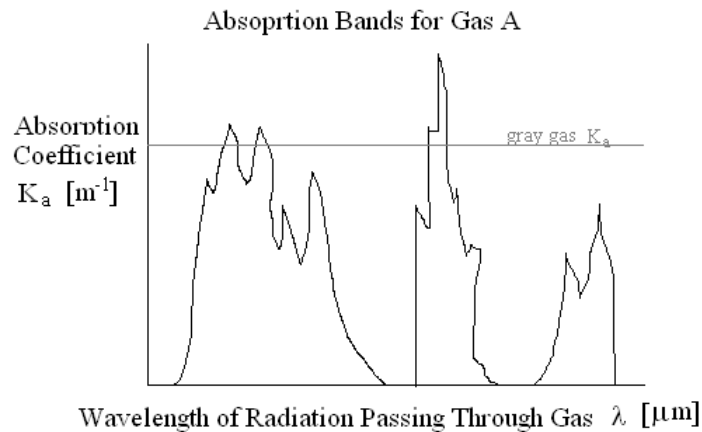


Figure 50. Dependence of Absorption Coefficient on Wavelength

Weighted-Sum-of-Gray-Gases Model

The weighted-sum-of-gray-gases model was developed to apply the mathematically simple properties of gray gases to a real gas. In the weighted-sum-of-gray-gases model, a real gas is represented as a number of gray gases with different absorption coefficients in different wavelength regions (Hottel and Sarofim, 1960; p. 248). Figure 51 shows fictional gas A represented as three gray gases with absorption coefficients K_{a1} , K_{a2} and K_{a3} and one clear gas with absorption coefficient K_{a0} .

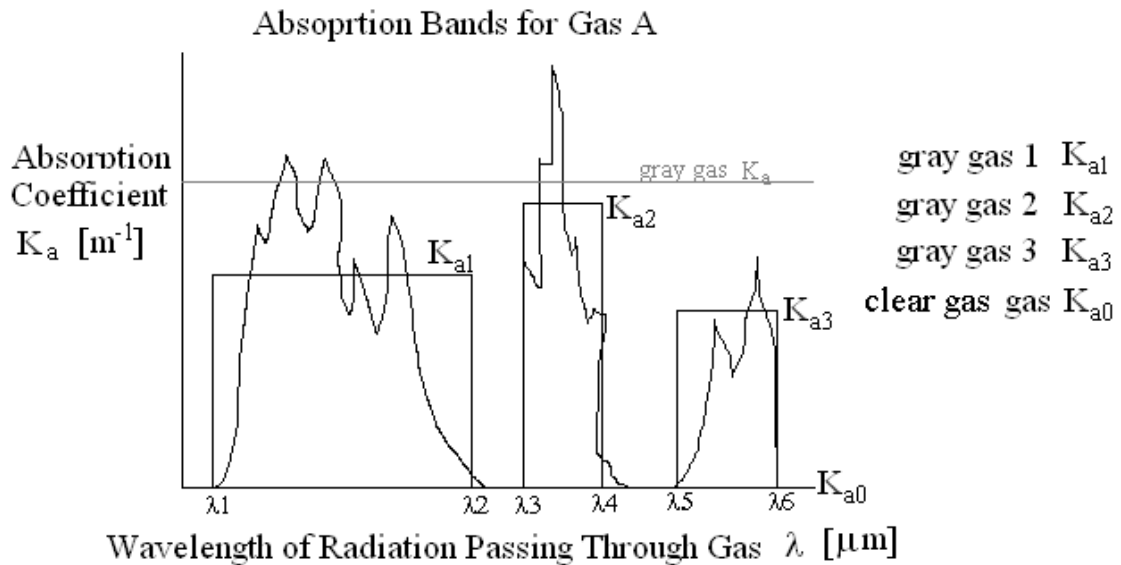


Figure 51. Representation of a Real Gas as Three Gray Gases and one Clear Gas

Recall that gas emissivity is the ratio of radiant energy emitted by a gray gas compared to a blackbody. For a real gas, the emissivity depends on the fraction of the blackbody emissive power emitted at each wavelength and can be expressed mathematically as shown in equation (76) (Howell and Siegel, 1972; p. 425).

$$\epsilon_g = \frac{\int_0^{\infty} \epsilon_\lambda E_{b,\lambda} d\lambda}{\int_0^{\infty} E_{b,\lambda} d\lambda} \quad (76)$$

Let ϵ_0 be the emissivity of the clear gas and ϵ_1 , ϵ_2 and ϵ_3 be the emissivities of gray gases 1, 2 and 3, respectively. Since the emissivity of each gray gas fraction is uniform over a particular wavelength region, equation (77) can be derived for the fictitious gas in Figure 51.

$$\varepsilon_g = \frac{\varepsilon_0 \int_0^{\lambda_1} E_{b,\lambda} d\lambda + \varepsilon_1 \int_{\lambda_1}^{\lambda_2} E_{b,\lambda} d\lambda + \varepsilon_2 \int_{\lambda_2}^{\lambda_3} E_{b,\lambda} d\lambda + \varepsilon_3 \int_{\lambda_3}^{\lambda_4} E_{b,\lambda} d\lambda + \varepsilon_4 \int_{\lambda_4}^{\lambda_5} E_{b,\lambda} d\lambda + \varepsilon_5 \int_{\lambda_5}^{\lambda_6} E_{b,\lambda} d\lambda + \varepsilon_6 \int_{\lambda_6}^{\infty} E_{b,\lambda} d\lambda}{\int_0^{\infty} E_{b,\lambda} d\lambda} \quad (77)$$

Let a_i be the fraction of the blackbody spectral region where the absorption coefficient is K_{ai} . The definition of a_i can be used to simplify equation (77) to equation (78). The fractions a_i in (78) are known as weighting coefficients and must sum to unity.

$$\varepsilon_g = a_0 \varepsilon_0 + a_1 \varepsilon_1 + a_2 \varepsilon_2 + a_3 \varepsilon_3 \quad \text{where} \quad \sum_{i=0}^3 a_i = 1 \quad (78)$$

The clear gas has an absorption coefficient of zero (resulting in $\varepsilon_0=0$). The emissivity of gray gases 1 to 3 can be replaced by the expression in equation (75) producing equation (79) (Hottel and Sarofim, 1960; p. 247).

$$\varepsilon_g = a_1 [1 - \exp(-K_{a_1} x)] + a_2 [1 - \exp(-K_{a_2} x)] + a_3 [1 - \exp(-K_{a_3} x)] \quad (79)$$

Equations (76) through (79) show that the emissivity of any real gas can be expressed as the weighted sum of any number of gray gases.

$$\varepsilon_g = \sum_i a_i [1 - \exp(-K_{a_i} x)] \quad (80)$$

In equation (80), as the number of gray gases, (each represented by the index i) increases, the weighted sum approximation approaches the real gas emissivity. The weighted-sum-of-gray-gases model is used in the Hottel Zone method to approximate real gas behaviour.

References

Hottel, H. C. and Sarofim, A. F. (1967) Radiative Heat Transfer. McGraw-Hill Book Company.

Rhine, J. M. and Tucker, R. J. (1991) Modeling of Gas-fired Furnaces and Boilers. McGraw-Hill Book Company.

Siegel, R. and Howell, J. R. (1972) Thermal Radiation Heat Transfer. McGraw-Hill Book Company.

Sparrow, E. M. and Cess, R. D. (1978) Radiation Heat Transfer, Augmented Edition. Hemisphere Publishing Corporation.

Appendix B

Hottel Zone Method

Zone Method Overview

The Hottel Zone method is used to model heat transfer in enclosures where radiation is a dominant heat-transfer mechanism. The zone method divides the furnace into volume and surface zones and performs an energy balance on each zone (Rhine and Tucker, 1991; p. 216).

An energy balance for a volume zone (81) and a surface zone (82) are shown below.

$$\begin{aligned} \text{Energy Accumulating} \\ \text{in Volume Zone} \end{aligned} = \begin{aligned} & \text{Radiation} \\ & \text{In} \end{aligned} - \begin{aligned} & \text{Radiation} \\ & \text{Out} \end{aligned} + \begin{aligned} & \text{Enthalpy} \\ & \text{In} \end{aligned} - \begin{aligned} & \text{Enthalpy} \\ & \text{Out} \end{aligned} - \begin{aligned} & \text{Heat Loss by} \\ & \text{Convection} \end{aligned} \quad (81)$$

$$\begin{aligned} \text{Energy Accumulating} \\ \text{in Surface Zone} \end{aligned} = \begin{aligned} & \text{Radiation} \\ & \text{In} \end{aligned} - \begin{aligned} & \text{Radiation} \\ & \text{Out} \end{aligned} + \begin{aligned} & \text{Heat in by} \\ & \text{Convection} \end{aligned} - \begin{aligned} & \text{Heat Loss by} \\ & \text{Conduction} \end{aligned} \quad (82)$$

If the furnace is assumed to operate at steady state, the energy accumulation terms in equation (81) and (82) will be zero and one algebraic equation will be produced for each zone. The algebraic equations are solved simultaneously for the temperature of each zone in the furnace.

The complexity of the Hottel Zone method comes from the radiation terms in the energy balance. Due to the media-less nature of radiative heat transfer, any zone in the furnace receives and transmits radiant energy to every other zone. The rates of radiative heat emission and absorption by a zone are proportional to the black emissive power (σT^4) of the emitting zone (Rhine and

Tucker, 1991; p. 216). The proportionality constant is known as a directed-flux area, and is represented by the symbol $\overrightarrow{Z_i Z_j}$ where zone i is the emitter and zone j is the receiver as shown in equations (83) and (84) (Rhine and Tucker, 1991; p. 216).

$$\text{Radiation In} = \text{Radiation Emitted by other Zones and Absorbed by Zone j} = \sum_{\text{all } i} \overrightarrow{Z_i Z_j} \sigma T_i^4 \quad (83)$$

$$\text{Radiation Out} = \text{Radiation Emitted by Zone j and Absorbed by other Zones} = \sum_{\text{all } i} \overrightarrow{Z_j Z_i} \sigma T_j^4 \quad (84)$$

Calculation of the directed-flux areas is the most challenging part of the Hottel Zone method.

The following sections explain in detail the three types of exchange areas used in the Hottel Zone method: direct-exchange areas, total-exchange areas and directed-flux areas. Also described is how the one-clear-three-gray-gas model of Talyor and Foster (1974) is used with the program RADEX to calculate the total-exchange areas used in this thesis. The radiative heat transfer model developed for this thesis relies on the following assumptions.

1. The composition of the furnace gas is uniform throughout the furnace. The composition is that of the completely combusted furnace feed
2. Perfect plug flow occurs on the furnace side. The furnace gas enters at the top of the furnace and exits at the bottom
3. The furnace is divided into zones, with uniform temperature within each zone

4. There are no soot particles in the furnace gas. (The furnace flame is non-luminous and there is no scattering of radiation by the furnace gas)
5. All surfaces in the furnace are gray Lambert surfaces. (They absorb and emit all wavelengths of radiation and they emit and reflect radiation equally in all directions)
6. The surface emissivity and absorptivity of the furnace walls are assumed to be independent of temperature.
7. The furnace gas is assumed to be composed of three gray gases plus one clear gas.
8. The furnace operates at steady state.

Exchange and Flux Areas

In the Hottel Zone method, there are three types of proportionality constants with units of area. They are direct-exchange areas, total-exchange areas and directed-flux areas. Each type of area is a proportionality constant for radiative heat transfer between zones in a furnace, with different simplifying assumptions.

Direct-Exchange Areas

Direct-exchange areas are proportionality constants for radiant energy that leaves the emitting zone and arrives directly at the absorbing zone. (Rhine and Tucker, 1991; p. 217) Direct-exchange areas are a function of the enclosure geometry and the intervening gas absorption coefficient. (Rhine and Tucker, 1991; p. 217) Direct-exchange areas are defined as the equivalent areas that would be required if all of radiation that arrives at the receiving zone is absorbed (Hottel and Sarofim, 1960; p. 258). In calculating direct-exchange areas, the absorptivity of all surface zones is set to one so that no surface reflection occurs.

Direct-exchange areas are represented by the notation $\overline{s_i s_j}$, $\overline{s_i g_j}$, $\overline{g_i g_j}$ or $\overline{z_i z_j}$. The letters s and g specify whether the zones involved are surface or volume zones and the letter z represents a generic zone (surface or volume). The first zone listed under the overbar is the emitting zone and the second zone listed is the receiving zone. For example, $\overline{s_i s_j}$ is the proportionality constant (with units of area) for radiation emitted by surface zone i (s_i) that arrives at surface zone j (s_j). Direct-exchange areas are subject to the summation rules shown in equations (85) and (86) and to the reciprocity rule shown in equation (87).

$$\sum_j \overline{s_i s_j} + \sum_j \overline{s_i g_j} = A_i \quad (85)$$

A_i is the true area of emitting surface zone i.

$$\sum_j \overline{g_i s_j} + \sum_j \overline{g_i g_j} = 4K_a V_i \quad (86)$$

V_i is the true volume of emitting volume zone i and K_a is the gray gas absorption coefficient for the gas contained in the volume zone.

$$\overline{z_i z_j} = \overline{z_j z_i} \quad (87)$$

The summation and reciprocity rules are inherent in the definition of direct-exchange areas (Rhine and Tucker, 1991; p. 225).

Total-Exchange Areas

Total-exchange areas are calculated from direct-exchange areas (Rhine and Tucker, 1991; p. 220). Total-exchange areas differ from direct-exchange areas in that they account for all of the radiation that leaves the emitting zone and is absorbed by the receiving zone, regardless of the path taken. Total-exchange areas include radiation that travels directly between the zones and radiation reflected off multiple intermediate zones, which arrives at and is eventually absorbed by the receiving zone (Rhine and Tucker, 1991; p. 220). Total-exchange areas are a function of enclosure geometry, the absorption coefficient of the intervening gas and the enclosure surface emissivities (Rhine and Tucker, 1991; p. 217), whereas direct-exchange areas do not depend on the enclosure surface emissivities. Total-exchange areas use the same notation as direct-exchange-areas with upper-case letters designating the zone type. Similar summation rules and the reciprocity rule apply to total-exchange areas (See equations (88)-(90)) (Rhine and Tucker, 1991; p. 225).

$$\sum_j \overline{S_i S_j} + \sum_j \overline{S_i G_j} = \epsilon_i A_i \quad (88)$$

$$\sum_j \overline{G_i G_j} + \sum_j \overline{G_i S_j} = 4K_i V_i \quad (89)$$

$$\overline{Z_i Z_j} = \overline{Z_j Z_i} \quad (90)$$

Total-exchange areas can be used in furnace models where the furnace gas is assumed to consist of a single gray gas. Total-exchange areas (and also direct-exchange areas) are independent of the

temperature of the emitting and receiving zone. As a result if the furnace geometry, gas properties and surface properties are constant, the direct and total-exchange areas only need to be calculated once for the given furnace enclosure (Rhine and Tucker, 1991; p. 217). The set of total-exchange areas will be valid for any temperature pattern in the furnace. Since the furnace geometry, gas properties and surface properties of the furnace are assumed to be constant in this thesis, the total-exchange areas are calculated once and stored for later use in the model equations.

Directed-Flux Areas

To more accurately model furnace-gas radiation, it is necessary to model the furnace gas as a real gas, rather than a single gray gas. In a real gas the gas emissivity is a function of gas composition, pressure, furnace geometry (which influences beam lengths) and gas temperature (Rhine and Tucker, 1991; p. 202). Real-gas absorptivity is dependent on the same variables as real-gas emissivity, but is additionally dependent on the temperature of the emitting zone (Rhine and Tucker, 1991; p. 202).

The emissivity of a real gas can be accurately modeled by assuming that the real gas is composed of multiple gray gases and one clear gas (Hottel and Sarofim, 1960; p. 247). The representation of a real gas as multiple gray gases is known as the weighted-sum-of-gray-gases model. The weighted-sum-of-gray-gases model is described in Appendix A. In equation (91) the symbol a_i is the weighting factor for gray gas i and ϵ_i is the emissivity of gray gas i . The temperature dependence of the real-gas emissivity is accounted for in the gray-gas weighting coefficients

(Hottel and Sarofim, 1960; p. 281). The gray-gas weighting coefficients are a function of the gas temperature (T_g).

$$\epsilon_g = a_0(T_g)\epsilon_0 + a_1(T_g)\epsilon_1 + a_2(T_g)\epsilon_2 + a_3(T_g)\epsilon_3 \quad (91)$$

The absorptivity of a real gas can also be modeled by assuming that the real gas is composed of multiple gray gases and one clear gas (Rhine and Tucker, 1991; p. 202). Although real-gas absorptivity is a function of emitter temperature and gas temperature, the absorptivity can be adequately modeled using only the temperature of the emitting zone (Rhine and Tucker, 1991; p. 207). Equation (92) shows the absorptivity of a real gas modeled as a weighted sum of the emissivities of multiple gray gases.

$$\alpha_g = a_0(T_{\text{emit}})\epsilon_0 + a_1(T_{\text{emit}})\epsilon_1 + a_2(T_{\text{emit}})\epsilon_2 + a_3(T_{\text{emit}})\epsilon_3 \quad (92)$$

Different models have been fit to obtain the weighting coefficients in equations (91) and (92) (Taylor and Foster, 1974; Smith et al., 1982). The simplest is a linear model proposed by Taylor and Foster (1974).

$$a_n(T) = b_{1,n} + b_{2,n}T \quad (93)$$

The temperature-dependent weighting coefficients from the weighted-sum-of-gray-gases model can be applied to total-exchange areas to produce temperature dependent directed-flux areas.

This allows the temperature dependence of real gases to be modeled using the Hottel Zone

method. What follows is an illustration of how the weighting coefficients from equation (91) can be used with total-exchange areas to model real gas behaviour.

Consider the transfer of radiant energy between a volume and surface zone separated by a single non-scattering gray gas. Equation (94) is an energy balance on the volume zone where all modes of heat transfer other than radiation are assumed negligible. The net rate of radiant energy transfer to the volume zone is proportional to the difference in the black emissive powers of the volume and surface zones as shown in equation (94).

$$q_{G \leftrightarrow S} = \frac{\text{Radiant Energy}}{\text{Emitted by Gas}} - \frac{\text{Radiant Energy}}{\text{Absorbed by Gas}} \quad (94)$$

$$q_{G \leftrightarrow S} = \overline{GS}(E_G - E_S)$$

\overline{GS} is the total-exchange area between the volume zone and the surface zone. To calculate separately the radiant energy emitted by the gas zone and the radiant energy absorbed by the gas zone, we can expand equation (94) and use the reciprocity rule (90) for total-exchange areas.

$$q_{G \leftrightarrow S} = \overline{GSE}_G - \overline{SGE}_S \left[\frac{\text{energy}}{\text{time}} \right] \quad (95)$$

The total-exchange area \overline{GS} acts like an emissivity since it determines how much radiant energy is emitted by the gas. The total-exchange area \overline{SG} acts like an absorptivity since it determines how much radiant energy is absorbed by the gas (Hottel and Sarofim, 1960; p. 281). However,

these total-exchange areas are not influenced by temperature. It is known from gas emissivity studies that the emissivity of a real gas should be a function of the gas temperature (T_G) and the absorptivity of a real gas should be a function of the emitting surface temperature (T_S) (Hottel and Sarofim, 1960; p. 283). These two pieces of information can be used to write equation (95) as equation (96). Note that in equation (96) $Q_{G\leftrightarrow S}$ is a radiant energy flux while in equation (95) $q_{G\leftrightarrow S}$ is the rate of radiant energy transfer.

$$Q_{G\leftrightarrow S} = \epsilon_G(T_G)E_G - \alpha_G(T_S)E_S \left[\frac{\text{energy}}{\text{time} \cdot \text{area}} \right] \quad (96)$$

Now, consider the radiative heat transfer between a surface zone and a gas zone that contains N gray gases (i.e., a real gas). The weighted-sum-of-gray-gases model could be applied to the emissivity and absorptivity in equation (96) to produce equation (97).

$$Q_{G\leftrightarrow S} = [a_0(T_G)\epsilon_0 + \dots + a_N(T_G)\epsilon_N]E_G - [a_0(T_S)\epsilon_0 + \dots + a_N(T_S)\epsilon_N]E_S \quad (97)$$

The since the total-exchange areas in equation (95) act like an emissivity and absorptivity, the weighting coefficients from the weighted-sum-of-gray-gases model can be applied to the total-exchange areas of the multiple gray-gases (Hottel and Sarofim, 1960; p. 283) resulting in equation (98).

$$q_{G\leftrightarrow S} = [a_0(T_G)\overline{GS}_0 + \dots + a_N(T_G)\overline{GS}_N]E_G - [a_0(T_S)\overline{GS}_0 + \dots + a_N(T_S)\overline{GS}_N]E_S \quad (98)$$

The terms $\left[a_0(T_G)\overline{GS}_0 + \dots + a_N(T_G)\overline{GS}_N \right]$ and $\left[a_0(T_S)\overline{GS}_0 + \dots + a_N(T_S)\overline{GS}_N \right]$ are directed-flux areas and are denoted \overline{GS} and \overline{SG} . Notice that when $T_G=T_S$, the directed flux areas for the gas and surface zones are equal. A formula for the directed-flux area of a generic zone for a three-gray-and-one-clear-gas model is given in equation (99).

$$\overline{Z_i Z_j} = \left[a(T_i)\overline{Z_i Z_j} \right]_{\text{gas}}^{\text{clear}} + \left[a(T_i)\overline{Z_i Z_j} \right]_{\text{gas 1}}^{\text{gray}} + \left[a(T_i)\overline{Z_i Z_j} \right]_{\text{gas 2}}^{\text{gray}} + \left[a(T_i)\overline{Z_i Z_j} \right]_{\text{gas 3}}^{\text{gray}} \quad (99)$$

Since the directed flux areas are a function of the temperature of the emitting zone, the reciprocity rules for direct and total-exchange areas only apply to directed-flux areas when the temperature of the emitting and receiving zones are the same (Rhine and Tucker, 1991; p. 226).

$$\overline{Z_i Z_j} = \overline{Z_j Z_i} \text{ only when } T_i = T_j \quad (100)$$

The surface zone summation rule for directed-flux areas is the same as for total-exchange areas but the volume zone summation rule must be modified to account for multiple gray gases.

$$\sum_j \overline{S_i S_j} + \sum_j \overline{S_i G_j} = \varepsilon_i A_i \quad (101)$$

$$\sum_j \overline{G_i S_j} + \sum_j \overline{G_i G_j} = 4V_i \left[a_0(T_i)\mathcal{K}_0 + a_1(T_i)\mathcal{K}_1 + a_2(T_i)\mathcal{K}_2 + a_3(T_i)\mathcal{K}_3 \right] \quad (102)$$

Calculation of Directed-Flux Areas

As described above directed-flux areas are calculated from total-exchange areas using the weighting coefficients from the sum-of-gray-gases model. Total-exchange areas can be calculated from direct-exchange areas using matrix inversion methods (Noble, 1975) or by the sole-emitter strategy (Hottel and Cohen, 1958). Direct-exchange areas can be calculated by evaluating the multiple integrals in equations (103)-(105) (Hottel and Sarofim, 1960; p. 258).

$$\overline{s_i s_j} = \iint_{A_i A_j} \frac{dA_i \cos \theta_i dA_j \cos \theta_j \tau(r)}{\pi r^2} \quad (103)$$

$$\overline{g_i s_j} = \iint_{V_i A_j} \frac{K_i dV_i dA_j \cos \theta_j \tau(r)}{\pi r^2} \quad (104)$$

$$\overline{g_i g_j} = \iint_{V_i V_j} \frac{K_i dV_i K_j dV_j \tau(r)}{\pi r^2} \quad (105)$$

Due to the complexity of these integrals, charts for commonly encountered geometries have been developed (Hottel and Cohen, 1958; Hottel and Sarofim, 1960; p. 260-279; Tucker, 1986). For more complex geometries, Monte Carlo ray-tracing methods have been used to evaluate direct-exchange areas (Vercammen and Froment, 1980; Lawson and Ziesler, 1996), which are then used to determine total-exchange areas, which, in turn, are used to compute directed-flux areas. A summary of how Monte Carlo ray-tracing methods are used in complex furnaces is provided in a review paper by Scholand (1983).

Total-Exchange Areas and Directed-Flux Areas in this Thesis

In this thesis, the program RADEX developed by Lawson and Ziesler (1996) is used to calculate total-exchange areas. As inputs, RADEX requires the furnace geometry, the surface radiative properties and the gray gas absorption coefficients. The furnace geometry and surface radiative properties were provided by the company. The weighted-sum-of-gray-gases model used in this thesis is the one-clear and three-gray gas model of Taylor and Foster (1974). The gray gas absorption coefficients are calculated using equation (106).

$$K_i = k_{g,i} P_{\text{fur}} 2X_{\text{CO}_2} \quad (106)$$

The gray gas fitting coefficient ($k_{g,i}$) is from Taylor and Foster (1974) for the combustion of natural gas in the absence of soot. The ratio of carbon dioxide to water in the combusted furnace gas was assumed to be near to one.

The total-exchange areas calculated by RADEX appear in the furnace-side energy balances. Directed-flux areas are calculated from the total-exchange areas using the Taylor and Foster (1974) weighting coefficients as shown in equation (107).

$$\overline{Z_i Z_j} = \left[a_0(T_i) \overline{Z_i Z_j} \right]_{\text{gas}}^{\text{clear}} + \left[a_1(T_i) \overline{Z_i Z_j} \right]_{\text{gas1}}^{\text{gray}} + \left[a_2(T_i) \overline{Z_i Z_j} \right]_{\text{gas2}}^{\text{gray}} + \left[a_3(T_i) \overline{Z_i Z_j} \right]_{\text{gas3}}^{\text{gray}} \quad (107)$$

Where $a_k = b_{1,k} + b_{2,k} T_i$ for gas-type k

The values of $b_{1,k}$ and $b_{2,k}$ can be found in Table 17.

References

Hottel, H. C. and Cohen, E. S. (1958) Radiant heat exchange in a gas-filled enclosure: allowance for the non-uniformity of gas temperature. vol. 4 pp. 3-14.

Hottel, H. C. and Sarofim, A. F. (1967) Radiative Heat Transfer. McGraw-Hill Book Company. pp. 203-204.

Lawson, D. A. and Ziesler, C. D. (1996) An accurate program for radiation modeling in the design of high-temperature furnaces. IMA Journal of Mathematics Applied in Business and Industry. vol. 7 pp. 109-116.

Noble, J. J. (1975) The zone method: explicit matrix relations for total exchange areas. International Journal of Heat and Mass Transfer. vol. 18 pp. 261-269.

Rhine, J. M. and Tucker, R. J. (1991) Modeling of Gas-fired Furnaces and Boilers. McGraw-Hill Book Company.

Scholand, E. (1983) Modern procedures for the calculation of radiant heat transfer in direct-fired tubed furnaces. International Chemical Engineering. vol. 23 pp. 600-610.

Smith, T. F., Shen, Z. F. and Friedman, J. N. (1982) Evaluation of coefficients for the weighted sum of gray gases model. Transactions of the American Society of Mechanical Engineers. vol. 104 pp. 602-608.

Taylor, P. B. and Foster P. J. (1974) The total emissivities of luminous and non-luminous flames. International Journal of Heat and Mass Transfer. vol. 17 pp. 1591-1605.

Tucker, R. J. (1986) Direct exchange areas for calculating radiation transfer in rectangular furnaces. Journal of Heat Transfer. vol. 108 pp. 707-710.

Vercammne, H. A. J. and Froment, G. F. (1980) An improved zone method using monte carlo techniques for the simulation of radiation in industrial furnaces. International Journal of Heat and Mass Transfer. vol. 23 pp. 329-337.

Appendix C

Derivation of Model Equations

Cube-Furnace Model Derivations

Furnace-Surface-Zone Energy Balance (f_i, i=1..6)

Energy Accumulating in Surface Zone 1 over period of time $\Delta t = 0$	$=$ Energy in by radiation from all furnace zones $-$ Energy out by radiation to all furnace zones $+$ Energy gained by convection from the furnace gas $-$ Energy lost to the surroundings by conduction	(108)
--	--	--------

Derive mathematical expressions for the terms on the right side of equation (108).

Energy in by radiation from all furnace zones	$= \sigma \sum_{\substack{\text{all furnace} \\ \text{zones } j}} \bar{Z}_j \bar{Z}_i T_j^4 \Delta t$ $= \left[\frac{\text{J}}{\text{h} \cdot \text{m}^2 \text{K}^4} \right] [\text{m}^2] [\text{K}^4] [\text{h}] = [\text{J}]$	(109)
--	--	--------

Energy out by radiation to all furnace zones	$= \sigma \varepsilon A T_i^4 \Delta t$ $= \left[\frac{\text{J}}{\text{h} \cdot \text{m}^2 \text{K}^4} \right] [\text{m}^2] [\text{K}^4] [\text{h}] = [\text{J}]$	(110)
--	--	--------

Energy gained by convection from the furnace gas	$= h_{\text{gso}} A (T_{\text{adj gas}} - T_i) \Delta t$ $= \left[\frac{\text{J}}{\text{m}^2 \text{hK}} \right] [\text{m}^2] [\text{K}] [\text{h}] = [\text{J}]$	(111)
--	---	--------

Energy lost to the surroundings by conduction	$= - \frac{k_{\text{refrac}}}{t_{\text{refrac}}} A (T_i - T_{\text{surr}}) \Delta t$ $= \left[\frac{\text{J}}{\text{m} \cdot \text{h} \cdot \text{K}} \right] \left[\frac{1}{\text{m}} \right] [\text{m}^2] [\text{K}] [\text{h}] = [\text{J}]$	(112)
---	---	--------

Combine equations (109) to (112) and divide all terms by Δt .

$0 = \sigma \sum_{\text{all furnace zones } j} Z_j Z_i T_j^4 - \sigma \epsilon A T_i^4 + h_{\text{gso}} A (T_{\text{adj gas}} - T_i) - \frac{k_{\text{refrac}}}{t_{\text{refrac}}} A (T_i - T_{\text{surr}})$	(113)
---	--------

Volume-Zone Energy Balance (f₇)

Energy Accumulating in Volume Zone 7 over period of time Δt	<ul style="list-style-type: none"> = Energy in by radiation from all furnace zones - Energy lost by radiation to all furnace zones - Energy lost by convection to surfaces + Enthalpy of gas in - Enthalpy of gas out + Heat released by combustion in the volume zone 	(114)
---	---	--------

Derive mathematical expressions for the terms on the right side of equation (114).

Energy in by radiation from all furnace zones	$= \sigma \sum_{\substack{\text{all furnace} \\ \text{zones } j}} \overline{Z_j Z_7} T_j^4 \Delta t$ $= \left[\frac{\text{J}}{\text{h} \cdot \text{m}^2 \text{K}^4} \right] * [\text{m}^2] * [\text{K}^4] * [\text{h}] = [\text{J}]$	(115)
---	---	--------

Energy lost by radiation to all furnace zones	$= 4KV_7 \sigma T_7^4 \Delta t$ $= \left[\frac{1}{\text{m}} \right] [\text{m}^3] \left[\frac{\text{J}}{\text{h} \cdot \text{m}^2 \text{K}^4} \right] [\text{K}^4] [\text{h}]$ $= [\text{J}]$	(116)
---	--	--------

Energy lost by convection to surfaces and obstacles	$= \sum_{\substack{\text{all surface} \\ \text{zones } j}} h_{\text{gso}} A_j (T_7 - T_j) \Delta t$ $= \left[\frac{\text{J}}{\text{m}^2 \text{h} \cdot \text{K}} \right] [\text{m}^2] [\text{K}] [\text{h}] = [\text{J}]$	(117)
---	--	--------

Enthalpy of gas in - Enthalpy of gas out	$= -\dot{m}_{\text{fur}} \int_{T_{\text{fur in}}}^{T_7} C_p dT \Delta t$ $= \left[\frac{\text{kg}}{\text{h}} \right] \left(\left[\frac{\text{J}}{\text{kg} \cdot \text{K}} \right] [\text{K}] \right) [\text{h}] = [\text{J}]$	(118)
--	---	--------

Heat released by combustion in	$= -\dot{n}_{\text{CH}_4} (\Delta H_{\text{comb}} - RT_7 \Delta n_{\text{comb}}) \Delta t$	(119)
--------------------------------	--	--------

the volume zone	$= \left[\frac{\text{gmol}}{\text{m}^3 \text{h}} \right] \left[\text{m}^3 \right] \left(\left[\frac{\text{J}}{\text{gmol}} \right] - \left[\frac{\text{J}}{\text{gmol} \cdot \text{K}} \right] \left[\text{K} \right] \right) \left[\text{h} \right]$ $= [\text{J}]$	
-----------------	---	--

Combine equations (115) to (119) and divide by Δt .

$0 = \sigma \sum_{\substack{\text{all furnace} \\ \text{zones } j}} \bar{Z}_j \bar{Z}_7 T_j^4 - 4KV_7 \sigma T_7^4 - \sum_{\substack{\text{all surface} \\ \text{zones } j}} h_{\text{gso}} A_j (T_7 - T_j) - \dot{m}_{\text{fur}} \int_{T_{\text{fur in}}}^{T_7} C_p dT$ $- \dot{n}_{\text{CH}_4} (\Delta H_{\text{comb}} - RT_7 \Delta n_{\text{comb}})$	(120)
--	--------

Segmented-Tube Model Derivations

Furnace Feed Calculations

The model accepts up to five user-defined furnace feed streams and calculates the combined uncombusted furnace feed temperature (T_6) and the heat released by isothermal and isobaric combustion of the furnace fuel (Q_{fur}). Stream 7 is the combined combusted furnace feed. Since the combustion of the furnace feed is assumed to occur isothermally, stream 7 will have the same temperature as stream 6 as shown in Figure 11.

Calculation of T_6 : Energy Balance on Mixing Point in Figure 11

Assumptions for Mixing-Point Calculation

1. No reactions take place during mixing.

2. The enthalpy of mixing is negligible (no heat is released or consumed by the mixing of gas molecules).
3. The reference states are the species as ideal gases at T_6 and 1atm.
4. There is no pressure or volume change during mixing.

Internal Energy Entering Mixing Point = Internal Energy Exiting Mixing Point	(121)
$\left(\widehat{H} - PV\right)_{in} = \left(\widehat{H} - PV\right)_{out} \text{ [J]}$	

Since there is no change in pressure or volume

$\widehat{H}_{in} = \widehat{H}_{out} \text{ [J]}$	
$\dot{n}_1 H_1 + \dot{n}_2 H_2 + \dot{n}_3 H_3 + \dot{n}_4 H_4 + \dot{n}_5 H_5 = \dot{n}_6 H_6 \text{ [J/h]}$	(122)
$\sum_{i=1}^5 \dot{n}_i H_i = \dot{n}_6 H_6$	

Expand the enthalpy term to account for the 15 species in the model

$\sum_{i=1}^5 \dot{n}_i \left(\sum_{j=1}^{15} X_j \int_{T_{ref}}^{T_i} C_{p,j} dT \right) = \dot{n}_6 \sum_{j=1}^{15} X_j \int_{T_{ref}}^{T_6} C_{p,j} dT$	(123)
---	--------

The constant pressure heat capacity (C_p) is assumed to follow a third-order polynomial in temperature as shown in equation (123) of Appendix E.

$C_{p,j} = A_j + B_j T + C_j T^2 + D_j T^3$	(124)
---	--------

Since the temperatures of the inlet streams (T_1 to T_5) are known, the left side of equation (123) can be evaluated. T_6 is determined by solving the fourth order polynomial on right-hand side of equation (123). Since there is no simple analytical solution to a fourth-order polynomial, the heat capacities for the species in stream 6 are assumed to be constant and the same as at T_{ref} . Using this assumption equation (123) can be solved for T_6 resulting in equation (125).

$T_6 = \frac{\sum_{i=1}^5 \dot{n}_i \left(\sum_{j=1}^{15} X_j \int_{T_{ref}}^{T_i} C_{p,j} dT \right)}{\dot{n}_6 \sum_{j=1}^{15} X_j C_{p,j,T_{ref}}} + T_{ref}$	(125)
---	--------

The magnitude of the error in T_6 as a result of the constant-heat-capacity assumption will depend on how well equation (126) approximates equation (127).

$\int_{T_{ref}}^{T_6} C_p dT = C_p T \Big _{T_{ref}}^{T_6} \quad (\text{linear function})$	(126)
--	--------

$\int_{T_{ref}}^{T_6} C_p dT = \int_{T_{ref}}^{T_6} A + BT + CT^2 + DT^3 dT = AT + \frac{B}{2} T^2 + \frac{C}{3} T^3 + \frac{D}{4} T^4 \Big _{T_{ref}}^{T_6}$ <p>(4th order polynomial)</p>	(127)
--	--------

If T_{ref} is close to T_6 , then the difference between equations (126) and (127) will be small and the error in T_6 will be minimal. Since T_{ref} can be assigned any temperature, a temperature close the

expected combined stream temperature (T_6) is calculated by an iterative procedure. The first iteration uses standard temperature ($T_{std} = 298 \text{ K}$) to calculate a T_{ref} close to T_6 .

$T_{ref} = \frac{\sum_{i=1}^5 \dot{n}_i \left(\sum_{j=1}^{15} X_j \int_{T_{std}}^{T_i} C_{p,j} dT \right)}{\dot{n}_6 \sum_{j=1}^{15} X_j C_{p,j,T_{std}}} + T_{std}$	(128)
---	--------

The second iteration uses T_{ref} from equation (128) in equation (125) to calculate T_6 . To achieve a more accurate estimate of T_6 , additional iterations can be added. In the pre-combustion section two iterations are used and result in T_{ref} within a few degrees of T_6 .

Calculation of the Heat Released by Combustion, Q_{fur} : Energy Balance on Isothermal Combustion Zone in Figure 11

Internal Energy	= Internal Energy + Pressure Volume Work In	(129)
Changes in Control	- (Internal Energy + Pressure Volume Work Out)	
Volume over time	- Heat Removed	
Δt	= Enthalpy In – Enthalpy Out – Heat Removed	

Enthalpy In	$= \dot{n}_6 \sum_{\text{species } i} X_{i,6} \int_{T_{ref}}^{T_6} C_{p,i} dT \Delta t$ $= \left[\frac{\text{gmol}}{\text{h}} \right] \left[\frac{\text{gmol}_i}{\text{gmol}} \right] \left[\frac{\text{J}}{\text{gmol}_i \text{K}} \right] [\text{K}] [\text{h}] = [\text{J}]$	(130)
-------------	--	--------

Enthalpy Out	$= \dot{n}_7 \sum_{\text{species } i} X_{i,7} \int_{T_{\text{ref}}}^{T_5} C_{p,i} dT \Delta t$ $= \left[\frac{\text{gmol}}{\text{h}} \right] \left[\frac{\text{gmol}_i}{\text{gmol}} \right] \left[\frac{\text{J}}{\text{gmol}_i \text{K}} \right] [\text{K}] [\text{h}] = [\text{J}]$	(131)
--------------	---	----------------

Heat Removed	$= Q_{\text{fur}} \Delta t$ $= \left[\frac{\text{J}}{\text{h}} \right] [\text{h}] = [\text{J}]$	(132)
--------------	--	----------------

Internal Energy Changes in Control Volume over time Δt	$= \Delta E_{\text{reaction}} + \Delta E_{\text{T-change}}$ $= \Delta H_{\text{reaction}} - \Delta(PV)_{\text{reaction}} + \Delta E_{\text{T-change}}$ $= \Delta H_{\text{reaction}} - \Delta(nRT)_{\text{reaction}} + \Delta E_{\text{T-change}}$ <p>Since combustion is isothermal there is no temperature change over period of time Δt ($\Delta E_{\text{T-change}} = 0$).</p> $= \Delta H_{\text{reaction}} - RT_6 \Delta n_{\text{reaction}}$	(133)
--	---	----------------

Since combustion is assumed to be complete and instantaneous, the rate of combustion for each combusting species is the rate at which the species is fed to the furnace. The enthalpy of combustion (ΔH_{comb}) for the combustible species is calculated using the enthalpy of reaction method outlined in Appendix E.

Combine the terms in the energy balance into one equation, divide by Δt and move all terms to the right-hand side to give

$0 = \dot{n}_6 \sum_{\text{species } i} X_{i,6} \int_{T_{\text{ref}}}^{T_6} C_{p,i} dT - \dot{n}_7 \sum_{\text{species } i} X_{i,7} \int_{T_{\text{ref}}}^{T_6} C_{p,i} dT - Q_{\text{fur}}$ $- \dot{n}_6 \sum_{\text{combustion species } j} X_{j,6} (\Delta H_{j,\text{comb}} - RT_6 \Delta n_{j,\text{comb}})$	(134)
---	----------------

Since $T_{\text{ref}} = T_6$, the integrals in the enthalpy terms evaluate to zero.

$Q_{\text{fur}} = \dot{n}_6 \sum_{\text{combustion species } j} X_{j,6} (\Delta H_{j,\text{comb}} - RT_6 \Delta n_{j,\text{comb}})$	(135)
---	----------------

Furnace-Surface Zone Energy Balance (f_i i=1..50)

Energy Accumulating in Surface Zone over period of time Δt	= Energy in by radiation from all furnace zones - Energy out by radiation to all furnace zones + Energy gained by convection from the furnace gas - Energy lost to the surroundings by conduction	(136)
--	--	----------------

Energy in by radiation from all furnace zones	$= \sigma \sum_{\text{furnace zones } j} (\overline{Z_j Z_i} T_j^4) \Delta t$	(137)
---	---	----------------

	$= \sigma \sum_{\substack{\text{furnace} \\ \text{zones } j}} \sum_{\substack{\text{gray gas} \\ \text{atmospheres } k}} (b_{1,k} + b_{2,k} T_j) \overline{Z_j Z_i} \Big _k T_j^4 \Delta t$ $= \left[\frac{\text{J}}{\text{h} \cdot \text{m}^2 \text{K}^4} \right] \left([\text{none}] + \left[\frac{1}{\text{K}} \right] [\text{K}] \right) [\text{m}^2] [\text{K}^4] [\text{h}] = [\text{J}]$	
--	--	--

The total-exchange areas in equation (137) are calculated using the program RADEX (Lawson and Ziesler, 1991) and the parameters $b_{1,k}$ and $b_{2,k}$ are from Taylor and Foster (1974). More information on directed-flux areas and total-exchange areas is available in Appendix B.

Energy out by radiation to all furnace zones	$= \sigma \varepsilon A_i T_i^4 \Delta t$ $= \left[\frac{\text{J}}{\text{h} \cdot \text{m}^2 \text{K}^4} \right] [\text{m}^2] [\text{K}^4] [\text{h}] = [\text{J}]$	(138)
--	--	--------

Energy gained by convection from the furnace gas	$= h_{\text{gso}} A_i (T_{\text{adj gas}} - T_i) \Delta t$ $= \left[\frac{\text{J}}{\text{m}^2 \text{h} \cdot \text{K}} \right] [\text{m}^2] [\text{K}] [\text{h}] = [\text{J}]$	(139)
--	---	--------

The furnace-gas-to-surface convective heat transfer coefficient is calculated using the Dittus-Boelter equation according to Appendix E.

Energy lost to the surroundings by conduction	$= \frac{k_{\text{refrac}}}{t_{\text{refrac}}} A_i (T_i - T_{\text{surr}}) \Delta t$	(140)
---	--	--------

	$= \frac{\left[\frac{J}{m \cdot h \cdot K} \right]}{[m]} [m^2] [K] [h] = [J]$	
--	--	--

Since the surface zone is at steady state, there is no energy accumulating in the zone over time Δt .

Combine equations (136)-(140) and divide by Δt .

$0 = \sigma \left(\sum_{\substack{\text{furnace} \\ \text{zones } j}} \sum_{\substack{\text{gray gas} \\ \text{atmospheres } k}} \left[(b_{1,k} + b_{2,k} T_j) \overline{Z_j Z_i} \Big _k T_j^4 \right] - \epsilon A_i T_i^4 \right)$ $+ h_{gso} A_i (T_{adj \text{ gas}} - T_i) - \frac{k_{refrac}}{t_{refrac}} A_i (T_i - T_{surr})$	(141)
--	---------------

Furnace-Obstacle-Zone Energy Balance (f_i, i=51..62)

The energy balance on an obstacle zone has the same form as the energy balance on a surface zone except that conduction occurs to the inner tube wall instead of to the external environment. Because of the similarities between furnace surface and furnace obstacle zone energy balances, only the conduction term is derived in this section.

Energy Accumulating in Obstacle Zone over period of time Δt	= Energy in by radiation from all furnace zones - Energy out by radiation to all furnace zones + Energy gained by convection from the furnace gas - Energy lost from the obstacle by conduction	(142)
---	--	---------------

Energy lost from the obstacle by conduction	$= \frac{2\pi k_{\text{tube}} \Delta y (T - T_{\text{in wall}})}{\ln\left(\frac{r_{\text{out}}}{r_{\text{in}}}\right)} \Delta t$ $= \left[\frac{\text{J}}{\text{h} \cdot \text{m} \cdot \text{K}} \right] [\text{m}] [\text{K}] [\text{h}] = [\text{J}]$	(143)
---	---	--------

Since the obstacle zone is at steady state, there is no energy accumulating in the zone over time Δt . Combine the terms and divide by Δt .

$0 = \sigma \left(\sum_{\substack{\text{furnace} \\ \text{zones } j}} \sum_{\substack{\text{gray gas} \\ \text{atmospheres } k}} \left[(b_{1,k} + b_{2,k} T_j) \overline{Z_j Z_i} \right]_k T_j^4 - \epsilon A_i T_i^4 \right) + h_{\text{gso}} A_i (T_{\text{adj gas}} - T_i)$ $- \frac{2\pi k_{\text{tube}} \Delta y (T_i - T_{\text{in wall}})}{\ln\left(\frac{r_{\text{out}}}{r_{\text{in}}}\right)}$	(144)
---	--------

Furnace-Volume-Zone Energy Balance (f_i, i=63..74)

Energy Changes in Volume Zone over period of time Δt	<ul style="list-style-type: none"> = Energy in by radiation from all furnace zones - Energy lost by radiation to all furnace zones - Energy lost by convection to surfaces and obstacles + Enthalpy of gas in from zone above - Enthalpy of gas out + Heat released into zone from combustion 	(145)
--	--	--------

Energy in by radiation from all furnace zones	$= \sigma \sum_{\text{furnace zones } j} \sum_{\text{gray gas atmospheres } k} (b_{1,k} + b_{2,k} T_j) \overline{Z_j Z_i} \Big _k T_j^4 \Delta t$	(146)
---	---	--------

Energy lost by radiation to all furnace zones	$= 4V\sigma T_i^4 \sum_{\text{gray gas atmospheres } k} [(b_{1,k} + b_{2,k} T_i) K_k] \Delta t$ $= [m^3] \left[\frac{J}{h \cdot m^2 \cdot K^4} \right] [K^4] \left([none] + \left[\frac{1}{K} \right] [K] \right) \left[\frac{1}{m} \right] [h] = [J]$	(147)
---	--	--------

The gray gas absorption coefficients are calculated from the non-luminous one-clear-plus-three gray-gas model of Taylor and Foster (1974).

Energy lost by convection to adjacent surfaces and obstacles	$= \sum_{\text{surface and obstacles } j} [h_{gso} A_j (T_i - T_j)] \Delta t$ $= \left[\frac{J}{m^2 h \cdot K} \right] [m^2] [K] [h] = [J]$	(148)
--	--	--------

Enthalpy of gas in from zone above - Enthalpy of gas out	$= \dot{n}_{\text{fur}} \sum_{\text{furnace species } j} X_j \int_{T_i}^{T_{\text{fur abv}}} C_{p,j} dT \Delta t$ $= \left[\frac{\text{gmol}_{\text{fur}}}{h} \right] \left[\frac{\text{gmol}_i}{\text{gmol}_{\text{fur}}} \right] \left[\frac{J}{\text{gmol}_i K} \right] [K] [h] = [J]$	(149)
---	--	--------

Heat released into zone from combustion over	$= \alpha(k_i) Q_{\text{fur}} \Delta t$	(150)
--	---	--------

time Δt	$= [\text{none}] \left[\frac{\text{J}}{\text{h}} \right] [\text{h}] = [\text{J}]$	
-----------------	--	--

Since the volume zone is at steady state, there is no energy accumulating in the zone over time Δt .

Combine the terms and divide by Δt .

$0 = \sigma \left(\sum_{\substack{\text{furnace} \\ \text{zones } j}} \sum_{\substack{\text{gray gas} \\ \text{atmospheres } k}} \left[(b_{1,k} + b_{2,k} T_j) \overline{Z_j Z_i} \Big _k T_j^4 \right] - 4V_i T_i^4 \sum_{\substack{\text{gray gas} \\ \text{atmospheres } k}} \left[(b_{1,k} + b_{2,k} T_i) K_k \right] \right)$ $- \sum_{\substack{\text{surface and} \\ \text{obstacles } j}} \left[h_{\text{gso}} A_j (T_i - T_j) \right] + \dot{n}_{\text{fur}} \sum_{\substack{\text{furnace} \\ \text{species } j}} X_j \int_{T_i}^{T_{\text{fur,abv}}} C_{p,j} dT + \alpha(k_i) Q_{\text{fur}}$	(151)
--	----------------

Inner-Tube-Surface Energy Balance ($f_i, i=75..86$)

Energy Accumulating at the inner tube surface of a tube segment of height Δy over time Δt	<p>= Energy entering by conduction over time Δt</p> <p>- Energy exiting by convection over time Δt</p>	(152)
---	--	----------------

Energy entering by conduction over time Δt	$= \frac{2\pi k_{\text{tube}} \Delta y (T_{\text{out wall}} - T_i)}{\ln \left(\frac{r_{\text{out}}}{r_{\text{in}}} \right)} \Delta t$ $= \left[\frac{\text{J}}{\text{h} \cdot \text{m} \cdot \text{K}} \right] [\text{m}] [\text{K}] [\text{h}] = [\text{J}]$	(153)
--	---	----------------

Energy exiting by convection over time Δt	$= h_{tg} 2\pi r_{in} \Delta y (T_i - T_{proc\ gas}) \Delta t$ $= \left[\frac{J}{m^2 h \cdot K} \right] [m][m][K][h] = [J]$	(154)
---	--	--------

The tube-to-process-gas convective heat-transfer coefficient is calculated in Appendix E. There is no energy accumulating at the inner tube wall surface over time Δt . Combine the terms and divide by Δt .

$0 = \frac{2\pi k_{tube} \Delta y (T_{out\ wall} - T_i)}{\ln\left(\frac{r_{out}}{r_{in}}\right)} - h_{tg} 2\pi r_{in} \Delta y (T_i - T_{proc\ gas})$	(155)
---	--------

The variables 2π and Δy are not cancelled from equation (155) to ensure the energy balance terms have the same units as other energy balance terms in the model. Upon solution the energy balance terms are summed to check design ratios and to calculate residuals. If the terms 2π and Δy are cancelled from equation (155) the units of the convection and conduction terms are inconsistent with the units of other energy balance equations.

Process-Gas Energy Balance (f_i, i=87..98)

Energy Changes in a control volume of gas enclosed in segment of height Δy over time Δt	$= \text{Enthalpy of Gas Entering at } y$ $- \text{Enthalpy of Gas Exiting at } y+\Delta y$ $+ \text{Energy gained by convection from the tube surface}$	(156)
---	--	--------

<p>Enthalpy of Gas Entering at y</p>	$= H _y$ $= \dot{m}_{\text{tot}} \sum_{\substack{\text{process} \\ \text{species } j}} \left(\frac{Y_j}{M_j} \int_{T_{\text{ref}}}^{T_i} C_{p,j} dT \right) \Big _y \Delta t$ <p>Where: $Y_j = \frac{P_j M_j}{\sum_{\substack{\text{process} \\ \text{species } k}} P_k M_k} = \frac{P_j M_j}{RT\rho_g}$</p> $= \dot{m}_{\text{tot}} \sum_{\substack{\text{process} \\ \text{species } j}} \left(\frac{P_j}{RT\rho_g} \int_{T_{\text{ref}}}^T C_{p,j} dT \right) \Big _y \Delta t$ <p>Unit analysis for only one term is shown.</p> $= \left[\frac{\text{kg}_{\text{total}}}{\text{h}} \right] \frac{[\text{kPa}_i]}{\left[\frac{\text{kPa} \cdot \text{m}^3}{\text{gmol} \cdot \text{K}} \right] [\text{K}] \left[\frac{\text{kg}_{\text{total}}}{\text{m}^3} \right]} \left[\frac{\text{J}}{\text{gmol}_i \text{K}} \right] [\text{K}] [\text{h}]$ $= [\text{J}]$	<p>(157)</p>
--	--	---------------

<p>Enthalpy of Gas Exiting at y+Δy</p>	$= H _{y+\Delta y}$ $= \dot{m}_{\text{tot}} \sum_{\substack{\text{process} \\ \text{species } j}} \left(\frac{P_j}{RT\rho_g} \int_{T_{\text{ref}}}^T C_{p,j} dT \right) \Big _{y+\Delta y} \Delta t$	<p>(158)</p>
--	---	---------------

	$= \left[\frac{\text{kg}_{\text{total}}}{\text{h}} \right] \frac{[\text{kPa}_i]}{\left[\frac{\text{kPa} \cdot \text{m}^3}{\text{gmol} \cdot \text{K}} \right] [\text{K}] \left[\frac{\text{kg}_{\text{total}}}{\text{m}^3} \right]} \left[\frac{\text{J}}{\text{gmol}_i \text{K}} \right] [\text{K}] [\text{h}]$ $= [\text{J}]$	
--	---	--

Energy gained by convection from the tube surface	$= h_{\text{tg}} 2\pi r_{\text{in}} \Delta y (T_{\text{in wall}} - T_i) \Delta t$ $= \left[\frac{\text{J}}{\text{m}^2 \text{h} \cdot \text{K}} \right] [\text{m}] [\text{m}] [\text{K}] [\text{h}]$ $= [\text{J}]$	(159)
---	---	-------

Energy changes in a volume of gas in segment of height Δy over time Δt	$= \Delta E_{\text{reaction}} + \Delta E_{\text{T-change}}$ $= \Delta H_{\text{reaction}} - \Delta(PV)_{\text{reaction}} + \Delta E_{\text{T-change}}$ $= \Delta H_{\text{reaction}} - \Delta(nRT_i)_{\text{reaction}} + \Delta E_{\text{T-change}}$ <p>Since the system is at steady state, there is no temperature change over period of time Δt.</p> $(\Delta E_{\text{T-change}}=0)$ $= \Delta H_{\text{reaction}} - RT_i \Delta n_{\text{reaction}}$ $= \Delta y \pi r_{\text{in}}^2 \rho_{\text{cat}} \sum_{\substack{\text{reforming} \\ \text{reactions } k}} \eta_k r_k \Delta H_k \Delta t$	(160)
--	--	-------

	$-RT\Delta y\pi r_{in}^2\rho_{cat}\sum_{\substack{\text{reforming} \\ \text{reactions } k}}\eta_k r_k \Delta n_k \Delta t$ $= \Delta y\pi r_{in}^2\rho_{cat}\sum_{\substack{\text{reforming} \\ \text{reactions } k}}\eta_k r_k (\Delta H_k - RT_i \Delta n_k) \Delta t$ $= [m][m^2]\left[\frac{kg_{cat}}{m^3}\right]\left[\frac{gmol}{kg_{cat}h}\right]$ $\left(\left[\frac{J}{gmol}\right] - \left[\frac{J}{gmol \cdot K}\right][K][\text{none}]\right)[h]$ $= [J]$	
--	---	--

The rates of the steam-methane reforming reactions are calculated by the Xu and Froment (1989a) kinetic model. The kinetic equations are given in Appendix E. Combine equations (157) to (160). Divide by Δt and move all the terms to the right-hand side of the equation. The process gas entering the volume at y is from the tube segment above the control volume. The process gas exiting at $y+\Delta y$ is at the same conditions as the process gas in the control volume. Change the indices in the enthalpy in and enthalpy out terms to indicate that y corresponds to the properties of the tube segment above and $y+\Delta y$ corresponds to the properties in the current tube segment.

$0 = \dot{m}_{tot} \sum_{\substack{\text{process} \\ \text{species } j}} \left(\frac{P_{j,seg\ abv}}{RT_{seg\ abv}\rho_{g,seg\ abv}} \int_{T_{ref}}^{T_{seg\ abv}} C_{p,j} dT \right) - \dot{m}_{tot} \sum_{\substack{\text{process} \\ \text{species } j}} \left(\frac{P_{j,seg}}{RT_i\rho_{g,seg}} \int_{T_{ref}}^{T_i} C_{p,j} dT \right)$	(161)
---	---------------

$+ h_{tg} 2\pi r_{in} \Delta y (T_{in\ wall} - T_i) - \Delta y \pi r_{in}^2 \rho_{cat} \sum_{\substack{\text{reforming} \\ \text{reactions } k}} \eta_k r_k (\Delta H_k - RT_i \Delta n_j) \Delta t =$	
--	--

Process-Gas Material Balance (f_i, i=99..170)

Mass of H ₂ Accumulating in a volume of gas enclosed in segment of height Δy over time Δt	= Mass of H ₂ flowing in at y - Mass of H ₂ flowing out at y+Δy + Change in H ₂ due to production or consumption by reforming reactions	(162)
--	--	----------------

Mass of H ₂ flowing in at y	$= \dot{m}_{tot} Y_{H_2} \Big _y \Delta t$ <p style="text-align: center;"> Where $Y_{H_2} = \frac{P_{H_2} M_{H_2}}{\sum_{\substack{\text{process} \\ \text{species } j}} P_j M_j} = \frac{P_{H_2} M_{H_2}}{RT\rho_g}$ </p> $= \dot{m}_{tot} \frac{P_{H_2} M_{H_2}}{RT\rho_g} \Big _y \Delta t$ $= \left[\frac{\text{kg}_{total}}{\text{h}} \right] \frac{\left[\text{kPa}_{H_2} \right] \left[\frac{\text{kg}_{H_2}}{\text{gmol}_{H_2}} \right]}{\left[\frac{\text{kPa} \cdot \text{m}^3}{\text{gmol} \cdot \text{K}} \right] \left[\text{K} \right] \left[\frac{\text{kg}_{total}}{\text{m}^3} \right]} [\text{h}]$ $= [\text{kg}_{H_2}]$	(163)
--	---	----------------

Mass of H ₂ flowing out at y+Δy	$= m_{\text{tot}} \frac{P_{\text{H}_2} M_{\text{H}_2}}{RT \rho_g} \Big _{y+\Delta y} \Delta t$ $= \left[\frac{\text{kg}_{\text{total}}}{\text{h}} \right] \frac{\left[\text{kPa}_{\text{H}_2} \right] \left[\frac{\text{kg}_{\text{H}_2}}{\text{gmol}_{\text{H}_2}} \right]}{\left[\frac{\text{kPa} \cdot \text{m}^3}{\text{gmol} \cdot \text{K}} \right] \left[\text{K} \right] \left[\frac{\text{kg}_{\text{total}}}{\text{m}^3} \right]} [\text{h}]$ $= [\text{kg}_{\text{H}_2}]$	(164)
---	--	----------------

Net Change in mass of H ₂ due to production or consumption by reforming reactions	$= M_{\text{H}_2} \Delta y \pi r_{\text{ini}}^2 \rho_{\text{cat}} (\eta_1 \xi_{1,\text{H}_2} r_1 + \eta_2 \xi_{2,\text{H}_2} r_2 + \eta_3 \xi_{3,\text{H}_2} r_3) \Delta t$ $= \left[\frac{\text{kg}_{\text{H}_2}}{\text{gmol}_{\text{H}_2}} \right] [\text{m}] \left[\text{m}^2 \right] \left[\frac{\text{kg}_{\text{cat}}}{\text{m}^3_{\text{segment}}} \right] *$ $\left[\frac{\text{gmol}_{\text{CH}_4 \text{ or CO}}}{\text{kg}_{\text{cat}} \text{ h}} \right] \left[\frac{\text{gmol}_{\text{H}_2}}{\text{gmol}_{\text{CH}_4 \text{ or CO}}} \right] [\text{h}]$ $= [\text{kg}_{\text{H}_2}]$	(165)
---	---	----------------

Since the process gas in the control volume is at steady state, there is no hydrogen accumulating in the tube segment over time Δt. Combine the terms and divide by Δt.

$0 = \dot{m}_{\text{tot}} \frac{P_{\text{H}_2} M_{\text{H}_2}}{RT \rho_g} \Big _y - \dot{m}_{\text{tot}} \frac{P_{\text{H}_2} M_{\text{H}_2}}{RT \rho_g} \Big _{y+\Delta y}$ $+ M_{\text{H}_2} \Delta y \pi r_{\text{ini}}^2 \rho_{\text{cat}} (\eta_1 \xi_{1,\text{H}_2} r_1 + \eta_2 \xi_{2,\text{H}_2} r_2 + \eta_3 \xi_{3,\text{H}_2} r_3)$	(166)
---	--------

Replace the subscript H₂ by generic species k and the subscript y by the above tube segment subscript.

$0 = \dot{m}_{\text{tot}} \frac{P_{\text{k,seg abv}} M_{\text{k}}}{RT_{\text{seg abv}} \rho_{\text{g,seg abv}}} - \dot{m}_{\text{tot}} \frac{P_{\text{k,seg}} M_{\text{k}}}{RT_{\text{seg}} \rho_{\text{g,seg}}}$ $+ M_{\text{k}} \Delta y \pi r_{\text{ini}}^2 \rho_{\text{cat}} (\eta_1 \xi_{1,\text{A}} r_1 + \eta_2 \xi_{2,\text{A}} r_2 + \eta_3 \xi_{3,\text{A}} r_3)$	(167)
--	--------

Pressure-Drop Correlation (f_i, i=171..174)

The pressure-drop correlation (168) was taken from Froment and Bischoff (1979; p. 403).

$\Delta P = -f \frac{\rho_{\text{pg}} v_s^2}{D_p} \Delta y \frac{1}{1000}$ $= [\text{none}] \frac{\left[\frac{\text{kg}}{\text{m}^3} \right] \left[\frac{\text{m}}{\text{s}} \right]^2}{[\text{m}]} [\text{m}] \frac{[\text{kPa}]}{[\text{Pa}]} = \left[\frac{\text{N}}{\text{m}^2} \right] \frac{[\text{kPa}]}{[\text{Pa}]} = [\text{kPa}]$	(168)
---	--------

The friction factor (f) in equation (168) is calculated in Appendix E. The pressure in a tube segment depends on the pressure of the gas entering the tube segment and the pressure drop that occurs over the tube segment.

$P_{\text{seg}} = P_{\text{seg abv}} + \Delta P$	(169)
--	---------------

Equation (169) is used to produce an algebraic equation that evaluates to zero.

$0 = P_{\text{seg abv}} - P_{\text{seg}} - f \frac{\rho_{\text{g,seg}} V_{\text{s,seg}}^2}{D_p} \Delta y \frac{1}{1000}$	(170)
--	---------------

The total pressure in a tube segment will be the sum of the partial pressure of all species in that tube segment. The purpose of the pressure drop correlation is not to solve for the pressure in the tube segment, but to provide an additional equation to solve for the gas density ($\rho_{\text{g,seg}}$) in the tube segment.

Average-Tube Model Derivations (10-Vertical-Section Model)

The model equations for the average-tube model are very similar to the model equations for the segmented-tube model. Terms that are common to both models are not completely derived in this section. The four major differences between the average-tube model equations and the segmented-tube model equations are i) the addition of isothermal water-cracking to remove higher alkanes; ii) an increase in the number of tubes in each vertical section from one tube in the segmented-tube model to N_{tubes} in the average-tube model; iii) the addition of coffin boxes on the furnace side of the average-tube model; iv) a change in the form of the radiation out terms on the furnace side to minimize numerical error.

Calculation of Q_{halokane} : Energy Balance on Isothermal Water-Cracking

The higher alkanes in the process-side feed are cracked isothermally using reaction (45) and the heat released is added to the top zone of the process side. The treatment of higher-alkanes as shown in Figure 16 is similar to the pre-combustion of furnace fuel.

Internal Energy Changes in Control Volume over time Δt	= Enthalpy In – Enthalpy Out – Heat Removed	(171)
---	---	---------------

Enthalpy In	$= \dot{n}_1 \sum_{\text{species } i} X_{i,1} \int_{T_{\text{ref}}}^{T_1} C_{p,i} dT \Delta t$ $= \left[\frac{\text{gmol}}{\text{h}} \right] \left[\frac{\text{gmol}_i}{\text{gmol}} \right] \left[\frac{\text{J}}{\text{gmol}_i \text{K}} \right] [\text{K}] [\text{h}] = [\text{J}]$	(172)
-------------	---	---------------

Enthalpy Out	$= \dot{n}_2 \sum_{\text{species } i} X_{i,2} \int_{T_{\text{ref}}}^{T_1} C_{p,i} dT \Delta t$ $= \left[\frac{\text{gmol}}{\text{h}} \right] \left[\frac{\text{gmol}_i}{\text{gmol}} \right] \left[\frac{\text{J}}{\text{gmol}_i \text{K}} \right] [\text{K}] [\text{h}] = [\text{J}]$	(173)
--------------	---	---------------

Heat Removed	$= Q_{\text{halokane}} \Delta t$ $= \left[\frac{\text{J}}{\text{h}} \right] [\text{h}] = [\text{J}]$	(174)
--------------	---	---------------

<p>Internal Energy Changes in Volume over time Δt</p>	$= \Delta H_{\text{reaction}} - RT_1 \Delta n_{\text{reaction}}$ <p>Since the water-cracking is instantaneous and goes to completion, the rate of reaction for each species is the molar flowrate of the higher alkane species on the process side. The enthalpy of water-cracking ($\Delta H_{j,\text{wcrack}}$) is calculated from the heat of formation of the reactants and products as shown in Appendix E.</p> $= \dot{n}_1 \Delta t \sum_{\substack{\text{higher-alkane} \\ \text{species } j}} X_{j,1} (\Delta H_{j,\text{wcrack}} - RT_1 \Delta n_{j,\text{wcrack}})$ $= \left[\frac{\text{gmol}}{\text{h}} \right] [\text{h}] \left[\frac{\text{gmol}_j}{\text{gmol}} \right] \left[\frac{\text{J}}{\text{gmol}_j} \right] = [\text{J}]$	<p>(175)</p>
--	--	----------------

Combine the terms in the energy balance into one equation. Divide by Δt and move all terms to the right hand side.

$0 = \dot{n}_1 \sum_{\text{species } i} X_{i,1} \int_{T_{\text{ref}}}^{T_1} C_{p,i} dT - \dot{n}_2 \sum_{\text{species } i} X_{i,2} \int_{T_{\text{ref}}}^{T_1} C_{p,i} dT - Q_{\text{halkane}}$ $- \dot{n}_1 \sum_{\substack{\text{higher-alkane} \\ \text{species } j}} X_{j,1} (\Delta H_{j,\text{wcrack}} - RT_1 \Delta n_{j,\text{wcrack}})$	<p>(176)</p>
---	----------------

Since $T_{\text{ref}} = T_1$, the integrals in the enthalpy terms evaluate to zero.

$Q_{\text{halkane}} = \dot{n}_1 \sum_{\substack{\text{higher-alkane} \\ \text{species } j}} X_{j,6} (\Delta H_{j,\text{comb}} - RT_6 \Delta n_{j,\text{comb}})$	(177)
---	----------------

Furnace-Surface-Zone Energy Balance (f_i, i=1..38)

Energy Accumulating in Surface Zone over period of time Δt	= Energy in by radiation from all furnace zones - Energy out by radiation to all furnace zones + Energy gained by convection from the furnace gas - Energy lost to the surroundings by conduction	(178)
--	--	----------------

The radiation-out term used in the average tube model is different from the radiation-out term used in the segmented-tube model. The complexity of the furnace in the average-tube model causes the summation rules for directed-flux areas to contain minor errors. To minimize the impact of these errors, the individual directed-flux areas are used in a summation to better match the directed-flux areas in the radiation-in term. Adopting this approach reduced E_{fur} by several percent.

Energy out by radiation to all furnace zones	$= \sigma \sum_{\substack{\text{furnace} \\ \text{zones } j}} (\overline{Z_i Z_j} T_i^4) \Delta t$ $= \sigma \sum_{\substack{\text{furnace} \\ \text{zones } j}} \sum_{\substack{\text{gray gas} \\ \text{atmospheres } k}} (b_{1,k} + b_{2,k} T_i) \overline{Z_i Z_j} \Big _k T_i^4 \Delta t$ $= \left[\frac{\text{J}}{\text{h} \cdot \text{m}^2 \text{K}^4} \right] [\text{m}^2 [\text{K}^4] [\text{h}]] = [\text{J}]$	(179)
--	---	----------------

$0 = \sigma \left(\sum_{\substack{\text{furnace} \\ \text{zones } j}} \sum_{\substack{\text{gray gas} \\ \text{atmospheres } k}} \left[(b_{1,k} + b_{2,k} T_j) \overline{Z_j Z_i} \Big _k T_j^4 - (b_{1,k} + b_{2,k} T) \overline{Z_i Z_j} \Big _k T_i^4 \right] \right)$ $+ h_{\text{gso}} A_i (T_{\text{adj gas}} - T_i) - \frac{k_{\text{refrac}}}{t_{\text{refrac}}} A_i (T_i - T_{\text{surr}})$	(180)
---	---------------

Furnace-Obstacle-Zone Energy Balance (f_i, i=39..51)

In the average-tube model there are two types of obstacle zones, tube-obstacle zones and coffin-box obstacle zones. The energy balance for a tube-obstacle zone in the average-tube model differs from an energy balance for a tube-obstacle zone in the segmented-tube model by the number of tubes contained in one vertical section. In the average-tube model there are N_{tubes} in each vertical section while in the segmented-tube model there is only one. The tube and coffin-box obstacle zone energy balances differ only in the conduction term. Since conduction through the coffin-box walls is assumed to be negligible the conduction term (the last term) in equation (183) is not present in the energy balance for a coffin box.

Energy Accumulating in Obstacle Zone over period of time Δt	= Energy in by radiation from all furnace zones - Energy out by radiation to all furnace zones + Energy gained by convection from the furnace gas - Energy lost from the obstacle by conduction	(181)
---	--	---------------

Energy lost from tubes by conduction	$= \frac{2\pi k_{\text{tube}} \Delta y N_{\text{tubes}} (T_i - T_{\text{in wall}})}{\ln\left(\frac{r_{\text{out}}}{r_{\text{in}}}\right)} \Delta t$ $= \left[\frac{\text{J}}{\text{h} \cdot \text{m} \cdot \text{K}} \right] [\text{m}] [\text{K}] [\text{h}] = [\text{J}]$	(182)
--------------------------------------	--	----------------

	$0 = \sigma \left(\sum_{\substack{\text{furnace} \\ \text{zones j}}} \sum_{\substack{\text{gray gas} \\ \text{atmospheres k}}} \left[(b_{1,k} + b_{2,k} T_j) \overline{Z_j Z_i} \Big _k T_j^4 - (b_{1,k} + b_{2,k} T_i) \overline{Z Z_j} \Big _k T_i^4 \right] \right)$ $+ h_{\text{gso}} A_i (T_{\text{adj gas}} - T_i) - \left[\frac{2\pi k_{\text{tube}} \Delta y N_{\text{tubes}} (T_i - T_{\text{in wall}})}{\ln\left(\frac{r_{\text{out}}}{r_{\text{in}}}\right)} \right]_{\text{tube zones only}}$	(183)
--	--	----------------

Furnace-Volume-Zone Energy Balance (f_i, i=52..62)

Energy Changes in Volume Zone over period of time Δt	= Energy in by radiation from all furnace zones - Energy lost by radiation to all furnace zones - Energy lost by convection to surfaces and obstacles + Enthalpy of gas in from zone above - Enthalpy of gas out + Heat released into zone by combustion	(184)
--	---	----------------

$f_i = 0 = \sigma \left(\sum_{\substack{\text{furnace} \\ \text{zones } j}} \sum_{\substack{\text{gray gas} \\ \text{atmospheres } k}} \left[(b_{1,k} + b_{2,k} T_j) \overline{Z_j Z_i} \Big _k T_j^4 - (b_{1,k} + b_{2,k} T_i) \overline{Z_i Z_j} \Big _k T_i^4 \right] \right)$ $- \sum_{\substack{\text{adjacent} \\ \text{surface and} \\ \text{obstacles } j}} [h_{\text{gso}} A_j (T_i - T_j)] - \dot{n}_{\text{fur}} \sum_{\substack{\text{furnace} \\ \text{species } j}} X_j \int_{T_i}^{T_{\text{fur,abv}}} C_{p,j} dT + \alpha(k_i) Q_{\text{comb}}$	(185)
---	----------------

Inner-Tube-Surface Energy Balance (f_i, i=62..71)

Energy Accumulating at the inner tube surface of a tube segment of height Δy over time Δt	= Energy entering by conduction over time Δt - Energy exiting by convection over time Δt	(186)
---	---	----------------

$0 = \frac{2\pi k_{\text{tube}} \Delta y N_{\text{tubes}} (T_{\text{out wall}} - T_i)}{\ln\left(\frac{r_{\text{out}}}{r_{\text{in}}}\right)} - h_{\text{tg}} 2\pi r_{\text{in}} \Delta y N_{\text{tubes}} (T_i - T_{\text{proc gas}})$	(187)
--	----------------

Process-Gas Energy Balance (f_i, i=72..81)

Energy changes in a control volume of gas enclosed in segment of height Δy over time Δt	= Enthalpy of Gas Entering at y - Enthalpy of Gas Exiting at y+Δy + Energy gained by convection from the tube surface	(188)
---	---	----------------

$0 = \dot{m}_{\text{tot}} \sum_{\text{process species } j} \left(\frac{P_{j,\text{seg abv}}}{RT_{\text{seg abv}} \rho_{g,\text{seg abv}}} \int_{T_{\text{ref}}}^{T_{\text{seg abv}}} C_{p,j} dT \right) - \dot{m}_{\text{tot}} \sum_{\text{process species } j} \left(\frac{P_{j,\text{seg}}}{RT_{\text{seg}} \rho_{g,\text{seg}}} \int_{T_{\text{ref}}}^{T_{\text{seg}}} C_{p,j} dT \right)$ $+ h_{\text{tg}} 2\pi r_{\text{in}} \Delta y N_{\text{tubes}} (T_{\text{in wall}} - T_{\text{seg}}) - \Delta y N_{\text{tubes}} \pi r_{\text{in}}^2 \rho_{\text{cat}} \sum_{\text{reforming reactions } j} \eta_j r_j (\Delta H_j - RT_{\text{seg}} \Delta n_j)$	(189)
--	----------------

Process-Gas Material Balance (f_i, i=82..140)

Mass of species k accumulating in a control volume of gas enclosed in segment of height Δy over time Δt	= Mass of k flowing in at y - Mass of k flowing out at y+Δy + Change in k due to production or consumption by reforming reactions	(190)
---	--	----------------

$0 = \dot{m}_{\text{tot}} \frac{P_{k,\text{seg abv}} M_k}{RT_{\text{seg abv}} \rho_{g,\text{seg abv}}} - \dot{m}_{\text{tot}} \frac{P_{k,\text{seg}} M_k}{RT_{\text{seg}} \rho_{g,\text{seg}}}$ $+ M_k \Delta y N_{\text{tubes}} \pi r_{\text{in}}^2 \rho_{\text{cat}} (\xi_{1,k} \eta_1 r_1 + \xi_{2,k} \eta_2 r_2 + \xi_{3,k} \eta_3 r_3)$	(191)
--	----------------

Pressure Drop Correlation (f_i, i=141..150)

The pressure drop correlation (192) was taken from Froment and Bischoff (1979; p. 403).

$\Delta P = -f \frac{\rho_{\text{pg}} V_s^2}{D_p} \Delta y \frac{1}{1000}$	(192)
--	----------------

$[\text{psia}] = [\text{none}] \frac{\left[\frac{\text{kg}}{\text{m}^3} \right] \left[\frac{\text{m}}{\text{s}} \right]^2}{[\text{m}]} [\text{m}] \frac{[\text{kPa}]}{[\text{Pa}]} = \left[\frac{\text{N}}{\text{m}^2} \right] \frac{[\text{kPa}]}{[\text{Pa}]} = [\text{kPa}]$	
--	--

$P_{\text{seg}} = P_{\text{seg abv}} + \Delta P$	(193)
--	----------------

Equation (193) is used to produce an algebraic equation that evaluates to zero. An algebraic equation of this form can be solved by the Newton-Raphson solver.

$0 = P_{\text{seg abv}} - P_{\text{seg}} - f \frac{\rho_{\text{pg,seg}} v_{\text{s,seg}}^2}{g_c D_p} \Delta y \frac{1}{144}$	(194)
--	----------------

Overall Energy Balances

To ensure the model equations are consistent an energy balance on the complete reformer (furnace and process sides) and separately on the furnace side and process side is performed. If the model equations are consistent, the solution vector \mathbf{x} will satisfy the overall-balance equations energy balances. In addition to checking for model consistency, the overall energy balances allow the calculation of performance ratios. Figure 17 is a simplified diagram of a reformer that shows the flow of energy in and out of the furnace and process sides.

Energy Balances on Furnace Side

Error in furnace side energy	= Enthalpy of inlet furnace gas	(195)
------------------------------	---------------------------------	----------------

balance	<ul style="list-style-type: none"> - Enthalpy of outlet furnace gas + Heat released by combustion - Heat lost to the process side - Heat lost to the surroundings 	
---------	---	--

$$E_{\text{fur}} = (H_{\text{fur,in}} - H_{\text{fur,out}} + Q_{\text{comb}} - Q_{\text{loss}} - Q_{\text{tube}}) \Delta t \quad [\text{J}] \quad (196)$$

$$H_{\text{fur,in}} = \dot{n}_{\text{fur}} \sum_{\text{species } i} X_i \int_{T_{\text{ref}}}^{T_{\text{fur,in}}} C_{p,i} dT \quad \left[\frac{\text{J}}{\text{h}} \right] \quad (197)$$

$$H_{\text{fur,out}} = \dot{n}_{\text{fur}} \sum_{\text{species } i} X_i \int_{T_{\text{ref}}}^{T_{\text{fur,out}}} C_{p,i} dT \quad \left[\frac{\text{J}}{\text{h}} \right] \quad (198)$$

$$Q_{\text{loss}} = \sum_{\substack{\text{refractory} \\ \text{zones } i}} Q_{i,\text{conduct}} = \sum_{\substack{\text{refractory} \\ \text{zones } i}} \frac{k_{\text{refrac}}}{t_{\text{refrac}}} A_i (T_i - T_{\text{surr}}) \left[\frac{\text{J}}{\text{h}} \right] \quad (199)$$

$$Q_{\text{tube}} = \sum_{\substack{\text{outer tubel} \\ \text{wall zones } i}} Q_{i,\text{conduct}} = \sum_{\substack{\text{outer tube} \\ \text{wall zones } i}} \frac{2\pi k_{\text{tube}} \Delta y N_{\text{tubes}} (T_i - T_{\text{in wall}})}{\ln\left(\frac{r_{\text{out}}}{r_{\text{in}}}\right)} \left[\frac{\text{J}}{\text{h}} \right] \quad (200)$$

$$Q_{\text{comb}} = -\dot{n}_{\text{fur}} \sum_{\substack{\text{combustion} \\ \text{species } j}} X_{j,5} (\Delta H_{j,\text{comb}} - RT_{\text{fur,in}} \Delta n_{j,\text{reaction}}) \left[\frac{\text{J}}{\text{h}} \right] \quad (201)$$

Substitute equations (197) to (201) into equation (196) and divide by Δt .

$E_{\text{fur}} = \dot{n}_{\text{fur}} \sum_{\text{species } i} X_i \int_{T_{\text{fur,out}}}^{T_{\text{fur,in}}} C_{p,i} dT + Q_{\text{comb}} - \sum_{\substack{\text{refractory} \\ \text{zones } i}} \frac{k_{\text{refrac}}}{t_{\text{refrac}}} A_i (T_i - T_{\text{surr}}) \\ - \sum_{\substack{\text{outer tube} \\ \text{wall zones } i}} \frac{2\pi k_{\text{tube}} \Delta y N_{\text{tubes}} (T_i - T_{i \text{ in wall}})}{\ln\left(\frac{r_{\text{out}}}{r_{\text{in}}}\right)}$	(202)
---	----------------

Energy Balance on the Process Side

Error in process-side energy balance	= Enthalpy of inlet process gas - Enthalpy of outlet process gas + Heat released by higher-alkane cracking - Heat released by reforming reactions + Heat transferred from the furnace side	(203)
--------------------------------------	--	----------------

$E_{\text{proc}} = (H_{\text{proc,in}} - H_{\text{proc,out}} + Q_{\text{halkane}} - Q_{\text{reform}} + Q_{\text{tube}}) \Delta t \quad [\text{J}]$	(204)
---	----------------

$H_{\text{proc,in}} = \dot{n}_{\text{proc,in}} \sum_{\text{species } i} X_i \int_{T_{\text{ref}}}^{T_{\text{proc,in}}} C_{p,i} dT \quad \left[\frac{\text{J}}{\text{h}} \right]$	(205)
---	----------------

$H_{\text{proc,out}} = \dot{m}_{\text{tot}} \sum_{\substack{\text{process} \\ \text{species } i}} \left(\frac{P_i}{RT\rho_g} \int_{T_{\text{ref}}}^T C_{p,i} dT \right) \Bigg _{\text{bot,seg}} \left[\frac{\text{J}}{\text{h}} \right]$	(206)
--	----------------

$Q_{\text{reform}} = \sum_{\text{segments } i} \left[\Delta y \pi r_{\text{in}}^2 \rho_{\text{cat}} \sum_{\substack{\text{reformin g} \\ \text{reactions } j}} \eta_j r_j (\Delta H_j - RT_i \Delta n_j) \right] \left[\frac{\text{J}}{\text{h}} \right]$	(207)
---	----------------

Substitute the appropriate terms into equation (204).

$E_{\text{proc}} = \dot{n}_{\text{proc,in}} \sum_{\substack{\text{process} \\ \text{species } i}} X_i \int_{T_{\text{ref}}}^{T_{\text{proc,in}}} C_{p,i} dT - \dot{m}_{\text{tot}} \sum_{\substack{\text{process} \\ \text{species } i}} \left(\frac{P_i}{RT\rho_g} \int_{T_{\text{ref}}}^T C_{p,i} dT \right) \Bigg _{\text{bot,seg}} + Q_{\text{halkane}}$ $- \sum_{\substack{\text{all tube} \\ \text{segments } i}} \left[\Delta y \pi r_{\text{in}}^2 \rho_{\text{cat}} \sum_{\substack{\text{reformin g} \\ \text{reactions } j}} \eta_j r_j (\Delta H_j - RT_i \Delta n_j) \right]$ $+ \sum_{\substack{\text{outer tube} \\ \text{wall zones } i}} \frac{2\pi k_{\text{tube}} \Delta y N_{\text{tubes}} (T_i - T_{\text{in wall}})}{\ln \left(\frac{r_{\text{out}}}{r_{\text{in}}} \right)}$	(208)
--	----------------

Energy Balance on the Reformer

Error in overall reformer balances	= Enthalpy of inlet furnace gas - Enthalpy of outlet furnace gas + Enthalpy of inlet process gas - Enthalpy of outlet process gas	(209)
---------------------------------------	--	----------------

	+ Heat released by higher-alkane cracking - Heat released by reforming reactions + Heat Released by combustion - Heat lost to the surroundings	
--	---	--

$(E_{\text{refrm}} = H_{\text{fur,in}} - H_{\text{fur,out}} + H_{\text{proc,in}} - H_{\text{proc,out}} + Q_{\text{halkane}} - Q_{\text{reform}} + Q_{\text{comb}} - Q_{\text{loss}})\Delta t$	
[J]	(210)

Appendix D

Solution of Model Equations

Newton-Raphson Method

All versions of the furnace model involve the solution of N non-linear algebraic equations and N unknowns. The non-linear equations are represented by the vector equation \mathbf{f} and the unknowns by the unknown vector \mathbf{x} . Since all models developed in this thesis are steady state, all the equations in \mathbf{f} evaluate to zero. The general form of the equations is:

$\mathbf{f} = \begin{bmatrix} f_1(x_1, x_2, \dots, x_N) \\ \vdots \\ f_N(x_1, x_2, \dots, x_N) \end{bmatrix} = 0$	(211)
---	----------------

To solve the N unknowns in vector \mathbf{x} , the N equations in \mathbf{f} are solved using the Newton-Raphson method. A brief overview of the Newton-Raphson method is given below.

$0 = \mathbf{f} = \begin{bmatrix} f_1(x_1, x_2, \dots, x_N) \\ \vdots \\ f_N(x_1, x_2, \dots, x_N) \end{bmatrix}$
Write the non-linear function \mathbf{f} as a linear approximation around \mathbf{x}_k

$$0 = f(\mathbf{x}_k) + \begin{bmatrix} \left. \frac{\partial f_1}{\partial \mathbf{x}_1} \right|_{\mathbf{x}_{1,k}} (\mathbf{x}_{1,k+1} - \mathbf{x}_{1,k}) + \cdots + \left. \frac{\partial f_1}{\partial \mathbf{x}_N} \right|_{\mathbf{x}_{N,k}} (\mathbf{x}_{N,k+1} - \mathbf{x}_{N,k}) \\ \vdots \\ \left. \frac{\partial f_N}{\partial \mathbf{x}_1} \right|_{\mathbf{x}_{1,k}} (\mathbf{x}_{1,k+1} - \mathbf{x}_{1,k}) + \cdots + \left. \frac{\partial f_N}{\partial \mathbf{x}_N} \right|_{\mathbf{x}_{N,k}} (\mathbf{x}_{N,k+1} - \mathbf{x}_{N,k}) \end{bmatrix}$$

Simplify by factoring $(\mathbf{x}_{k+1} - \mathbf{x}_k)$

$$0 = f(\mathbf{x}_k) + \begin{bmatrix} \left. \frac{\partial f_1}{\partial \mathbf{x}_1} \right|_{\mathbf{x}_{1,k}} & \cdots & \left. \frac{\partial f_1}{\partial \mathbf{x}_N} \right|_{\mathbf{x}_{N,k}} \\ \vdots & & \vdots \\ \left. \frac{\partial f_N}{\partial \mathbf{x}_1} \right|_{\mathbf{x}_{1,k}} & \cdots & \left. \frac{\partial f_N}{\partial \mathbf{x}_N} \right|_{\mathbf{x}_{N,k}} \end{bmatrix} \begin{bmatrix} (\mathbf{x}_{1,k+1} - \mathbf{x}_{1,k}) \\ \vdots \\ (\mathbf{x}_{N,k+1} - \mathbf{x}_{N,k}) \end{bmatrix}$$

Replace the partial derivative term by the Jacobian (\mathbf{J}) and write \mathbf{x}_{k+1} and \mathbf{x}_k in vector form.

$$0 = f(\mathbf{x}_k) + \mathbf{J}(\mathbf{x}_k)(\mathbf{x}_{k+1} - \mathbf{x}_k)$$

Solve for the vector \mathbf{x}_{k+1} .

$$\mathbf{x}_{k+1} = -\mathbf{J}(\mathbf{x}_k)^{-1} f(\mathbf{x}_k) + \mathbf{x}_k$$

An iterative method is used to solve the non-linear equation \mathbf{f} .

1. Choose an initial guess \mathbf{x}_k
2. Compute $\mathbf{J}(\mathbf{x}_k)^{-1}$ and $\mathbf{f}(\mathbf{x}_k)$
3. Check tolerance criteria for \mathbf{f} : $\sum \frac{|f_i|}{|\beta|} < f$ tolerance.

Where β is the magnitude of the terms in equation f_i

 - a. If tolerance criteria are met then \mathbf{x}_k is the solution
 - b. Else continue to step 4.
4. Compute \mathbf{x}_{k+1}
5. Check tolerance criteria for \mathbf{x} : $\sum \frac{|x_{k+1,i} - x_{k,i}|}{|\kappa|} < x$ tolerance

Where κ is the magnitude of the solution x_i

 - a. If tolerance criteria are met the solution is \mathbf{x}_{k+1}
 - b. Else set \mathbf{x}_k to \mathbf{x}_{k+1} and repeat steps 2-5.

The Newton-Raphson method used in the model was developed from the True Basic version on the Numerical Recipes code cd-rom (Press et al., 2002b). An explanation of the algorithm and its subroutines is available in Numerical Recipes textbook (Press et al., 2002a; p. 1194).

Initial Guesses

The three methods of that were developed for generating initial guesses for the segmented-tube model and average-tube model and are i) the common-vertical-segment method ii) the sequential-solution method and iii) the direct-assignment method.

Common-Vertical-Segment Initial-Guess Method

The robustness of the Newton-Raphson solver appears to be sensitive to the initial guesses for the process-side partial pressures, temperatures and density, but relatively insensitive to the initial guesses for the furnace zone temperatures. In the common-vertical-segment initial-guess method the properties of one segment are assigned to all process-side segments and common temperatures

are assigned to all furnace-zone types. The process-side gas temperature, species partial pressures and gas density from the outlet of an industrial SMR are used as default initial segment properties and are assigned to all tube segments. The furnace-zone initial guesses and tube-segment initial guesses are shown in Table 24.

Table 24. Furnace-Zone Type and Process-Side Segment Initial Guesses for the Common-Vertical-Segment Initial-Guess Method

Name and Units	Value
Furnace Gas Inlet Temperature [K]	1340
Furnace-Surface-Zone Temperature [K]	1256
Outer-Tube-Wall Temperature [K]	978
Coffin-Box-Surface Temperature [K]	1144
Furnace-Volume-Zone Temperature [K]	1367
Inner-Tube-Wall Temperature [K]	1144
Process-Gas Temperature [K]	1144
Partial Pressure of H ₂ in the process gas [kPa]	1506
Partial Pressure of CO in the process gas [kPa]	285
Partial Pressure of CH ₄ in the process gas [kPa]	146
Partial Pressure of N ₂ in the process gas [kPa]	6
Partial Pressure of CO ₂ in the process gas [kPa]	172
Partial Pressure of H ₂ O in the process gas [kPa]	1048
Process-Gas Density $\left[\frac{\text{kg}}{\text{m}^3} \right]$	3.84

The common-vertical-segment initial-guess method appeared to be the most reliable initial-guess method as it rarely lead to solver failure. It is flexible since it can be used with models that contain different numbers of vertical sections. However, the method can be inefficient since the

solution vector \mathbf{x} is typically very different from the initial guess, resulting in many iterations before solver convergence.

Sequential-Solution Initial-Guess Method

The sequential-solution initial-guess method almost never leads to solver failure, but appears to be inefficient. In the sequential-solution method, temperatures are assigned to all furnace-zone types and the tube segments are turned on one at a time starting with the top segment. The initial guesses for the top segment are the process inlet temperatures and compositions. All remaining tube segments are assigned the temperature, composition and density of the process-side outlet and their energy and material balances are turned off. The solver is called and the process-gas temperature, composition and density for the top segment are calculated. The second segment from the top is now activated, and the solution to the top zone is entered as the initial guess in the second segment. The solver is called again and the second segment process-gas temperature, composition and density are calculated. The procedure is repeated for some or all of the segments. Typically once the top five or six zones are calculated sequentially the energy and material balances of all zones can be activated and the solver will converge. This method is time-consuming since it requires many calls of the Newton-Raphson solver. However, the sequential nature of solving for initial guesses means the sequential-solution initial-guess method rarely fails.

Direct-Assignment Initial-Guess Method

The direct-assignment initial-guess method leads to rapid solver convergence but has a greater chance of failing than the other two methods. In the direct-assignment method, the results of a

previous successful solution are used as the initial guess to the next solution. If the previous solution occurred with very different inlet conditions then the solver may not converge.

References

Press, W. H., Teukolsky, S. A., Vetterling, W. T., Flannery, B. P. and Metcalf, M. (2002a)
Numerical recipes in Fortran 90: The Art of Scientific Computing. Cambridge University Press,
New York, NY.

Press, W. H., Teukolsky, S. A., Vetterling, W. T. and Flannery, B. P. (2002b) Numerical recipes
code cdrom v 2.10. Cambridge University Press, New York, NY.

Appendix E

Supplemental Correlations Used in Model

Enthalpy of Reaction

The enthalpies of reaction at a given temperature are calculated using the heats for formation of the reactants and products at the reaction temperature. This method was used to calculate the enthalpy of reaction for the combustion of furnace fuel, for steam-methane reforming and for the water-cracking of higher alkanes.

$\Delta H_{\text{reaction}}^T = \sum_{\substack{\text{reaction} \\ \text{species } i}} \xi_i \Delta H_{f,i}^T \left[\frac{\text{J}}{\text{gmol}} \right]$	(212)
--	---------

$\Delta H_{f,i}^T = \Delta H_{f,i}^\circ + \int_{298\text{K}}^T C_{p,i} dT * 4.186$	(213)
$\left[\frac{\text{J}}{\text{gmol}} \right] = \left[\frac{\text{J}}{\text{gmol}} \right] + \left[\frac{\text{cal}}{\text{gmol}} \right] \left[\frac{\text{J}}{\text{cal}} \right]$	

Values for the standard heat of formation were taken from Reid et al. (1977).

Constant Pressure Heat Capacity

The constant pressure heat capacities are evaluated using a third order polynomial expression (Reid et al. 1977, p. 226).

$C_{p,i} = A_i + B_i T + C_i T^2 + D_i T^3 \left[\frac{\text{cal}}{\text{gmol} \cdot \text{K}} \right]$ <p>The temperature used in the integral must be in Kelvin.</p> $\int_{T_{\text{ref}}}^T C_{p,i} dT = \left[\left(A_i T + \frac{B_i}{2} T^2 + \frac{C_i}{3} T^3 + \frac{D_i}{4} T^4 \right) \right] * 4.186$ $\left[- \left(A_i T_{\text{ref}} + \frac{B_i}{2} T_{\text{ref}}^2 + \frac{C_i}{3} T_{\text{ref}}^3 + \frac{D_i}{4} T_{\text{ref}}^4 \right) \right] * 4.186$ $\int_{T_{\text{ref}}}^T C_{p,i} dT = \left[\frac{\text{cal}}{\text{gmol}} \right] * \left[\frac{\text{J}}{\text{cal}} \right] = \left[\frac{\text{J}}{\text{gmol}} \right]$	<p>(214)</p>
--	-----------------------

Furnace-Gas-to-Tube Convective-Heat-Transfer Coefficient

The furnace-gas-to-surface convective heat transfer coefficient is calculated using the Nusselt number and the Dittus-Boelter correlation (Incropera and DeWitt, 2002; p. 491).

$h_{\text{gso}} = \frac{\lambda_{\text{fg}}}{D_{\text{fur hydr}}} 0.023 \text{Re}^{\frac{4}{5}} \text{Pr}^{\frac{1}{3}}$ $\left[\frac{\text{J}}{\text{m}^2 \text{h} \cdot \text{K}} \right] = \left[\frac{\text{J}}{\text{m} \cdot \text{h} \cdot \text{K}} \right] \left[\frac{1}{\text{m}} \right] [\text{none}]$	<p>(215)</p>
--	-----------------------

The furnace gas thermal conductivity is calculated according to the Gas Thermal Conductivity Calculations in Appendix E. The Reynolds number and Prandtl number for the furnace gas are calculated from equations (216) and (217).

$\text{Re} = \frac{D_{\text{fur hydr}} \frac{\dot{m}_{\text{fur}}}{A_{\text{fur cross}}}}{\mu_{\text{fg}}}$ $[\text{none}] = \frac{[\text{m}] \frac{[\text{kg}]}{[\text{m}^2]} \frac{[\text{h}]}{[\text{m}^2]}}{[\frac{\text{kg}}{\text{m} \cdot \text{h}}]}$	(216)
---	---------------

$\text{Pr} = \frac{C_{p, \text{avg}} \mu_{\text{fg}}}{M_{\text{avg}} \lambda_{\text{fg}}}$ $[\text{none}] = \frac{[\frac{\text{J}}{\text{gmol} \cdot \text{K}}] [\frac{\text{kg}}{\text{m} \cdot \text{h}}]}{[\frac{\text{kg}}{\text{gmol}}]} \div [\frac{\text{J}}{\text{m} \cdot \text{h} \cdot \text{K}}]$	(217)
---	---------------

The gas viscosity in equations (216) and (217) is calculated according to the Gas Viscosity Calculations in Appendix E.

Tube-to-Process-Gas Convective-Heat-Transfer Coefficient

The tube-to-process gas convective heat transfer coefficient was determined using the correlation developed by Leva and Grummer (1948).

$h_{tg} = 0.813f \frac{\lambda_{pg}}{2r_{in}} \exp\left(-6 \frac{D_p}{2r_{in}}\right) \left(\frac{D_p G_s}{\mu_{pg}}\right)^{0.9}$ $\left[\frac{J}{m^2 h \cdot K}\right] = \frac{\left[\frac{J}{m \cdot h \cdot K}\right]}{[m]} \exp\left(\frac{[m]}{[m]}\right) \left(\frac{[m] \left[\frac{kg}{m^2 \cdot h}\right]}{\left[\frac{kg}{m \cdot h}\right]}\right)^{0.9}$	(218)
--	----------------

Gas Viscosity Calculations

The gas viscosity was determined using first order Chapman-Enskog kinetic theory with Wilke's approximation to determine the interaction coefficient ($\phi_{i,j}$). (Reid et al. 1977; p. 411)

$\mu_{gas} = \frac{\sum_{i=0}^{species} X_i \mu_i}{\sum_{j=0}^{species} X_j \phi_{i,j}}$ $\mu_{gas} = \left[\frac{kg}{m \cdot h}\right]$ <p style="text-align: center;">Wilke interaction coefficients: $\phi_{i,j} = \frac{\left[1 + \left(\frac{\mu_i}{\mu_j}\right)^{\frac{1}{2}} \left(\frac{M_j}{M_i}\right)^{\frac{1}{4}}\right]^2}{\left[8 \left(1 + \frac{M_i}{M_j}\right)\right]^{\frac{1}{2}}} = [\text{none}]$</p>	(219)
---	----------------

The pure component viscosities were calculated using Chapman and Enskog method for non-polar pure gases at low pressure (Reid et al. 1977; p. 395).

$\mu_i = \frac{5}{16} \frac{(\pi MRT)^{\frac{1}{2}}}{(\pi \sigma^2) \Omega_v Na} \bigg _i * \frac{3600}{0.4536 \cdot 3.28}$ $\mu_i = \frac{\left(\left[\frac{\text{kg}}{\text{gmol}} \right] \left[\frac{\text{kg} \cdot \text{m}^2}{\text{s}^2 \cdot \text{gmol} \cdot \text{K}} \right] [\text{K}] \right)^{\frac{1}{2}}}{\left[\text{m}^2 \right] \left[\frac{1}{\text{molecule}} \right] \left[\frac{\text{molecule}}{\text{gmol}} \right]} \left[\frac{\text{lb}_m}{0.4536 \text{kg}} \right] \left[\frac{\text{m}}{3.281 \text{ft}} \right] \left[\frac{3600 \text{s}}{\text{h}} \right]$ $\mu_i = \left[\frac{\text{kg}}{\text{m} \cdot \text{s}} \right] \left[\frac{3600 \text{s}}{\text{h}} \right]$ $\mu_i = \left[\frac{\text{kg}}{\text{m} \cdot \text{h}} \right]$ <p>Where $\Omega_v = \left(\frac{Aw}{T_*^{Bw}} \right) + \frac{Cw}{\exp(DwT_*)} + \frac{Ew}{\exp(FwT_*)}$, for $0.3 \leq T_* \leq 100$</p> $T_* = \frac{kT}{\Sigma}, T \text{ in } \Omega_v \text{ is given in [K]}$	(220)
--	----------------

Gas Thermal Conductivity Calculations

The gas thermal conductivity is calculated using the Wassilijewa equation. (Reid et al. 1977, p. 508) The Wassilijewa equation is analogous to the relationship for gas viscosity mixtures.

$\lambda_{\text{gas}} = \frac{\sum_{i=0}^{\text{species}} X_i \lambda_i}{\sum_{j=0} X_j A_{i,j}}$ $\lambda_{\text{gas}} = \left[\frac{\text{J}}{\text{m} \cdot \text{h} \cdot \text{K}} \right]$	(221)
---	----------------

Lindsey and Bromely Interaction coefficients ($A_{i,j}$) are used in the Wassilijewa equation. (Reid et al. 1977, p. 509)

$A_{i,j} = \frac{1}{4} \left\{ 1 + \left[\frac{\mu_i}{\mu_j} \left(\frac{M_j}{M_i} \right)^{\frac{3}{4}} \left(\frac{T + S_i}{T + S_j} \right) \right]^{\frac{1}{2}} \right\}^2 \left(\frac{T + S_{i,j}}{T + S_i} \right) = [\text{none}]$ <p>Where $S_i = 1.5T_{\text{boil},i}$ and $S_{i,j} = S_{j,i} = C_s (S_i S_j)^{\frac{1}{2}}$</p> <p>$C_s = 1$ for non-polar and moderately polar gases</p>	(222)
---	----------------

To calculate the thermal conductivity of pure gases the Eucken Method for ideal gases is used. (Reid et al. 1977, p. 473)

$\lambda_i = \frac{\mu_i}{M_i} \left(C_{v,i} + \frac{9}{4} R \right)$ $\lambda_i = \frac{\left[\frac{\text{kg}}{\text{m} \cdot \text{h}} \right]}{\left[\frac{\text{kg}}{\text{gmol}} \right]} \left[\frac{\text{J}}{\text{gmol} \cdot \text{K}} \right] = \left[\frac{\text{J}}{\text{m} \cdot \text{h} \cdot \text{K}} \right]$	(223)
--	---------

Steam-Methane Reforming Reaction Kinetics

The rates of reaction were calculated using the rate expressions derived by Xu and Froment (1989a).

$\text{CH}_4(\text{g}) + \text{H}_2\text{O}(\text{g}) \xrightleftharpoons[k_{-1}]{k_1} 3\text{H}_2(\text{g}) + \text{CO}(\text{g}) \quad \Delta H_1$ $r_1 = \frac{k_1}{P_{\text{H}_2}^{2.5}} \left(P_{\text{CH}_4} P_{\text{H}_2\text{O}} - \frac{P_{\text{H}_2}^3 P_{\text{CO}}}{K_1} \right) / (\text{DEN})^2$ $r_1 = \frac{\left[\frac{\text{kgmol} \cdot \text{bar}^{\frac{1}{2}}}{\text{kg}_{\text{cat}} \text{h}} \right]}{\left[\text{bar}^{\frac{5}{2}} \right]} \left[\text{bar}^2 \right] = \left[\frac{\text{kgmol}}{\text{kg}_{\text{cat}} \text{h}} \right] \left[\frac{1000 \text{gmol}}{\text{kgmol}} \right]$ $r_1 = \left[\frac{\text{gmol}}{\text{kg}_{\text{cat}} \text{h}} \right]$	(224)
--	---------

Where DEN = $1 + K_{CO} P_{CO} + K_{H_2} P_{H_2} + K_{CH_4} P_{CH_4} + \frac{K_{H_2O} P_{H_2O}}{P_{H_2}}$ [none]	
--	--

$CH_4(g) + 2H_2O(g) \xrightleftharpoons[k_{-2}]{k_2} 4H_2(g) + CO_2(g) \quad \Delta H_2$ $r_2 = \frac{k_2}{P_{H_2}^{3.5}} \left(P_{CH_4} P_{H_2O}^2 - \frac{P_{H_2}^4 P_{CO_2}}{K_2} \right) / (DEN)^2$ $r_2 = \frac{\left[\frac{\text{kgmol} \cdot \text{bar}^{\frac{1}{2}}}{\text{kg}_{\text{cat}} \cdot \text{h}} \right]}{\left[\text{bar}^{\frac{7}{2}} \right]} [\text{bar}^3] = \left[\frac{\text{kgmol}}{\text{kg}_{\text{cat}} \cdot \text{h}} \right] \left[\frac{1000 \text{gmol}}{\text{kgmol}} \right]$	(225)
---	--------

$CO(g) + H_2O(g) \xrightleftharpoons[k_{-3}]{k_3} H_2(g) + CO_2(g) \quad \Delta H_3$ $r_3 = \frac{k_3}{P_{H_2}} \left(P_{CO} P_{H_2O} - \frac{P_{H_2} P_{CO_2}}{K_3} \right) / (DEN)^2$ $r_3 = \frac{\left[\frac{\text{kgmol}}{\text{kg}_{\text{cat}} \cdot \text{h} \cdot \text{bar}} \right]}{\left[\text{bar} \right]} [\text{bar}^2] = \left[\frac{\text{kgmol}}{\text{kg}_{\text{cat}} \cdot \text{h}} \right] \left[\frac{1000 \text{gmol}}{\text{kgmol}} \right]$	(226)
---	--------

The equilibrium constants, free energy of reaction, entropy of reaction and enthalpy of reaction for reactions 1, 2 and 3 are calculated using the following equilibrium expressions.

Thermodynamic constants used in the expressions are from Reid et al (1977).

All expressions are given for reforming reaction i and species j.

$$K_i = \exp\left(\frac{-\Delta G_i^T}{RT}\right) = \exp\left(\frac{\left[\frac{\text{kJ}}{\text{gmol}}\right]}{\left[\frac{\text{kJ}}{\text{gmol} \cdot \text{K}}\right][\text{K}]}\right) = [\text{none}]$$

$$\Delta G_i^T = \Delta H_i^T - T\Delta S_i^T = \left[\frac{\text{J}}{\text{gmol}}\right] + [\text{K}]\left[\frac{\text{J}}{\text{gmol} \cdot \text{K}}\right]$$

$$\Delta S_i^T = \sum_{\substack{\text{reaction} \\ \text{species } j}} \xi_{i,j} \Delta S_{f,j}^T = \left[\frac{\text{J}}{\text{gmol} \cdot \text{K}}\right]$$

$$\Delta H_i^T = \sum_{\substack{\text{reaction} \\ \text{species } j}} \xi_{i,j} \Delta H_{f,j}^T = \left[\frac{\text{J}}{\text{gmol}}\right]$$

$$\Delta S_{f,j}^T = \Delta S_{f,j}^{\circ} + \int_{298\text{K}}^T \frac{C_{p^?j}}{T} dT * 4.186$$

$$\Delta S_{f,X}^T = \left[\frac{\text{J}}{\text{gmol} \cdot \text{K}}\right] + \left[\frac{\text{cal}}{\text{gmol} \cdot \text{K}}\right] \left[\frac{\text{J}}{\text{cal}}\right] = \left[\frac{\text{J}}{\text{gmol} \cdot \text{K}}\right]$$

$$\Delta S_{f,X}^{\circ} = \frac{\Delta H_{f,X}^{\circ} - \Delta G_{f,X}^{\circ}}{T_{\text{std}}} = \frac{\left[\frac{\text{J}}{\text{gmol}}\right]}{[\text{K}]} = \left[\frac{\text{J}}{\text{gmol} \cdot \text{K}}\right]$$

(227)

$\Delta H_{f,X}^T = \Delta H_{f,X}^o + \int_{298K}^T C_p dT * 4.186 \left[\frac{J}{gmol} \right]$	
--	--

The reaction rate constants were calculated for reaction i using the Arrhenius equation and the adsorption equilibrium constants were calculated for species j using a thermodynamic expression for the adsorption equilibrium constant. (Xu and Froment 1989a)

$k_i = A_i \exp\left(\frac{-E_i}{RT}\right) \text{ units depend on the reforming reaction}$	(228)
$K_j = A_j \exp\left(\frac{-\Delta H_{adsb,j}}{RT}\right) \text{ units depend on the species in adsorption equilibrium}$	

Friction Factor

The friction factor developed by Ergun (1952) in the form provided by Froment and Bischof (1979; p. 406) is used in the pressure drop correlation.

$f = \frac{(1-\phi)}{\phi^3} \left[1.75 + \frac{150(1-\phi)}{Re} \right]$	(229)
--	--------

References

Incropera, F. P. and DeWitt, D. P. (2002) Fundamentals of heat and mass transfer. John Wiley and Sons, Hoboken, NJ.

Lawson, D. A. and Ziesler C. D. (1996) An accurate program for radiation modeling in the design of high-temperature furnaces. IMA Journal of Mathematics and Applied in Business and Industry. vol. 7 pp. 109-116.

Leva, M. and Grummer M. (1948) Heat transfer to gases through packed tubes: Effect of particle characteristics. Industrial and Engineering Chemistry. vol. 40 pp. 415-419.

Reid, C. R., Prausnitz, J. M. and Sherwood, T. K. (1977) The properties of Gases and Liquids. McGraw-Hill Book Company, New York, NY.

Taylor, B. P. and Foster, P. J. (1974) The total emissivities of luminous and non-luminous flames. International Journal of Heat and Mass Transfer. vol. 17 pp. 1591-1605.

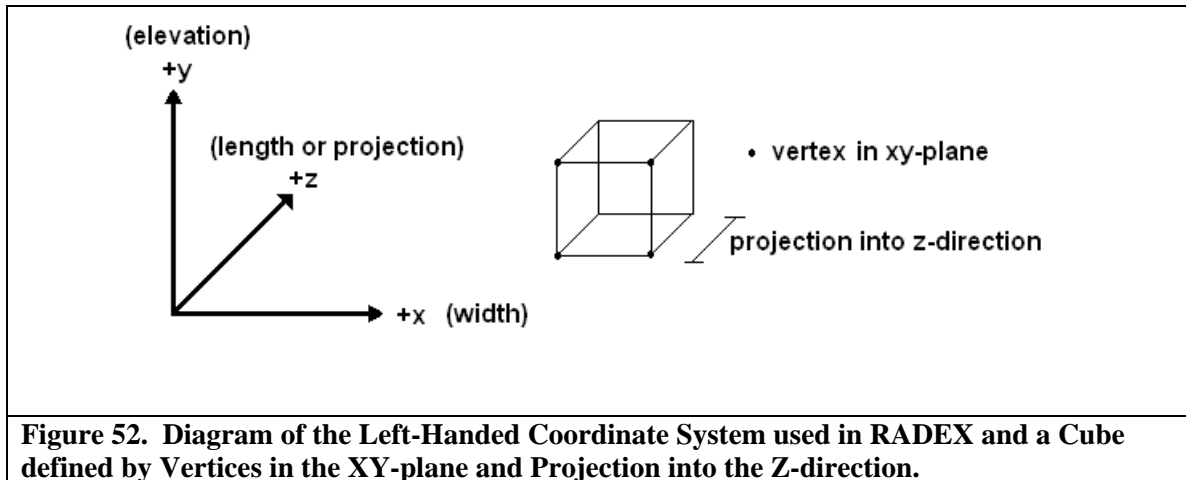
Xu, J. and Froment, G. F. (1989a) Methane steam reforming, methanation and water-gas shift: I Intrinsic Kinetics. AIChE Journal. vol. 35 pp. 88-96.

Appendix F

Geometric Restrictions, Furnace-Geometry Storage and Process-Side Geometry Storage

Geometric Subset of RADEX Understood by Model

In RADEX three-dimensional furnace geometries are defined by drawing the cross-section of the furnace in two-dimensions and then projecting the cross-section into a third dimension. As a result RADEX can only simulate furnaces that have a uniform cross-section. The RADEX manual uses a left-handed coordinate system. For the purpose of this thesis, elevation is defined as the positive y-direction and width as the positive x-direction. The furnace cross-section is drawn using vertices in the xy-plane. The z-direction is the direction of cross-section projection and is known as the furnace length (See Figure 52). The coordinate system used in RADEX and an illustration of how a cube is defined in RADEX is shown in Figure 52.



In addition to defining the shape of the furnace, tubes and boxes can be added to the furnace interior. Tubes must have their principal axis aligned with one of the coordinate axes and boxes must be aligned with all three coordinate axes. The average-tube model will only function with a subset of the furnace geometries possible in RADEX. The subset of geometric configurations that the average-tube model will read and understand is defined by geometry rules 1 to 8.

1. The cross section of the furnace in the xy-plane must be rectangular. Since RADEX projects the xy-plane cross-section in the z-direction the furnace must always be a rectangular prism.
2. The cross section in the xy-plane must have a height and width greater than one foot.
3. The first vertex defined in the xy-plane must be (0,0).
4. All vertices in the xy-plane must have positive x- and y-coordinates. All projections into the z-plane must be positive.
5. All tubes (tubes are called cylinders in RADEX) must have the same external radius
6. All tubes must be oriented vertically and must reach from the roof of the furnace to the floor
7. All coffin boxes (coffin boxes are called boxes in RADEX) must reach from the front of the furnace in the xy-plane to the back of the furnace.
8. All coffin boxes must have the same height

Numbering of Zones in RADEX

In RADEX, there are three zones types: surface zones, obstacle zones and volume zones. Surface zones are numbered first followed by obstacle zones and then volume zones. The numbering of

volume zones and obstacle zones is straight forward while the numbering of surface zones is more complicated. A complete description of zone numbering in RADEX is provided in the RADEX User Guide (Lawson, 1991). The next section gives a brief description of the RADEX numbering pattern and shows its application to a 2-by-2-by-2 cube (Figure 53), to the segmented-tube model (Figure 54) and to the average-tube model (Figure 55).

Numbering of Surface Zones in RADEX

The rectangular furnace volume is divided into zones by planes. In Figure 53, the x-grid planes are at $x=0$, $x=2$, and $x=4$; y-grid planes at $y=0$, $y=2$ and $y=4$ and the z-grid planes at $z=0$, $z=2$ and $z=4$. These planes divide the furnace enclosure into 24 surfaces. The RADEX user manual refers to these planes as the coarse grid or heat-transfer grid. The coarse grid is distinguished from the fine grid or geometric grid in the RADEX User Guide (Lawson, 1991). The fine grid is not discussed in this section. The coarse-grid planes divide the furnace into zones for radiative heat transfer. The surfaces defined by the coarse-grid planes are numbered by cycling through the z-planes, then the y-planes and then the x-planes. A simple example is given in Figure 53 and the surface-zone numbering of the segmented-tube model and average-tube model with ten vertical sections are shown in Figure 54 and Figure 55 respectively. A complete explanation of the surface numbering technique is given in Chapter 6 of the RADEX User Guide (Lawson, 1991). In Figure 55, the two bottom surface zones in the smallest and largest x-planes (the zones shaded in gray) are not numbered. This is because the surface zones are blocked by box obstacle zone and have zero area. RADEX only numbers surface zones that have non-zero area.

Numbering of Volume and Obstacle Zones in RADEX

The coarse-grid planes also create furnace-volume zones. Volume zones are numbered in the same fashion as surface zones by cycling through the z-planes, then the y-planes, and then the x-planes. If no obstacle zones are present, then volume zones are numbered after surface zones. For example in Figure 53 volume-zone 25 is numbered after the last surface zone 24. If obstacle zones are present, then they are numbered before volume zones in the order of their enclosing volume zones. For example in Figure 54, the volume zones are numbered from bottom to top starting at 63 and ending at 74. The obstacle zones in Figure 54 are numbered in the order of their enclosing volume zones starting at 51 at the bottom and finishing at 62 at the top. A volume zone may contain up to two separate obstacle zones. When an obstacle is added to the furnace interior in RADEX it must be declared as a sink or a source. For the purpose of this thesis no meaning is given to the terms sink and source they are simply terms used to distinguish two different obstacles in the same volume zone. If two obstacles exist in one volume zone then the sink is numbered first and the source second. If no obstacles exist in a volume zone then obstacle numbering continues with the next obstacle encountered. For example, in Figure 55, the bottom volume zones contain eight boxes and 336 tubes. Since only two obstacle zone types can exist in any given volume zone the 336 tubes are group together and assigned the label sink. The eight boxes are grouped together and assigned the label source. Since sink obstacles are numbered first, the tubes are assigned the number 39 and the boxes the number 40. The volume zones numbered 53 and 54 in Figure 55 also contain two different obstacle zones. However, volume zones 55 to 61 in Figure 55 contain only on type of obstacle zone. As a result the tube obstacles are numbered continuously in volume zones 55 to 61 in Figure 55. Again a more through

explanation of volume and obstacle zone numbering is available in the RADEX user manual (Lawson, 1991).

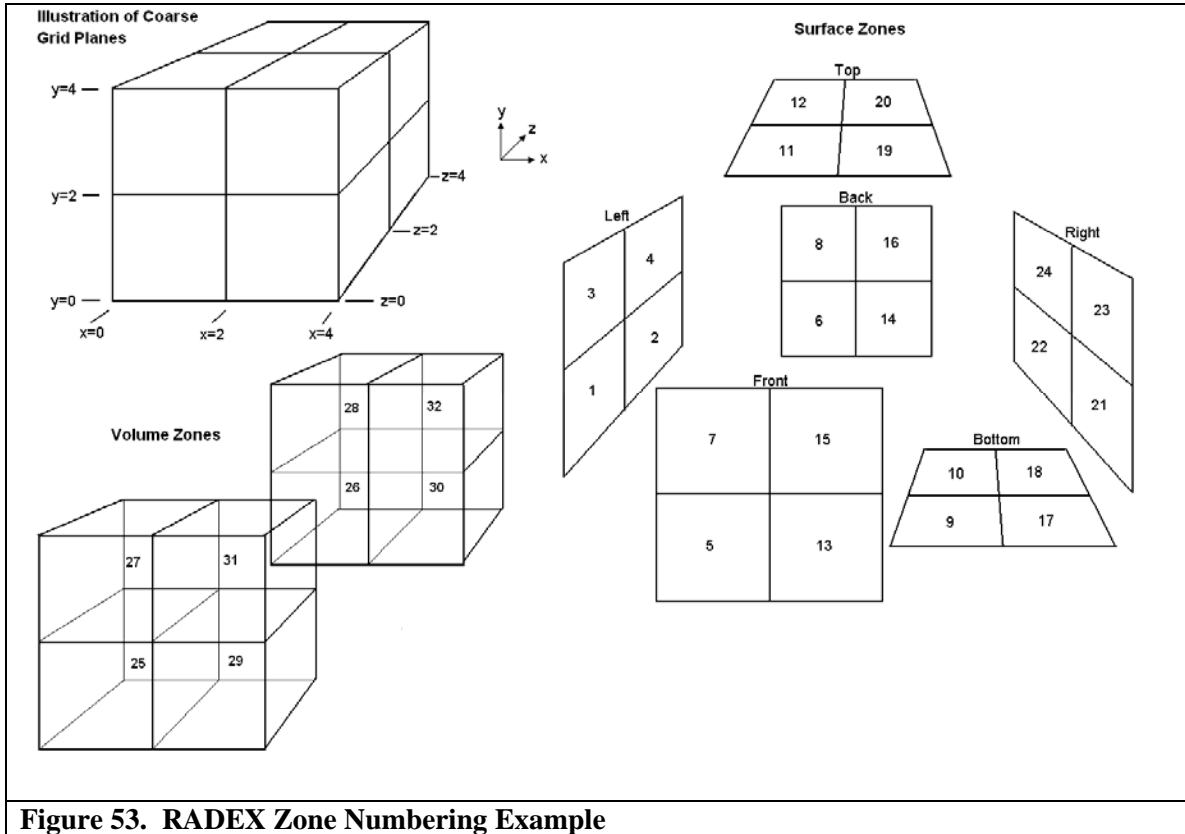


Figure 53. RADEX Zone Numbering Example

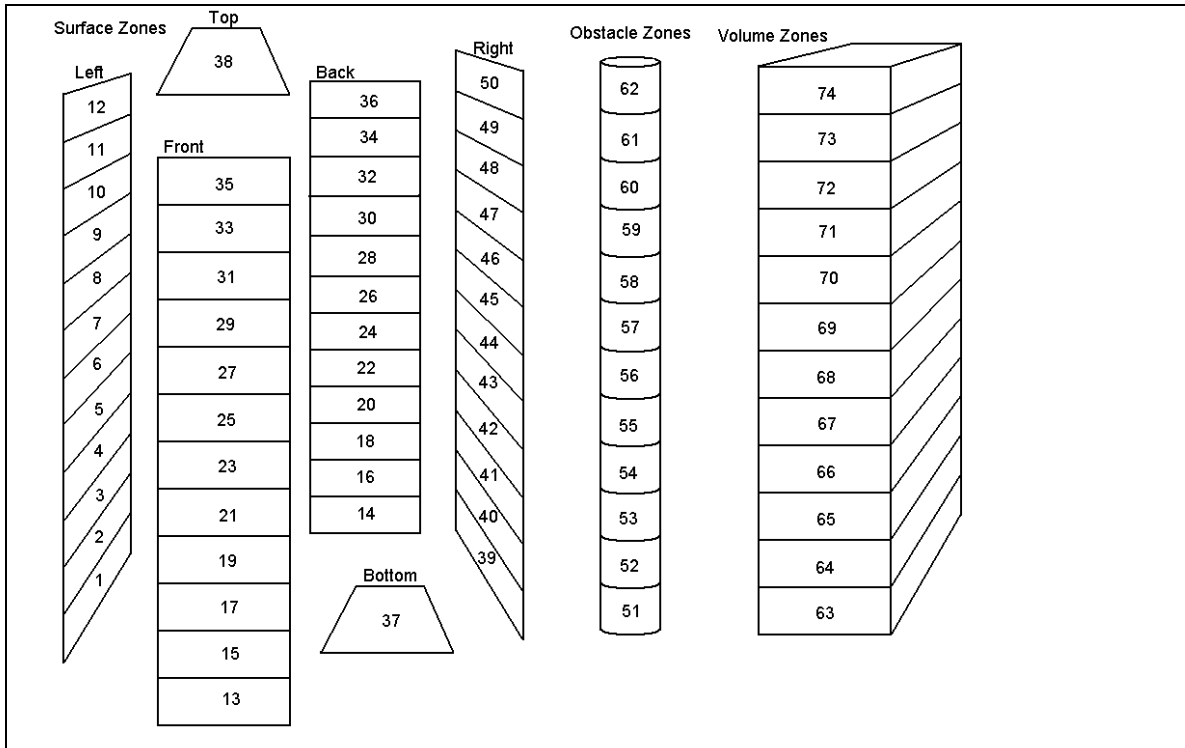


Figure 54. Segmented-Tube Model Zone Numbering

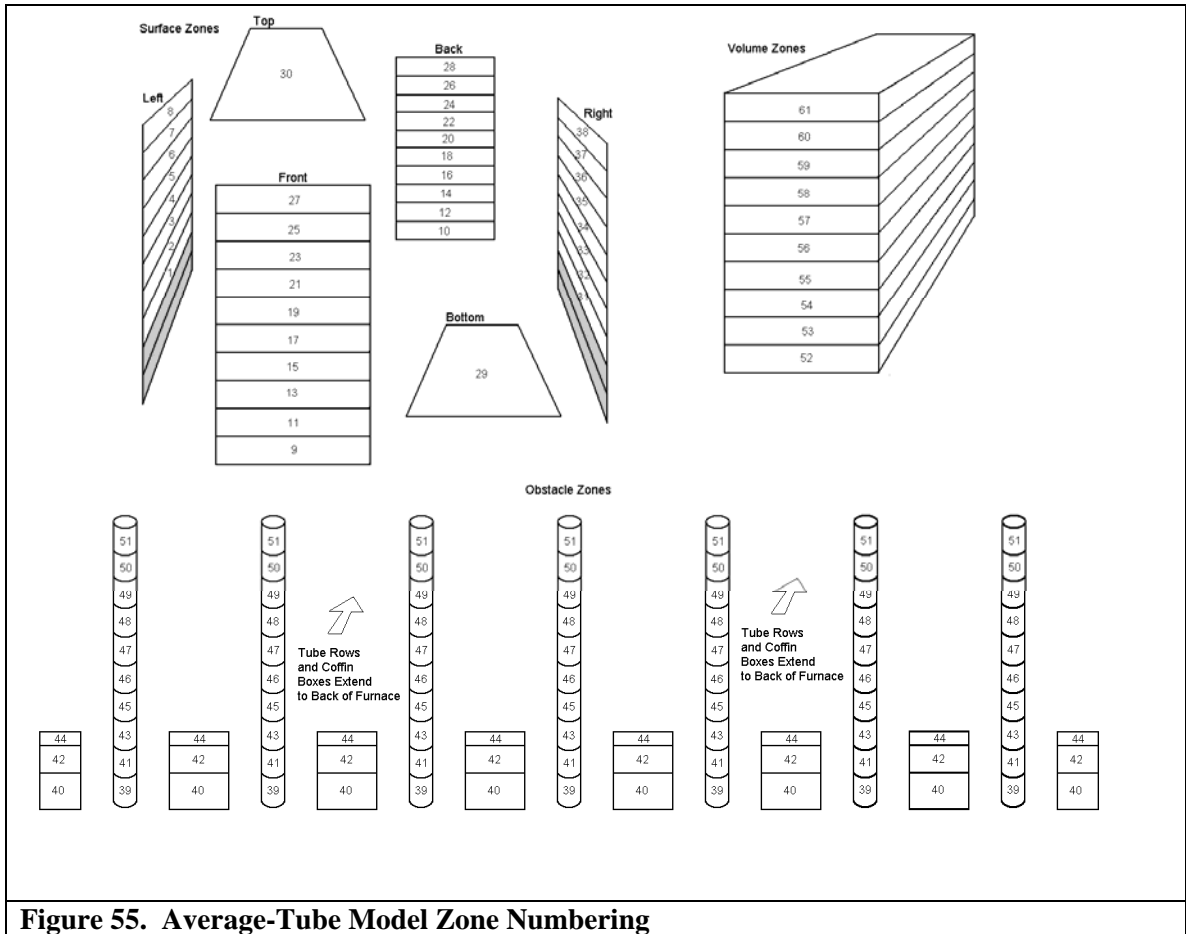


Figure 55. Average-Tube Model Zone Numbering

Storage and Recollection of Furnace-Zone Properties

The average-tube model performs calculations on furnace zones and process-side tube segments.

Because the furnace is organized by zone, the arrays in the average-tube model are indexed with a zone number. To simplify reading information from RADEX, the average-tube model uses the same zone-numbering pattern as RADEX.

The zone numbering pattern assigned by RADEX is used in the vector equation \mathbf{f} , in the vector of unknowns \mathbf{x} , in the total-exchange-area matrices and the furnace-zone properties database. This organization allows the temperature, properties and total-exchange areas for a furnace zone to be recalled using its zone number.

The average-tube model stores information about furnace zones in an array called furnace-zone properties (furZnProp).

This array stores the geometric location of a furnace zone in the form of three reference coordinates. The array also stores information about the zones volume or area, its gray gas absorption coefficients or emissivity and the zone type.

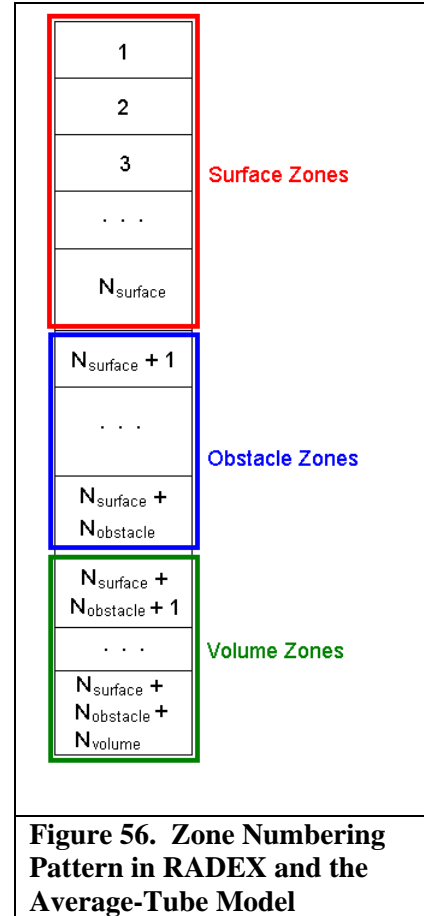


Figure 56. Zone Numbering Pattern in RADEX and the Average-Tube Model

Table 25. Structure of the Furnace Zone Properties Database

Zone Number	x-ref coord	y-ref coord	z-ref coord	Area or Volume	Emissivity	1 st Gray Gas Absorption Coefficient	2 nd Gray Gas Absorption Coefficient	3 rd Gray Gas Absorption Coefficient	Zone Type
index 1↓ index2→	1	2	3	4	5	6	7	8	9
1									

...									
N									

Storage of Relative Furnace Geometry in Reference Coordinates

The zone type can be determined from the zone number and knowledge of the number of surface, obstacle and volume zones in the furnace. However, it is not possible to determine the orientation of zones with respect to one another. For example, which surface zones bound a volume zone? What obstacle zone exists in a given volume zone? The three-dimensional geometry of the furnace is stored in three reference coordinates (x, y and z) in the array furZnProp. The reference coordinates are assigned automatically by the model based on the zone numbering pattern used by RADEX but can also be assigned manually using the following rules.

Volume and Obstacle-Zone Reference Coordinates

A zones reference coordinate is found by finding the intersection of the smallest x, y and z planes that bound the zone. For volume zones, the smallest x, y and z planes are the reference coordinate. Obstacle zones have the same reference coordinate as the volume zone they occupy. This means that sink obstacles, source obstacles and volume zones can have the same reference coordinate. To distinguish volume zones from obstacle zones based on their reference coordinate, the zone type must be given. The zone type is available in the array furZnProp. The number 0 represents a surface zones, 1 a tube-obstacle zone, 2 a box obstacle zone and 3 a volume zone.

Surface-Zone Reference Coordinates

Since the geometry of the furnace is restricted to a rectangle, surfaces must lie in either the largest or smallest x, y or z planes. Negative reference coordinates are used to designate the plane of the surface. The smallest plane in the x, y or z –direction will always be zero because of the geometric restrictions imposed by the model. A value of -1 for a reference coordinate indicates that the surface lies in the smallest plane in the given direction. A reference coordinate equal to the negative value of the largest plane indicates that the surface lies in the largest plane in a given direction. The largest plane in a given direction cannot have a value of one because of geometry rule 2. The remaining non-negative reference coordinates are the intersection of the smallest planes that bound the surface. For example a surface with a reference coordinate (-1, 2, 3) lies in the smallest x-plane (left most wall of the furnace) and is bounded by the planes $y=2$ and $z=3$. A surface with the reference coordinate (0, -5, 1) lies in the largest y-plane (roof of the furnace) and is bounded by the planes $x=0$ and $z=1$. Figure 57 shows the reference coordinates for the average tube model.

Recollection of Furnace Geometry

The relative geometry of the furnace is recalled using searching functions. These searching functions use the reference coordinates and zone type of a given zone to find the zones geometrically related to it. The furnace geometry searching functions are listed below.

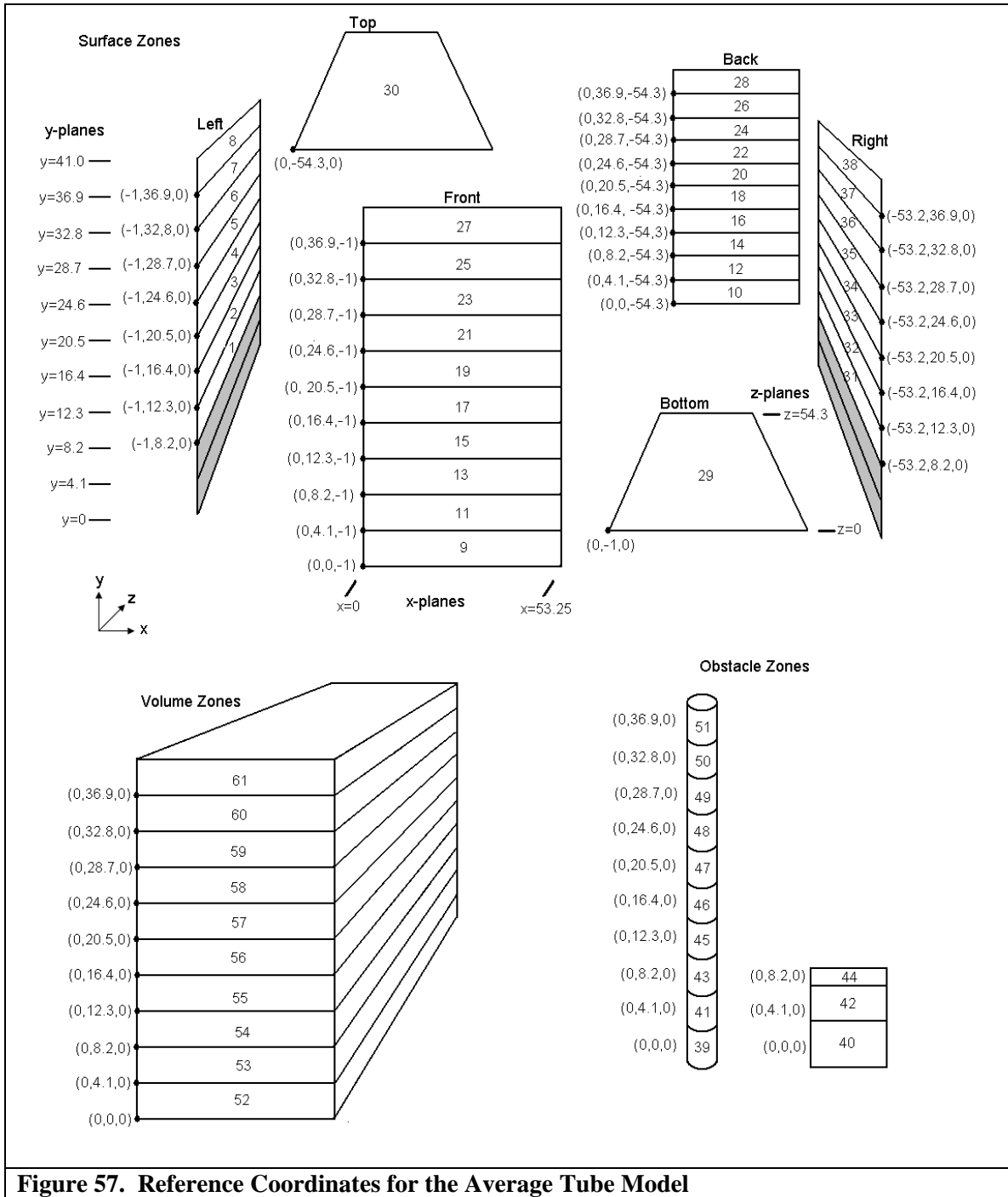


Figure 57. Reference Coordinates for the Average Tube Model

FndIndxRefPt() (Find Index Reference Point)

Given the reference point and zone type of a furnace zone, this function returns the index of the furnace zone in the array furZnProp.

FndIndxVolZnAdjSurZn() (Find Index of Volume Zone Adjacent to Surface Zone)

Given the index of a surface zone in furZnProp, this subprocedure returns the index of the adjacent volume zone in furZnProp. This function will not accept obstacle zones indices. If an obstacle zone index is entered, -1 is returned. To find an obstacle zone in a volume zone FndIndxRefPt() is used with the reference coordinate of the volume zone and the obstacle zone type.

FndIndxSurObstclZnAdjVolZn() (Find Index of Surface or Obstacle Zone Adjacent to Volume Zone)

Given the index of a volume zone in furZnProp, this subprocedure returns an array with the indices of the surface and obstacle zones in furZnProp adjacent to the volume zone.

FndIndxVolZnAbv() (Find the Index of the Volume Zone Above)

Given the index of a volume zone in furZnProp, this subprocedure returns the index of the volume zone above it in the furnace. If the volume zone is at the top of the furnace, -1 is returned.

Process-Side Geometry

For a given tube segment the inner tube wall temperature, process gas temperature, partial pressure of the six process-side species (H_2 , CO , CH_4 , N_2 , CO_2 , H_2O) and process-gas density are calculated by the average-tube model. The process side differs from the furnace side since each tube segment has nine unknowns instead of one. These unknowns are organized by unknown type in the unknown vector \mathbf{x} . For example, the inner tube wall temperatures are stored together, followed by the process-gas temperatures, then the process-species-partial pressures and finally the process-gas density. The process-side unknowns are stored in \mathbf{x} after the furnace side unknowns as shown in Figure 58.

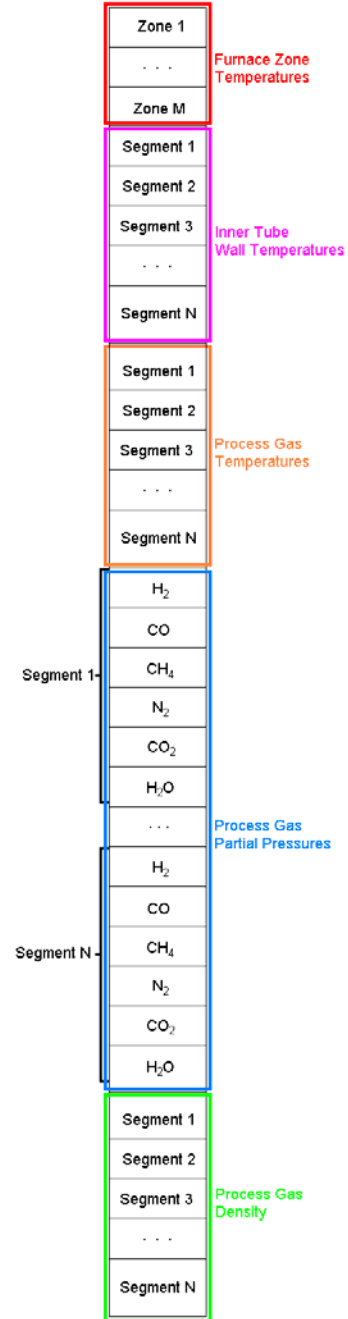


Figure 58. The Location of Unknowns on the Process Side of the Average Tube Model

Recollection of Process Geometry

Process side geometry is recalled using the tube segment number and the sub-procedure CalcIndxTubSeg().

CalcIndxsTubSeg() (Calculate the Indices of the tube segment)

Given the tube segment number, this subprocedure calculates the index in **x** of the segment temperature, the index in **x** of the H₂ partial pressure and the index in **x** of the segment density.

Inversely, the tube segment number and variable type can be determined from an index in **f** or **x** and knowledge of the number of furnace zones and tube segments.

Table 26. Summary of How to Switch Between Zone Indices and Tube Segments

surface-zone index → volume-zone index	FndIndxVolZnAdjSurZn()
obstacle-zone index → volume-zone index	FndIndxRetPt() -use zone type = 2 to find a volume -obstacle zones have the same reference point as the volume zones that contain them
volume-zone index → surface and obstacle zones indices	FndIndxSurObstclZnAdjVolZn()
volume-zone index → surface-zone index	FndIndxSurObstclZnAdjVolZn() -then remove the non-obstacle zones from the array using the zone type in furZnProp
volume-zone index → tube or box zone index	FndIndxRetPt() -use zone type = 1 to find tubes -use zone type = 2 to find boxes

tube segment → inner wall temperature index, temperature index, start of species partial pressures index, density index	CalcIndxsTubSeg()
--	--------------------------

References

Lawson, D. A. (1991) RADEXF: A user guide. Department of Mathematics Research Report.
Coventry Polytechnic. West Midlands, Coventry.

Appendix G

Validation of RADEX

In this thesis the reformer model was developed progressively starting with a cube furnace, followed by a single tube in a rectangular furnace and ending with a complete reformer. The progression of the model development is shown in Table 5. The purpose of this progression was to verify the furnace modeling techniques for simple geometries before applying the modeling techniques to complex geometries.

The reformer model developed in this thesis relies on the program RADEX (Lawson and Ziesler, 1996) for the calculation of total-exchange areas. Although the outputs from RADEX were verified by Lawson and Ziesler (1996), due diligence requires that RADEX be independently verified for this study. To verify RADEX, direct-exchange areas from RADEX were compared to direct-exchange areas from a chart published by Hottel and Sarofim (1967) (See figure 7-13 p. 268 of Hottel and Sarofim, 1968). The side length of the cube and the gray gas absorption coefficient were varied to test RADEX over a range of values. The results for three different cubes are shown in Table 27. A ray density of 20 000 rays per m^2 was used in the RADEX runs. Increasing the ray density to 200 000 rays per m^2 did not change the values for the direct-exchange areas calculated by RADEX.

Table 27. Comparison of total exchange areas from RADEX and figure 7-13 of Hottel and Sarofim (1968) for cubes with different side lengths and absorption coefficients

Trial	1	2	3
Cube Side Length [m]	0.305	0.610	0.164
Absorption Coefficient [1/ft]	32.8	9.84	131
RADEX direct exchange area \overline{gs} [ft ²]	0.0855	1.34	105
Hottel and Sarofim (1967) direct exchange \overline{gs} [ft ²]	0.0930	1.43	101
Percent Error	8.0	6.3	3.9

The percent error between the direct-exchange areas calculated by RADEX and the Hottel and Sarofim chart ranges from 4 to 8 percent. The Hottel and Sarofim chart used numerical integration to evaluate the integral in equation (104). It is not know what assumptions were made by Hottel and Sarofim (1968) in evaluating the integral in equation (104). These assumptions could account for the error between the two sets of values.

As further validation, the view factors calculated by RADEX for a cylinder in a rectangular box were compared to view factors calculated using an analytical integral provided by Sparrow and Cess (1978). The analytical integral was for a cylinder of finite length adjacent to a rectangle of finite length (See configuration 4 in Appendix A of Sparrow and Cess, 1978). This type of view factor does not account for the effects of the intervening gas between the two surfaces. The integral was evaluated using the program Maple (Maplesoft, 2008). The test geometry is shown in Figure 59 and the view factor comparison is shown in Table 28.

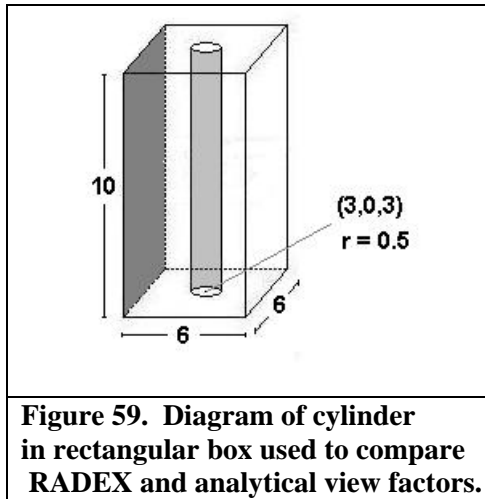


Table 28. Comparison of view factors from RADEX and configuration 4 of Sparrow and Cess (1978) for the geometry in Figure 59.

RADEX View Factor $F_{\text{side-tube}}$ [none]	0.1058
Sparrow and Cess (1978) Analytical View Factor $F_{\text{side-tube}}$ [none]	0.1069
Percent Error	1.0

The percent error for the view factor calculation is one percent. This shows that RADEX is accurate in accounting for cylindrical obstacles in the furnace. The ray density in RADEX was 20 000 rays per m^2 . Increasing the ray density by a factor of 10 did not change the view factor calculated by RADEX.

References

Hottel, H. C. and Sarofim, A. F. (1967) Radiative Heat Transfer. McGraw-Hill Inc, New York, NY.

Maplesoft. (2008) Maple 12.0: The essential tools for mathematics and modeling. Waterloo Maple Inc.

Sparrow, E. M. and Cess, R. D. (1978) Radiation Heat Transfer, Augmented Edition.
Hemisphere Publishing Corporation.

Appendix H

Plant Data

Four sets of plant data were available for this thesis. The data is from third party reformer surveys performed on four separate dates. Although the data is from three different plants, all the plants are identical.

Plant Input Data

Table 29. Furnace-Side Input Data

Symbol	Units	Plant A	Plant B	Plant C1	Plant C2
T_{fl}	[°C]	15.6	22.7	15.6	21.1
P_{fl}	[kPa]	101.3	101.3	101.3	101.3
n_{fl}	[gmol/h]	1.253E+05	1.341E+05	1.784E+05	1.042E+05
$X_{H_2,fl}$	[none]	0.0000	0.0000	0.0000	0.0000
$X_{CO,fl}$	[none]	0.0000	0.0000	0.0000	0.0000
$X_{CH_4,fl}$	[none]	0.9553	0.9549	0.9536	0.9464
$X_{C_2,fl}$	[none]	0.0165	0.015	0.0161	0.0229
$X_{C_3,fl}$	[none]	0.0037	0.0035	0.0032	0.0052
$X_{i-C_4,fl}$	[none]	0.0000	0.0000	0.0000	0.0000
$X_{n-C_4,fl}$	[none]	0.0018	0.0018	0.0015	0.0023
$X_{i-C_5,fl}$	[none]	0.0000	0.0000	0.0000	0.0000
$X_{n-C_5,fl}$	[none]	0.0007	0.0007	0.0006	0.0008
$X_{neo-C_5,fl}$	[none]	0.0000	0.0000	0.0000	0.0000
$X_{n-C_6,fl}$	[none]	0.0011	0.0011	0.0005	0.0006
$X_{N_2,fl}$	[none]	0.0023	0.0025	0.0042	0.0054
$X_{CO_2,fl}$	[none]	0.0187	0.0204	0.0203	0.0165
$X_{H_2O,fl}$	[none]	0.0000	0.0000	0.0000	0.0000

T _{f2}	[°C]	15.6	30.7	15.6	23.9
P _{f2}	[kPa]	101.3	101.3	101.3	101.3
n _{f2}	[gmol/h]	2.835E+06	2.523E+06	2.540E+06	1.878E+06
X _{H2,f2}	[none]	0.2686	0.2440	0.2476	0.2428
X _{CO,f2}	[none]	0.0786	0.0882	0.1002	0.0827
X _{CH4,f2}	[none]	0.1933	0.2036	0.1787	0.1908
X _{C2,f2}	[none]	0.0000	0.0000	0.0000	0.0000
X _{C3,f2}	[none]	0.0000	0.0000	0.0000	0.0000
X _{i-C4,f2}	[none]	0.0000	0.0000	0.0000	0.0000
X _{n-C4,f2}	[none]	0.0000	0.0000	0.0000	0.0000
X _{i-C5,f2}	[none]	0.0000	0.0000	0.0000	0.0000
X _{n-C5,f2}	[none]	0.0000	0.0000	0.0000	0.0000
X _{neo-C5,f2}	[none]	0.0000	0.0000	0.0000	0.0000
X _{n-C6,f2}	[none]	0.0000	0.0000	0.0000	0.0000
X _{N2,f2}	[none]	0.0016	0.0018	0.0031	0.0039
X _{CO2,f2}	[none]	0.4579	0.4623	0.4704	0.4798
X _{H2O,f2}	[none]	0.0000	0.0000	0.0000	0.0000
X _{O2,f2}	[none]	0.0000	0.0000	0.0000	0.0000
T _B	[°C]	331.1	315.6	337.8	299.8
P _B	[kPa]	101.3	101.3	101.3	103.2
n _B	[gmol/h]	1.079E+07	1.058E+07	9.654E+06	7.412E+06
X _{H2,f3}	[none]	0.0000	0.0000	0.0000	0.0000
X _{CO,f3}	[none]	0.0000	0.0000	0.0000	0.0000
X _{CH4,f3}	[none]	0.0000	0.0000	0.0000	0.0000
X _{C2,f3}	[none]	0.0000	0.0000	0.0000	0.0000
X _{C3,f3}	[none]	0.0000	0.0000	0.0000	0.0000
X _{i-C4,f3}	[none]	0.0000	0.0000	0.0000	0.0000
X _{n-C4,f3}	[none]	0.0000	0.0000	0.0000	0.0000
X _{i-C5,f3}	[none]	0.0000	0.0000	0.0000	0.0000
X _{n-C5,f3}	[none]	0.0000	0.0000	0.0000	0.0000

$X_{\text{neo-C5,f3}}$	[none]	0.0000	0.0000	0.0000	0.0000
$X_{\text{n-C6,f3}}$	[none]	0.0000	0.0000	0.0000	0.0000
$X_{\text{N2,f3}}$	[none]	0.7826	0.767	0.7826	0.7752
$X_{\text{CO2,f3}}$	[none]	0.0003	0.0003	0.0003	0.0003
$X_{\text{H2O,f3}}$	[none]	0.0096	0.0293	0.0096	0.0189
P_{fur}	[kPa]	101.3	101.3	101.3	103.4

Table 30. Process-Side Input Data

Symbol	Units	Plant A	Plant B	Plant C1	Plant C2
n_{p1}	[gmol/h]	7.886E+06	7.073E+06	9.654E+06	5.355E+06
$X_{\text{H2,p1}}$	[none]	0.0004	0.0018	0.0027	0.0025
$X_{\text{CO,p1}}$	[none]	0.0000	0.0000	0.0000	0.0000
$X_{\text{CH4,p1}}$	[none]	0.2421	0.2487	0.2458	0.2401
$X_{\text{C2,p1}}$	[none]	0.0042	0.0039	0.0041	0.0058
$X_{\text{C3,p1}}$	[none]	0.0009	0.0009	0.0008	0.0013
$X_{\text{i-C4,p1}}$	[none]	0.0000	0.0000	0.0000	0.0000
$X_{\text{n-C4,p1}}$	[none]	0.0005	0.0005	0.0004	0.0006
$X_{\text{i-C5,p1}}$	[none]	0.0000	0.0000	0.0000	0.0000
$X_{\text{n-C5,p1}}$	[none]	0.0002	0.0002	0.0002	0.0002
$X_{\text{neo-C5,p1}}$	[none]	0.0000	0.0000	0.0000	0.0000
$X_{\text{n-C6,p1}}$	[none]	0.0003	0.0003	0.0001	0.0002
$X_{\text{N2,p1}}$	[none]	0.0006	0.0007	0.0011	0.0014
$X_{\text{CO2,p1}}$	[none]	0.0047	0.0053	0.0052	0.0042
$X_{\text{H2O,p1}}$	[none]	0.7462	0.7377	0.7395	0.7437
$X_{\text{O2,p1}}$	[none]	0.0000	0.0000	0.0000	0.0000
$T_{\text{proc,in}}$	[°C]	611.4	613.9	617.8	606.7
$P_{\text{proc,in}}$	[kPa]	3006.0	2944.0	3026.7	2808.5

Plant Output Data

Table 31. Model Outputs and Plant Data used in Parameter Estimation

Symbol	Units	Plant A	Plant B	Plant C1	Plant C2
$T_{\text{proc,out}}$	[°C]	832.4	834.0	848.9	835.8
$P_{\text{proc,out}}$	[kPa]	2846.1	2804.0	2879.8	2723.4
$\eta_{\text{proc,out}}$	[gmol/h]	1.085E+07	9.776E+06	1.001E+07	7.422E+06
$X_{\text{H}_2,\text{proc,out}}$	[none]	0.458247	0.463134	0.471325	0.465506
$X_{\text{CO}_2,\text{proc,out}}$	[none]	0.082013	0.084529	0.088874	0.084954
$X_{\text{CH}_4,\text{proc,out}}$	[none]	0.050455	0.0526	0.045364	0.048226
$X_{\text{N}_2,\text{proc,out}}$	[none]	0.000455	0.000461	0.000795	0.000986
$X_{\text{CO}_2,\text{proc,out}}$	[none]	0.058182	0.057538	0.055894	0.057359
$X_{\text{H}_2\text{O},\text{proc,out}}$	[none]	0.350649	0.341738	0.337748	0.34297
T_{upper}	[°C]	822.8	809.2	838.0	802.5
T_{lower}	[°C]	858.9	857.7	878.4	853.1
$T_{\text{fur,out}}$	[°C]	1012.3	998.1	1005.9	940.9

Appendix I

Sensitivity of the Average-Tube Model to Radiation Parameters

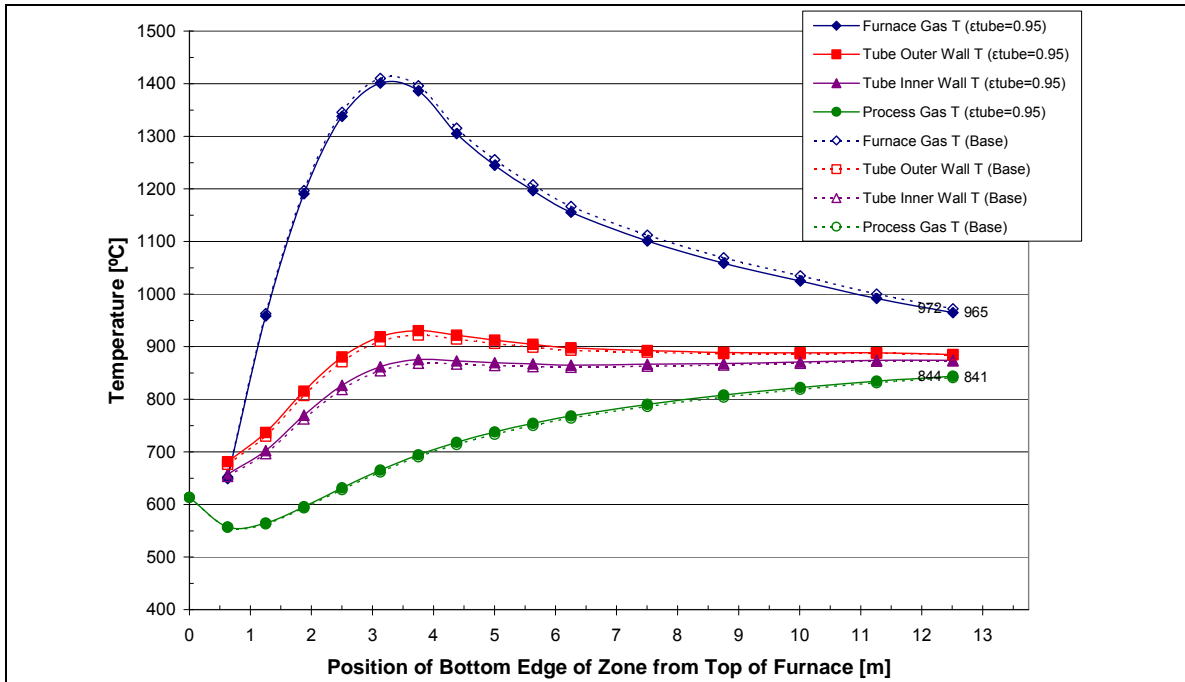


Figure 60. Comparison of Temperature Profiles between the base case (tube emissivity of 0.85) and a case with a tube emissivity of 0.95. The values of the adjustable parameters are shown in Table 18 with the exception of the heat-release profile which is the 3.66 m profile from Table 20. The input data is from Plant B.

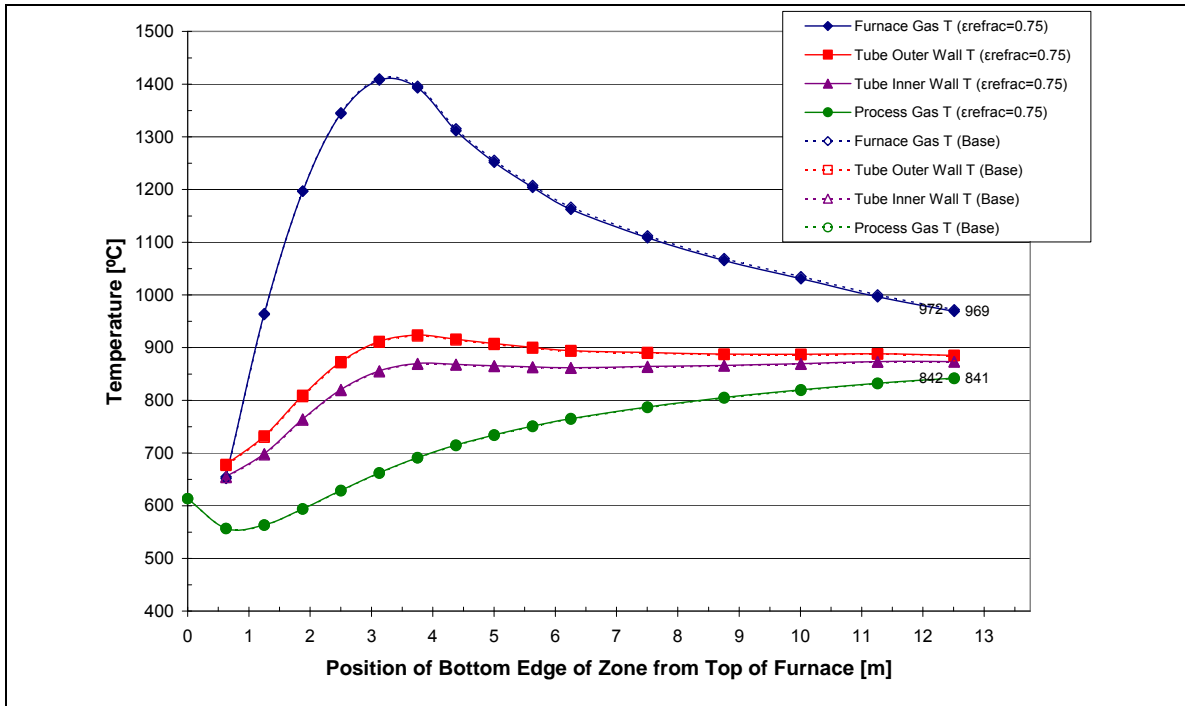


Figure 61. Comparison of Temperature Profiles between the base case (refractory emissivity of 0.60) and a case with a refractory emissivity of 0.75. The values of the adjustable parameters are shown in Table 18 with the exception of the heat-release profile which is the 3.66 m profile from Table 20. The input data is from Plant B.

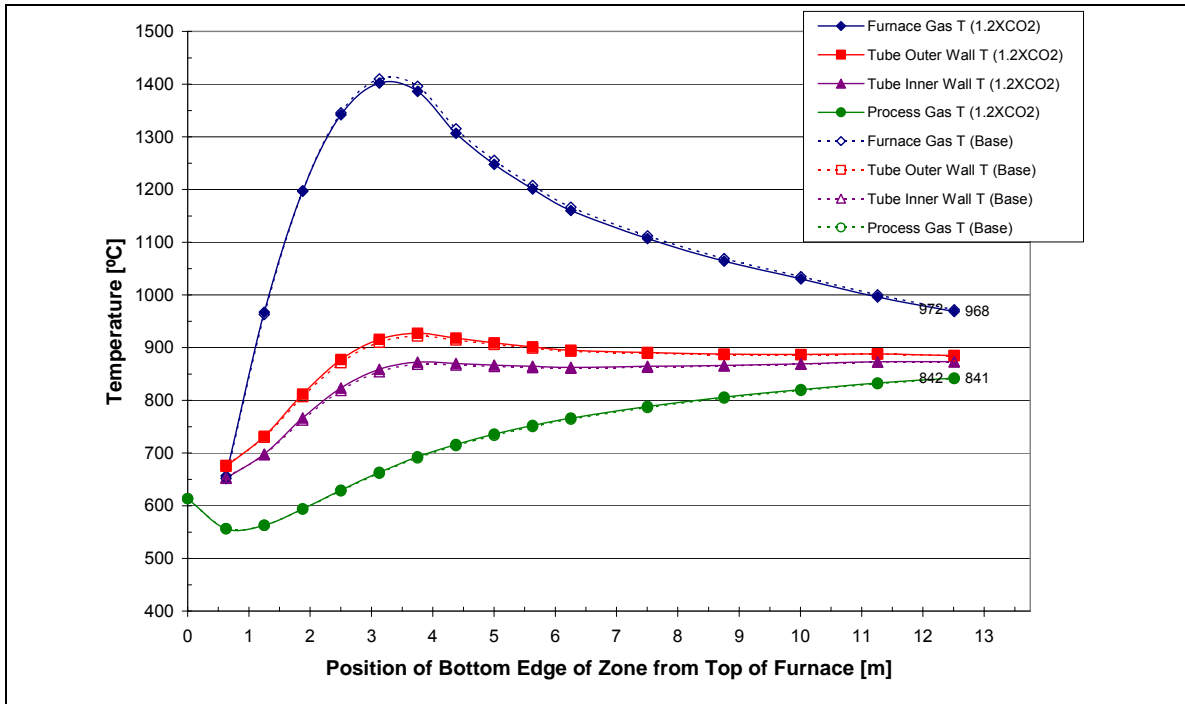
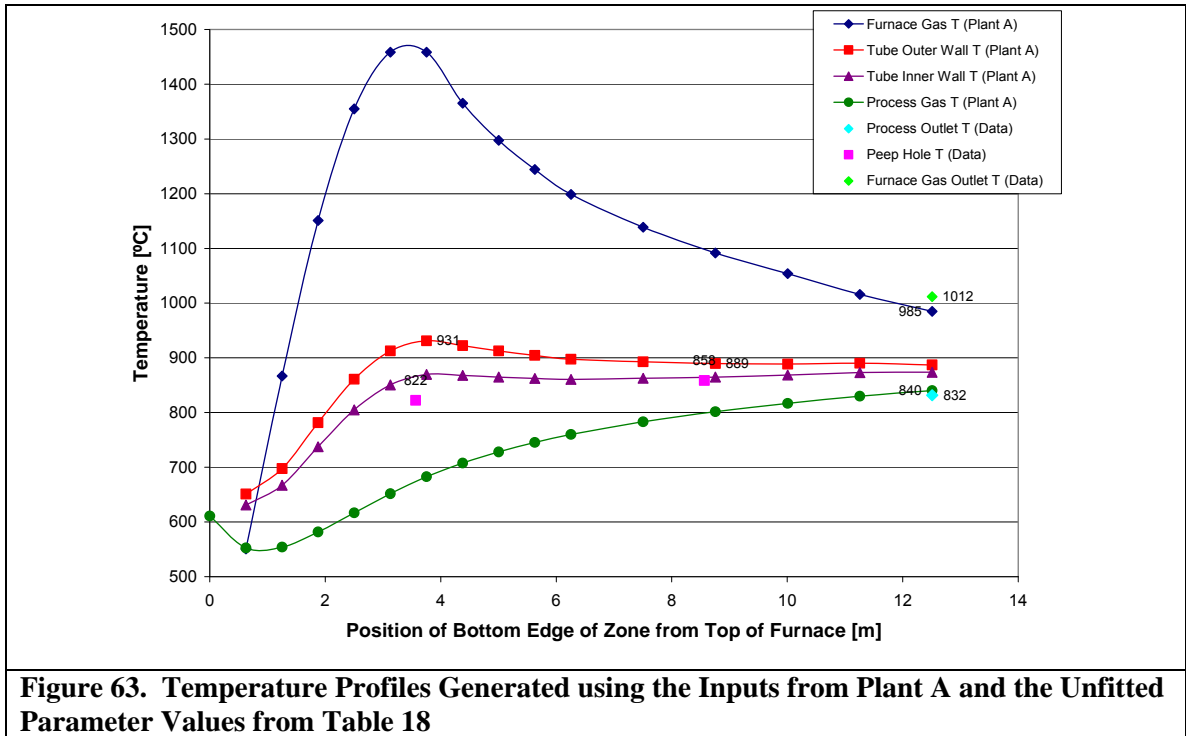


Figure 62. Comparison of Temperature Profiles between the base case ($K_1 = 0.300 \text{ m}^{-1}$ $K_2 = 3.10 \text{ m}^{-1}$ and $K_3 = 42.9 \text{ m}^{-1}$) and a case with 20% more carbon dioxide in the furnace gas ($K_1 = 0.331 \text{ m}^{-1}$ $K_2 = 3.72 \text{ m}^{-1}$ $K_3 = 51.5 \text{ m}^{-1}$). The values of the adjustable parameters are shown in Table 18 with the exception of the heat-release profile which is the 3.66 m profile from Table 20. The input data is from Plant B.

Appendix J

Unfitted Preliminary Simulation Results



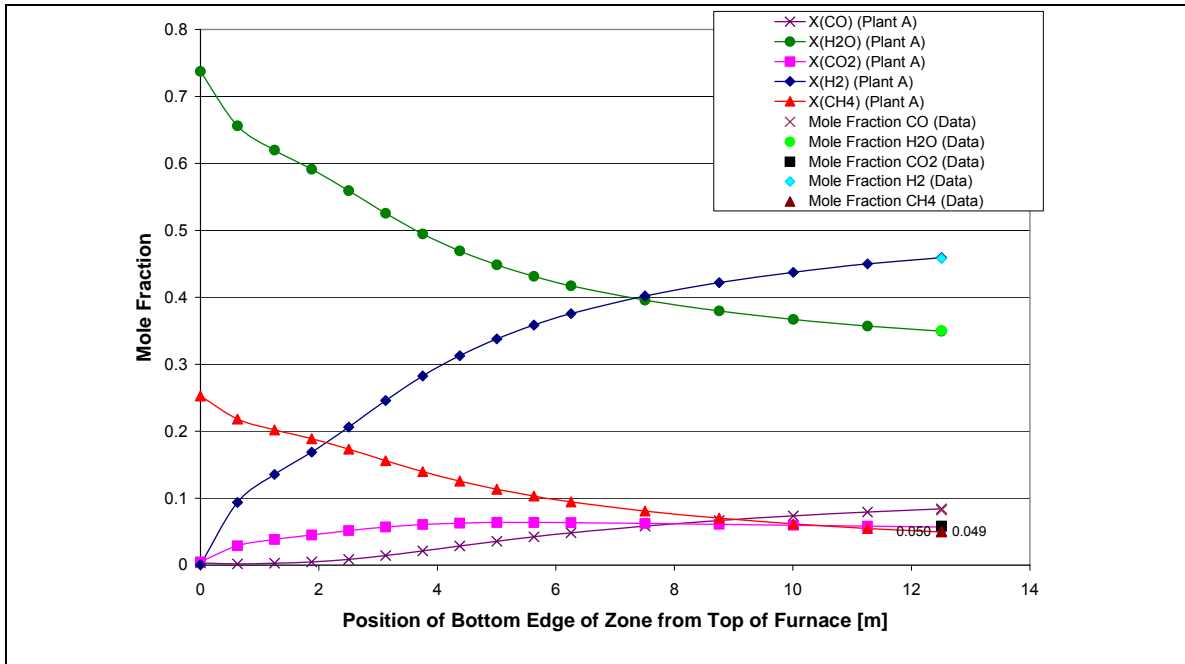


Figure 64. Composition Profiles Generated using the Inputs from Plant A and the Unfitted Parameter Values from Table 18

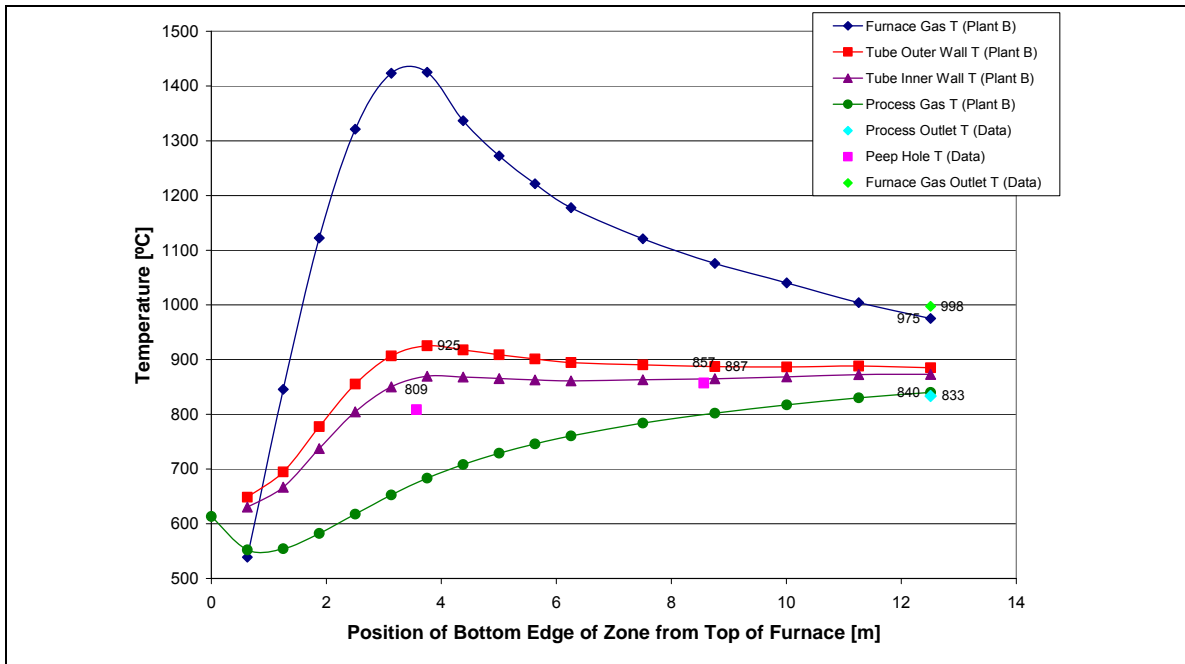


Figure 65. Temperature Profiles Generated using the Inputs from Plant B and the Unfitted Parameter Values from Table 18

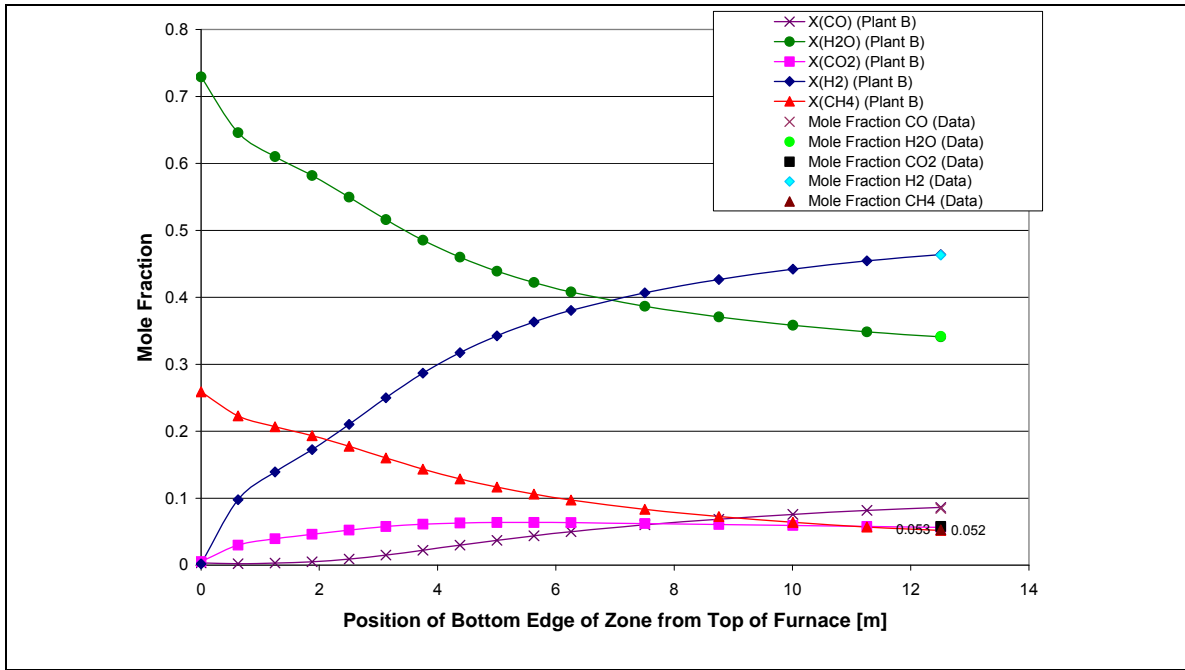


Figure 66. Composition Profiles Generated using the Inputs from Plant B and the Unfitted Parameter Values from Table 18

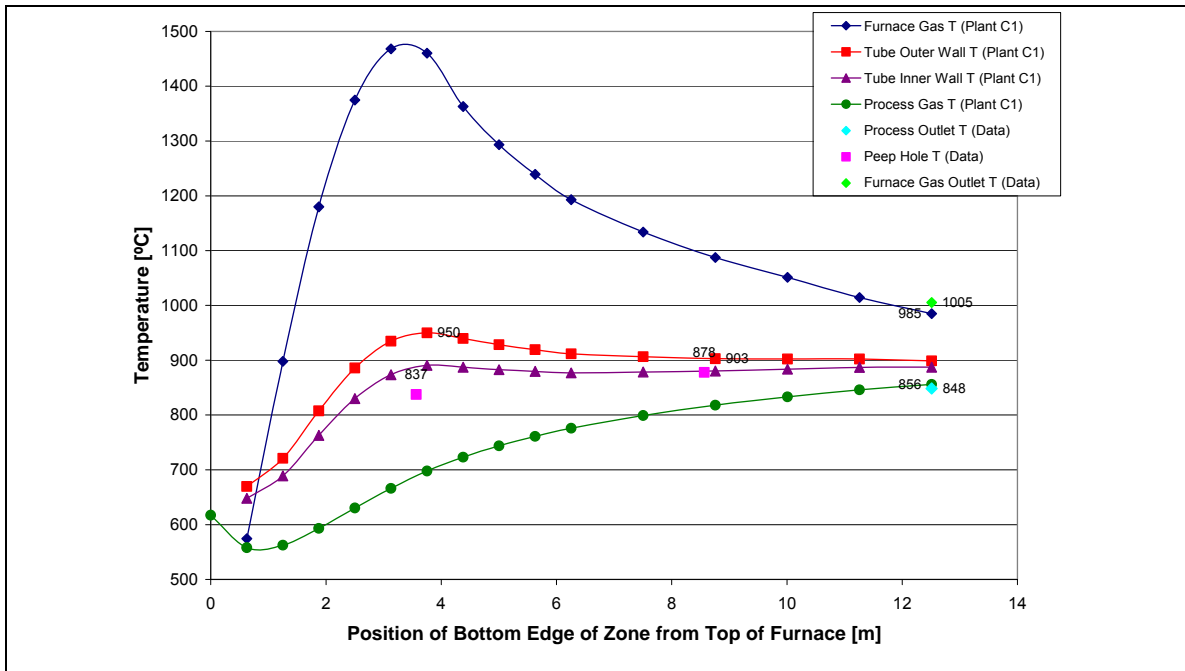


Figure 67. Temperature Profiles Generated using the Inputs from Plant C1 and the Unfitted Parameter Values from Table 18

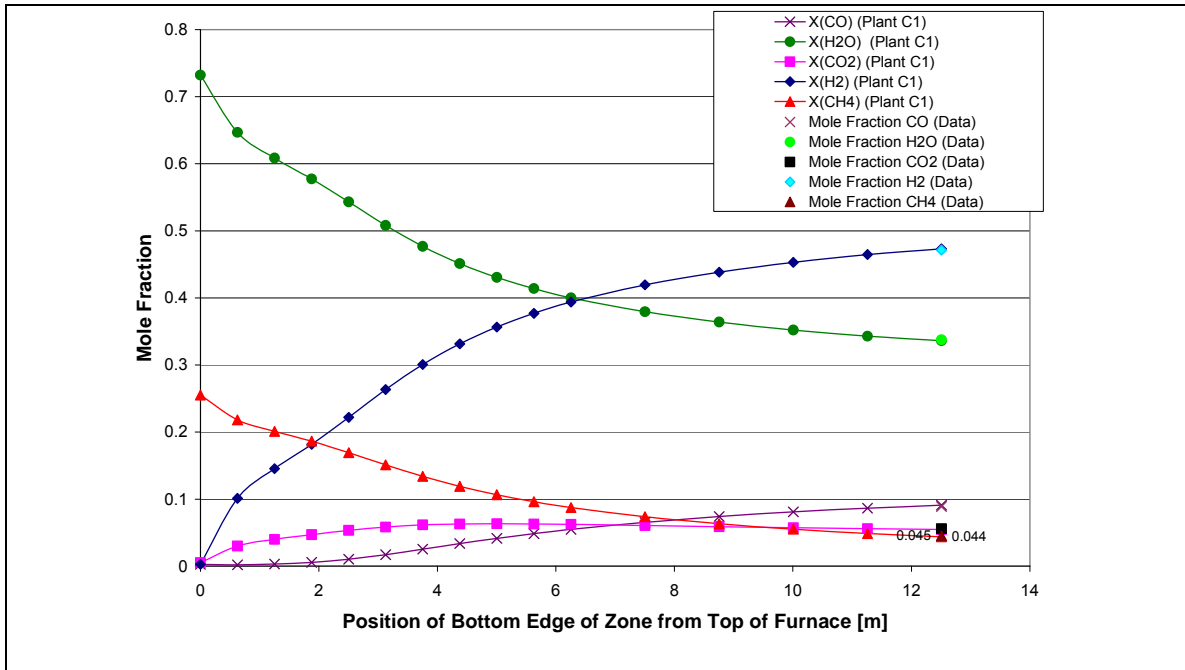


Figure 68. Composition Profiles Generated using the Inputs from Plant C1 and the Unfitted Parameter Values from Table 18

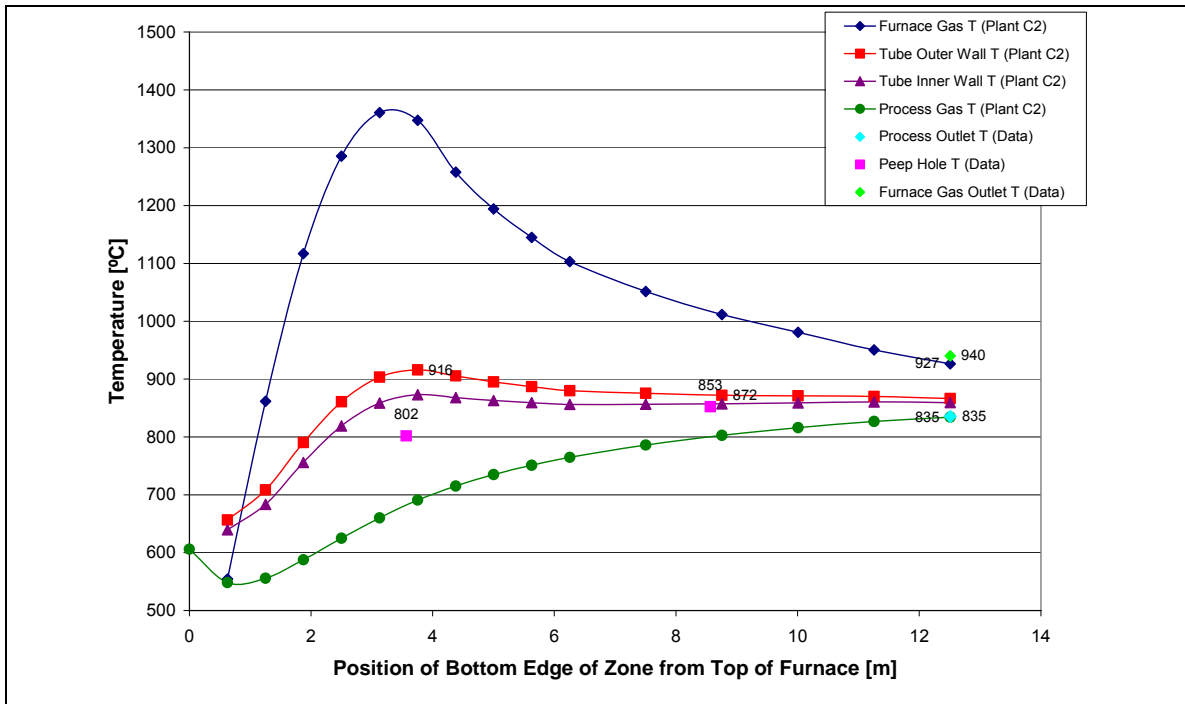


Figure 69. Temperature Profiles Generated using the Inputs from Plant C2 and the Unfitted Parameter Values from Table 18

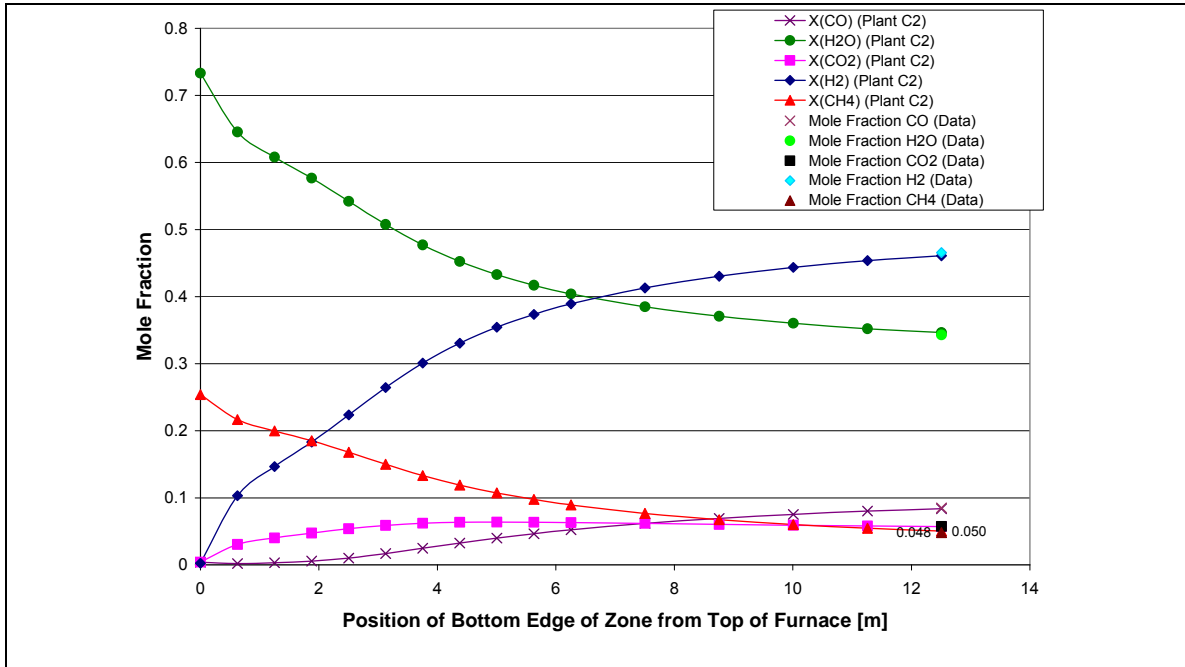


Figure 70. Composition Profiles Generated using the Inputs from Plant C2 and the Unfitted Parameter Values from Table 18

Appendix K

Parameters Values, Temperature Profiles and Composition

Profiles for Additional Parameter Sets that Fit the Plant Data

Table 32. Parameter Values for the 4.88 m Heat-Release Length with 4 Fitted Parameters

Parameter (Symbol) [units]	Best Fit Value
Heat-release Length (L_q) [m]	4.88
Adjustable Factor for Tube-to-process-gas Convective-heat-transfer Coefficient (f_{htg}) [none]	1.67
Fraction of Combustion Enthalpy Released in the Top Furnace-volume Zone (α_{top}) [none]	0.0062
Adjustable Factor for the PSA Off-gas Flow Rate ($f_{nOffGas}$) [none]	0.887
Porosity of the Packed Bed (ϕ) [none]	0.609
Adjustable Factor for the Combustion Air Flow Rate ($f_{nCombAir}$) [none]	0.900
Adjustable Parameter for the Pre-exponential Factor of the Reforming Reactions (f_{prx})	1.00
Adjustable Factor for the Furnace-Gas-to-Tube Convective Heat Transfer Coefficient (f_{ctube})	1.00

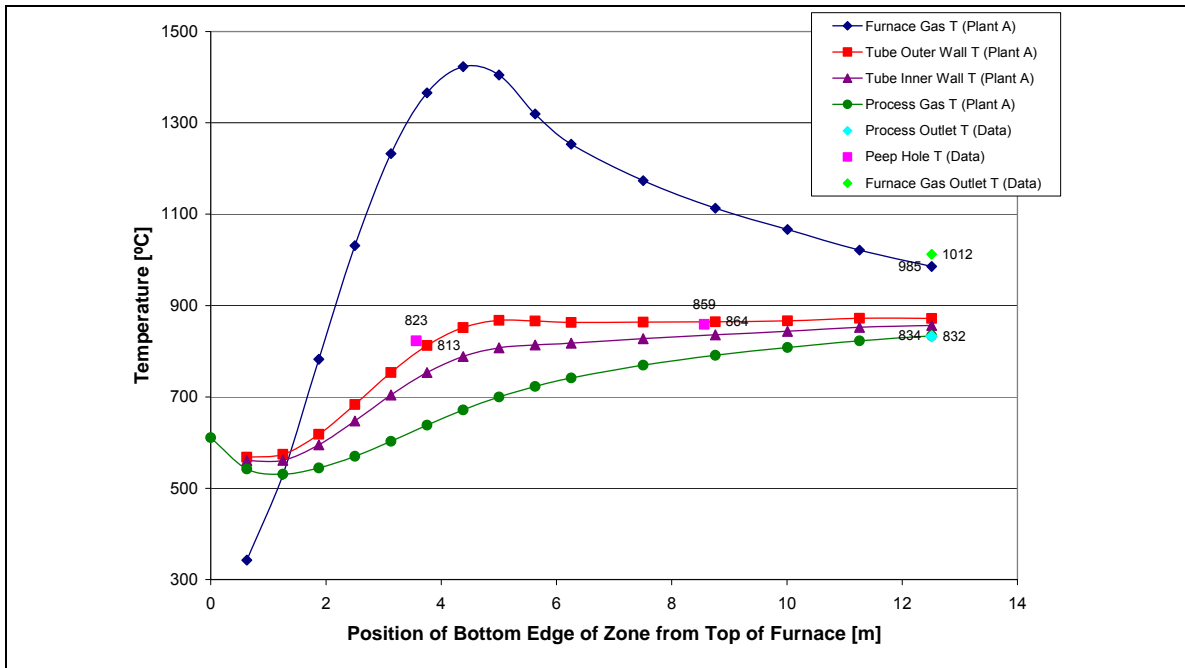


Figure 71. Temperature Profiles Generated using the Inputs from Plant A and the Parameter Values from Table 32

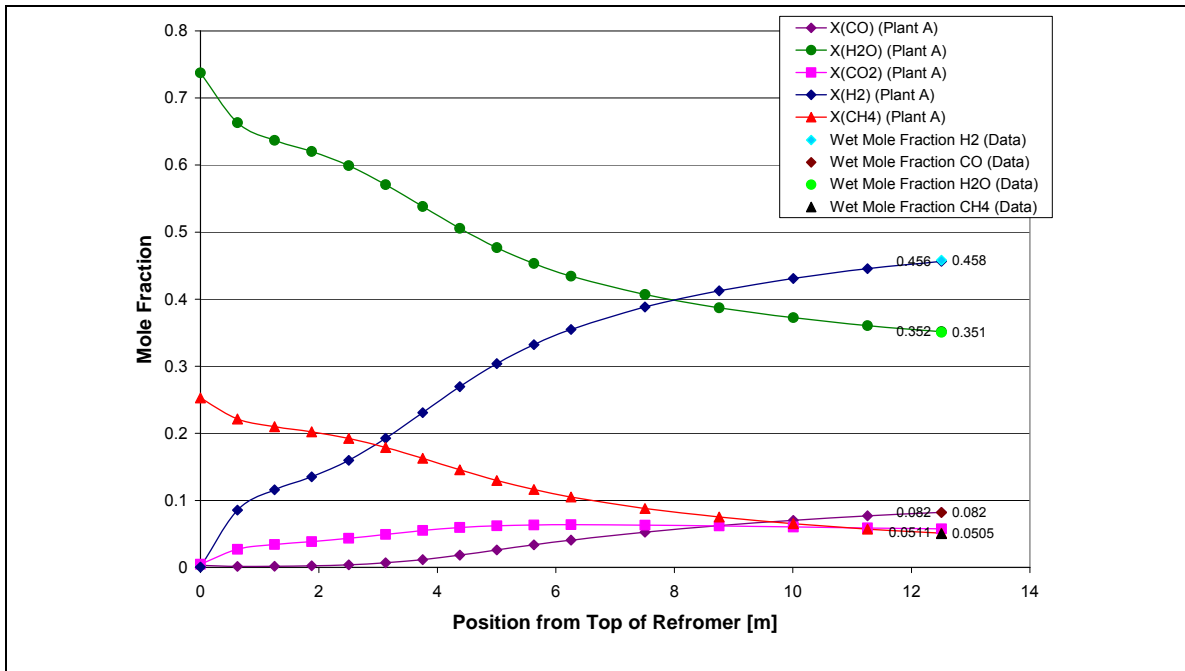


Figure 72. Composition Profiles Generated using the Inputs from Plant A and the Parameter Values from Table 32

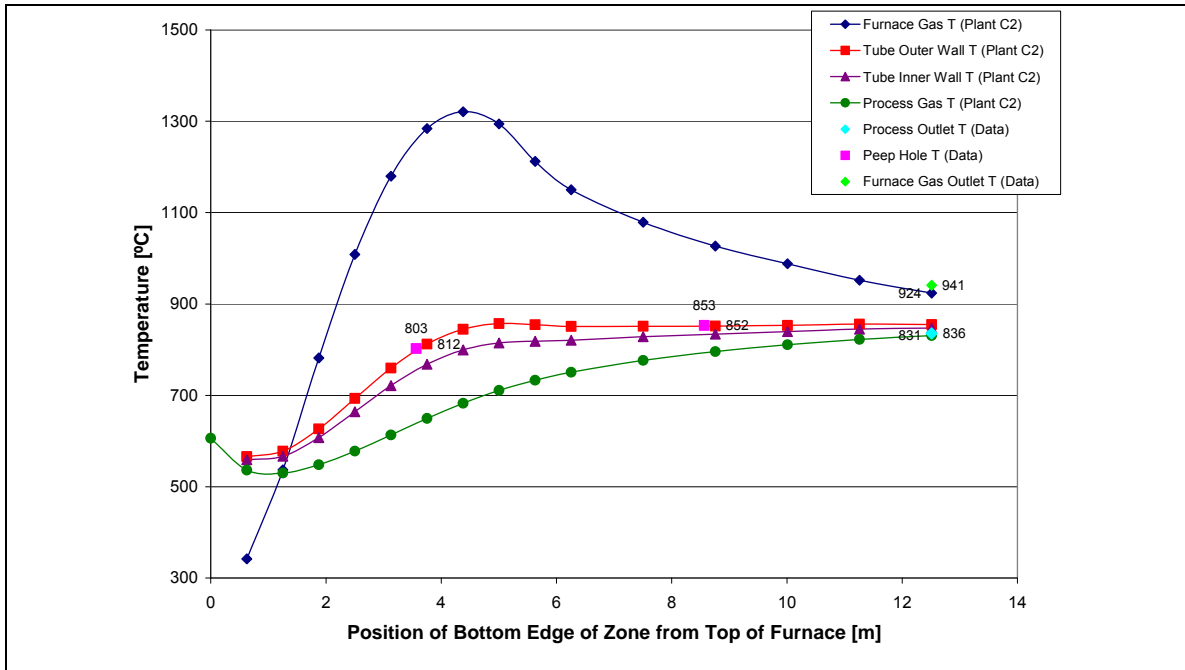


Figure 73. Temperature Profiles Generated using the Inputs from Plant C2 and the Parameter Values from Table 32

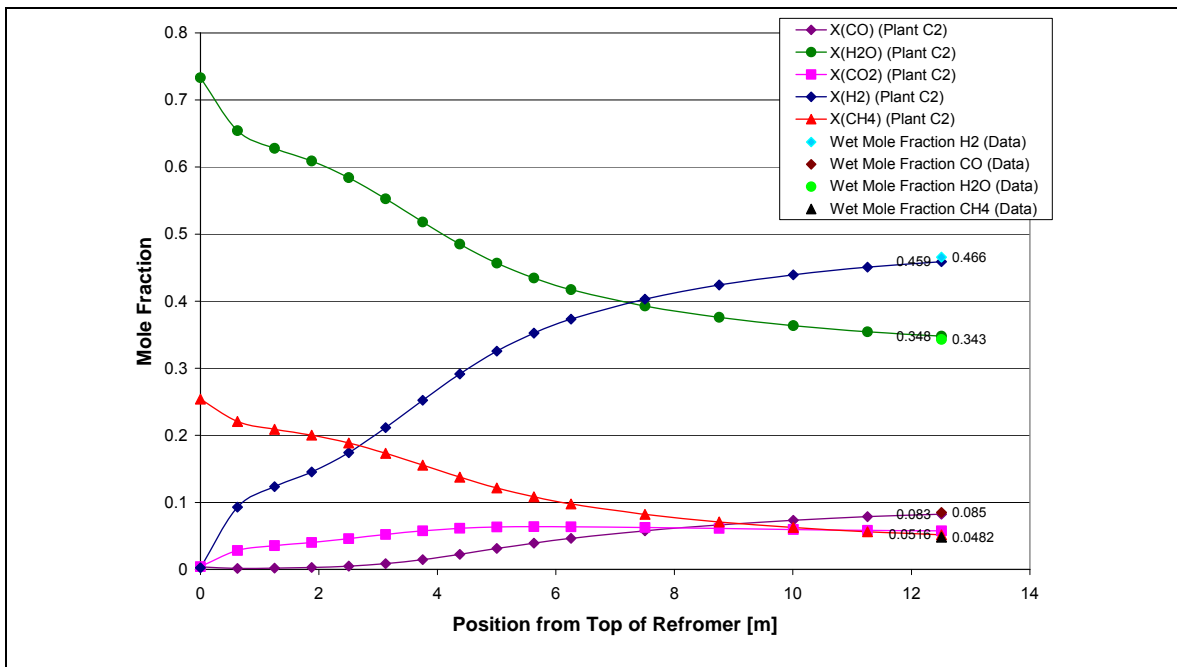


Figure 74. Composition Profiles Generated using the Inputs from Plant C2 and the Parameter Values from Table 32

Table 33. Parameter Values for the 5.49 m Heat-Release Length with 7 Fitted Parameters

Parameter (Symbol) [units]	Best Fit Value
Heat-release Length (L_q) [m]	5.49
Adjustable Factor for Tube-to-process-gas Convective-heat-transfer Coefficient (f_{htg}) [none]	1.60
Fraction of Combustion Enthalpy Released in the Top Furnace-volume Zone (α_{top}) [none]	0.125
Adjustable Factor for the PSA Off-gas Flow Rate ($f_{nOffGas}$) [none]	0.883
Porosity of the Packed Bed (ϕ) [none]	0.614
Adjustable Factor for the Combustion Air Flow Rate ($f_{nCombAir}$) [none]	0.900
Adjustable Parameter for the Pre-exponential Factor of the Reforming Reactions (f_{prx})	0.685
Adjustable Factor for the Furnace-Gas-to-Tube Convective Heat Transfer Coefficient (f_{ctube})	0.837

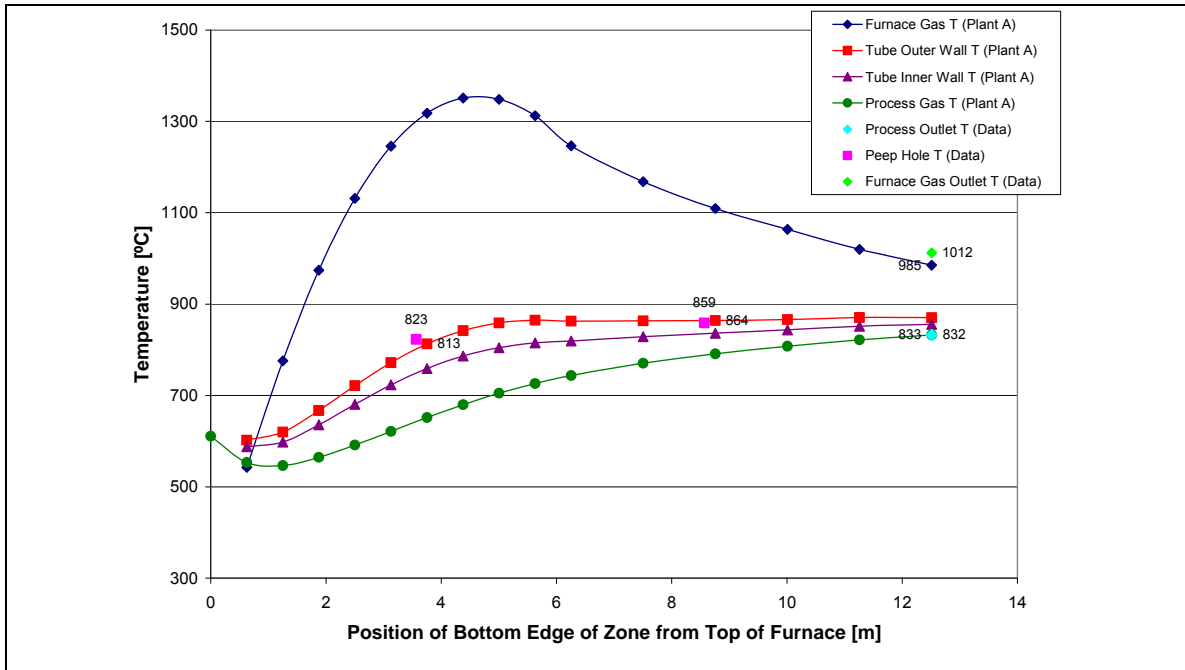


Figure 75. Temperature Profiles Generated using the Inputs from Plant A and the Parameter Values from Table 33

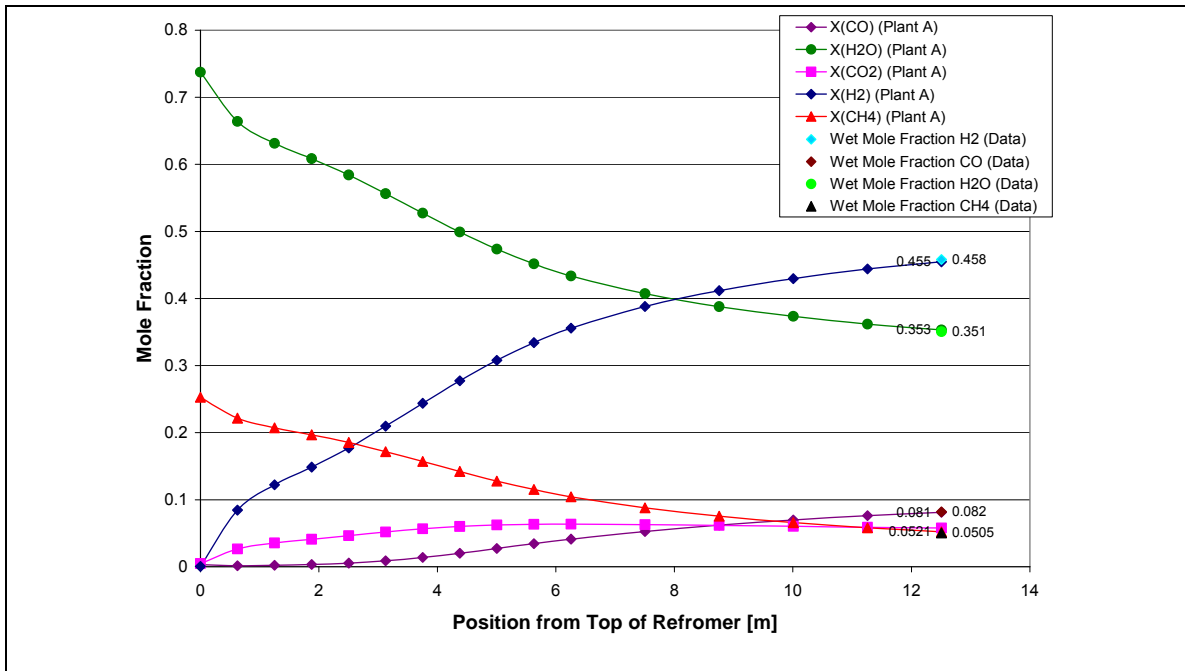


Figure 76. Composition Profiles Generated using the Inputs from Plant A and the Parameter Values from Table 33

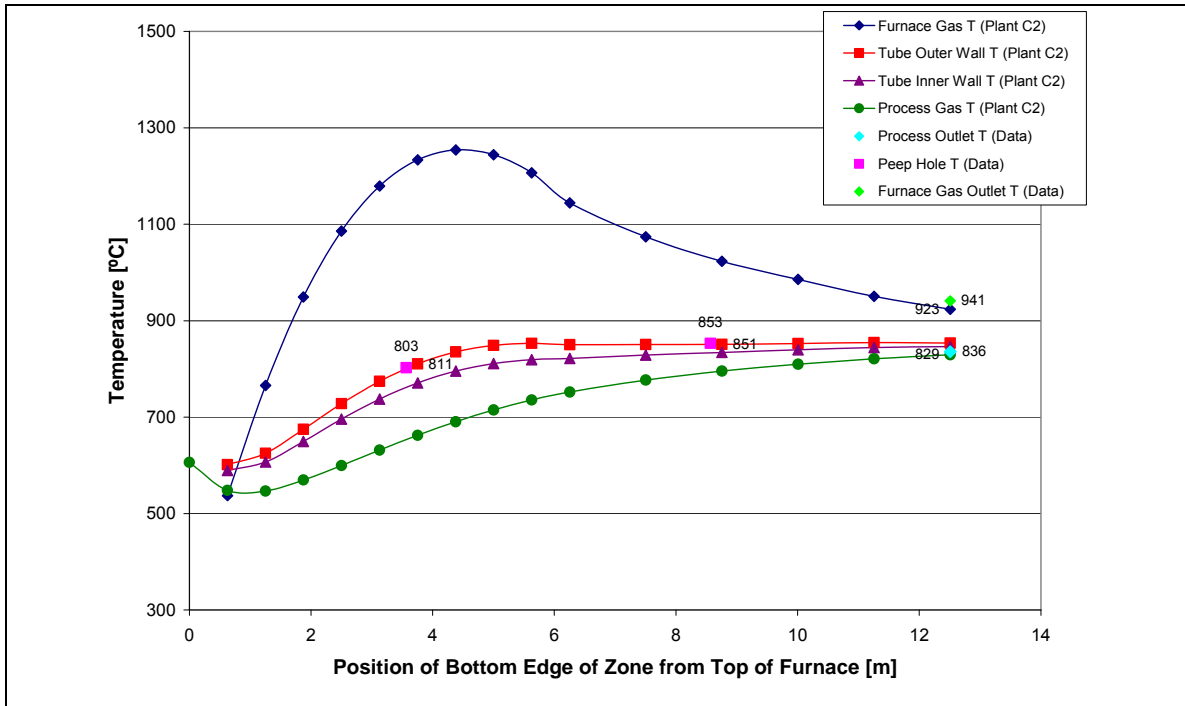


Figure 77. Temperature Profiles Generated using the Inputs from Plant C2 and the Parameter Values from Table 33

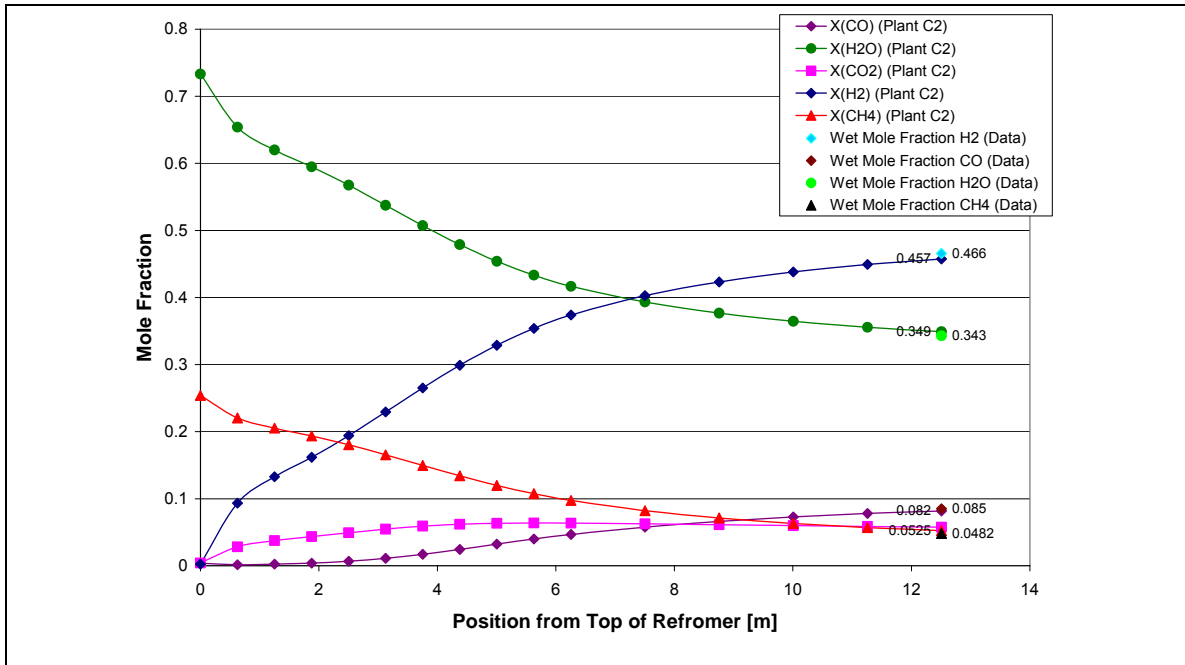


Figure 78. Composition Profiles Generated using the Inputs from Plant C2 and the Parameter Values from Table 33

